

# Classical and Non-Classical Laser Sources for Current and Future Gravitational Wave Detectors

Der Fakultät für Mathematik und Physik  
der Gottfried Wilhelm Leibniz Universität Hannover

zur Erlangung des akademischen Grades  
Doktor der Naturwissenschaften  
Dr. rer. nat.

genehmigte Dissertation von

**M. Sc. Fabian Meylahn**

2022

Referent:	Apl. Prof. Dr. Benno Willke Gottfried Wilhelm Leibniz Universität Hannover
Korreferentin:	Prof. Dr. Michèle Heurs Gottfried Wilhelm Leibniz Universität Hannover
Korreferent:	Prof. Dr. Stefan Hild Maastricht University
Tag der Promotion:	2. Dezember 2022

# Abstract

Current and future gravitational wave detectors (GWDs) place high demands on their sub-systems to reach their sensitivity target. Therefore, the stabilized laser systems and squeezed light sources have to fulfill the highest requirements to allow for the anticipated sensitivity.

Currently, second-generation GWDs use lasers at a wavelength of 1064 nm to measure differential arm length changes in their Michelson interferometers and since 2015 they are detecting gravitational waves. In this thesis, Nd:YVO<sub>4</sub> solid-state laser amplifiers with output powers of up to 114 W and a very high spatial purity down to 2.9% higher order mode content were set up, tested, and integrated into a GWD laser stabilization environment. The amplifiers allowed for low noise and highly reliable operation, such that they were integrated into the laser systems of currently operating GWDs.

Future ground-based third-generation GWDs, like the Einstein Telescope or Cosmic Explorer, are supposed to increase their sensitivity by more than one order of magnitude compared to the current generation. One foreseen improvement is to lower the mirrors' thermal noise by installing cryogenically-cooled silicon mirrors in some of their interferometers. Due to the required transparency of silicon, a change of the laser wavelength to either 1550 nm or 2  $\mu\text{m}$  is necessary. A detailed characterization of laser sources and amplifiers at 1550 nm is presented in this thesis to select a suitable configuration for a GWD laser system at this wavelength. High-bandwidth frequency and power stabilization schemes were designed for the selected laser system, which were tailored for the needs of GWDs. These laser stabilizations were operated simultaneously and characterized by out-of-loop sensors. Independent measurements proved a shot noise limited operation of the power stabilization, below a relative power noise of  $1 \times 10^{-8} \text{ Hz}^{-1/2}$  between 100 Hz to 100 kHz, and a frequency noise down to 400 mHz  $\text{Hz}^{-1/2}$ , achieved with an active frequency stabilization with a unity-gain frequency above 2 MHz.

The generation of strongly squeezed vacuum states of light is a key technology for current and future ground-based GWDs to reach sensitivities beyond their classical quantum noise limit. By employing the stabilized laser system in a newly designed squeezed light source, the direct measurement of up to 11.5 dB squeezing at 1550 nm wavelength over the entire detection bandwidth of future ground-based GWDs ranging from 10 kHz down to below 1 Hz was demonstrated, for the first time in literature. Furthermore, the direct observation of a quantum shot-noise reduction of up to  $(13.5 \pm 0.1)$  dB at MHz frequencies allowed to derive a precise constraint on the absolute quantum efficiency of the photodiodes used for balanced homodyne detection.

All these results provide important knowledge regarding laser systems and squeezed light sources for future GWDs, as well as for the whole field of high precision metrology or cryptography, where ultra-low noise laser systems and non-classical states of light are of great interest.

**Keywords:** stabilized laser system, squeezed states of light, 1550 nm wavelength, 1064 nm solid-state laser amplifier, characterization of lasers, gravitational wave detectors.



# Kurzfassung

Die derzeitigen und zukünftigen Gravitationswellen-Detektoren (GWD) stellen hohe Anforderungen an ihre Teilsysteme, um ihre vorgesehene Empfindlichkeit zu erreichen. Somit müssen auch deren stabilisierte Lasersysteme und Quetschlicht-Quellen die höchsten Anforderungen erfüllen, um die gewünschte Empfindlichkeit zu erreichen.

Aktuell nutzen GWD der zweiten Generation Laser mit einer Wellenlänge von 1064 nm, um die differentiellen Armlängenänderungen in ihren Michelson-Interferometern auszuwerten und so, seit 2015, Gravitationswellen nachzuweisen. In dieser Arbeit wurden Nd:YVO<sub>4</sub>-Festkörperlaserverstärker mit Ausgangsleistungen von bis zu 114 W und mit sehr reinem Strahlprofil, mit nur 2,9 % der Moden in höheren Ordnungen, aufgebaut, getestet und in eine GWD-Laserstabilisierungsumgebung integriert. Die Verstärker ermöglichten einen rauscharmen und äußerst zuverlässigen Betrieb, so dass sie in die Lasersysteme aktueller GWD integriert wurden.

Die geplante, dritte Generation von GWD auf der Erde beinhaltet das Einstein-Teleskop und dem Cosmic Explorer. Gegenüber der aktuellen Generation sollen deren Empfindlichkeiten um mehr als eine Größenordnung gesteigert werden. Eine der vorgesehenen Verbesserungen besteht darin, das thermische Rauschen der Spiegel zu verringern, indem einige der Interferometer mit kryogen gekühlten Siliziumspiegeln ausgestattet werden. Auf Grund der erforderlichen Transparenz von Silizium ist es notwendig, die genutzte Laserwellenlänge auf 1550 nm oder 2  $\mu$ m zu ändern. In dieser Arbeit wird eine detaillierte Charakterisierung von Laserquellen und -verstärkern bei 1550 nm vorgestellt, um eine geeignete Konfiguration für ein GWD-Lasersystem auszuwählen. Für das ausgewählte Lasersystem wurden Frequenz- und Leistungsstabilisierungen mit hoher Bandbreite entwickelt, die auf die Bedürfnisse von GWD zugeschnitten sind. Diese Laserstabilisierungen wurden gleichzeitig betrieben und währenddessen durch unabhängige Sensoren charakterisiert. Diese Messungen belegen einen Schrotrausch-limitierten Betrieb der Leistungsstabilisierung zwischen 100 Hz und 100 kHz, unterhalb eines relativen Leistungsrauschens von  $1 \times 10^{-8} \text{ Hz}^{-1/2}$ . Mithilfe einer aktiven Frequenzstabilisierung mit einer Regelbandbreite von über 2 MHz, konnte das Frequenzrauschen bis auf 400 mHz  $\text{Hz}^{-1/2}$  verringert werden.

Die Erzeugung von stark gequetschten Vakuumzuständen des Lichts ist eine Schlüsseltechnologie für aktuelle und zukünftige GWD auf der Erde, um Empfindlichkeiten jenseits deren klassischer Quantenrausch-Limitierung zu erreichen. Durch den Einsatz des stabilisierten Lasersystems für eine neu entwickelte Quetschlicht-Quelle, konnte zum ersten Mal die direkte Messung von bis zu 11,5 dB gequetschtem Licht im Detektionsband der erwähnten zukünftigen GWD von 10 kHz bis unterhalb von 1 Hz bei einer Wellenlänge von 1550 nm gezeigt werden. Darüber hinaus ermöglichte die direkte Messung der Reduzierung des Quantenrauschens um bis zu  $(13,5 \pm 0,1) \text{ dB}$  bei MHz-Frequenzen eine genaue Bestimmung der absoluten Quanteneffizienz der Fotodioden, die für die Homodyndetektion verwendet wurden.

Diese Ergebnisse liefern wichtige Erkenntnisse für die Lasersysteme und Quetschlicht-Quellen für künftige GWD, sowie für den gesamten Bereich der Präzisionsmetrologie und Kryptographie, bei denen rauscharme Lasersysteme und nichtklassische Zustände ebenfalls von großem Interesse sind.

**Stichwörter:** stabilisiertes Lasersystem, gequetschte Zustände des Lichts, 1550 nm Wellenlänge, 1064 nm Festkörperlaserverstärker, Charakterisierung von Lasern, Gravitationswellen-Detektoren.



---

## Contents

---

<b>1</b>	<b>Introduction</b>	<b>1</b>
1.1	Gravitational waves . . . . .	1
1.2	Current and future ground-based gravitational wave detectors . . . . .	1
1.3	Structure of the thesis . . . . .	4
<b>2</b>	<b>Laser Systems for Gravitational Wave Detectors</b>	<b>5</b>
2.1	Optical layout of a gravitational wave detector . . . . .	5
2.1.1	Quantum noise . . . . .	7
2.1.2	Coating thermal noise . . . . .	8
2.2	Laser system main parameters . . . . .	10
2.3	Technical laser noise in gravitational wave detectors . . . . .	12
2.3.1	Frequency noise coupling . . . . .	12
2.3.2	Frequency stabilization . . . . .	16
2.3.3	Power noise coupling . . . . .	18
2.3.4	Power stabilization . . . . .	19
2.4	Laser system design . . . . .	21
<b>3</b>	<b>Nd:YVO<sub>4</sub> High-Power Master Oscillator Power-Amplifier Laser System for Second Generation Gravitational Wave Detectors</b>	<b>23</b>
3.1	Experimental setup . . . . .	24
3.2	Characterization . . . . .	25
3.3	Integration of a neoVAN-4S-HP into an aLIGO pre-stabilized laser system . . . . .	29
3.4	Power stabilization via pump diode current . . . . .	30
3.4.1	Feedback stabilization . . . . .	32
3.4.2	Stability and noise suppression . . . . .	34
3.5	Conclusion and outlook . . . . .	36
<b>4</b>	<b>Characterization of Laser Systems at 1550 nm Wavelength for Future Gravitational Wave Detectors</b>	<b>39</b>
4.1	Experimental setup . . . . .	40
4.1.1	Characterized laser systems . . . . .	42
4.2	Laser characterization . . . . .	43
4.3	Stabilization . . . . .	50
4.3.1	Multiple-path feedback control . . . . .	51
4.3.2	Stabilized laser frequency . . . . .	55
4.3.3	Laser power stabilization . . . . .	56
4.4	Conclusions and outlook . . . . .	59

<b>5</b>	<b>Stabilized Laser System at 1550 nm Wavelength for Future Gravitational Wave Detectors</b>	<b>61</b>
5.1	Experimental setup . . . . .	62
5.1.1	Pre-mode-cleaner design . . . . .	63
5.1.2	Nonlinear noise coupling . . . . .	64
5.1.3	Seed frequency stabilization . . . . .	67
5.1.4	Frequency stabilization to an isolated reference cavity . . . . .	68
5.1.5	Power stabilization . . . . .	70
5.1.6	Quantum correlation measurement . . . . .	71
5.2	Results and discussion . . . . .	73
5.2.1	Frequency stabilizations . . . . .	74
5.2.2	Power stabilization . . . . .	77
5.3	Conclusion and outlook . . . . .	78
<b>6</b>	<b>Squeezed States of Light for Future Gravitational Wave Detectors at a Wavelength of 1550 nm</b>	<b>81</b>
6.1	Squeezed states of light . . . . .	82
6.1.1	Quantization of the electromagnetic field . . . . .	83
6.1.2	Generation of squeezed vacuum states . . . . .	84
6.1.3	Balanced homodyne detection . . . . .	86
6.1.4	Optical loss and phase noise . . . . .	91
6.2	Experimental setup . . . . .	92
6.3	Quantum efficiency of the used 1550nm photodiodes . . . . .	93
6.4	Bowtie squeezer . . . . .	95
6.5	Squeezed states at low frequencies . . . . .	97
6.6	Conclusion and outlook . . . . .	99
<b>7</b>	<b>Summary and Outlook</b>	<b>101</b>
	<b>Acknowledgments</b>	<b>103</b>
	<b>Bibliography</b>	<b>105</b>
	<b>List of Figures</b>	<b>121</b>
	<b>Appendix</b>	<b>123</b>
A.1	Note on the terms classical and non-classical light . . . . .	123
A.2	Merging data from different signal whitening stages . . . . .	124
A.3	Nonlinear noise coupling simulation . . . . .	125
A.4	Circuit schematics . . . . .	126
	<b>Publications</b>	<b>127</b>
	<b>Curriculum Vitae</b>	<b>137</b>



---

 Acronyms
 

---

AACC	analog automatic current control
AC	alternating current
aLIGO	Advanced Laser Interferometer Gravitational-Wave Observatory
AOM	acousto-optic modulator
AR	anti-reflective
BHD	balanced homodyne detector
BOA	booster optical amplifier, short for the BOA1004P amplifier
BW	bandwidth
CSD	cross-spectral density
CTN	coating thermal noise
DARM	differential arm
DBB	diagnostic breadboard
DBS	dichroic beam splitter
DC	direct current
ECDL	external cavity diode laser
EOM	electro-optical modulator
Er <sup>3+</sup> :Yb <sup>3+</sup>	erbium-ytterbium-doped
ET	Einstein Telescope
ET-HF	Einstein Telescope High Frequency
ET-LF	Einstein Telescope Low Frequency
FFT	fast Fourier transformation
FSR	free spectral range
FWHM	full width at half maximum
GWD	gravitational wave detector
HOM	higher order mode
HP	high power
HR	highly reflective
InGaAs	indium gallium arsenide
KAGRA	Kamioka Gravitational Wave Detector
LIGO	Laser Interferometer Gravitational-Wave Observatory
LISA	Laser Interferometer Space Antenna
LO	local oscillator
MC	mode cleaner cavity
MOPA	master oscillator power amplifier
Nd:YAG	neodymium-doped yttrium aluminum garnet

---

---

Nd:YVO <sub>4</sub>	neodymium-doped yttrium orthovanadate
NPRO	non-planar ring oscillator
O3	third observation run
OPA	optical parametric amplifier
PDH	Pound–Drever–Hall
PIN	positive-intrinsic-negative
PLL	phase lock loop
PMC	pre-mode-cleaner
PPKTP	periodically poled potassium titanyl phosphate
ppm	parts per million
PSL	pre-stabilized laser system
PZT	piezo-electric length control element
QRPN	quantum radiation pressure noise
RAM	residual amplitude modulation
RBW	resolution bandwidth
RF	radio frequency
RMS	root mean square
RPN	relative power noise
SHG	second harmonic generator
SN	shot noise
SQZ	squeezed states
UGF	unity-gain frequency
ULE	ultra-low expansion glass ceramic
VBW	video bandwidth

---

## List of Symbols

---

$c$	speed of light
$\delta\alpha(t)$	tilt of the Gaussian beam
$d_{coating}$	coating thickness
$\delta x(t)$	transverse shift of the Gaussian beam
$\varepsilon(t)$	complex beam pointing parameter
$\mathcal{F}$	cavity finesse
$f_{eff}$	corner frequency of the laser amplifier transfer function
$f$	measurement (Fourier) frequency
$f_p$	(average) pole frequency of a cavity
$h$	gravitational strain
$\hbar$	reduced Planck constant
$h_{QRPN}(f)$	equivalent gravitational strain for the quantum radiation pressure noise
$h_{SN}(f)$	equivalent gravitational strain for the shot noise
$L$	average length of the interferometer arms or cavity length
$l$	optical path length
$\lambda$	laser wavelength
$m$	(mirror) mass
$n$	refractive index
$\nu$	optical laser frequency
$P$	(laser) power
$\phi_{eff}(T)$	effective mechanical loss angle (of the coating)
$P_{intra}$	intra-cavity light power
$P_{trans}$	power in transmission of the cavity
$R_1$	power reflectivity of the incoupling mirror
$R_2$	power reflectivity of the outcoupling mirror
$S_\nu$	amplitude spectral density of the laser frequency noise
$S_P$	amplitude spectral density of the laser power noise
$S_{rel. CSD}$	relative amplitude spectral density of the cross-correlation
$S_\varphi$	amplitude spectral density of laser the phase noise
$T$	(coating) temperature
$T_1$	power transmissivity of the incoupling mirror
$T_2$	power transmissivity of the outcoupling mirror
$\Theta_D$	half divergent angle of the Gaussian beam
$w_0$	Gaussian beam waist radius
$w_{beam}$	laser beam radius

---

---

$\hat{a}$	annihilation operator
$\hat{a}^\dagger$	creation operator
$\alpha$	coherent amplitude
$\chi^{(2)}$	second-order nonlinear susceptibility
$ \alpha\rangle$	coherent state
$\Delta^2$	variance of an operator
$\delta(f)$	Dirac delta function
$\hat{E}(t)$	electric field operator
$E_0$	electric field amplitude
$\varepsilon$	balanced homodyne detector imbalance
$\eta$	optical efficiency
$\mathcal{F}[\ ]$	Fourier transformation
$k$	wave number
$ \Psi\rangle$	quantum state $\Psi$
$\Delta^2 \hat{X}_+$	normalized variances of the anti-squeezed quadrature
$\Delta^2 \hat{X}_-$	normalized variances of the squeezed quadrature
$\phi$	quadrature angle or phase
$P_{thr}$	threshold power
$\hat{S}(\xi)$	squeezing operator
$\tau$	time delay constant
$\theta_{pn}$	standard deviation of the phase noise
$ 0\rangle$	vacuum state
$\hat{X}_1$	amplitude quadrature operator
$\hat{X}_2$	phase quadrature operator

---

# CHAPTER 1

---

## Introduction

---

### 1.1 Gravitational waves

Since 14 September 2015, the detection of gravitational waves has opened a new view at the Universe by detecting signals of inspiraling black holes and neutron stars. Gravitational waves are ‘ripples’ in the fabric of space-time, theoretically predicted as solutions of general relativity’s linearized field equations. Accelerated masses that generate a time variation of their quadrupole moment emit gravitational waves, which propagate with the speed of light [Sau16]. The first direct detection of gravitational waves was made in 2015 by the two Advanced Laser Interferometer Gravitational-Wave Observatories (aLIGOs) [Aas15], located in the United States. The origin of this detected wave was attributed to the inspiral and collision of the most compact objects in the Universe, two black holes, which were about a billion light-years away from Earth [Abb16]. Since then, a network of gravitational wave detector (GWD) has measured signals from inspiraling and merging binaries of neutron stars, black holes, and neutron star black hole systems [Abb20a].

The gravitational wave catalogs summarize and compare these detections from the observation runs in the recent years and currently contain 90 gravitational wave events [Abb21e; Abb21a; Abb20b; Abb19]. In 2017, the GWD network and various optical instruments recorded the first multi-messenger detection, originating from a binary neutron star merger [Abb17a; Abb17d].

These detections improved the understanding of astrophysical and cosmological processes, like the Universe’s expansion [Abb17c; Abb21d], the neutron stars’ equation of state [Abb18], the population and creation of black hole binaries [Abb21b; Abb21g; Ng21] or tests of the general theory of relativity [Abb21c; Abb21f].

Future observation runs with improved sensitivities of current second-generation and planned third-generation GWDs will allow for even more detections with perhaps new signals originating, e.g., from supernovae [Sri19], deformations of neutron stars causing continuous gravitational waves [Abb22b] or the post-merger of collided binaries [Abb17b; Cla16]. This could lead to better insights into the evolution of our Universe, the regimes of strongest gravity, and the dynamics of highly dense matter [Mag20; Eva21].

### 1.2 Current and future ground-based gravitational wave detectors

Gravitational waves can be detected by precise measurements of the distances between free-falling masses. A passing gravitational wave would change the lengths differently along perpendicular two axes, as shown in Figure 1.1 as time snapshots of a ring of free-falling masses. Hence, we typically define the gravitational wave strain  $h$  by the relative length

change along two orthogonal axes  $x$  and  $y$  to be [CM22]:

$$h = \frac{\Delta L_x - \Delta L_y}{L} = \frac{\Delta L}{L}, \quad (1.1)$$

for an average measurement length of  $L$  and an induced differential length change of  $\Delta L = \Delta L_x - \Delta L_y$ . A gravitational wave traveling perpendicular to the measurement directions will cause the highest strain amplitude if its polarization is aligned with the measurement directions.

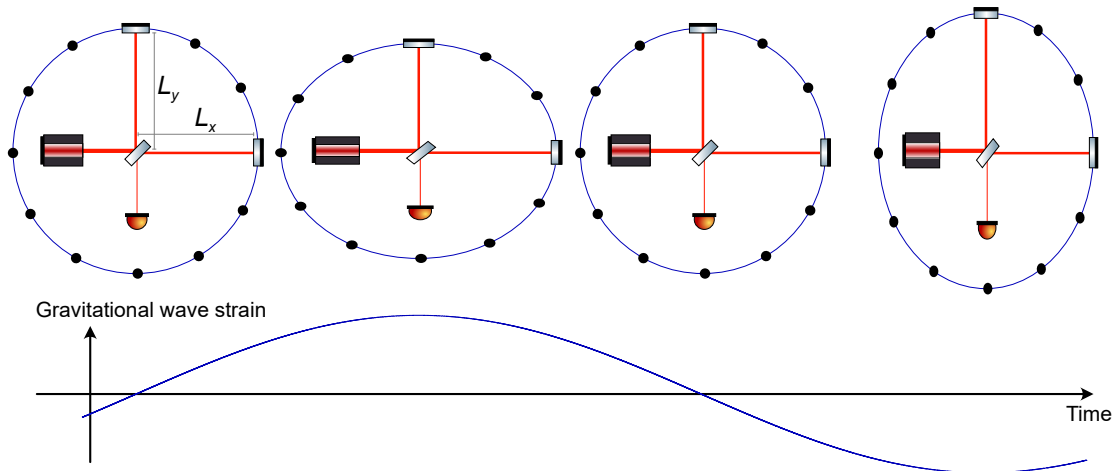


**Figure 1.1:** A gravitational wave affects the distances between free-falling masses, depicted as time snapshots for a ring of these masses. A passing gravitational wave, with a polarization parallel to the shown Michelson interferometer arms, compresses and stretches the distance between the masses and thereby causes a modulation of the interferometer’s output signal.

This measurement principle can be realized on Earth in a Michelson laser interferometer with suspended mirrors, which is shown in the mass ring in Figure 1.1. Here, the length difference between the two interferometer arms is measured by the phase difference of the two interfering beams at the beam splitter. This phase difference causes a signal at the detector output.<sup>1</sup>

With this technique, the successful detection of gravitational waves became possible with the second generation of ground-based GWDs, which detect gravitational wave strains even below  $1 \times 10^{-21}$ . These GWDs are highly complex instruments, with km-scale interferometer arms and they use several signal enhancement techniques to reach this sensitivity in a frequency band between 20 Hz and a few kHz. In general, their sensitivity to gravitational waves can be characterized by the measured or predicted sum from all noise sources projected to the strain measurement. A frequency-domain representation of this total noise is the amplitude spectral density of the sum of the projected noise, which allows comparing the sensitivities of the second to the third-generation GWDs in Figure 1.2.

The second-generation GWDs are, at the time of writing this thesis, the current GWDs: the two aLIGO [Aas15] located in Livingston and Hanford in the United States with 4 km

<sup>1</sup> See Chapter 2 and Figure 2.1 for a more detailed explanation of a GWD.

arm-length, and the Advanced Virgo detector [Ace15] in Cascina, Italy, with 3 km long arms. In addition, the GEO600 detector in Ruthe, Germany, with 600 m long folded arms, and the Kamioka Gravitational Wave Detector (KAGRA) [KAG19; Aku20] in Hida, Japan, with 3 km long arms, are large-scale interferometric GWs demonstrating technology for current and future GWs, but have not yet detected gravitational waves.

KAGRA is already testing proposed improvements for the next and third generation of GWs. It is located underground to lower the coupling of local gravitational gradients and seismic noise. Cryogenic cooling of its interferometer mirrors should help to reduce thermal-noise induced position fluctuations of the reflection points at the mirrors.

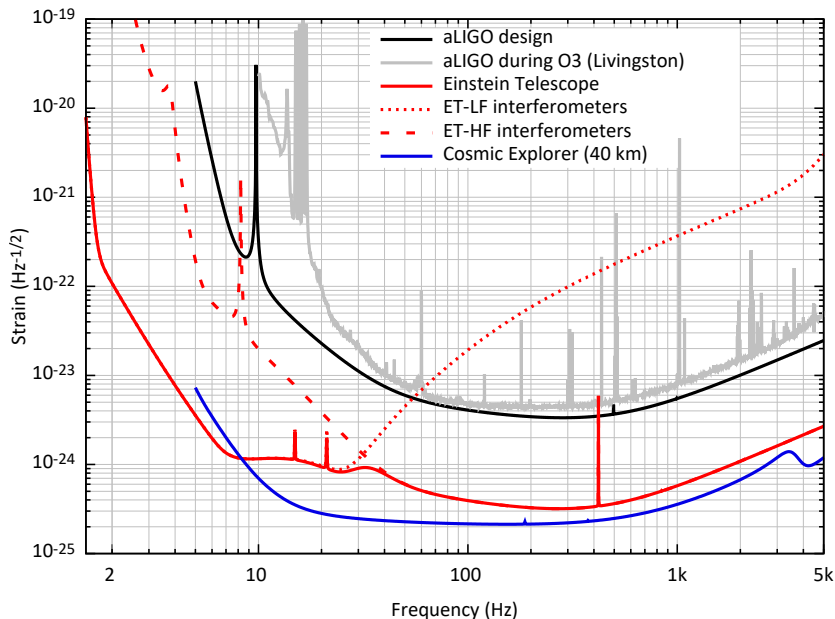


**Figure 1.2:** The amplitude spectral density of the strain sensitivity of a current GWD, aLIGO, is compared to future proposed third-generation ground-based GWs. The sensitivities to gravitational waves should increase for the third generation of GWs, like the Einstein Telescope or Cosmic Explorer, by more than a factor of 10. Such a sensitivity improvement would result in a significant increase in the observable part of the Universe. The measured sensitivity of aLIGO (grey line) contains more noise sources than considered for the design sensitivity (black curve), and some design requirements were not completely achieved. Hence, the aLIGO design sensitivity is not fully met by the detector in Livingston during the third observation run (O3). Data sources: [Bar18; ET 18; Kun22; Eva20].

A third generation of GWs is currently under development, with the goal of significantly improved sensitivities accompanied by more stringent requirements for all detector subsystems. The Einstein Telescope and the Cosmic Explorer are the two most developed proposals for third-generation ground-based interferometric GWs [ET 20; Rei19a].

The actual design of the Einstein Telescope (ET) proposes a detector composed of six Michelson interferometers arranged in a 10 km long, triangular configuration [ET 20]. These interferometers will be placed underground on a site in Europe. Three shall operate as the Einstein Telescope High Frequency (ET-HF) interferometers with high

laser powers and mirrors at room temperature, covering the upper gravitational wave detection band. The other three are colocated to the ET-HF interferometers. They are the Einstein Telescope Low Frequency (ET-LF) interferometers with higher sensitivity at lower detection frequencies, utilizing cryogenically cooled optics and lower laser powers.

The Cosmic Explorer design proposes one or two on-ground detectors located in the United States with 20 km or 40 km arm length [Eva21]. Depending on the upgrade stage, room temperature or cryogenically cooled interferometer optics are proposed.

To further extend the spectrum of observable gravitational waves, other kinds of GWDs are in development [Bai21], like the space-based Laser Interferometer Space Antenna (LISA) [Bak19], which is designed to measure gravitational waves in the mHz band.

### 1.3 Structure of the thesis

This thesis will focus on the two important light sources needed in ground-based GWDs. First, the main laser system that provides the classical, coherent light field for interferometric length measurements. Second, a squeezed light source for future detectors to improve their quantum noise limitation with non-classical states of light.<sup>1</sup>

In Chapter 2, the optical setup of a ground-based interferometric GWD is introduced to discuss the demands on the laser system and the use of squeezed light. Based on the description of the quantum noise and the coating thermal noise in the detector, the main parameters of the laser system and the need for squeezed vacuum states coupled to the detector output are discussed. Finally, a description of technical laser frequency noise and power noise coupling motivates the design concept of the laser system and the need for laser stabilization.

With this understanding of the laser source requirements, two single-pass solid-state laser power amplifiers at 1064 nm wavelength were characterized for the second-generation GWDs. The results are presented in Chapter 3. In addition, the integration into a GWD laser stabilization environment and the power stabilization via the amplifier's pump current is shown.

The following part of the thesis will focus on light sources for third-generation GWDs. The proposed Einstein Telescope requests novel laser systems at 1550 nm for the ET-LF interferometers, to be compatible with cooled silicon optics [ET 20]. A detailed characterization of different laser sources and amplifiers at this wavelength, as well as a test of their actuators for laser stabilization is presented in Chapter 4. Based on these results, a prototype of a stabilized laser system was set up and is presented in Chapter 5. Sensors for laser frequency and power, which are independent of the sensors used for laser stabilization, allow for a complete characterization of the stabilization performance.

With the optimized laser system presented in Chapter 5, which is suited for the needs of future GWDs, a squeezed light source is operated to demonstrate the required generation and efficient detection of squeezed states of light at 1550 nm wavelength in the entire detection band of third-generation GWDs. Chapter 6 shows the setup and measurement results with two different squeezed light sources, concluding with the achieved squeezing levels at MHz frequencies and in the detection band of GWDs.

Finally, Chapter 7 provides a conclusion and an outlook.

---

<sup>1</sup> See appendix A.1 for a note on the terms classical and non-classical.



# CHAPTER 2

---

## Laser Systems for Gravitational Wave Detectors

---

To achieve the design sensitivity of a gravitational wave detector (GWD) requirements are placed to all its subsystems. These requirements shall ensure that the sum of all noise sources coupling to the detector is low enough to measure the gravitational wave strain  $h$  (see Equation 1.1) of gravitational waves. This thesis will focus on investigating two main light sources of a ground-based, interferometric GWD: the pre-stabilized laser system (PSL), also referred to as laser system, which provides the high power beam for the interferometric differential arm length sensing and the squeezed vacuum light source, which helps to overcome the quantum noise limitation of the gravitational wave detection.

Usually, the design of a subsystem places requirements on other subsystems. This leads to an iterative process of defining requirements for the subsystems (to be discussed in Section 2.3.1) and ideally results in the best trade-off between optimization efforts at different systems. Since the detailed design of future proposed GWDs is currently still under discussion, detailed requirements for their subsystems have not yet been defined. Nevertheless, the understanding of the limitations in current GWDs helps to predict important characteristics, which will be needed for the future proposed GWD's subsystems. Since the sensitivity of these future GWD shall be improved significantly compared to current detectors, see Figure 1.2, they will most likely impose more stringent requirements than the current generation to the subsystems.

This chapter starts by introducing a simplified optical layout of a ground-based, interferometric GWD. In the same section, two important fundamental noise sources in GWDs are introduced: quantum noise in Subsection 2.1.1 and coating thermal noise in Subsection 2.1.2. These two noise sources will be the base to understand the requirements for the laser system investigated in this chapter. The next two sections will focus on the needed laser system for interferometric GWDs. They will start with basic laser parameters in Section 2.2 and followed by the coupling and stabilization of laser frequency and power noise in a GWD in Section 2.3. In Section 2.4, the results from the previous sections are related to the design of laser systems for GWDs.

### 2.1 Optical layout of a gravitational wave detector

The basic optical layout of the detector has to be considered for further discussion of the demands on the main laser system. Figure 2.1 shows the sketch of a simplified optical layout of a GWD like one of the aLIGO [Aas15] or the Advanced Virgo Plus detector [Ace15; Fla20].

First, the laser beam provided by the laser system is coupled into the main vacuum system (not shown on the Figure 2.1) of the GWD, which hosts the suspended optics.

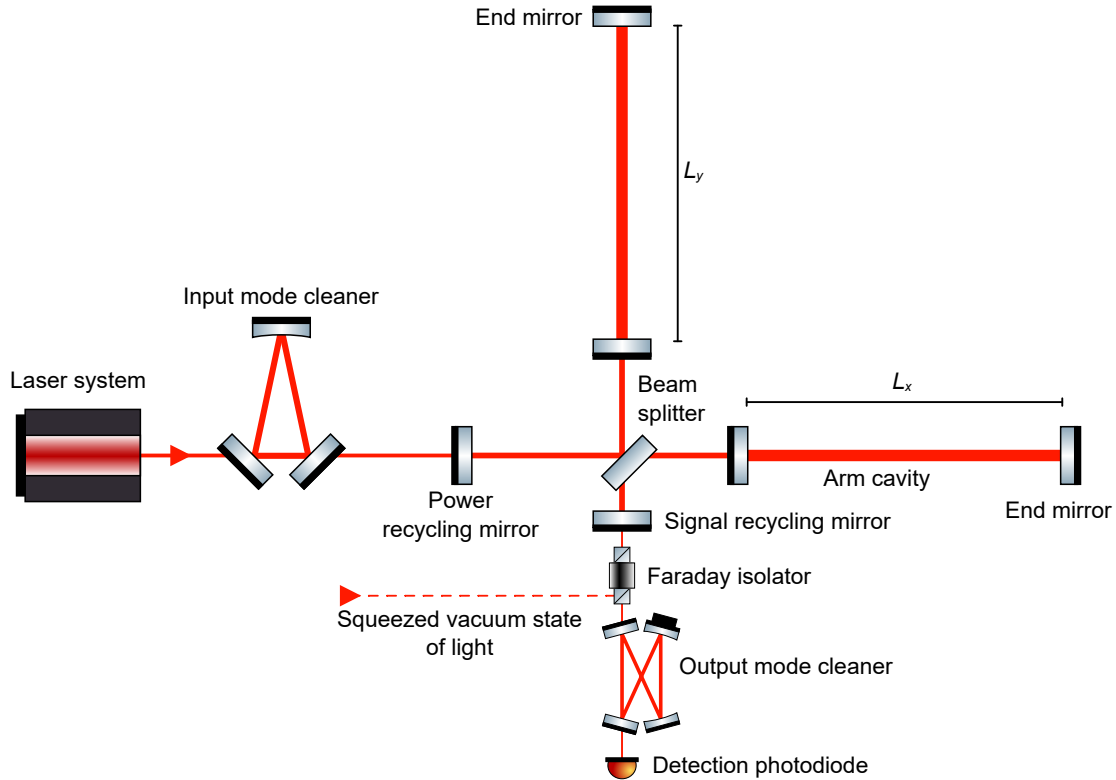


**Figure 2.1:** Simplified optical layout of a typical ground-based gravitational wave detector. The laser beam is filtered by a suspended mode cleaner cavity and is injected to the main interferometer. The beam splitter of the Michelson interferometer equally distributes the beam power to the two interferometer arms, where the laser power builds up in the arm cavities. A differential arm length change, e.g. from a gravitational wave, results in a signal that is resonantly amplified by the signal recycling cavity and leaves the interferometer towards the signal recycling mirror. This leaking signal field is filtered in its spacial mode by an output mode cleaner. For the detection of the signal a photodiode is placed at the transmission port of the output mode cleaner. For quantum noise improvement, a squeezed state of light can be injected to the output port of the interferometer via a Faraday isolator.

This beam passes an input mode cleaner cavity, which filters the laser noise at high frequencies (see Figure 2.4 below), cleans the spatial laser mode, filters the polarization, and reduces beam pointing noise [Mue16]. The transmitted light of the input mode cleaner cavity is sent to the Michelson interferometer of the GWD, where the gravitational waves cause a differential phase modulation of the beams in the two interferometer arms. This modulation is converted to amplitude modulation at the beam splitter and can then be detected with the output photodiode. This arm-cavity enhanced Michelson interferometer is operated close to the dark fringe of the output port. Therefore, most of the laser power is back-reflected to the input port. To reuse this laser power, the power recycling mirror is tuned to resonance of the cavity formed together with the interferometer. This leads to a laser power build up inside the interferometer, which is typically higher than the power at

the output of the laser system. Furthermore, the arm cavities on resonance additionally increase the circulating laser power between end mirrors and the inner test masses of the Michelson interferometer. In the case of the aLIGO detectors, power recycling gains are 44 to 47 leading to up to 240 kW circulating power in the arm cavities, with laser powers of up to 38 W in transmission of the input mode cleaner [Bui20b].

This laser power enhancement by the arm cavities and power recycling cavity is important in order to increase the signal-to-noise ratio at the detector readout, due to shot noise, as it will be explained in the next subsection.

### 2.1.1 Quantum noise

The classical quantum noise limitations in a GWD can be expressed as the incoherent sum of the quantum radiation pressure noise (QRPN) and shot noise (SN). They can both be understood in the photon picture, by the quantum nature of light where the photons arrival's time at a certain location follows a Poisson distribution [Sau16]. The photodetector at the GWD output experience this noise in form of shot noise, which can be expressed as an equivalent strain  $h_{\text{SN}}(f)$  of a signal detected by the GWD. The quantum radiation pressure noise is caused by the momentum transfer of the Poisson distributed photons being reflected at the suspended mirrors of the interferometer. This momentum transfer in combination with the gravitational restoring force of the suspended mirrors result in mirror motion. These movements of the interferometer mirrors cause a relative phase modulation of the beams interfered at the beam splitter that can be expressed as an equivalent strain  $h_{\text{QRPN}}(f)$ . The amplitude spectral densities due to shot noise and quantum radiation pressure noise can be expressed for a simple Michelson interferometer with an input power of  $P$  [Sau16] as

$$h_{\text{SN}}(f) = \frac{1}{L} \sqrt{\frac{\hbar c \lambda}{2\pi P}}, \quad (2.1)$$

$$h_{\text{QRPN}}(f) = \frac{1}{mL} \frac{1}{f^2} \sqrt{\frac{\hbar P}{2\pi^3 c \lambda}}. \quad (2.2)$$

Here  $c$  is the speed of light,  $\hbar$  the reduced Planck constant, and  $\lambda$  the wavelength of the laser light. The equations show that with increasing average length  $L$  of the interferometer arms, the quantum noise limitations improve. The radiation pressure noise contribution depends on the measurement frequency  $f$  following  $1/f^2$  for frequencies larger than the resonance of the mirror suspensions. In addition to that, the contribution of quantum radiation pressure noise term decreases with increasing mirror mass  $m$ , but increase with the square root of the laser power  $P$  inside the interferometer. In contrast to that, the shot noise contribution shows no frequency dependence and decreases with an increased laser power  $P$ . Hence, the contribution of quantum radiation pressure noise is usually larger than shot noise at low frequencies.

The quantum noise limitation of a dual recycled Michelson interferometer with arm cavities, like current operating GWDs, is further shaped by the response of the detector. This is determined by the pole frequency of the arm cavities as well as the pole frequency and tuning of the signal recycling cavity. As described above, the arm cavities of the

Michelson interferometer lead to a significant increase of the laser power  $P$  used to sense gravitational waves. But they also limit the response of the detector at frequencies above the pole frequency of the arm cavities. This can be seen in Figure 2.2 that shows the noise budget of an aLIGO Michelson interferometer. In that figure, the total quantum noise is plotted, besides other important noise contributions that limit the sensitivity for detecting gravitational waves.

The signal-to-noise ratio due to quantum noise can further be improved by injecting quadrature squeezed states of light in the output port of the Michelson interferometer. These states of light show a decrease in uncertainty in one of their measurement quadratures, which are linearized descriptions of the light phase and amplitude, as further discussed in Chapter 6. Depending on the quadrature in which the quantum noise is reduced, the shot noise or the quantum radiation pressure noise lowers. This technique is used in current GWDs [Tse19; Ace19] and was first demonstrated for a large scale GWD in the GEO600 detector [Aba11].

For future GWDs and the updates of second-generation GWDs, it is proposed to inject squeezed vacuum states with a frequency depending squeezing angle in order to reduce the quantum radiation pressure noise at low frequencies and the shot noise at high measurement frequencies. Thereby, at all frequencies the quantum noise limitation of the detector can be improved.

Another proposed modification is the update of the readout scheme of GWDs from the currently used direct current (DC) readout to a balanced homodyne readout [Eva21; ET 20]. In the DC readout scheme the interferometer is operated with a DC offset from the dark fringe. Hence, a low power light field is leaking to the output port of the interferometer and this field is used as the local oscillator to enhance the signal sideband detection.

In the balanced homodyne detector (BHD) readout scheme a separate local oscillator field is overlapped with the signal field at a 50:50 beam splitter in the detector output. This allows to operate the Michelson interferometer at the dark fringe without a DC offset and further more to read out an arbitrary quadrature of the signal field [FEF14]. Depending on the chosen readout angle, quantum noise correlations can cancel the quantum radiation pressure noise in a small frequency band [Kim01]. By the balanced detection, which is the detection of the signal at both output ports of the 50:50 beam splitter, technical power noise of the local oscillator beam can be subtracted. Nevertheless, the complexity of the readout scheme is increased with the BHD and thereby additional noise sources, like the phase noise or beam pointing of the local oscillator beam, have to be tackled [FEF14].

### 2.1.2 Coating thermal noise

Not only the quantum nature of the laser beam adds noise to the GWD readout but also the effective point of reflection for the laser beam at the interferometer mirrors is noisy due to thermal noise. A detailed introduction of thermal noise in GWDs can be found in [Sau16]. In Figure 2.2, the thermal noise contribution due to suspension, substrate and coating thermal noise (CTN) is shown and it is dominated above 30 Hz by the CTN of the arm cavity mirrors. This CTN is dominated by Brownian thermal noise of the dielectric coating on the mirrors. The CTN mitigation is one important criteria for the selection of the mirror materials and by that the possible laser wavelengths are constrained.

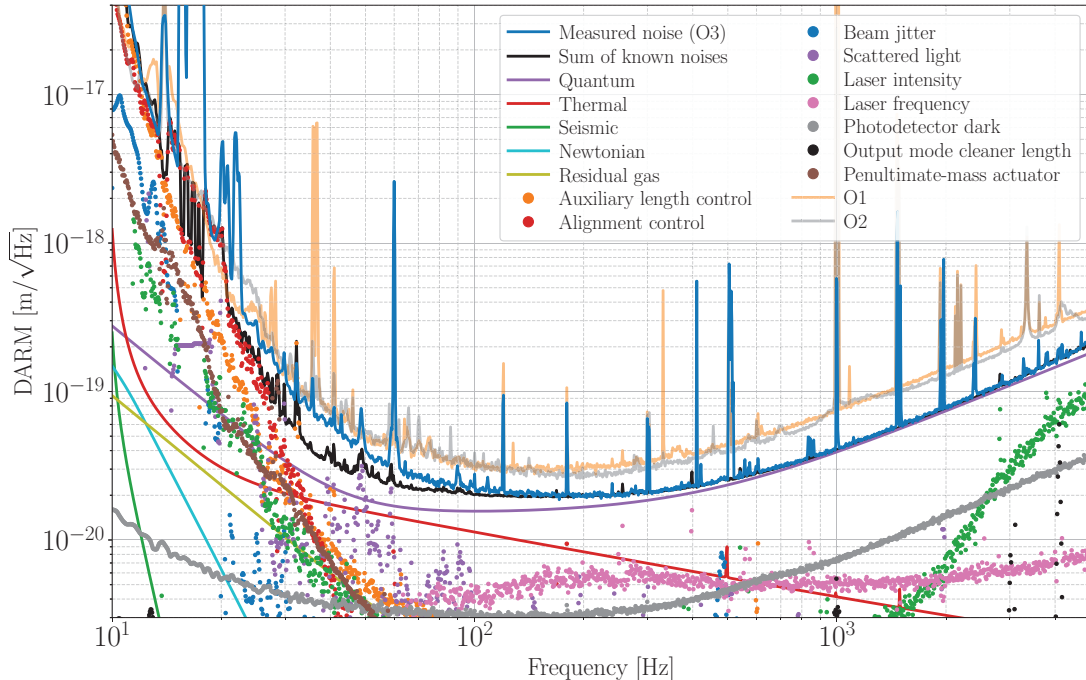


**Figure 2.2:** The noise budget of aLIGO Hanford during the O3 is shown, as an example for the noise budget of second-generation GWDs. The noise is calibrated as an equivalent to differential arm (DARM) length change. Dividing by the 4 km arm length of the detector, this would be a equivalent gravitational wave strain  $h$ . The calculated noise contributions are plotted in solid lines and measured noise contributions are shown as dots. The total noise in the previous observation runs are also shown. This Figure was published in [Bui20b] and the file source is [Bui20a].

The Brownian thermal noise caused by the dielectric mirror coating can be related to an equivalent gravitational wave strain as [YGE15; Abb17e]:

$$h_{\text{CTN}}(f) \propto \frac{\sqrt{T d_{\text{coating}} \phi_{\text{eff}}(T)}}{w_{\text{beam}} L} \frac{1}{\sqrt{f}}$$

The noise level is proportional to the square root of the coating temperature  $T$ , its thickness  $d_{\text{coating}}$  and the temperature dependent effective mechanical loss angle of the coating  $\phi_{\text{eff}}(T)$ , which contains the material parameters of the coating and its structure. With increasing beam radius  $w_{\text{beam}}$  on the mirrors and the interferometer arm length  $L$  the contribution of the CTN to the total detector noise decreases. The measurement frequency dependence of the noise scales approximately with  $f^{-1/2}$  [GE18].

Different approaches are proposed to lower the thermal noise that already limits current GWDs in the mid frequencies of their detection band [Bui20b]. One possibility

is to increase the beam diameter on the optics, which requires larger optics and vacuum tubes but also helps to reduce the quantum radiation pressure noise due to higher mirror mass (see Equation 2.2). Another approach is the optimization of the coating material for a lower effective loss angle and lower coating thickness, e.g. by multilayer coatings [YGE15; Cra19].

Furthermore the temperature of the mirrors can be decreased from room temperature to cryogenic temperatures. As long as with lower temperatures the effective mechanical loss angle of the coating  $\phi_{\text{eff}}(T)$  does not degrade, the CTN reduces. For fused silica mirrors, as used in the second-generation GWDs, the mechanical loss angle increases with decreasing temperature but for sapphire and silicon not. Sapphire mirrors are compatible with the currently used wavelength in GWDs of 1064 nm and are implemented in the first cryogenic km-scale GWD KAGRA [Aku19]. In comparison to sapphire, silicon is available for larger mirror sizes but requires a change of the laser wavelength to 1550 nm or to the 2  $\mu\text{m}$  region for low transmission loss [ET 20; Eva21; Deg13; Adh20].

## 2.2 Laser system main parameters

Ground-based, interferometric GWDs are significantly more complex than the optical layout presented in Figure 2.1 and have several more noise sources than shown in Figure 2.2. However, the simplified description along with the thermal and quantum noise will be sufficient to discuss the requirements imposed on the main laser systems for GWDs in this section.

The above described optical GWD design and noise limitations constrain the parameters of the main laser system for the GWD: The wavelength, the spatial mode, and the power level of the laser beam form the base parameters of a laser system needed for a GWD. In Tabular 2.1 the wavelength and power level of the laser systems for second and third-generation ground-based GWDs are compared.

The wavelength defines the spatial oscillation period of the coherent electromagnetic laser field. Hence, this is the scale for the readout of the Michelson interferometer of a GWD. The wavelength for a GWD is chosen by the trade-off between good characteristics<sup>1</sup> of available laser sources, low absorption mirror materials, available high quantum-efficiency photodetectors, and expected light scattering [ET 20; Eva21].

For second-generation GWDs a laser wavelength of 1064 nm was chosen. A non-planar ring oscillator (NPRO) made from neodymium-doped yttrium aluminum garnet (Nd:YAG) [KB85] is used as the seed laser for laser amplifiers. The single-pass amplification in solid state neodymium-doped yttrium orthovanadate (Nd:YVO<sub>4</sub>) amplifiers was used in the last and third observing run in current GWDs to reach the needed laser power levels (see Chapter 3). Some future GWDs take another approach for the improvement in the mid region and lower frequency range of the detection band: The CTN shall be decreased by cryogenic cooling of the interferometer mirrors, which shall be therefore made out of silicon. As silicon shows high absorption at a laser wavelength of 1064 nm, the use of laser sources at 1550 nm or in the 2  $\mu\text{m}$  region is proposed [ET 20; Rei19b; Eva21].

---

<sup>1</sup> Like available power levels and laser noise, which is discussed in the following sections.

**Table 2.1:** Overview of the laser wavelength and power for current and future GWDs.**Current detectors**

Detector	Wavelength	Input power <sup>a</sup>	Comments
aLIGO [Aas15]	1064 nm	up to 125 W	In O3 limited to less than 40 W due to radiation pressure induced instabilities and absorption of the test masses [Bui20b].
Advanced Virgo [Ace15]	1064 nm	up to 125 W	Typically 18 W were injected to the main interferometer during O3 [Ace19].
KAGRA [LCG09; Aku20]	1064 nm	75 W	Cryogenic cooled sapphire interferometer mirrors used with 5 W after O3 [Abb22a; KAG22].

**Future detectors**

ET-LF [ET 20]	1550 nm	3 W	Interferometer with cryogenic cooled silicon interferometer mirrors.
ET-HF [ET 20]	1064 nm	500 W	Room temperature interferometers to covering the mid and high frequency detection band.
Cosmic Explorer [Rei19b; Eva21]	1064 nm or 2 $\mu$ m	140 W or more	Either as a room temperature detector or with cryogenic cooled silicon interferometer mirrors.

<sup>a</sup> Depending on the injection power loss to the interferometer, about 40% more laser power is needed from the laser source.

The spatial profile of the laser beam in current GWDs is the fundamental Gaussian mode. This mode is an eigenmode of optical resonators with spherical curved mirrors and is thereby highly compatible with the interferometer optics [BK62]. Because of this high compatibility with optical cavities and low susceptibility to optics' imperfections, the fundamental Gaussian mode profile is also proposed for third-generation GWDs.

The output power level of the laser system in combination with the power recycling gain and arm cavity power build up has to match the desired quantum noise level, discussed in Section 2.1.1. Future proposed GWDs take two different approaches on the laser systems to increase their sensitivities. The first approach, increasing the laser power results in a reduction of the readout shot noise, which improves the detector sensitivity at the higher detection frequencies, proposed for the Cosmic Explorer and ET-HF interferometers [ET 20; Eva21]. As a penalty, this will cause an increase in quantum radiation pressure noise at lower frequencies that can be tackled for example, by increasing the mass of the interferometer mirrors. The second approach is to operate the interferometer at a lower power level to improve the quantum noise limited sensitivity at low frequencies, as proposed for the



ET-LF interferometers [ET 20].

Finally, a reliable long-term operation and stability is required for all of the GWD's laser systems, as typical observation runs last more than a year. Necessary readjustments, repairs, or replacements reduce the amount of science data containing potential gravitational wave signals. Besides the basic parameters presented in this section, the stability of the laser frequency and power are crucial parameters of a laser system for GWDs. The coupling of these technical laser noise sources to the GWD readout and the noise reduction are discussed in the following section.

### 2.3 Technical laser noise in gravitational wave detectors

High precision measurements usually require the control of several noise sources, which could disturb or mask the measurement. A common approach is to avoid noise and fluctuations by e.g. choosing a low noise laser source. The reduction of the coupling to the measurement signal is another approach, e.g. by the common mode rejection of the noise. Finally, a stabilization of relevant laser parameters to reach the necessary noise level for the measurement could be needed, like the here discussed active and passive laser stabilization.

The coupling of technical and fundamental noise sources to the GWD output signal can be depicted in the so-called noise budget of a GWD. As a typical example of the noise budget of a current GWD, Figure 2.2 shows the noise budget from the aLIGO Hanford detector during the O3 [Bui20b]. Based on such noise budgets, it is possible to confirm the validity of simulated noise coupling models by comparison to the measured noise coupling strength. Consequently, this can test the set requirements for the subsystems of the current GWDs. The models for noise coupling paths can further be used to infer couplings for proposed detectors and the resulting noise requirements for their subsystems.

The laser noise coupling for current and future GWDs are presented in the following subsections in detail, based on the discussion in references [CMS21], and [Som06; Som07]. The discussion of the noise budget in Figure 2.2 [Bui20b] is constrained to curves relevant in the context of the laser system.

#### 2.3.1 Frequency noise coupling

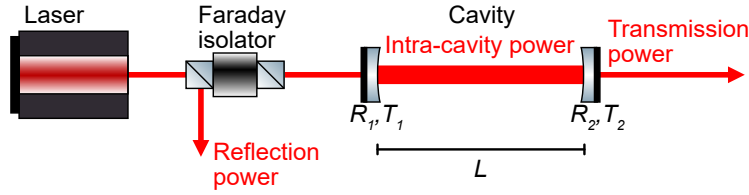
The frequency noise of a laser is the fluctuation of its instantaneous frequency, which can be measured by comparing it to a stable frequency reference. In the context of GWDs commonly the resonance frequency of optical cavities is compared to the laser frequency. This can be used to determine the frequency noise of a laser beam, if the optical cavity resonance frequency is of higher stability. For further discussion of the noise coupling mechanisms, properties of optical cavities are introduced below.

Figure 2.3 shows the linear configuration of an optical cavity.<sup>2</sup> The optical path length  $l = 2nL$  of the cavity is defined by the refractive index  $n$  of the medium between the mirrors and the distance between the mirrors  $L$ . The intra-cavity light power  $P_{intra}$  of a lossless<sup>3</sup>

<sup>2</sup> For cavities with more mirrors, the parameters of the second mirror can be extended in the formulas by the properties of the other mirrors, like the multiplication of all reflectivities.

<sup>3</sup> Intra-cavity losses can be modeled by a reduced power reflectivity of one cavity mirror.





**Figure 2.3:** Schematic view of a laser beam coupled to an optical cavity. Main characteristics of the cavity are defined, by the distance  $L$  between the mirrors, the power reflectivities  $R_1$ ,  $R_2$  of the mirrors and their power transmissivities  $T_1$ ,  $T_2$ . The curvature of the mirrors define the stability, resonance conditions and beam parameters of the resonating modes in the cavity.

cavity can be calculated to be [Bon16]:

$$P_{intra} = \frac{T_1}{1 + R_1 R_2 - 2\sqrt{R_1 R_2} \cos(2\pi l/\lambda)}, \quad (2.3)$$

with the power reflectivities  $R_1$ ,  $R_2$  of the mirrors, their power transmissivities  $T_1$ ,  $T_2$  and the wavelength of the laser light  $\lambda$ . The power in transmission of the cavity is then  $P_{trans} = T_2 P_{intra}$ . The resonance condition is reached, if the round trip length  $l$  is an integer multiple of the wavelength  $\lambda$ .<sup>4</sup> Hence, either the cavity length can be adjusted accordingly to match the laser wavelength or the laser wavelength can be changed to match the cavity resonance condition.

The distance between two consecutive resonances can be expressed in laser frequency change, called the free spectral range (FSR):

$$\text{FSR} = \frac{c}{l}, \quad (2.4)$$

with the speed of light  $c$ . The linewidth of the resonance can be characterized by the full width at half maximum (FWHM) of the resonance peak or its pole frequency  $f_p = \text{FWHM}/2$  of the cavity [Bon16]:

$$f_p = \frac{\text{FSR}}{\pi} \arcsin\left(\frac{1 - \sqrt{R_1 R_2}}{2(R_1 R_2)^{1/4}}\right). \quad (2.5)$$

The ratio between the FSR and the FWHM defines the finesse  $\mathcal{F} = \text{FSR}/\text{FWHM}$  of the cavity. The finesse is proportional to the effective number of round-trips for the light in the cavity.

To stabilize the laser frequency or the cavity length to resonance, different readout schemes for the resonance condition can be used [Dre83; HC80; SGM99]. The Pound–Drever–Hall (PDH) technique [Dre83] is most common in the GWD context. Here, a linear error signal for

<sup>4</sup> For Gaussian eigenmodes of the cavity, an additional phase term, the Gouy-phase modify this resonance condition depending on the transversal mode order [Bon16].

the mismatch between the cavity resonance and the laser frequency is generated within the FWHM of the resonance peak. For that, a single frequency phase modulation is imprinted on the input beam and the reflected power measurement is demodulated at the same frequency. With appropriate adjustment of the demodulation phase the generated error signal can be used in a feedback control loop to preserve the resonance condition between laser and cavity. In a feedback control loop, the error signal is electronically feed-back to an actuator, which change the laser frequency to reduce the measured error, as discribed in more detail in Section 3.4.1. The error signal also contain the necessary information to derive the frequency noise of the laser relative to the cavity resonance frequency.

The amplitude spectral density [Ben10] of the frequency noise  $S_\nu$  is directly related to the amplitude spectral density of the phase noise  $S_\varphi$  by

$$S_\nu = S_\varphi \cdot f . \quad (2.6)$$

where  $f$  is the measurement Fourier frequency. Frequency and phase noise describe the same physical noise process. In this thesis, the laser frequency noise description is used because of the proportionality of the PDH error signal to it at frequencies below the cavity pole  $f_p$  [Bla01].<sup>5</sup>

The frequency noise could cause a signal at the GWD output that mimic the signal of a differential arm length change of the Michelson interferometer. This effect could mask a gravitational wave detection. To prevent this, the coupling factor from the frequency noise of the input laser field to the GWD output signal have to be low enough. As an example, the frequency noise coupling to the GWD readout is shown in the noise budget of the aLIGO Hanford (see Figure 2.2). It is derived by the measured frequency noise  $S_\nu$  in the interferometer input multiplied by a coupling function. The frequency noise in the interferometer is measured at the reflection of the coupled-cavity consisting out of the power recycling mirror and the arm cavities, using the PDH technique. The coupling function is derived by adding an excitation to the laser frequency and monitoring the coupling to the interferometer output signal. The increase of the output signal's power spectrum is normalized by the power spectrum of the excitation and results in the coupling function for the power spectrum of the laser frequency noise [Bui20b].

In an ideal Michelson interferometer, with two identical arms, the effect of frequency noise of the laser beam is suppressed by a perfect common mode rejection at the output port [CMS21]. In current and future GWDs the intended and unintended asymmetries between the detector arms lead to a limited common mode rejection of the frequency noise and thereby to a coupling of frequency noise to the GWD's readout. In [CMS21] a model

---

<sup>5</sup> Above the pole frequency of the optical cavity the PDH signal is proportional to the phase noise of the mismatch between cavity resonance and the laser light.

for the laser frequency noise coupling in the aLIGO Hanford is presented:

$$\begin{aligned} \frac{\Delta h_\nu}{\Delta \nu}(f) = & \frac{\lambda}{4\pi f_p L} \frac{1+r_a}{r'_a} \frac{1}{1+if/f_{cc}} \\ & \times \left[ -\delta r_a - \frac{\delta f_p}{f_p}(1+r_a) + \frac{2\pi l_{sch} r_a f_p}{c} \left(1 - i \frac{f}{r_a f_p}\right) \left(1 + i \frac{f}{f_p}\right) \right] \\ & + \frac{k_{HOM}}{L} \end{aligned} \quad (2.7)$$

The coupling is expressed by the transfer function from a laser frequency modulation  $\Delta \nu$  to the gravitational wave strain signal  $\Delta h_\nu$ . The arm cavities are described by their average pole frequency  $f_p$ , the difference between the pole frequencies  $\delta f_p$ , the average arm cavity amplitude reflectivity  $r_a$  on resonance (which is close to one), and the difference between the arm cavities  $\delta r_a$ . In addition, the derivative of the arm reflectivity with respect to the round trip phase  $r'_a$  is used. The coupled pole frequency of the power recycling cavity with the arm cavities is  $f_{cc}$ .  $L$  is the arm length of the interferometer. The Schnupp asymmetry of the interferometer  $l_{sch}$  give its macroscopic arm length difference, which is commonly at a few centimeter for radio frequency (RF) sideband transmission. The factor  $k_{HOM}$  describes the frequency noise coupling caused by higher order modes (HOMs) in the inner Michelson interferometer.

The laser's frequency noise is low pass filtered by the power recycling cavity above its pole frequency<sup>6</sup>  $f_{cc}$ , which is 0.6 Hz for the aLIGO Hanford interferometer. The residual noise couples via the difference of the reflectivity of the two arm cavities  $\delta r_a$ , the difference of their pole frequencies  $\delta f_p$  and the Schnupp asymmetry  $l_{sch}$  to the gravitational wave measurement signal. For the aLIGO Hanford detector it was found, that the difference of up to 5% in pole frequencies of the arm cavities is clearly the main coupling effect for the laser frequency noise. The other factors seem to be more than a factor of 1000 below [CMS21].

A frequency independent coupling path is introduced by higher order laser modes, originated from imperfections in the signal and power recycling cavities. These modes get completely reflected from the arm cavities and therefore dismiss the low-pass filter effect above 0.6 Hz of the coupled cavity pole. Back conversion to the fundamental mode, e.g. due to a mode mismatch between the arm cavity modes, let them interfere at the output port with the signal field. This effect limits the common mode rejection for the frequency noise above 1 kHz in the aLIGO Hanford. To reduce this effect, output mode cleaner cavities are installed in GWDs in front of the detection photodiodes.

Besides for the coupling to the sensitivity of GWDs, a pre-stabilization of the laser frequency is required for the aLIGO interferometers for successful lock acquisition of the high finesse arm cavities, because the free running laser noise of currently used lasers are too high for direct lock acquisition [CM22].

In future ground-based Michelson interferometer GWDs the same frequency noise coupling paths will appear. Beyond improving the symmetry in the two interferometer arms, it will be necessary to lower the laser frequency noise of the laser beam coupled to the

---

<sup>6</sup> See passive noise filtering in Section 2.3.2.

interferometer. If the other parameters stay similar, the higher order laser mode coupling will be dominating at lower frequencies, for longer detectors with lower coupled-cavity pole frequencies.

### 2.3.2 Frequency stabilization

Besides the optimization of the GWD's enhanced Michelson interferometer symmetry for a high common mode rejection of the laser frequency noise, it is still necessary to stabilize the laser frequency. Therefore, the laser frequency is pre-stabilized before coupling to the Michelson interferometer and in a second step it is stabilized to the cavities in the enhanced Michelson interferometer. This laser frequency stabilization is typically done in multiple nested active and passive stabilization stages.

#### Passive noise filtering

The frequency noise and power noise of the intra-cavity field is filtered above the pole frequency of an optical cavity. Thus, also in transmission of the cavity on resonance the noise is reduced. This passive filter effect is shown as a transfer function in Figure 2.4. The passive noise suppression is reduced around and vanishes at frequencies, which are a multiple of the cavity's FSR.

In most current operating GWDs the passive noise filtering is performed in two stages: the pre-stabilized laser system uses a rigid mode cleaner cavity, which filters the noise at MHz frequencies. This typical lab size rigid cavities, like the pre-mode-cleaner in Chapter 5, have a pole frequency in the higher kHz range and their free spectral range is in the mid MHz band or higher. Inside the main vacuum system of the GWDs long input mode cleaner cavities show relevant noise suppression already at kHz frequencies. But only the coupled cavity of the power recycling mirror and the arm cavities filters noise in the full detection band of a GWD, this pole frequency is e.g. for the aLIGO interferometers at 0.6 Hz [CMS21].

#### Active stabilization

The passive noise reduction by optical cavities is not enough to lower the technical laser noise in the detection band of current and third-generation GWDs. Hence, active stabilizations are additionally used. These active feedback stabilizations sense a laser parameter and send a correction signal back to an actuator.

For an active frequency stabilization scheme, the frequency mismatch between the laser frequency and a resonance frequency of an optical cavity is first measured. This measured signal, the so-called error signal, is amplified and send back as the control signal to a laser frequency (or phase) actuator. The feedback stabilization scheme is explained in more detail in Sections 3.4.1 and 4.3.

The introduced PDH sensing scheme is fundamentally limited by shot noise at the photodiode in reflection of the cavity. To reach this limit, the technical laser noise at the RF modulation frequency has to be below the sensing shot noise [Dre83; CMS21]. Furthermore, shot noise from reflected light on resonance add incoherently. This reflected light comes typically from an imperfect impedance matching of the cavity and higher order spatial modes, which are not resonant in the cavity [Bon16].

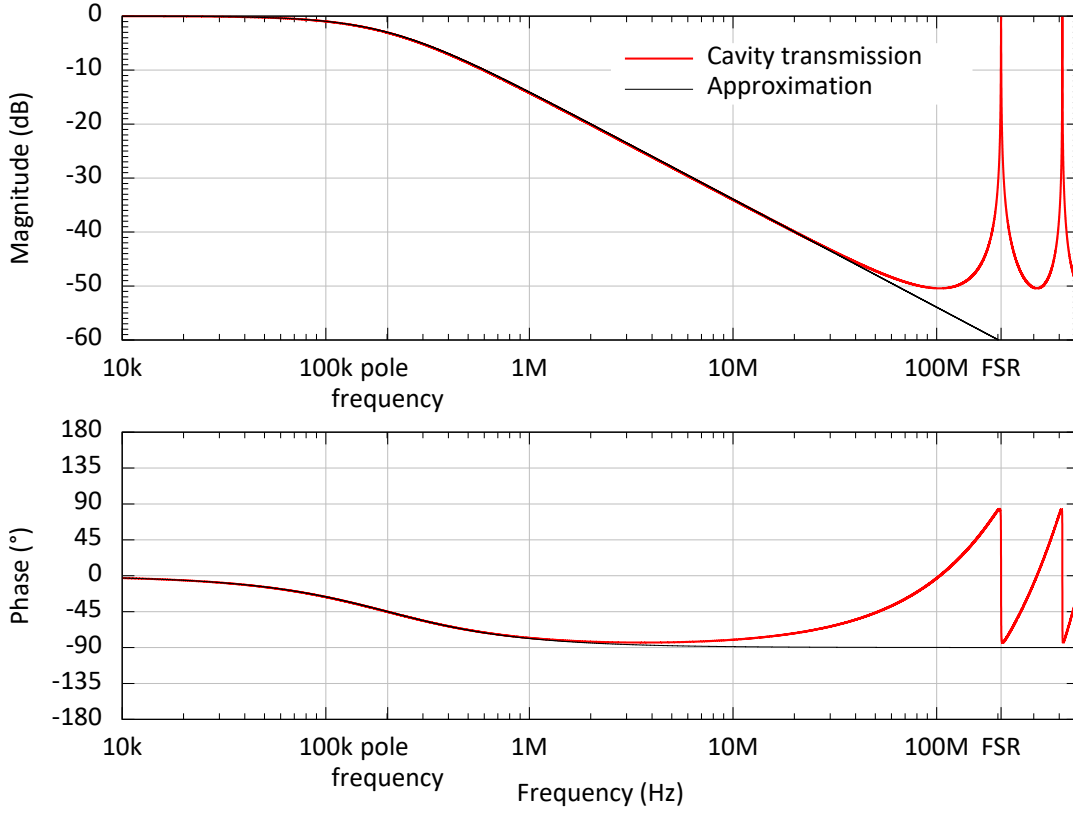


**Figure 2.4:** The transfer function of an optical cavity from power or frequency modulation sidebands of the laser input field to the field in transmission (red curve). This transfer function depicts the passive filter effect on laser noise, when the laser beam is transmitted through an optical cavity on resonance. At frequencies below half of the FSR a good approximation is a first order low pass filter with the cavity pole frequency as corner frequency (black curve). The cavity FSR and the pole frequency are taken from the parameters of the later introduced pre-mode-cleaner of the 1550 nm laser system, see Chapter 5. The filter function of cavities are e.g. further described in [Bon16].

The shot noise limit of the PDH detection in terms of an equivalent frequency noise spectral density is [CMS21]:

$$S_{\nu,PDH}(f) = \sqrt{\frac{4\pi\hbar c}{\lambda P}} \sqrt{\frac{3}{2} + \varepsilon \frac{2}{\Gamma^2} |f_p + if|}, \quad (2.8)$$

where the first square root is the relative shot noise of the input beam with power  $P$  and wavelength  $\lambda$ . The factor  $\varepsilon$  is the relative reflection power of the beam due to a limited impedance matching and higher order modes. For the best noise limit, the phase modulation index  $\Gamma$  is adjusted so that the relative reflected power in the sidebands is similar to  $\varepsilon$  resulting in  $\varepsilon \frac{2}{\Gamma^2} \approx 1$  [CMS21]. At low frequencies, the shot noise limit of the PDH sensing is frequency independent and above the pole frequency of the cavity  $f_p$  it

risers with the measurement frequency  $f$ .

The shot noise limit for the frequency sensing in Equation 2.8 describe the fundamental limitation for an active feedback stabilization of the laser frequency to a stable optical cavity with pole frequency  $f_p$ .

### Considerations on frequency stabilization in gravitational wave detectors

Several limitations for laser frequency stabilizations in GWDs have to be considered: Ideally, the input laser beam must be shot noise limited at the phase modulation frequency for the PDH error signal. Passive noise filtering by a cavity is often used to achieve this. The detectable power by a photodiode is typically limited to less than 100 mW. Depending on the input power  $P$  and the reflection factor  $\epsilon$ , it is required to attenuate in front of the photodiode, which degrades the shot noise limit by the square root of the power attenuation factor. The electronic noise of the sensor and demodulation circuit could further degrade the performance.

The feedback control loop stabilizes the laser frequency to a resonance frequency of the cavity. Cavity's length fluctuations are coupled to the resonance frequencies and, thus, are imprinted by the feedback control on the laser frequency. Therefore, the stability of the reference cavity is crucial to achieving a high laser frequency stability by active stabilization to that reference.

A stable feedback control loop's highest achievable stabilization bandwidth is limited by delays in the control loop and in the case of very long cavities, like the GWD's arm cavities, by the cavity's free spectral range frequency. Hence, the best is to start with fast active stabilization and then passively filter with low pole frequency cavities. This is implemented in current GWDs and is also the proposed design for future GWDs [Kwe12; CMS21].

Within the detection band of the GWD, the final feedback stabilization loop for the laser frequency uses the error signal of the coupled-cavity of the enhanced Michelson interferometer. For current and future GWD, the signal-to-noise ratio of the error signal can further be improved by mode filtering in front of the stabilization photodiode and better impedance matching of the power recycling cavity. Additionally, redesigning or omitting the pre-stabilization to a fixed spacer reference cavity with a laser frequency shifter could reduce noise. Especially the so-called whistle glitches that are attributed to the beat between two radio frequency signals with crossing signal frequencies. They were found to partially be caused by the beat signal between the oscillator used for the laser frequency shifter and other interfering signals, like radio station signals [Kwe12; Bui20b].

### 2.3.3 Power noise coupling

The technical power noise coupling in Michelson interferometers shows many similarities to the coupling of technical frequency noise. For an ideal, totally symmetric Michelson interferometer operated at the dark fringe, the technical power noise of the laser does not couple to the readout. Hence, again the asymmetries of the interferometer result in a finite common mode rejection of the power noise.

These asymmetries cause according to Equation 17 and 66 in [Som06; Som07] the following coupling: The coupling to the readout signal of the GWD can happen via the

imbalance of the transfer function of the two arm cavities<sup>7</sup>, defined by their pole frequencies and the reflection at the arm cavities. In addition, radiation pressure noise originating from technical laser power noise, excited differently in the two interferometer arms, by mirror mass differences, different intra-cavity laser powers or pole frequency differences add new coupling paths compared to the frequency noise coupling. Similar as for the frequency noise, the power noise of the laser system is filtered by the coupled-cavity pole of the enhanced Michelson interferometer.

As with noise coupling of frequency noise, there could also be a coupling term that is not filtered by the coupled cavity. This coupling is explained for the frequency noise by higher order modes (see  $k_{HOM}$  in Equation 2.7), reflected by the arm cavities and being back converted to the detection mode. Power noise of these modes would couple as well to the readout of the interferometer.

An additional coupling path arises, when operating the interferometer at a DC offset from the dark fringe. Then the laser power noise can couple proportion to the DC offset. In case of proposed balanced homodyne detection of the output signal as a replacement for the DC offset readout scheme,<sup>8</sup> the power noise of the local oscillator can be suppressed by the common mode rejection of the balanced homodyne detection. See Section 6.1.3 for a more detailed discussion on power noise coupling to balanced homodyne detection.

Laser beam pointing could generate additional power noise of the laser beam inside the detector. Beam pointing leads to fluctuations of the coupling to the resonating mode, which causes power noise of the intra-cavity power and thus power noise in transmission of the cavity.

As already mentioned in the previous section, power noise at the PDH phase modulation frequencies for error signal generation could degrade the quality of the error signals and thereby indirectly degrade the sensitivity of the GWD [CMS21].

#### 2.3.4 Power stabilization

In the context of this thesis, the power noise is measured as an amplitude spectral density  $S_P$  and is normalized by the average laser power  $P$  to

$$S_{\text{rpn}} = \frac{S_P}{P}, \quad (2.9)$$

the so-called relative power noise. The advantage of this quantity is that the spectral density of technical power noise is independent of the absolute laser power used for the measurement. Hence, classical attenuation or amplification of the laser power does not change the technical noise spectral densities as long as the process does not add excess noise.

Similar as for the frequency noise, the frequency band of most importance for the power noise is the detection band of the GWDs. Nevertheless, the power noise at the phase modulation frequencies used for the error signal generations for the detector control and the slow power drifts have to be low enough, to ensure the desired operation of all feedback control loops of the GWD.

<sup>7</sup> The shape of this transfer function is similar to the inverse of the transfer function shown in Figure 2.4.

<sup>8</sup> See end of Section 2.1.1.



### Passive noise filtering

For passive stabilization, optical cavities on resonance filter the power noise of the input beam by their transfer function, see Figure 2.4. This technique is applied in GWDs with mode cleaner cavities in front of the interferometer. These cavities simultaneously filter frequency and power noise above their pole frequencies. The first, a rigid mode cleaner, the pre-mode-cleaner on the laser table, reduces the laser noise at MHz frequencies. The pole frequency of the pre-mode-cleaner is designed to ensure a shot noise limited laser noise at the MHz phase modulation frequencies, which are used to generate error signals for stabilization of the interferometer. In the GWD's vacuum system, the input mode cleaner filters the laser beam above its pole frequency, which is in the lower kHz range [CMS21]. In addition, active stabilization must be used because passive noise reduction is not sufficient to decrease the laser power noise to the required level.

### Active stabilization

The quantization of the light field, which can be depicted as the Poisson distribution of the photons limit the precision of the power measurement. This quantum noise limitation, the shot noise of the measurement, written as relative power noise is:

$$S_{\text{relSN}} = \sqrt{\frac{4\pi\hbar c}{\lambda P}} \quad (2.10)$$

It is a frequency independent noise that depends on the photon energy  $2\pi\hbar c/\lambda$  and the absolute laser power  $P$ . This is the classical power noise limit of a laser beam with power  $P$ .<sup>9</sup>

As sensors for the power stabilization, photodiodes with transimpedance amplifiers that convert the photocurrent into a voltage signal, are used. The power measurement with a photodiode is a destructive measurement, as the photons are absorbed in the semiconductor of the photodiode. Therefore, only a fraction of the main laser beam can be sent to these power sensors.

From the photodiode signal a constant reference signal is subtracted to generate the error signal for a feedback stabilization. The feedback is sent to a power actuator, which is placed in the main beam prior the sensing pickoff, see Section 3.4 for a detailed explanation. There are two kinds of actuators: bidirectional actuators, which can increase and lower the laser power, like actuation on the gain of a laser amplifier and others, which can only lower the laser power and therefore have to be operated at an offset to also compensate for a power decrease on the sensor.

Active power stabilization can also compensate the slow power drifts of the laser power. Similar to the frequency stabilization, the active power stabilization is typically limited by sensing noise, the achievable bandwidth of the feedback control loop, and its noise suppression. Besides the shot noise in Equation 2.10, sensing noise can be caused e.g. by beam pointing coupling to a spatial dependent responsivity of the power sensor used for stabilization [Bui20b].

---

<sup>9</sup> With non-classical states, like squeezed states of light this limit can be surpassed [Vah18].



### Considerations in gravitational wave detectors

The power noise of the laser beam injected to the enhanced Michelson interferometer of a GWD is passively filtered by its coupled cavity. Therefore, highest requirements to the power stability of the injected laser beam are placed in the lower detection band, as there the passive filter effect from the coupled cavity is the smallest.

In addition, the mode cleaner cavities act as a reference for the laser mode and thereby beam pointing noise<sup>10</sup> is converted to power noise in transmission of it. This laser power noise is sensed behind these cavities together with the power noise originating from the laser source. The total laser power of the transmitted beam can be suppressed with active stabilization [Mue05; Avi06; Wil08].

In current laser systems, the laser power is pre-stabilized within air photodiodes with a high control bandwidth to reduce the necessary loop gain for the subsequent final power stabilization. Behind the input mode cleaner, power sensors are placed in vacuum for final stabilization [Kwe12]. For the final power noise levels close to  $1 \times 10^{-9} \text{ Hz}^{-1/2}$  are anticipated in the detection band of the GWD, which require detected photocurrents in the 200 mA range to reach the required shot noise level, as well as careful stray light shielding and beam pointing control on the sensors [Kwe09; KWD09; Cle21].

This high photocurrent start to exceed the damage threshold or low noise operation range of single photodiodes [Sei10]. As an alternative, the laser beam can be distributed on several photodiodes arranged in an array. The signals of the transimpedance amplifiers of the individual sensors are then added and, after the subtraction of a reference signal, used as the error signal for feedback stabilization [KWD09]. The achievable noise level with this technique is limited, because the relative shot noise lowers with the square root of the sensed power. A noise improvement of a factor of 10, which could be necessary for future GWDs if the power noise coupling stay similar to current GWDs, would increase the needed power for the power stabilization to the 20 W level. Hence, arrays of 100 to 400 photodiodes are necessary and a significant part of the total laser power is lost.

New concepts for power noise sensing are proposed to overcome this problem. Squeezed light enhanced power sensing can lower the shot noise limit of the detection without an increase of the photocurrent [Vah18]. Optical AC coupling sense the power noise in reflection of an impedance matched cavity and thereby reduce the total power sensed with the photodiodes but not the noise signal [KW19]. Indirect power sensing techniques, like via radiation pressure could offer another non destructive way of power sensing for high laser powers [Ner21; Ner22].

### 2.4 Laser system design

The Michelson interferometer of a GWD is highly complex. Thus many technical and fundamental noise couplings can limit its sensitivity. Current and future ground-based GWD designs are fundamentally limited by quantum and coating thermal noise in most of their detection band, as discussed in subsections 2.1.1 and 2.1.2. Besides the requirements for other subsystems of the GWD, the main laser system has to fulfill some basic requirements

---

<sup>10</sup> Also named beam jitter noise.

on output power, laser wavelength, and mode shape. These basic parameters of the laser system and their impact were discussed in Section 2.2.

Two factors determine if technical laser noise is limiting the sensitivity of a GWD: the noise amplitudes of the input laser beam and the coupling factors to the differential arm length measurement. This connection between input laser noise and its coupling results in an relation of the laser system's requirements for the technical laser noise and the interferometer optics and layout, which defines most of the noise coupling factors by their asymmetries, see Section 2.3. For example, the optical design decision to use wedged input test masses or plane ones, which show etalon effects [Hil08], could be influenced by the expected laser noise, while expected asymmetries between the arm cavities result in constraints for the laser noise amplitude to reach the proposed sensitivities.

These consideration resulted in requirements for the laser system of current GWDs, like for aLIGO [Wil11]. Especially the laser frequency noise and power noise are constrained. Here, the laser systems embed the fast active stabilizations and actuation inputs for the stabilization to references in the main vacuum system of the GWD. Therefore, it is called the pre-stabilized laser system (PSL).

This thesis presents the improvements for pre-stabilized laser systems of current GWDs and the developed prototype of a stabilized laser system for future GWDs, as well as the generation of squeezed states of light for the demands of future GWDs. The following three chapters present the results of experiments that characterize and stabilize the laser noise of the laser system for GWDs. In Chapter 3 laser sources at 1064 nm wavelength are investigated for current GWDs followed by experiments at 1550 nm wavelength for future GWDs with silicon interferometer mirrors in the next two chapters. Active, high bandwidth stabilizations are investigated that allow the injection of control signals generated from a sensor in the main vacuum system of the GWD. In Chapter 6, the stabilized laser system is used to generate squeezed states of light in the whole detection band of ground-based interferometric GWDs.

## CHAPTER 3

---

### Nd:YVO<sub>4</sub> High-Power Master Oscillator Power-Amplifier Laser System for Second Generation Gravitational Wave Detectors

---

This chapter reports on the characterization, integration and stabilization of solid-state laser amplifiers in a laser system environment of second-generation gravitational wave detectors (GWDs), which are the current generation of GWDs at the time of writing of this thesis. The laser system provides the high power and stabilized laser beam for the interferometric gravitational wave measurement in the vacuum system of the GWD.

In current GWDs laser systems at 1064 nm wavelength are integrated to provide the laser beam for gravitational wave detection [Kwe12; Bod20] [Ace15; CCK19] [Aku20] [Doo16]. They are based on a non-planar ring oscillator (NPRO) seed laser [KB85]. The seed laser output power is then amplified to the required power level. Three different laser amplification concepts are considered for GWDs' laser systems:

- A single-pass amplification of a free space laser beam passing through a pumped solid-state laser medium to increase the laser power by stimulated emission,
- an amplification by an injection locked laser resonator, which was used in the original Advanced Laser Interferometer Gravitational-Wave Observatory (aLIGO) pre-stabilized laser system (PSL) to reach the requested output power [Win11]. Here, the active laser media was placed inside a resonator, which is tuned to resonance of the injected seed laser by an active length stabilization, and
- fiber amplifiers, which are considered for future GWDs to enable an even higher output power [Wel20; Hoc21]. The optical fibers are doped, to not only guide the laser light, but also to serve as the active laser media for laser amplification.

The complexity of the control and optical setup of injection locked laser resonators made their operation and noise mitigation challenging in the past. While fiber amplifiers are considered in proposals for current GWDs [Ace15], they have not yet proven their long-term stability and reliability in a stabilization environment convincing enough for current GWDs, like aLIGO. In addition to that, due to thermal and control issues of the GWDs' interferometer optics, laser powers well below 100 W are injected to the interferometer [Bui20b]. Hence, improved single-pass neodymium-doped yttrium orthovanadate (Nd:YVO<sub>4</sub>) amplifiers became an option to replace or extend former laser amplifiers, like the injection locked laser resonator at aLIGO [Win11].

To investigate the potential of these amplifiers, a detailed characterizations of two different single-pass Nd:YVO<sub>4</sub> power amplifiers is performed, presented in Section 3.2 and

the integration into a copy of the laser stabilization environment of a GWD's laser system is demonstrated and reported in Section 3.3. Using a pump-power actuation in one of the amplifiers, a power stabilization without an external laser power actuator was demonstrated at high laser power levels in Section 3.4. These results are published in Optics Letters [Thi19] and paved the way to the integration of these amplifiers in current GWDs [Bod20; CCK19; Aku20]. The content of this chapter is closely based on the publication [Thi19]<sup>1</sup> with the addition of a detailed description of the active feedback power stabilization in Section 3.4 and an outlook that take recent publications into account.

### 3.1 Experimental setup

A copy of the aLIGO PSL [Kwe12], called the reference system, was used as the environment to tests two slightly different solid-state Nd:YVO<sub>4</sub> amplifiers. The first amplifier was a neoVAN-4S and the second a neoVAN-4S-HP, both manufactured by neoLASE.

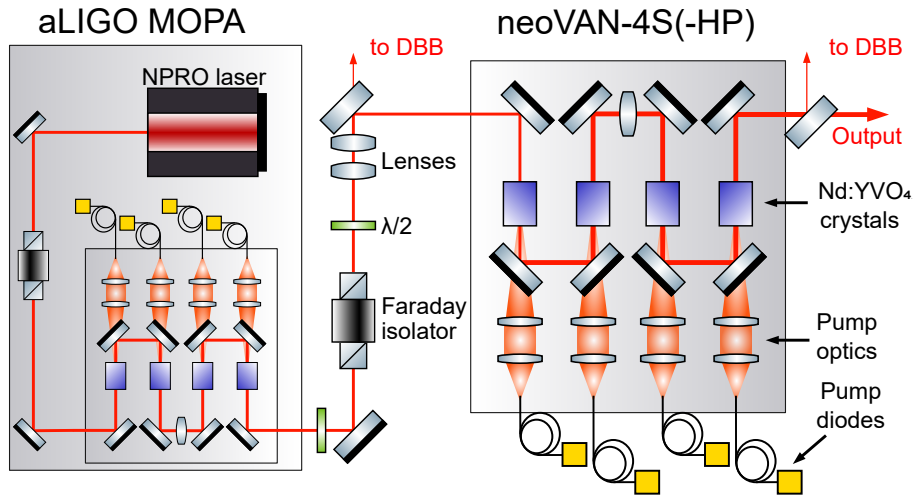


**Figure 3.1:** Schematic setup of the light power amplifier system with the aLIGO master oscillator power amplifier (MOPA) laser as the seed source, which hosts another four stage Nd:YVO<sub>4</sub> solid-state amplifier [Fre07]. A fraction of the light from the aLIGO MOPA laser and from the neoVAN amplifier is used for characterization with the diagnostic breadboard (DBB). Modified figure from [Thi19].

The neoVAN-4S and neoVAN-4S-HP amplifiers consist of four Nd:YVO<sub>4</sub> crystals. Each crystal is pumped with a fiber-coupled laser diode, as depicted in Figure 3.1. The crystals of the neoVAN-4S amplifier are optimized for the used pump wavelength of 808 nm, while the crystals of the high power (HP) version are optimized for the pump wavelength of 878 nm. For the neoVAN-4S a pump power of 30 W to 35 W of the maximal available 45 W per crystal is used with standard current drivers. The neoVAN-4S-HP amplifier uses 50 W to 55 W of the maximal available 65 W per crystal with external low-noise current supplies for the laser diodes. Both amplifier types are seeded with s-polarized laser light at 1064 nm wavelength and in the fundamental Gaussian mode. Their laser heads, as well as the pump

<sup>1</sup> The first author is Fabian Meylahn, birth name Thies.

laser diodes are water cooled.

A master oscillator power amplifier (MOPA) laser of the aLIGO laser system [Win11; Fre07] is used as seed laser for the investigations of the neoVAN amplifiers and the diagnostic breadboard (DBB) [KW08] of this system is used to characterize the amplified laser beams (see Figure 3.1).

The DBB performs a fully automated characterization of the lasers by measuring its higher order mode (HOM) content, relative power noise, frequency noise and pointing noise of the laser beam relative to an acoustically shielded Fabry-Pérot ring cavity. The length of the cavity is stabilized to the laser frequency and the input beam alignment is stabilized to the fundamental eigenmode of the cavity. The error and control signal of the feedback control loops were used to calculate the amplitude spectral density of the noises in a frequency range from 1 Hz to 10 kHz, which is the most relevant range for current GWDs. In addition, the measurement of the higher order spatial mode content is performed by multiple length scans over the free spectral range of the cavity.

### 3.2 Characterization

The neoVAN-4S amplifier was tested with a seed power of 28 W. For this test, the total HOM content of the seed laser was 7.1%. This resulted in an amplified output power of 72 W in linear polarization with a HOM content of 10.7%, measured with the DBB. This neoVAN amplifier was sent to and installed at one of the aLIGO detectors after characterization.

Furthermore, two neoVAN-4S-HP amplifiers were operated and tested with output powers of 111 W and 114 W. The first one was afterward used at the Virgo GWD and the second one was characterized in detail for more than 45 days in our lab. The performance data of the second amplifier is hereby presented.

For the neoVAN-4S-HP test the power of the seed beam was reduced to 27 W, in order to reduced its HOM content to 2.7%. With this seed beam the output beam of the neoVAN-4S-HP amplifier was analyzed to have only 2.9% HOM content and an optical output power of 114 W.

In Figure 3.2, the output power of the neoVAN-4S-HP amplifier is shown as a function of the seed power. The extracted power computed as the power added by the amplifier to the seed power is higher than 80 W for seed powers above 5 W. For this measurement, the seed power was attenuated by a half wave plate and polarizing beam splitter combination.

To purify the spatial beam profile and reduce beam pointing, the beam of GWD lasers are filtered by pre-mode-cleaners (PMCs) [Kwe12]. Hence, the amplified beam was coupled to an aLIGO PMC. The measured transmitted power through the PMC is plotted as an additional data set in Figure 3.2.

For different seed powers no realignment of neither the amplifier nor the cavities downstream the amplifier was necessary. A complete set of DBB beam characterization measurements was performed for different seed powers (1.7 W, 12 W and full seed power). Here, the results for the neoVAN-4S-HP seeded with 27 W in blue and the neoVAN-4S seeded with 28 W in red are presented. The measurements of the corresponding seed laser beams are plotted in dotted lines.

The relative power noises are shown in Figure 3.3. At low frequencies the transfer

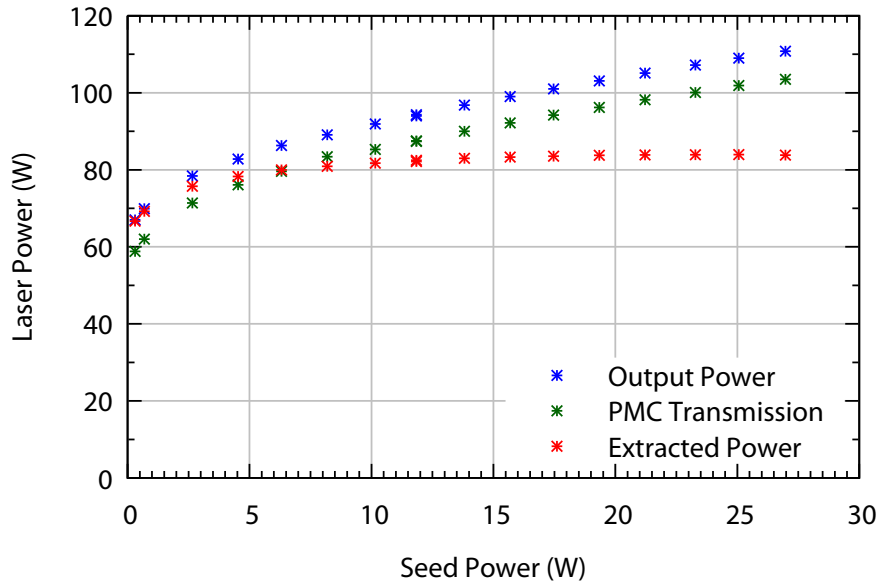


**Figure 3.2:** The output power of the neoVAN-4S-HP amplifier and the power transmitted by a pre-mode-cleaner (PMC) filter cavity are shown as a function of the seed power. The difference between the power after and before the amplifier (extracted power) is nearly constant for seed powers above 5 W. Figure from [Thi19].

function from seed power fluctuations to the output power of largely seed power saturated amplifiers is much smaller than the transfer function of pump power fluctuations to the output power [NM02; TWF05]. Hence, the power noise at the output of the neoVAN amplifiers is most likely dominated by fluctuations in the power of the pump laser diodes and correspondingly by fluctuations of their current source. For the investigations of the neoVAN-4S-HP the standard power supplies of the laser diodes (used for the neoVAN-4S measurement) were replaced by low-noise Delta SM800 power supplies. Due to unavailable data on the pump light fluctuations and on the saturation level of the different amplifier stages, no quantitative pump-light noise projection was possible. Nevertheless, the measurements clearly indicate the benefit of a lower noise power supply. As a complementary plot, Figure 3.4 shows a measurement of the relative power noise of the neoVAN-4S-HP for frequencies up to 100 MHz.

The free running frequency noise at the output of the amplifiers was characterized using the DBB and is shown in Figure 3.5 in comparison to the free-running noise of the seed laser. In the full measured Fourier frequency band, the frequency noise at the output of the amplifiers is similar to the noise of our aLIGO MOPA laser, which is close to the typical NPRO seed laser noise [KW08].

The beam pointing was measured with the automatic alignment system of the DBB. The quantity  $\varepsilon(t) = \delta x(t)/w_0 + i\delta\alpha(t)/\Theta_D$  was used, with the transverse shift of the beam  $\delta x(t)$  normalized by the beam waist radius  $w_0$  and the tilt  $\delta\alpha(t)$  normalized to the half divergent angle of the beam  $\Theta_D$  to quantify the relative beam pointing. The pointing noise

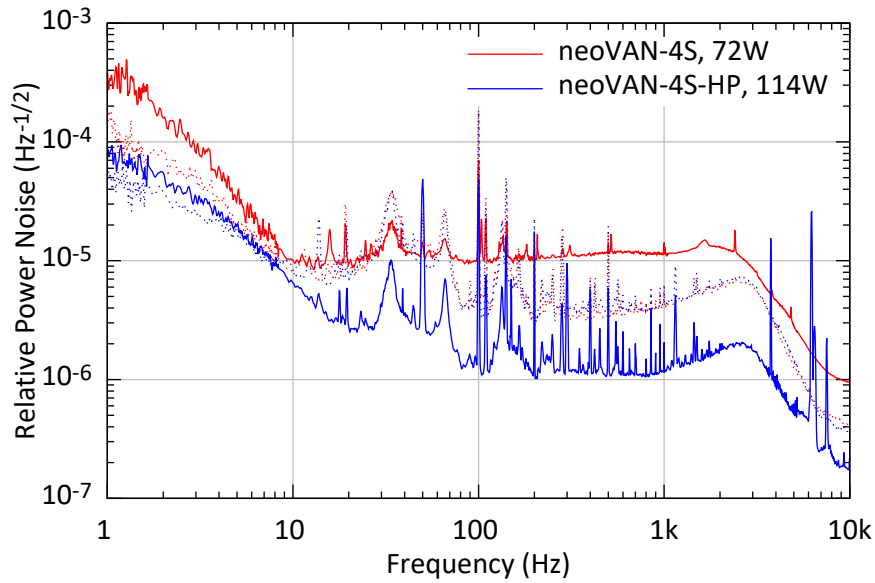


**Figure 3.3:** Amplitude spectral density of the free-running relative power noise of the 72 W and 114 W laser beams (solid lines) and of the corresponding seed laser beams (dotted lines). Modified figure from [Thi19].

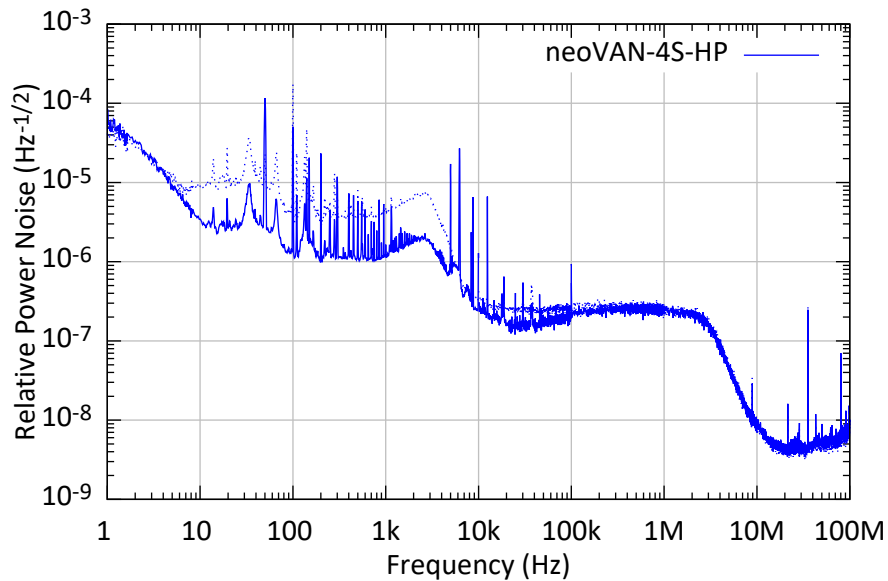


**Figure 3.4:** Amplitude spectral density of the free-running relative power noise of the 114 W laser beam from the neoVAN-4S-HP (solid line) and of the corresponding seed laser beam (dotted line) for Fourier frequencies up to 100 MHz. Beyond 20 MHz the measured noise is close to the relative shot noise of the detected photocurrent ( $3 \times 10^{-9} \text{ Hz}^{-1/2}$ ). The peak at 35 MHz corresponds to modulation sidebands used for the feedback control loops. Modified figure from [Thi19].

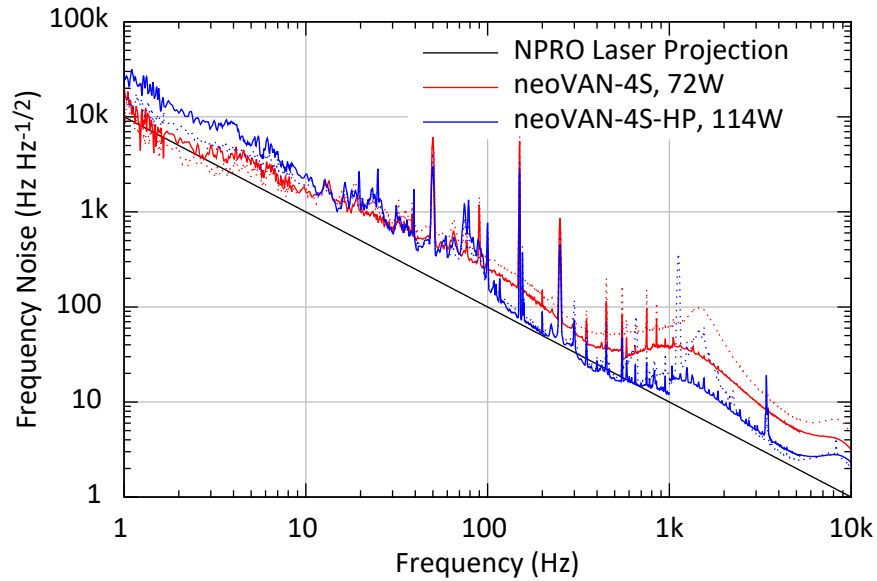


**Figure 3.5:** The amplitude spectral densities of the free-running frequency noise are shown, measured with the DBB. The frequency noise curves of the free-running amplifiers (solid lines) are mostly dominated by the frequency noises of the seed laser (dotted lines) and are close to the typical frequency noise of NPRO lasers. Modified figure from [Thi19].

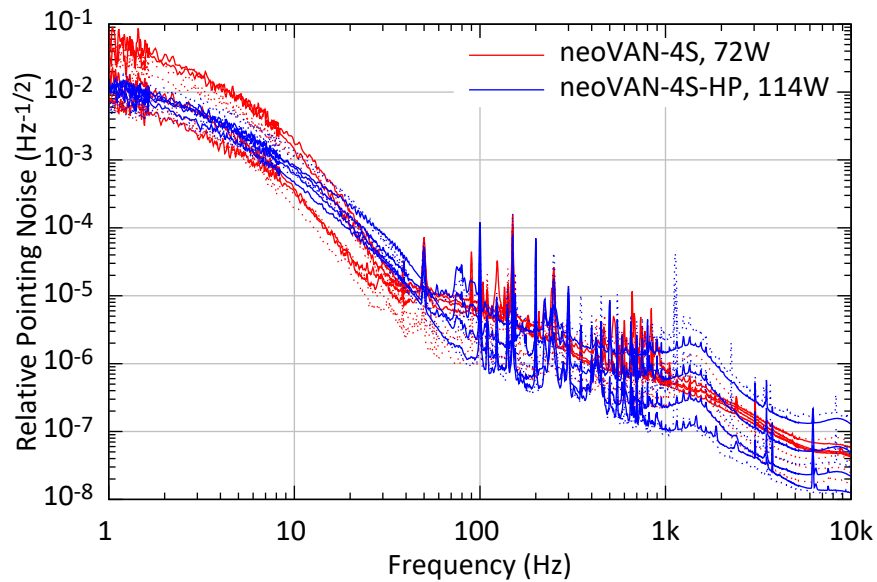


**Figure 3.6:** Pointing noise in all four alignments degrees of freedom is shown as a amplitude spectral density over the Fourier frequency. The pointing noise of the amplifiers (solid lines) is dominated by the pointing noise of the seed laser (dotted lines). Modified figure from [Thi19].



measurements were taken at  $+45^\circ$  and  $-45^\circ$  Gouy phase position, corresponding to the readout of  $\varepsilon(t)$  projected under these angles. By measuring the pointing in the horizontal and vertical directions, 4 noise spectral densities were recorded in total [KW08]. As shown in Figure 3.6, the pointing noise of the amplified beams is close to the low noise level of the seed laser. The pointing noise of the neoVAN-4S-HP was analyzed in daily measurements over 45 days and did not show significant variations.

The noise characterization of the neoVAN amplifiers in this section showed their potential for the use in second-generation GWD's main laser system. Especially the neoVAN-4S-HP with the low noise power supplies, show a very good beam profile, lowest noise and higher output power. To confirm the long-term reliable operation and the possible implementation into the laser (pre-)stabilization of a GWD, one neoVAN-4S-HP was integrated into a reference system of the aLIGO PSLs. The results of this integration are described in next section.

### 3.3 Integration of a neoVAN-4S-HP into an aLIGO pre-stabilized laser system

For further testing, one neoVAN-4S-HP amplifier was implemented into a copy of the aLIGO PSL. The PSL contains the laser source with amplifiers but also host the laser pre-stabilizations and interfaces for integration into the full GWD [Kwe12]. The laser frequency and power are actively stabilized with interfaces for outer nested feedback control loops, the laser beam is filtered by a PMC, and the system is automated using a computer control and data acquisition system.

The integration of the neoVAN amplifier into the aLIGO PSL required only a simple modification of the optical beam path. This modification routes the aLIGO MOPA into the neoVAN amplifier and its output beam into the original high power beam path towards the aLIGO PMC. As this PMC serves as the spatial interface towards the main interferometer and the power and frequency stabilization subsystems. Thus, a matching of the neoVAN output beam to the PMC simultaneously provides a good alignment to these systems. Such a modification was performed at the aLIGO PSL reference system. All PSL feedback control loops could be engaged without major modification and achieved the stability requirements of aLIGO.

The output power of the neoVAN-4S-HP amplifier and the transmitted power through the PMC are shown in Figure 3.7 for an operation time of about 45 days. The average transmitted power through the PMC is 95 % of the incident power.<sup>1</sup> This is consistent with the results of the mode scans performed with the DBB. Due to temperature fluctuations in the laboratory, alignment mirrors mounts moved and the laser beam to the PMC had to be realigned after several days to stay at the high power transmission level.

The frequency stabilization control loop of the laser system to a reference cavity [Kwe12] is not affected by the integration of the amplifier and thereby reached its design stability and unity-gain frequency. The power stabilization of the system was performed using a high power acousto-optic modulator (AOM) to split off power into the first diffraction

---

<sup>1</sup> The injected power to the PMC is about 5 % less than the output power of the amplifier, due to several optics between the amplifier output and the injection to the PMC, like an acousto-optic modulator (AOM) or a polarization cleaning stage.

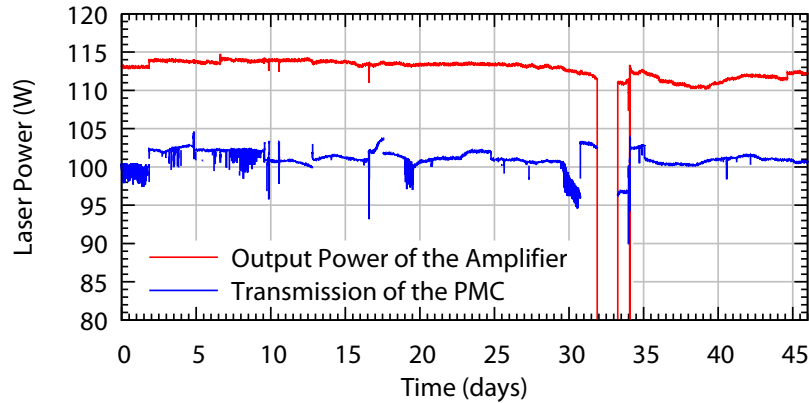


**Figure 3.7:** The long-term measurement of the output power of the neoVAN amplifier and power in transmission of the PMC shows the stability of the system over time. The PMC transmission shows dips due to automatic re-locking of the laser system. Between day 34 and 37, the laser system was switched off and on again and recovered operation at the same performance as before without any realignment of the amplifier. Figure from [Thi19].

order [Kwe12]. Two photodiodes detecting a photocurrent of 2.8 mA are used as the in-loop and out-of-loop sensor for the active feedback stabilization of the laser power in transmission of the PMC (similar to the stabilization described in Section 3.4). This stabilization reaches the stability as good as the original PSL. In a frequency range from 20 Hz to 2 kHz, the achieved stability is limited by the shot noise of the sensors, see Figure 3.11.

### 3.4 Power stabilization via pump diode current

A fast power control of the pump light for the last laser crystal in the neoVAN-4S-HP amplifier makes a power stabilization without an AOM in the beam path possible. Such an AOM adds additional power loss and can produce stray light, thermal lens or spatial beam distortion.

An in-house developed controllable bypass resistor was used to control the current through one laser diode of the neoVAN-4S-HP amplifier and thereby its output power. This circuit is a high-current version of the actuator used in reference [AK01] with a current modulation bandwidth of 800 kHz, achieved with a feedback controlled metal-oxide-semiconductor field-effect transistor and low inductance resistors for current sensing and limiting, see Figure A.2 in the appendix.

The transfer function from a modulation of the pump laser diodes current to the power modulation at the output of the solid-state amplifier is a combination of two transfer functions: the transfer function from the current modulation to output power of the pump diodes and the transfer function from power of the pump diodes to power modulation at the output of the amplifier. In the here consider frequency span, ideally the pump diode current instantaneously defines its output power. Hence, their response is frequency independent. The expected transfer function from the pump power modulation to the amplifier output power can be described by a first order low-pass filter, similar as for fiber amplifiers [NM02; Tün12].

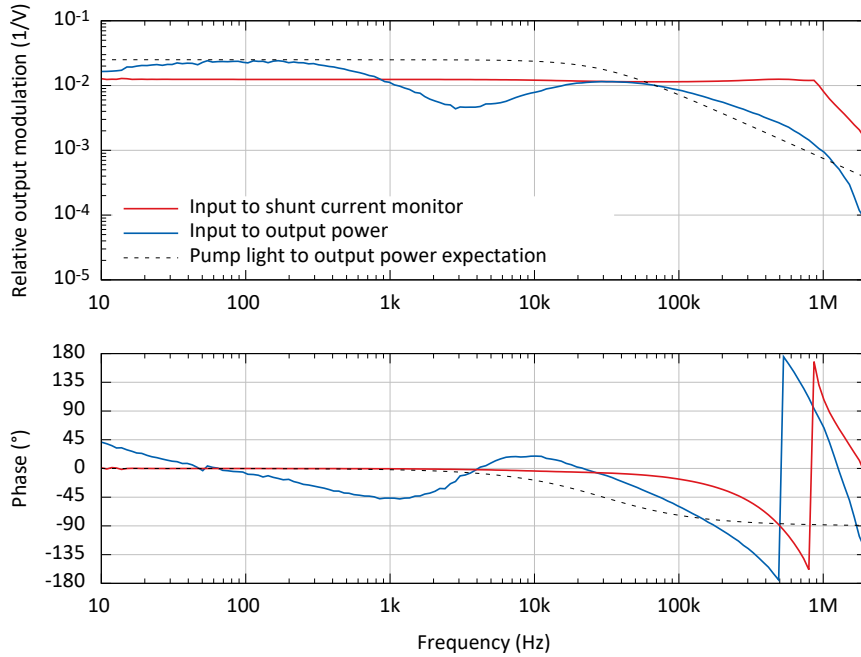


**Figure 3.8:** Bode plot of the transfer functions from the input of the current modulator to the amplifier output power, normalized by the mean output power, are shown in units of  $\text{W W}^{-1} \text{V}^{-1}$ . The expected transfer function to the amplifiers output power is plotted as a dashed line, it is a first order low-pass with a corner frequency of about 30 kHz. This characteristic corner frequency is defined by the response of the amplifier to pump or seed power changes. For a similar amplifier, this was measured in more detail in [BMW20]. In addition, the transfer function of the current modulator is shown in units of  $\text{A A}^{-1} \text{V}^{-1}$ , normalized to the total DC current of 40 A, which is used for the laser diodes. Its modulation index is  $1 \text{ V A}^{-1}$ .

Figure 3.8 shows the measured transfer function from the shunt current modulation to the amplifier output power normalized by its mean output power (blue). This transfer function contains the response of the shunt current modulator (red) in addition to the two above discussed transfer functions. For comparison, the expected transfer function is plotted as a dashed line. The lower than expected output power modulation below 30 Hz can be caused by thermal effects in the laser crystals, which counteract the pump power modulation. The dip around 2.5 kHz can originate from a non-ideal impedance of the laser diodes' current source. The specified output capacity of the current supply is  $80 \mu\text{F}$  [Del22] and in combination with a  $50 \mu\text{H}$  output inductor<sup>1</sup> this could explain the drop in the power modulation around this frequency.

<sup>1</sup> This is not specified for the used power supply but a reasonable component to filter high frequency noise from the current source. As for example the in-house build current source in Section 4.1.1 use also such an inductor.

### 3.4.1 Feedback stabilization

In general, an active feedback stabilization uses an error signal to feedback to an actuator that changes the physical quantity measured by a sensor. The error signal is the difference computed from the reference value and the signal by a sensor. In the ideal case, the error signal is close to zero when the feedback control is operating, meaning that the negative feedback is ensuring that the sensor reading is equal to the reference value.

In the case of the power stabilization, a fraction of the laser power behind the amplifier is sensed by a photodiode with transimpedance amplifier generating the in-loop sensor signal  $U_S$ . This signal is subtracted from a reference voltage  $U_R$  to generate an error signal  $U_E$ , see Figure 3.9. This error signal is amplified and frequency dependent filtered by a servo controller to generate the control signal  $U_C$ , which is send to the actuator, in this case the shunt current control of a pump laser diode. For stabilization purposes, the reference is ideally a constant DC value, which here represents the sensor reading for the desired output power of the laser.

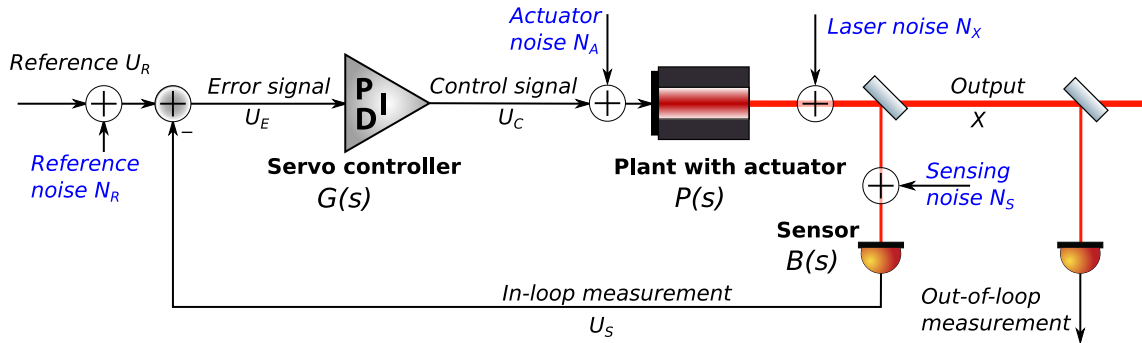


**Figure 3.9:** The signal flow diagram of a simple feedback control loop is shown. Here the sensors and actuators for a power stabilization are shown. In addition, virtual adders are inserted to model the coupling of different noise sources (represented in blue) to the system. Finally, the performance of the feedback control can be cross-checked with an out-of-loop detector.

As a necessary pre-condition for a feedback stabilization, a strict monotone dependence between the sensor reading and the quantity to be controlled is required. This should be the case at least within the foreseen operation range, where the stabilization should operate. Additionally an actuator for this quantity with a strict monotone response is necessary. These pre-conditions ensure that the sign of the feedback does not depend on its DC working point and thus, the design of a negative feedback loop becomes possible.

For simpler design and description, the modules of the control loop are approximated to be linear time invariant around their points of operation. In the scope of this thesis, the modules are characterized by their transfer functions in frequency domain.<sup>1</sup> The methods presented here can be found in [AC00].

The linear time invariant systems can be characterized by their transfer function,

<sup>1</sup> Other descriptions, like the time-domain state space representation or poles and zeros in the  $s$ -plane are beneficial, if good analytical models of the physical systems are available and time domain measurements/optimizations are planned [LW05].

visualized in a bode plot like Figure 3.8. The transfer function is defined as the ratio between the input and the output signal in frequency domain. For the frequency domain representation, the Laplace transformation is commonly used and depends on the complex frequency parameter  $s = \sigma + 2\pi if$  [AC00]:

$$X_{out}(s) = A(s)X_{in}(s) . \quad (3.1)$$

Here, the transfer function  $A(s)$  describing the signal transformation from the input  $X_{in}(s)$  to the output of a system  $X_{out}(s)$ . In practice the  $\sigma$  is set to zero, so that the Laplace transformation simplifies to a Fourier transformation. The system is then described by the complex frequency response to sinusoidal signals  $A(f)$ , depending on the Fourier frequency  $f$ .

The control loop in Figure 3.9 can be described by the open-loop transfer function  $L(s) = B(s)G(s)P(s)$ . This transfer function describes the signal transformation for a signal passing once all sub-systems. Two other transfer functions can be also used for the control loop characterization, the noise suppression transfer function  $N(s)$  and the closed-loop transfer function  $C(s)$ :

$$N(s) = \frac{1}{1 + L(s)} , \quad (3.2)$$

$$C(s) = \frac{L(s)}{1 + L(s)} . \quad (3.3)$$

The closed-loop transfer function describe the frequency response of the engaged control loop from a modulation of the reference  $U_R$  to the sensor signal  $U_S$ , which represents the measurement of the controlled quantity  $X$ . The noise suppression transfer function describe the reduction of a disturbance  $N_x$  added to the plant.

From the closed-loop transfer function  $C(s)$  one can derive that for  $|L(s)| > 1$  the active feedback reduces the difference between reference and sensor signal. This frequency range is called active control bandwidth of stabilization. The boundaries of the control band are given by the unity-gain frequencies (UGFs)  $f_{UG}$ , which are defined by<sup>1</sup>

$$|L(s = 2\pi if_{UG})| = |L(f_{UG})| = 1 . \quad (3.4)$$

The open-loop transfer function can be calculated from a measurement of the noise suppression transfer function or the closed-loop transfer function by inverting either Equation 3.2 or 3.3, but the accuracy in the frequency band where they are close to 1. Hence, a combined measurement of both transfer functions allow for a more accurate estimation of the open-loop transfer function by calculating

$$L(s) = \frac{C(s)}{N(s)} . \quad (3.5)$$

---

<sup>1</sup> In case  $|L(0\text{ Hz})| > 1$ , the control bandwidth starts at 0 Hz.

This calculation is actually done for all measurements of open-loop transfer functions presented in this thesis.

### 3.4.2 Stability and noise suppression

As discussed in [AC00], the stability of a control loop can be determined from the bode diagram of the open-loop transfer function, like in Figure 3.10. From the denominator in Equation 3.3 follows that for  $L(s) = -1$  the control loop is unstable. This is equivalent to the phase of the complex function  $L(s)$  being  $+180^\circ$  or  $-180^\circ$  at the unity-gain frequency (UGF)  $f_{UG}$ , where the magnitude is 1 (0 dB).<sup>1</sup> To determine the stability of the feedback control, the phase and gain margin can be used, as illustrated in Figure 3.10. The phase margin is the minimal distance of the phase of the open loop transfer function  $L(f_{UG})$  at the UGFs  $f_{UG}$  from  $180^\circ$  or  $-180^\circ$ , for a stable feedback control loop. The gain margin is the minimal gain change, of the open-loop transfer function  $L(s)$ , to get unstable.

These two stability parameters describe the region around the unity-gain frequency. Depending on the combination of magnitude and phase of the open-loop transfer function an amplification of the free running (not stabilized) noise could occur, typically around the unity-gain frequency. This is visible as a so-called servo bump in the noise spectrum or in the noise suppression transfer function, see blue curve in Figure 3.10.<sup>2</sup>

The greater the phase and gain margin, the higher the stability of the control loop and the lower the servo bump. In the time domain, the servo bump results in overshoot and ringing of the control loop when excited by e.g. a jump of the reference signal.

The residual noise at the controlled variable  $X$  depends on the insertion points of the noise sources and on their noise levels (see also Figure 3.9):

$$X = -N_S \frac{L}{1+L} + \frac{(U_R + N_R)}{B} \cdot \frac{L}{1+L} + N_A \cdot P \frac{1}{1+L} + N_X \frac{1}{1+L} . \quad (3.6)$$

The output value  $X$  is stabilized to the reference  $U_R/B(s)$  within the control bandwidth, where the closed-loop transfer function is close to one, see Equation 3.3. The sensor noise  $N_S$  directly couples within the control bandwidth to the output. Hence, a low noise sensor is highly relevant for low noise performance of the feedback control. The noise on the reference  $N_R$  is scaled by the inverse sensor transfer function  $B(s)$ . To lower its coupling to the output, it is beneficial to use a sensor with a high gain. The actuator noise  $N_A$  is suppressed by the noise suppression transfer function and scaled by the actuator transfer function. Thus, it is largely suppressed within the control bandwidth but if the actuator transfer function  $P(s)$  still have significant gain outside the control bandwidth it can directly couple to the output  $X$ . Finally, the free running laser noise  $N_X$  is suppressed by the noise suppression transfer function.

1 If the phase is larger than  $+180^\circ$  or smaller than  $-180^\circ$  at the unity-gain frequency the feedback loop is also unstable. In the switch-on process of the control loop the  $+180^\circ$  or  $-180^\circ$  at unity-gain has to be crossed and so the loop gets unstable before reaching the full open-loop gain.

2 In this figure and in all following Bode plots within this thesis only the magnitudes of the noise suppression transfer functions are shown, as meanings of its phase are not further discussed.

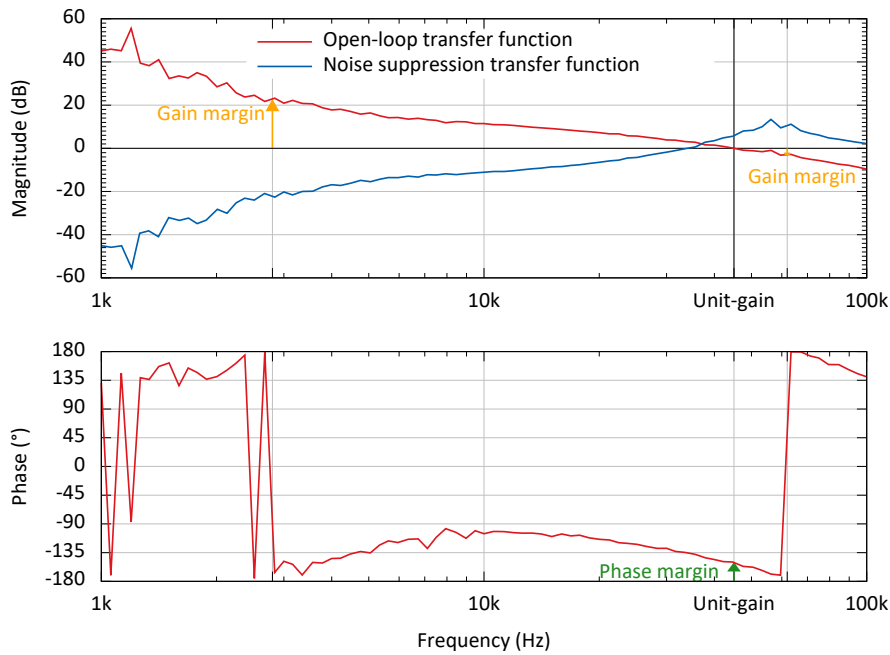


**Figure 3.10:** A bode plot of the open-loop transfer function of the power stabilization with actuation on the pump current is shown (red). The points relevant for the stability of the feedback control loop are marked. Due to noise in the control loop and a limited dynamic range of the analyzer, variations in the transfer function measurement are visible below 10 kHz. The calculated magnitude of the noise suppression transfer function (blue) shows the predicted noise reduction below the unity-gain frequency and the predicted noise amplification around this frequency.

Sensor noise directly couples to the output  $X$ , but it is suppressed by the feedback control in the in-loop sensor signal  $U_S$ . Therefore, an independent sensor, called out-of-loop sensor, has to be used to measure the residual noise in  $X$ . With an in-loop sensor, it is not possible to get a reliable measurement of the stabilized output noise because the sensor noise can be imprinted with a negative sign to the output and thereby cancel the sensor noise of the in-loop detector.

The noise suppression of the feedback control depends on the open-loop gain  $L(s)$ . To achieve a high noise suppression the magnitude of the open-loop-transfer function has to be maximized, see Equation 3.2. Besides the stability this is the second design goal for a high performance feedback control loop. The optimization is done with the design of the servo controller, such that the open-loop transfer function complies with the requested stability and noise suppression.

The ultimate limit for the noise suppression of the laser noise  $N_X$  is typically the in-loop sensor noise  $N_S$ . Therefore, loop gains much higher than  $N_X/N_S$  do not lower the noise of the stabilized output signal  $X$ . The loop gain increase is limited by the phase loss due to the signal propagation delay in the control loop and the amplitude to phase relation in the filter transfer functions.



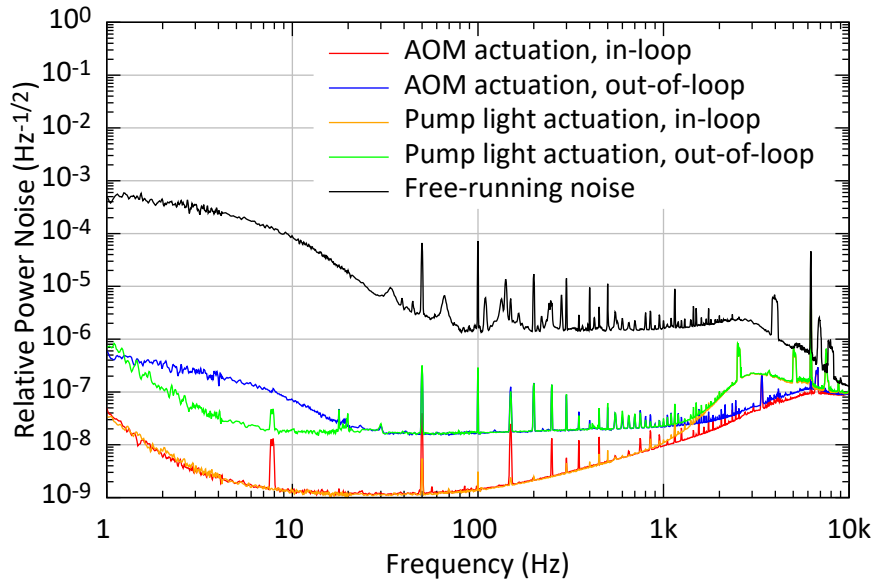


**Figure 3.11:** Two independent photodiodes of the same kind were used to perform a measurement of the relative power noise. This is shown as an amplitude spectral density over the Fourier frequency. One photodiode was used as an out-of-loop detector while the other one was used as an in-loop sensor for the active feedback stabilization. The power stabilization of the system was performed with two different power actuators (see text). Modified figure from [Thi19].

With this considerations, the open-loop transfer function shown in Figure 3.10 was designed for a sensor noise limited operation below 1 kHz. This power stabilization could be operated with the required high noise suppression. The used feedback stabilization had therefore an unity-gain frequency of 45 kHz. In Figure 3.11, the resulting noise is compared to the stabilization with the AOM. At frequency below 20 Hz the power noise with the pump light actuation is lower, probably because of less actuation noise, less dust in the air, or airflow during this measurement. The dust and airflow lead to beam pointing and time depending scattering resulting in an increase in power noise, especially in front of the in-loop power sensor.

A more complex design of the servo controller transfer function<sup>1</sup> should allow for an even higher noise suppression at frequencies above 1 kHz.

### 3.5 Conclusion and outlook

In this chapter, detailed characterizations of the power noise, frequency noise, pointing noise, and HOM content of two kinds of solid-state, single-pass laser amplifiers for 1064 nm wavelength are presented. Their added laser noise and HOM content are lower than the former used high-power oscillator in the aLIGO PSLs [Kwe12; Win11]. Therefore, they are

<sup>1</sup> The dip in transfer function of the plant was not fully compensated by the servo controller, see Figure 3.8 and Figure 3.10



sufficient to be used in second-generation GWDs, especially as their lower output powers match the injection powers needed for the interferometers. The results presented in this chapter showed that such an amplifier could be integrated into a copy of the aLIGO PSL with only minor modifications to the optical setup. The embedded power actuation via pump current bypassing in the amplifier driver electronic reduces the number of needed external actuators. Finally, the low complexity, high reliability, and high efficiency make them a suitable replacement for previously used injection-locked oscillators for high power generation [Win11].

Those results were essential for second-generation GWDs to take the risk of redesigning their laser systems and integrating the tested solid-state amplifiers [CCK19; Bod20]. As a follow-up investigation, we tested a neoVAN-4S-HP amplifier with a power and frequency stabilized seed laser. With an extended seed power range, we demonstrated output powers of up to 195 W [BMW20].

These experiments [Thi19; BMW20], the operation in second-generation GWDs [CCK19; Bod20] and further investigations [Bod22] confirm the high reliability of the tested amplifiers and reproducibility of the presented results.

For future GWDs, fiber amplifiers are proposed [ET 20; Eva21]. They showed the ability to generate even higher output powers to be used in GWDs of up to 336 W [Wel20; Hoc21]. To the time of writing this thesis, the full integration and stabilization into a GWD's PSL with this kind of amplifier have still to be demonstrated, as well as the final demonstration of long-term reliability, which is essential for the use in a GWD.

If the reliability of proposed fiber amplifiers at 1064 nm wavelength is not sufficient for future GWDs, the solid-state laser amplifiers discussed in this chapter are maybe a fallback option. Further optimizations on the laser crystals might provide high output power levels sufficient for future GWDs, e.g. by improved crystal cooling and beam parameter optimization of the pump and seed laser beams. Then, the coherent beam combination technique allows to further increase the laser power by combining the output of multiple amplifiers in a single, coherent laser beam [Wel21; Bod22].

For future GWDs, not only lasers at 1064 nm wavelength are proposed, but also lasers with longer wavelength are considered [Abb17e; ET 20; Eva21]. In the next chapters, the performance of laser sources at 1550 nm wavelength are investigated and their stabilization is presented, considering the needs of GWDs.



## CHAPTER 4

---

### Characterization of Laser Systems at 1550 nm Wavelength for Future Gravitational Wave Detectors

---

Some proposed third-generation gravitational wave detectors (GWDs) will use cryogenically cooled silicon mirrors, which require a change in laser wavelength from 1064 nm to a longer wavelength like 1550 nm or 2  $\mu\text{m}$ . Section 2.2 described the proposed change of wavelength and mirror material in more detail. This chapter begins with a short introduction, recapitulating why a laser system at 1550 nm is considered for third-generation GWDs, followed by the presentation of results closely based on the publication in MDPI Instruments [MW22]. Section 4.1 contains a detailed characterization of seed lasers, pre-amplifiers and power amplifiers at 1550 nm wavelength. Finally, an experiment to test the laser power and frequency stabilizations in an all-in-fiber-actuator setup is presented in Section 4.3. In addition to the results from [MW22], the function of a multiple-path feedback control loop is described in more detailed in Subsection 4.3.1. This kind of feedback control loop configuration is used for the frequency stabilization presented in Subsection 4.3.2.

The sensitivities of currently operating, second-generation GWDs are fundamentally limited by quantum noise as well as coating thermal noise of the interferometer mirrors, often called test masses. Future GWDs need to reduce, in particular, these noise contributions to achieve their anticipated ten fold sensitivity improvement. The quantum noise at higher Fourier frequencies can be reduced by increasing the laser power circulating inside the GWD interferometers and can independently be further improved by the injection of squeezed light into the interferometer's output port [Tse19; Ace19]. Meanwhile, the coating thermal noise is dependent on the coating properties and temperature. By reducing the temperature of the test masses, the coating thermal noise can generally be lowered, unless an increase in the mechanical loss of the coatings at low temperature cancels the direct temperature effect as discussed in Section 2.2 and in [Har02; Ste18]. The first large scale GWD, which uses cryogenic temperatures to lower the thermal noise is the KAGRA detector [Aku19; Aku20]. Here, sapphire test masses are used with a 1064 nm wavelength laser source.

Test masses made from silicon are likely to be used in future GWDs, as they show more promising material characteristics and are probably available in larger sizes than sapphire test masses [ET 20; Adh20]. As silicon is not transparent at the currently used wavelength of 1064 nm, this test mass material needs a laser wavelength between 1.5  $\mu\text{m}$  and 2.2  $\mu\text{m}$  to be successfully implemented in future GWDs [Adh20]. The Einstein Telescope (ET) proposes three interferometers for the low frequency detection band and three for the

high frequency detection band arranged in a triangular configuration. The low frequency interferometers shall have silicon test masses and 1550 nm lasers, which can deliver 3 W of optical power behind the input mode cleaner cavity [ET 20]. The Laser Interferometer Gravitational-Wave Observatory (LIGO) Voyager and Cosmic Explorer, future plans for GWDs in the United States, shall use laser powers from 200 W up to 1 kW with a laser wavelength compatible with silicon optics [Abb17e; LIG19].

As pointed out in Chapter 2, ground-based GWDs generally place very high demands on their laser systems. The laser sources have to be single frequency, single mode, linear polarization, and low noise. In particular, the frequency noise, power noise, and beam pointing noise<sup>1</sup> in the detection band between a few Hz and typically a few kHz are most essential. The second important frequency band is at phase modulation frequencies of the interferometer's length and alignment control systems. This band spans from a few MHz up to the mid MHz range, depending on the chosen highest modulation frequency for the detector control [Bui20b; All20]. As no free-running laser meets the demanding GWD stability requirements, multiple stages of active feedback control and passive noise filtering are needed in the so-called laser pre-stabilization to prepare the lasers for injection into the GWD interferometers.

Frequency stabilizations of low-power lasers in the range of 1.5  $\mu\text{m}$  wavelength were reported from various fields, such as the stabilization for a frequency comb [Dol13], stabilization to ultra stable silicon cavities [Mat17] or stabilization to a high Q fiber resonator [BLF20]. A frequency and power stabilized system with fiber optics and an output power of 10 mW was demonstrated [TAT08]. None of these experiments simultaneously achieved the stability demanded by GWDs for all relevant laser parameters and not all technologies needed for a GWD PSL were fully demonstrated.

For the presented laser characterizations in this and the next chapter, a well-tested setup, the so-called diagnostic breadboard (DBB) was used. The DBB was developed for 1064 nm [KW08] and was then adapted for use at 1550 nm. With this DBB, different seed lasers and power amplifiers were characterized. An external cavity diode laser (ECDL) from RIO [Opt21] was tested and the measurements are compared to other published results on this seed laser [Num10; Tsu11]. Fiber lasers from NKT Photonics [NKT21] with different amplifiers and a seed source from NP Photonics [NP ] were characterized subsequently. In addition, two low power amplifiers, a booster optical amplifier (BOA) from Thorlabs [Tho21], and a fiber amplifier built in a collaboration with the Laser Zentrum Hannover e.V. [Las] were tested. Their free-running laser noise and their actuators for potential use in stabilization control loops are discussed in Section 4.2. Based on these results, Section 4.3 reports on the active feedback stabilization of a low power laser system build from the ECDL and the BOA.

#### 4.1 Experimental setup

For the laser characterization, a DBB for 1550 nm based on the original 1064 nm version was built [KW08]. 1550 nm optics, germanium quadrant photodiodes and increased trans-

---

<sup>1</sup> Beam pointing noise typically couples to power noise at the next mode selective element, like a cavity.

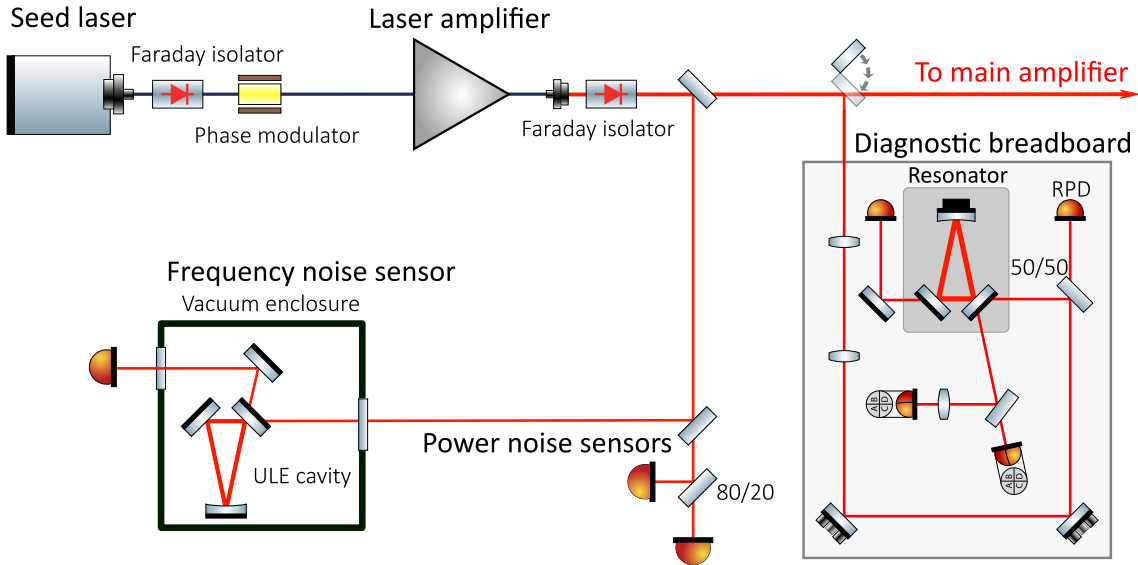


**Figure 4.1:** The simplified stabilization setup shows the seed laser with 1550 nm wavelength, which was coupled via a fiber Faraday isolator to the fiber phase modulator and was amplified by the booster optical amplifier. A Faraday isolator was placed in the 115 mW free space beam. This was to prevent reflections back to the amplifier. Parts of the beam were sent to power sensors and the frequency reference cavity. The main fraction of the beam was analyzed with the diagnostic breadboard. Figure from [MW22].

impedance gains of the photodiodes were implemented. The increased transimpedance gains were required to allow measurements at input powers of 5 mW to 35 mW as compared to the standard DBB with maximal 150 mW input power. This change was necessary to characterize the seed lasers without any power amplifier. A schematic layout of the DBB is shown at the right-hand side of Figure 4.1.

With this DBB, free space laser beams can be analyzed in their noise and spatial mode properties. A beam is coupled via two adjustable mode-matching lenses and two piezo alignment mirrors to a triangular optical ring resonator. A low noise indium gallium arsenide (InGaAs) photodiode (RPD)<sup>1</sup> in front of the resonator is used to perform power noise measurements at Fourier frequencies between 1 Hz and 100 MHz. A photocurrent of up to 18 mA can be detected. After optimization of the fundamental mode transmission by alignment and mode-matching of the incoming beam, the mode decomposition of this beam can be analyzed by scanning the length of the cavity and measuring the transmitted power. The frequency noise of the laser beam can be calculated from DBB measurements by stabilizing the resonator length with the dither modulation technique on a resonance for the laser frequency. The dither modulation is imprinted at 1 MHz on the resonator's piezoelectric element. The error signal for the length control loop is generated by demodulation of the light power measured in reflection of the resonator. The error signal

<sup>1</sup> The abbreviation is used in the original publication on the DBB [KW08] and refers to relative intensity noise photodiode.

and the control signal of the length feedback stabilization are captured to calculate the frequency noise between Fourier frequencies of 1 Hz to 500 kHz. An equivalent technique in combination with the quadrant photodiodes is used for differential wavefront sensing based alignment control loops to stabilize the beam pointing [Mor94; And84]. This also enables the measurement of beam pointing noise. In addition to the noise measurements, the calibrated sensors of the DBB are used for transfer function measurements of the laser modulation inputs.

For all measurements, the beam path and the environmental conditions, such as airflow, devices in operation in the lab, or room light conditions, were kept constant to achieve comparable results. The measurements were performed repeatedly over more than one day to confirm a stable performance of the tested lasers. Modulation inputs of the lasers are terminated or disabled during the noise measurements.

#### 4.1.1 Characterized laser systems

An overview of the characterized seed lasers and laser amplifiers is given in Table 4.1.

**Table 4.1:** Tested laser sources and amplifier.

Product Name <sup>a</sup>	Technology	Output Power
Seed laser sources		
<b>Orion</b> laser source, RIO3135-3-34-5 [Opt21]	external cavity diode laser (ECDL)	10 mW
Koheras <b>Adjustik</b> E15, K822-125-102 version 1 <sup>b</sup> K822-125-102 version 2 <sup>b</sup> [NKT21]	erbium fiber lasers	40 mW
<b>NPP Seed laser</b> of a high power laser module [NP ]	erbium fiber laser	28 mW <sup>c</sup>
Pre-amplifier		
Booster optical amplifier (BOA), <b>BOA1004P</b> [Tho21]	semiconductor waveguide amplifier	117 mW <sup>c</sup>
<b>Fiber pre-amplifier</b> [Las]	erbium fiber amplifier	50 mW <sup>c</sup>
Power amplifier		
<b>NKT Boostik 2W</b> , K532-015-100 [NKT21]	erbium fiber amplifier	2 W
<b>NKT Boostik 10W<sup>d</sup></b> , K532-015-120 [NKT21]	erbium fiber amplifier	10 W
<b>RIO Grande</b> laser, RIO1175-9-34-5 [Opt21]	erbium fiber amplifier with integrated ECDL seed laser	2 W

<sup>a</sup> The **bold** marked names are used in the text as a designation for the laser and amplifiers. <sup>b</sup> The versions are internal versions by the manufacturer and do not correspond to different data sheet specifications.

<sup>c</sup> Measured output power. <sup>d</sup> Two amplifiers of this kind were characterized.

Commercial seed lasers were chosen, which are based on different technologies and have promising data sheet specifications for use in the field of ground-based gravitational wave detection. Single mode, single frequency operation with high stability in power and frequency within the gravitational wave detection band, as well as in the MHz range, were the most important selection criteria. In addition, an option for frequency control is needed to further stabilize the laser frequency.

Doped fiber-based and semiconductor-based seed lasers were tested. Both topologies achieve single frequency operation with a Bragg reflector for distributed feedback [Num10; Sto08; Bar06; NKT21]. To pre-amplify the seed power, two different types of amplifiers were investigated. A booster optical amplifier (BOA) based on a fiber coupled InP/InGaAsP quantum well layer structure in a waveguide was tested [Tho21]. It was operated at an output power of 117 mW. The characterized fiber erbium pre-amplifier is core pumped at 976 nm wavelength with a Bragg grating stabilized laser diode and was built in cooperation with the Laser Zentrum Hannover e.V. [Las]. For both amplifiers, an in-house built, low noise current source was used with a fast modulation input, which is based on the designs presented in [Eri08; TED11]. The Boostik power amplifiers were tested with different seed lasers to test their influence on the actuation and noise characteristics. To distinguish between the two different Boostik amplifiers, they are named by their slightly different output power levels of 10.4 W and 11 W later in the text. The tested Grande fiber amplifier has an integrated, non-exchangeable seed source, which is similar to the Orion laser.

## 4.2 Laser characterization

First, the different free-running laser systems and MOPA combinations were characterized with the DBB. The transversal mode purity and the pointing noise of all tested lasers were measured. All show a low higher order mode content, as all lasers have polarization maintaining, single mode fiber output ports and no significant pointing was measured.

The frequency noise measurements in Figure 4.2 show that only the seed lasers contribute in the measurement band to the total frequency noise of the modular systems. Small deviations at 100 Hz to 300 Hz are due to slightly different unity gain frequencies for the DBB resonator's stabilization loop. All shown noise measurements are captured as a set of fast Fourier transformed measurements, which were averaged over multiple samples and normalized by the resolution bandwidth to achieve an amplitude spectral density. Multiple measurements with different spans were performed and stitched together to improve the resolution for the logarithmic frequency scales. The samples with different spans are plotted with a small overlap to account for transfer function uncertainties and different sensor whitening of different frequency spans. The lowest frequency noise is measured for the Adjustik lasers, followed by the Orion laser source. Both have a frequency noise comparable to the noise of the seed laser used in current GWD PSLs at frequencies below 1 kHz. The seed lasers with 1064 nm wavelength used in current GWDs are NPRO. Their typical frequency noise is plotted as the NPRO projection [KW08] in Figure 4.2.

The relative power noise (RPN) of the seed lasers is shown in Figure 4.3 as an amplitude spectral density. The RPN of the Orion has a different spectral shape compared to fiber lasers. The noise of the Orion laser roughly follows a  $f^{-1/2}$  slope, down to the detection shot noise of  $1 \times 10^{-8} \text{ Hz}^{-1/2}$ . This low noise was achieved by replacing the supplied external

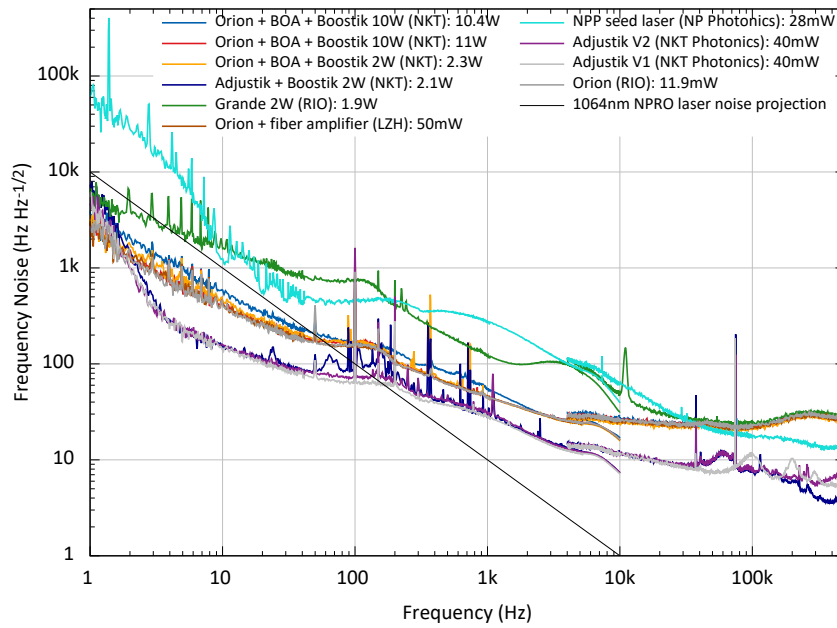


**Figure 4.2:** The free-running frequency noise of the different seed lasers and MOPA combinations is shown. The frequency noise of the MOPA systems is dominated by their seed laser noise. Figure from [MW22].

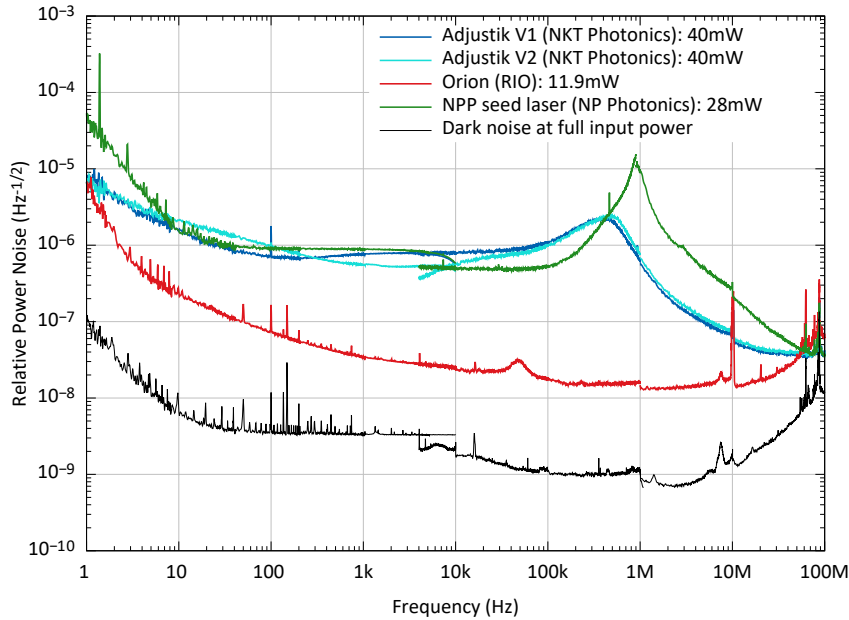


**Figure 4.3:** The free-running relative power noise (RPN) of the seed lasers, plotted as amplitude spectral density, follow two characteristic shapes. The Orion laser has a very low free-running noise. The fiber lasers have a higher noise floor and a characteristic relaxation oscillation peak. Figure from [MW22].



5 V switching power supply by a linearly stabilized supply with lower noise coupling to the laser. The relaxation oscillation of the ECDL is typically at GHz frequencies, because of the short lifetime of the upper laser level in the semiconductor [Day22].

The RPN of the fiber lasers are, to the current understanding, limited by the RPN of the used pump diodes, excess noise due to the reabsorption by the erbium ions, and the relaxation oscillation [Ral99; CEK03] within the laser resonator at 500 kHz for the Adjustik laser and at 1 MHz for the NPP seed laser. The peak at 10 MHz in the measurements is caused by a timing signal for the data acquisition system. The measurement of the Orion laser is influenced by dark noise above 30 MHz due to low available laser power.

The response and power cross-coupling of the frequency actuation inputs of the seed lasers are compared in figures 4.4 and 4.5. The frequency of the fiber laser was tuned with a piezo electric element [NKT], which has characteristic resonances above 40 kHz and shows only a significant coupling from the frequency modulation to the output power of the laser at Fourier frequencies around 70 kHz. The resonances limit the usable bandwidth of this actuator in feedback controls loop for a frequency stabilization.

The frequency of the Orion laser is controlled by the pump current of the semiconductor, which introduces a carrier density-dependent refractive index change in the laser resonator. Hence, no mechanic resonances are present in the transfer function, but a direct coupling to the optical gain and, by that, to the output power can be observed. The transfer function decays with multiple poles, which can be easily compensated in a feedback control. This makes the delay equivalent phase loss in the transfer function to be the ultimate limit of the control bandwidth for a stabilization. A slow, high range tuning of the frequency is possible for both lasers by a temperature control of the laser resonator.

The RPN of the pre-amplifiers was tested with the Orion laser as seed laser, as it has the lowest RPN. For the fiber pre-amplifier, as well as for the BOA, exactly the same low noise current driver was used with a relative current noise of  $3 \times 10^{-9} \text{ Hz}^{-1/2}$  above 100 Hz. The noise spectral densities are presented in Figure 4.6. The higher RPN of the fiber pre-amplifier in comparison to the BOA could be caused by reabsorption of the seed in the quasi three laser level system of erbium or amplified spontaneous emission [Dig01]. In addition, the RPN of the pump diodes for the fiber pre-amplifier was measured to be at the same level as its output power noise. Tests with a pump diode, stabilized to more than a factor of 10 less RPN than the free-running pump light, were performed. These tests showed an improvement of less than a factor of two in the output RPN of the amplifier. Thus, the noise of the pump light seemed to be not the only relevant noise source.

Figure 4.6 shows the difference between BOA and fiber pre-amplifier systems. The system based on the fiber pre-amplifier has a noise floor close to  $1 \times 10^{-6} \text{ Hz}^{-1/2}$  for low frequencies. At a corner frequency of about 10 kHz the RPN decreases, which is due to the reduced response of the fiber amplifier to power noise of its pump source (see Figure 4.7). In comparison, the noise of the BOA pre-amplifier decreases roughly with a  $f^{-1/2}$  slope. Measurements were taken at the maximal output power of 117 mW and at 40 mW, which is the pre-amplifier's output power used in this thesis to seed the subsequent NKT power amplifiers. The relative current noise is clearly below the power noise of both amplifiers and thereby does not limit their noise performance, assuming a linear coupling mechanism, see Figure 4.6.

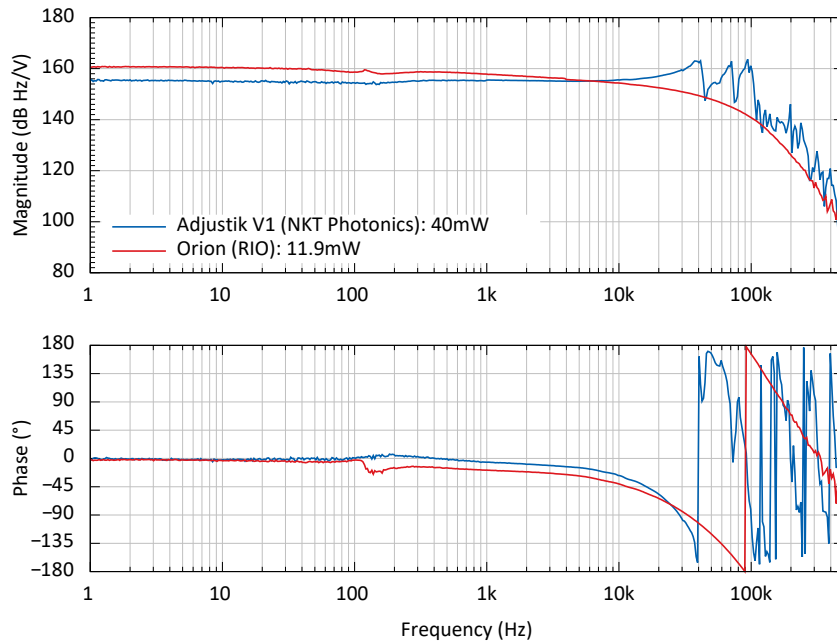


**Figure 4.4:** The frequency actuation transfer functions of the fiber laser and of the Orion laser show a similar magnitude at low frequencies. Resonances in the fiber laser’s transfer function reduce the usable actuation bandwidth significantly compared to the Orion laser. Figure from [MW22].

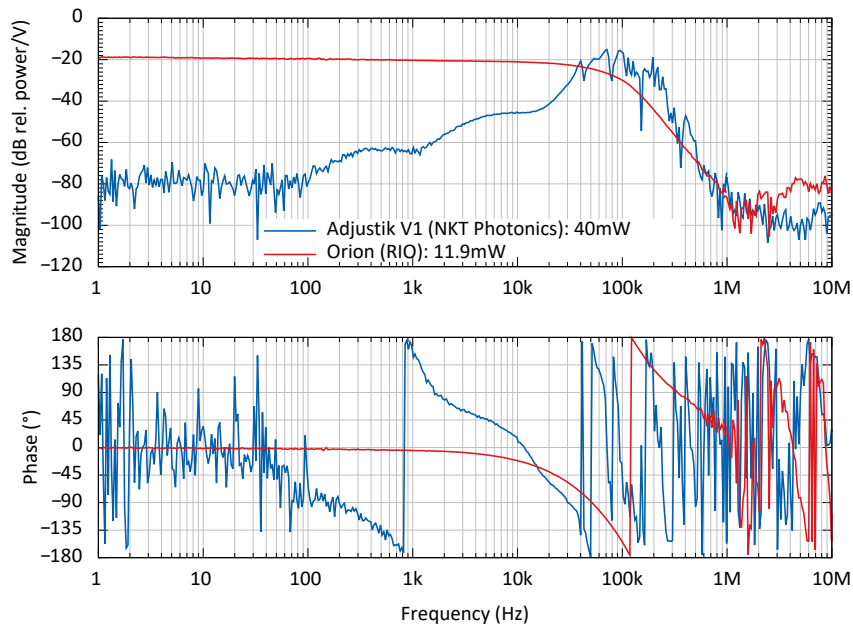


**Figure 4.5:** The cross-couplings from frequency actuation to the output power of the Orion laser and fiber laser is shown. As the pump current for the Orion laser also defines the output power, a direct coupling is observed. Meanwhile, the output power of the fiber laser shows a strong coupling only around 30 kHz. Figure from [MW22].

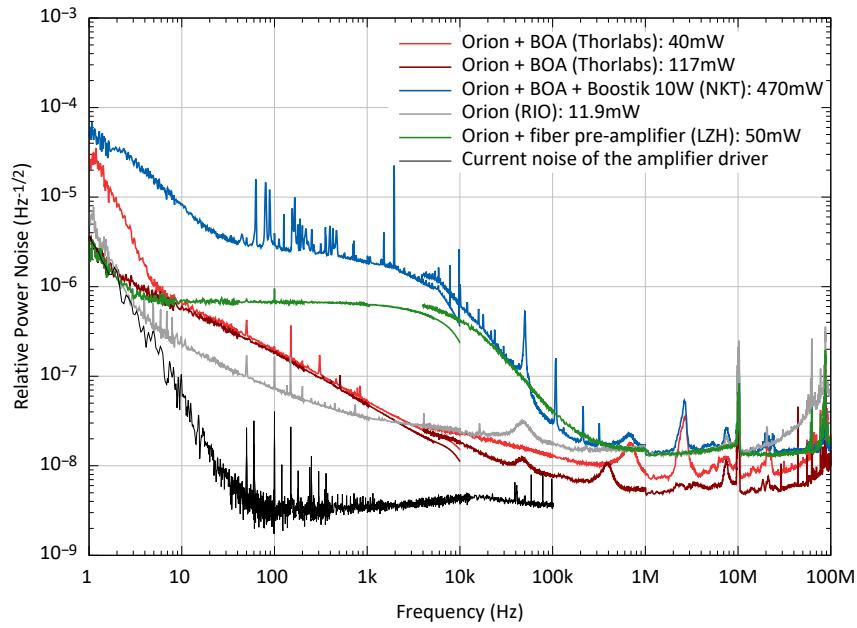


**Figure 4.6:** The free-running RPN at the output of the pre-amplifiers is shown. For all measurements, the Orion laser is used as the seed source (grey curve). Figure from [MW22].

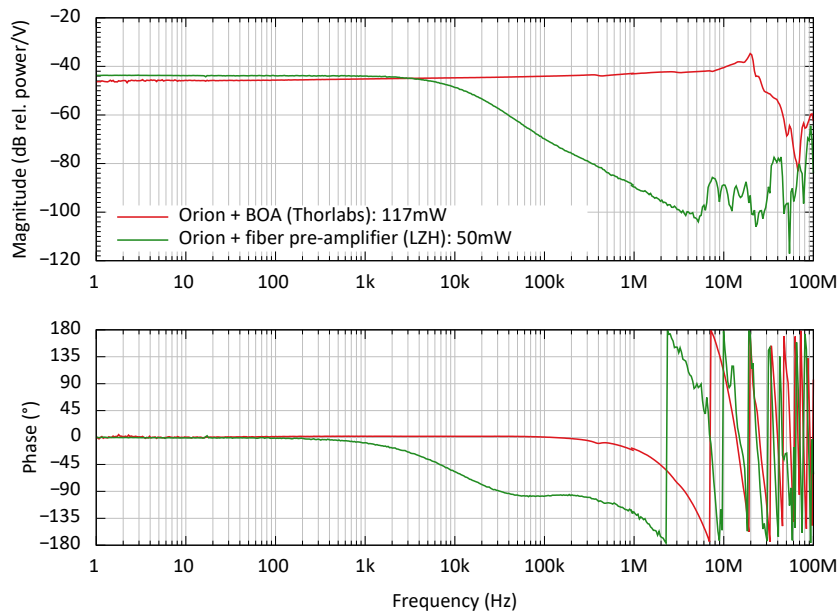


**Figure 4.7:** The pump current of the BOA and fiber pre-amplifier's pump diodes is modulated to measure the transfer function to the pre-amplifier's output power. Figure from [MW22].

The Boostik 10 W amplifier from NKT consists of a pre-amplifier and a power amplifier. The pre-amplifier was tested with the unpumped power amplifier. Its noise (blue curve in Figure 4.6) shows several sharp peaks that might be caused by internal electronics. The noise level could also be increased due to the transmission through the unpumped active fiber, where reabsorption could happen. The shot noise limits for the amplifier measurements shown in Figure 4.6 were between  $4 \times 10^{-9} \text{ Hz}^{-1/2}$  and  $6 \times 10^{-9} \text{ Hz}^{-1/2}$  and in the case of the Orion seed laser (grey curve) at  $1 \times 10^{-8} \text{ Hz}^{-1/2}$ , as only a lower optical power was available on the power sensor in the DBB.

In Figure 4.7, the transfer functions of the pre-amplifiers from pump current to output power are shown. The pump currents are modulated with a  $5 \text{ mA V}^{-1}$  modulation response on a total pump current of 522 mA for the fiber amplifier and 600 mA for the BOA. The transfer functions are calibrated as relative power modulation per input voltage. This transfer function typically forms a low-pass, where the corner frequency  $f_{\text{eff}}$  defines how fast the population of the upper laser level can adapt to the change in pump power [Tün12].<sup>1</sup> The corner frequency of the fiber pre-amplifier is determined by a fit to  $f_{\text{eff}} = 6.7 \text{ kHz}$ . In contrast, the BOA's transfer function is limited by the speed of its current driver. The typical corner frequency  $f_{\text{eff}}$  of these semiconductor-based laser amplifiers is above 100 MHz [Ebe93].

The response of the fiber pre-amplifier to seed power modulation (see Figure 4.8) is suppressed at low frequencies with the amplifier gain, due to the seed power saturation of the amplifiers. Above the corner frequency  $f_{\text{eff}}$ , the seed power modulation is amplified by the full power gain of the amplifiers [Tün12]. The seed power modulation sent to the BOA is suppressed in the whole bandwidth of the seed power modulator, due to the high corner frequency  $f_{\text{eff}}$  corresponding to this amplifier.

The RPN of the all-fiber power amplifiers is plotted in Figure 4.9. The typical flat noise for frequencies up to 10 kHz, which was discussed for the pre-amplifiers, is again clearly visible. Above 10 kHz the power noise differs with the used seed laser sources. Slightly different RPN levels were measured for the two nominal similar 10 W power level amplifiers, which might be caused by different noise levels of internal current drivers for the pump diodes. The narrow peaks in the RPN measurements of the amplifier can be caused by internal electronics in the amplifier modules, such as temperature controllers or digital controls.

The transfer functions in Figure 4.10 show how the output power of the power amplifiers can be controlled by modulating their seed laser power. The Grande MOPA laser does not allow to change the power of its integrated seed separately from its frequency. The response of its analog power control is shown for comparison. This input allows to change the pump current with a bandwidth of less than 10 Hz. The other power amplifiers only provide a slow digital control of their output power. Fast output power control is only possible via control of the seed or pre-amplifier power. Due to the seed power saturation of the power amplifiers, they show a reduced response to power modulations of the seed below their corner frequency  $f_{\text{eff}}$  of the coupling transfer function. This makes it difficult

---

<sup>1</sup> This effect is similar as for the solid state amplifier transfer function in Section 3.4.

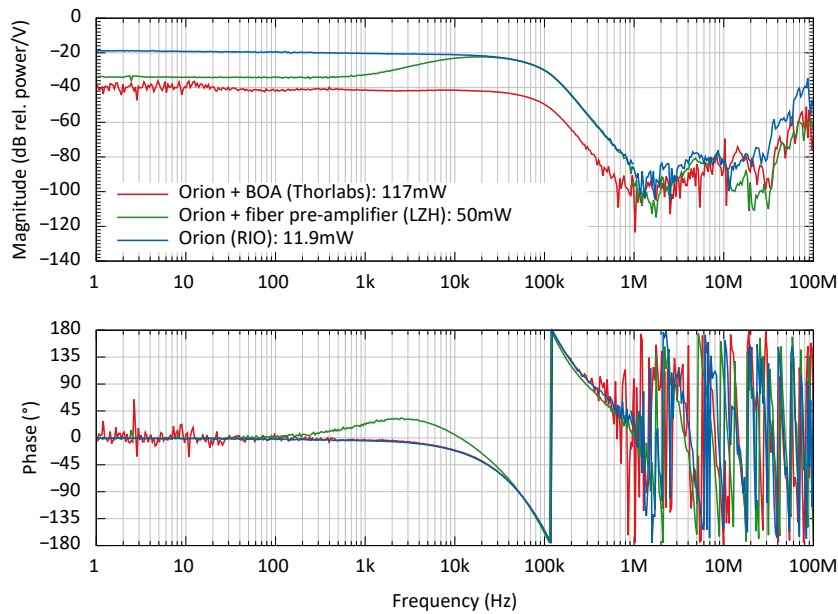


**Figure 4.8:** The seed power is modulated to measure the transfer function to the output power of the pre-amplifiers. The seed power modulation (blue curve) is transferred to the output of the pre-amplifiers (green and red curves). Figure from [MW22].

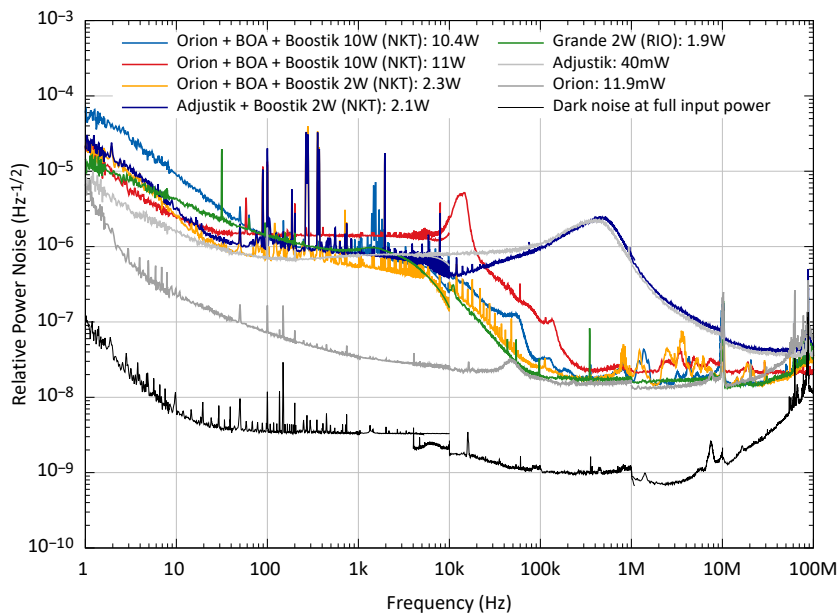


**Figure 4.9:** The free-running RPN spectral densities at the output of the power amplifiers are shown. At low frequencies, the power noise of the power amplifiers is dominated by their pump power noise. Figure from [MW22].

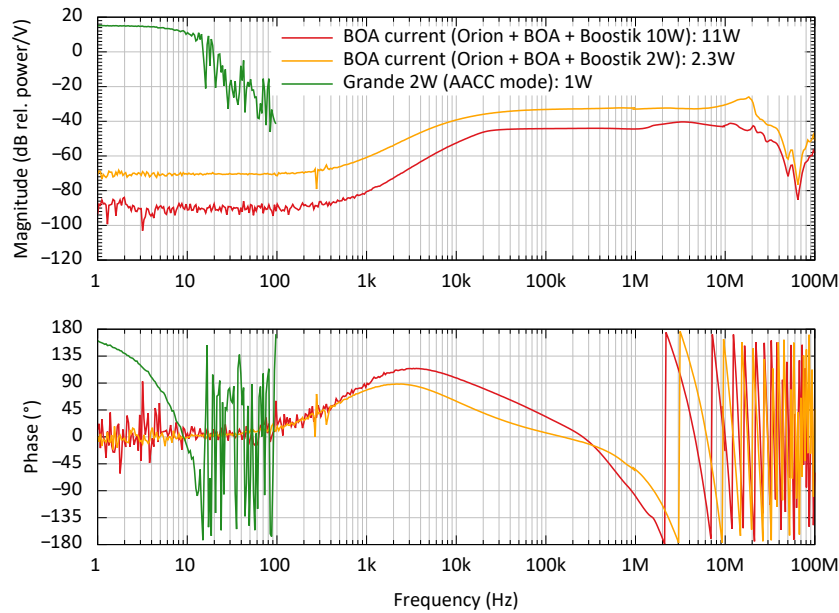


**Figure 4.10:** The transfer functions from seed power modulations to power modulations of the power amplifier output have the same shapes as the measurements with the fiber pre-amplifiers in Figure 4.8. The Grande laser is the only high power amplifier tested, which offer any analog power control. The laser pump diode current can be controlled, when the laser is in analog automatic current control (AACC) mode. Figure from [MW22].

to use only the pre-amplifier seed power to stabilize the power amplifier’s output power.

The relaxation oscillation frequency of the fiber seed laser is at or above the corner frequency of this transfer function. Thereby, its magnitude in a relative power noise spectral density is not attenuated, as can be seen in the power amplifier’s output noise in Figure 4.9.

The frequency modulation transfer functions from the pre-amplifier to the power amplifiers are up to small delay-driven phase losses given by the seed transfer function (see Figure 4.4). The delay is caused by the propagation time through the optical fibers of the amplifiers.

### 4.3 Stabilization

An experiment was build to demonstrate the capabilities of the actuators and sensors for a GWD’s stabilized laser system. The Orion laser and the BOA were identified as the best MOPA combination for this test, as they offer actuators for frequency and power stabilization with high range and bandwidth. This combination form an all-in-fiber-actuation MOPA laser. Thus, no free space actuators are used to control the laser power or frequency. The frequency noise of this combination is higher compared to the NKT fiber lasers, which has been weighed against the resonance-free frequency actuation of the Orion laser and its lower power noise. A simplified sketch of the setup is given in Figure 4.1. The output power of this MOPA system was 115 mW. No power amplifiers were included in the stabilization setup as they are not expected to influence the frequency noise and as the

currently available models do not provide appropriate power actuators.

For the power stabilization, in- and out-of-loop photodiodes with transimpedance amplifiers were used. The photodiodes were Perkin Elmer C30642. Both readout electronics are based on electrical circuit designs used in the aLIGO PSL's [Kwe12]. The in-loop detector has an improved bias circuit and an updated low noise operational amplifier to increase the achievable bandwidth of the stabilization [MK20].

The laser frequency was stabilized to an ultra-low expansion glass ceramic (ULE) spacer, triangular reference cavity with a finesse of roughly 59 000 and a free spectral range of 702 MHz. Two plane mirrors are optically contacted to the spacer while the curved mirror is glued to it. The cavity is placed with fluorine rubber vibration isolation pads in a vacuum tank at a pressure of 1 mbar to reduce acoustical noise coupling. The laser frequency was stabilized with the Pound–Drever–Hall (PDH) sensing scheme to the cavity [Dre83; Bla01]. A fiber phase modulator was integrated to add phase modulation sidebands at 44 MHz for the PDH sensing and for fast actuation in the frequency stabilization feedback control loop, while the laser current was used for the slow frequency actuation. The function and stability criteria for this two-actuator feedback control loop are introduced in the following subsection.

#### 4.3.1 Multiple-path feedback control

This subsection continues the introduction in feedback control theory from Section 3.4.1 and is based on the techniques described in [AC00]. Feedback control loops with several actuators can be designed with a modification of the stability criteria introduced in Section 3.4.1 for single-feedback control loops.

The frequency stabilization of the pre-amplified Orion laser is used as the example to study the multiple-path feedback control. It is realized by acting on the ECDL's pump current and on the fiber phase actuator. Below 100 kHz, the pump current of the seed laser was used to control the laser frequency to be on resonance with the reference cavity. The actuation on the laser frequency in this frequency span is beneficial, because of the actuator range of 200 MHz and a gain of  $100 \text{ MHz V}^{-1}$  (see Figure 4.4). This high modulation gain and range are beneficial to reduce the high noise amplitude at low Fourier frequencies.<sup>1</sup> Furthermore, the large range is required to compensate for even slower frequency drifts, e.g. caused by thermal drifts of the seed laser.

Due to the limited response of the laser actuator at Fourier frequencies above 100 kHz and the delay of the actuation, this actuator is not a suitable actuator for higher Fourier frequencies. Here, the fiber phase modulator is a more appropriate actuator because of its lower delay and higher actuation gain at these Fourier frequencies. An applied voltage to the electro-optical phase actuator results in a frequency actuation of  $0.5 \text{ Hz V}^{-1} \cdot f/1 \text{ Hz}$ , which is a factor 100 higher than a typical free-space phase modulator.

---

<sup>1</sup> The calculated root mean square (RMS) value for an amplitude spectral density with  $1/f$ -shape is dominated by the noise at low frequencies, while for white (frequency independent) noise the RMS value depends on the noise bandwidth.



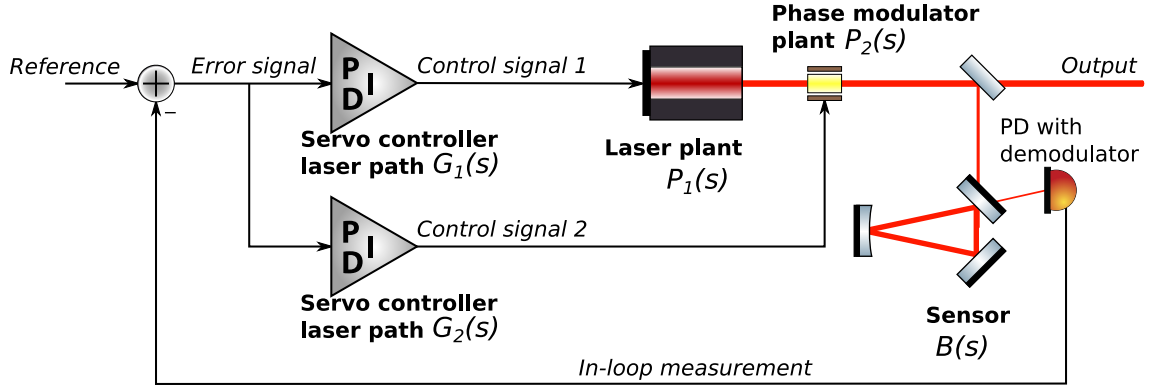


**Figure 4.11:** The signal flow diagram of a multiple-path feedback control loop is shown. This can be seen as an extension of the simple control loop design shown in Figure 3.9.

These two actuators are implemented in two parallel servo controller paths, as visible in the signal flow diagram in Figure 4.11. Both servo controllers use the same error signal, generated with the PDH technique from the comparison of the laser frequency to a resonance frequency of an optical cavity. The control signals 1 and 2 are sent to the individual actuators, which both control the output quantity to be stabilized. The open-loop transfer function  $L(x)$  of this system is given as

$$\begin{aligned} L(s) &= B(s) [G_1(s)P_1(s) + G_2(s)P_2(s)] \\ &= B(s)G_1(s)P_1(s) + B(s)G_2(s)P_2(s) . \end{aligned} \quad (4.1)$$

The first line of this equation can be rewritten to the second line, where the open-loop transfer function is the sum of two individual loops with their common sensor transfer function  $B(s)$ .

In Figure 4.12, the simulated total open-loop transfer function is compared to a measurement of it. The open-loop transfer function was calculated from a noise suppression transfer function measurement (see Equation 3.2). Additionally, simulations of the open-loop transfer function containing only the phase modulator feedback (phase modulator path) and only the laser feedback (laser path) are shown.

The achieved unity gain frequency is 1.3 MHz. At this frequency, similar as for a single loop control loop (see Subsection 3.4.2), the stability criteria apply and the loop's stability can be quantified by the phase and gain margins. The stability criterium does not need to be fulfilled by both pathes individually. Instead, the gain dominating path at the unity gain frequency can be evaluated, which is in this case the phase modulator path.

Additionally, the crossover between the control paths has to be stable. The crossover frequency is defined as the Fourier frequency at which both control paths' transfer functions have the same magnitude. For the frequency control loop this is the case at 100 kHz, visible in Figure 4.12. At this point, the more relevant compensation of the error is handed over from the low frequency actuator to the high frequency actuator. At the crossover frequency, the same stability criteria as at the unity gain frequency apply, but measured relative between the two paths' transfer functions. Thus, at the crossover frequency the phase difference between the paths has to be less than  $180^\circ$  for the multiple-path loop to be stable.



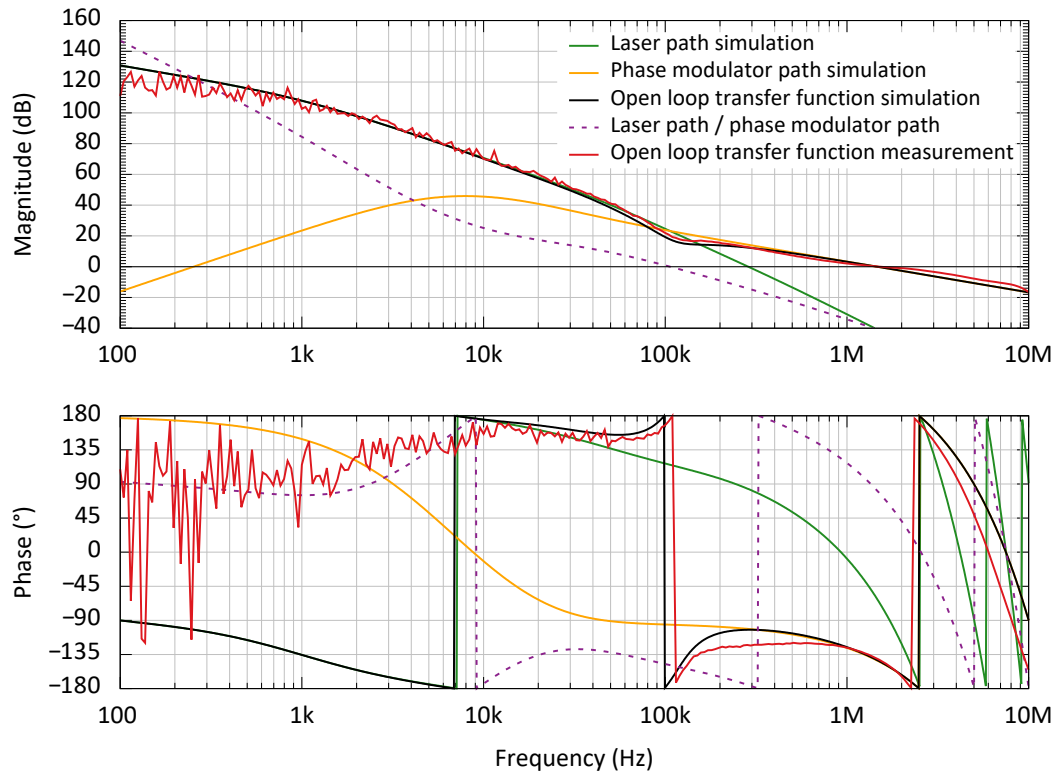


**Figure 4.12:** The open-loop transfer function of the laser’s frequency stabilization to the resonance of the reference cavity is shown. A unity gain bandwidth of 1.3 MHz was achieved by utilizing a crossover between feedback to the seed laser (green curve) and to the fiber phase modulator (orange curve) at 100 kHz. The single control paths were simulated and added to the total open-loop transfer function simulation (black curve). Extended Figure from [MW22].

Otherwise, the actuators would counteract each other resulting in a macroscopic oscillation at the crossover frequency. The phase margin of a stable crossover is then defined by the phase distance to the instability. The gain margin at this frequency describes a possible gain change in one control loop path without getting unstable at the crossover.

This modified stability criteria can be also mathematically reformulated as taking one actuation path’s open-loop transfer function  $L_2(s) = B(s)G_2(s)P_2(s)$  as the normalization for the other  $L_1(s) = B(s)G_1(s)P_1(s)$ :

$$\tilde{L}(s) = \frac{L_1}{L_2} = \frac{G_1(s)P_1(s)}{G_2(s)P_2(s)} \quad (4.2)$$

and then applying the unmodified stability criteria for a feedback control loop on this open-loop transfer function [AC00]. The phase margin and gain margin definitions can be applied to  $\tilde{L}(s)$  as described in Subsection 3.4.2 for a single path feedback control loop. For the frequency stabilization this normalized control loop path is plotted as a dashed line in Figure 4.12.

Applying the described stability criteria to the transfer functions in Figure 4.12, the phase margin at the crossover frequency is  $30^\circ$  and the gain margin is 16 dB. These stability margins causes already the visible dip in the open-loop transfer function at 107 kHz, close to the crossover frequency. At the unity gain frequency of 1.3 MHz, the phase margin is  $45^\circ$  and the gain margin is 3 dB.

These four margins describe the two frequency regions relevant for the stability of the presented multiple-path frequency stabilization. Phase margins above  $45^\circ$  in combination with gain margins above 10 dB typically result in robust feedback control with low excess noise above their unity gain frequency. However, for higher noise suppression or bandwidth, compromises have to be made. For the presented frequency stabilization, the margin which influences the excess noise above the unity gain frequency, is the gain margin of 3 dB. The control bandwidth of this stabilization is limited by the required low-pass in the demodulation electronics of the PDH sensing and electronic delays. The crossover between the two parallel control paths is less critical and its stability is limited by the delay and decreasing gain of the Orion laser's actuator.

The reliable operation of a parallel path feedback stabilization depends in practice also on the control ranges of the actuators and the open-loop stability of the individual paths. If saturation in one of the parallel signal paths occurs, which breaks the approximation of a linear time invariant system, its loop gain decreases significantly. Then, only the transfer function of the not saturating path is relevant for the stability of the whole loop. If that path is not stable at its unity-gain frequency by its own, the output quantity of the control loop starts to macroscopically oscillate and typically does not recover to functioning state by its own. This described situation occurs e.g. when the phase modulator of the discussed frequency stabilization saturates and the loop stability criteria applies to the isolated laser path in Figure 4.12. Different approaches can be used to deal with this problem:

- The actuator ranges can be chosen much larger than the expected range needed to compensate the laser noise. This approach was chosen for the frequency stabilization discussed in this chapter. Nevertheless, the constrain of the maximal amplitude is not possible, if the signal contains Gaussian noise [Ben10]. Hence, for reliable long-term operation an additional strategy is beneficial. Despite this fact, the advantage of this approach is the operation with defined noise suppression and no need for additional control or monitoring electronics.
- With an automated control and monitoring system, the state of the control loop can be guarded. The system needs an algorithm to detect the oscillation state or another malfunction. Then, the algorithm has to recover the normal operation of the control loop. This is typically done by turning the stabilization stages off and on in the required order. This method is used for the inner frequency stabilization loop in the aLIGO PSL [Kwe12; BO12].
- Alternatively, each control loop path can be designed such that it is stable at its unity-gain frequency. For this case, a saturation in one control path cannot cause an unstable oscillation in the feedback control loop. Thus, if this path recovers to normal operation the total parallel feedback loop should recover to normal operation. This approach was taken for the frequency stabilization described in Chapter 5.

The other multiple-path feedback design applied in the context of this thesis is the nested control loop design. Here, a fast inner loop is operated, and a slower outer loop injects signals to the inner loop. If the outer control loop uses its own sensor, its control signal is injected into the reference signal adder of the inner loop. Otherwise, when the outer loop uses another actuator, the actuator signal of the inner loop is used as the error signal for the outer control loop.

Hence, the closed-loop transfer function, defined in Equation 3.3, of the inner loop, gets a part of the outer feedback control loop. In the context of this chapter, the single operational amplifier stages in the servo controller are each inner control loops nested in the (outer) laser stabilization control loop. In the next chapter, the temperature control of the PMC or the frequency stabilization to two cavities are examples for nested control loops.

The design of stable nested control loops can be less complicated as of parallel control loops, but they require a gain hierarchy. Meaning, the control bandwidth of the inner loop has to contain the frequencies of active control of the outer control loop [AC00]. Then, at frequencies relevant for the outer control loop design, the closed-loop transfer function of the inner loop is close to one.

In the case of the frequency stabilization presented in this chapter, such a configuration was not found. Because the phase modulator and laser actuator have different frequency ranges, non of them are suitable for such an inner loop.

#### 4.3.2 Stabilized laser frequency

In this subsection, the noise reduction ability of the designed parallel feedback control loop for the laser frequency stabilization is investigated. Therefore, the laser frequency noise of the stabilized laser was measured and compared to the calibrated control loop signals.

The control signal and the error signal in the frequency stabilization loop are captured to compute the amplitude spectral density of the in-loop frequency noise. The calibration of the control signals was derived by the actuator transfer functions measured with the DBB as a frequency sensor. The error signal calibration was derived from the plant transfer function of the frequency stabilization, calculated from the measured noise suppression transfer function and the transfer function of the feedback controller. For the stabilized frequency noise measurements shown in Figure 4.13, the power stabilization was in operation, see Subsection 4.3.3. No cross-couplings from the operating power stabilization to frequency noise were found. This was tested by comparing the laser frequency noise with activated power stabilization to the noise with free-running laser power.

The control signals sent to the laser frequency actuator and to the phase actuator with the closed frequency control loop is consistent with the free-running frequency noise measured with the DBB. Only excess noise peaks at 1.95 Hz and harmonics were present due to a ground-loop coupling to the modulator input of the Orion laser. In addition, a servo bump at 2 MHz is visible. The ground-loop coupling is totally suppressed by the high loop gain and is not visible in the error signal noise. At frequencies above 100 kHz, the phase actuator is used for frequency control. According to Equation 3.6, the calibrated error point noise should be reduced in amplitude by the noise suppression compared to the calibrated noise in the control signal within the control bandwidth. From the total transfer function of the control loop, shown in Figure 4.12, a factor of 5 noise suppression

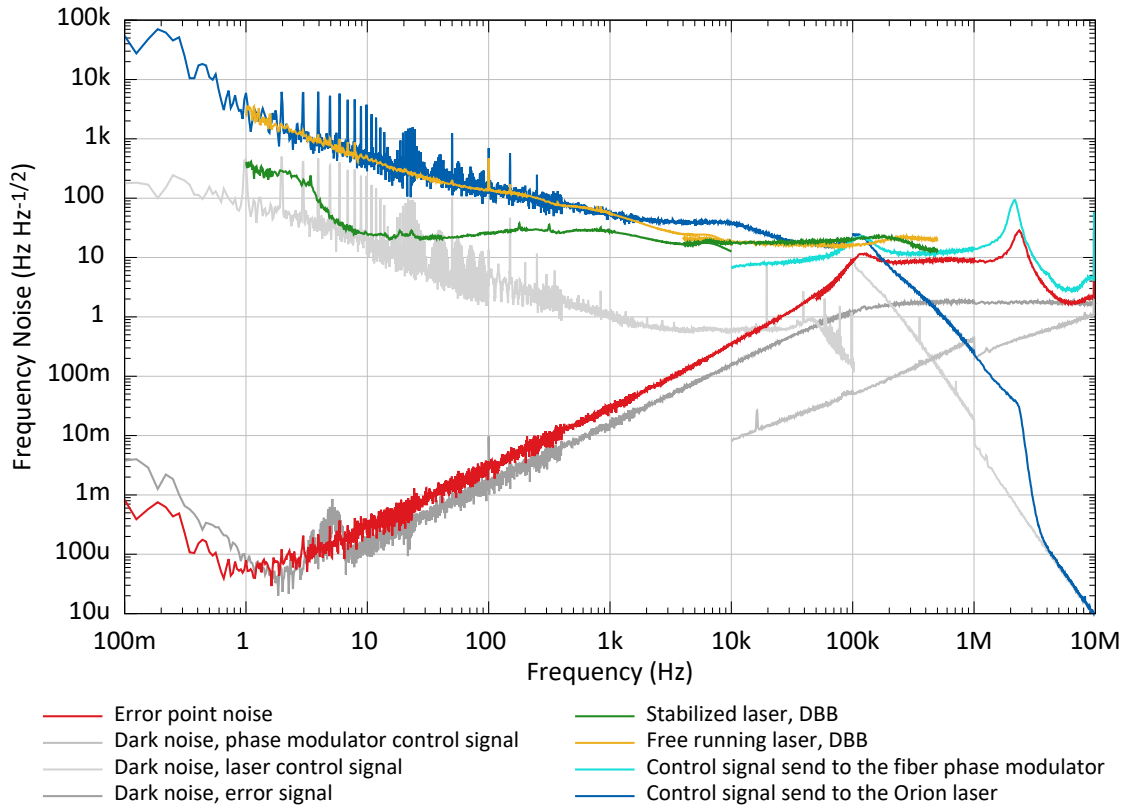


**Figure 4.13:** The calibrated control signal noise (blue) and the calibrated error signal noise (red) are plotted for the frequency stabilization. In addition, measurements with the DBB are added as well as the dark noise. Modified figure from [MW22].

is expected at 300 kHz. Thus, this factor is also expected between noise curves of the phase actuator control signal and the error point, in Figure 4.13. But, because of an electronic cross-coupling of the control signal to the error signal, the error point is higher than expected. A common printed-circuit board can explain the electronic cross-coupling between the signals for error signal generation and fiber phase modulator control.

The frequency noise of the stabilized system was also measured with the DBB and is shown in Figure 4.13. This measurement was for frequencies below 1 kHz most likely limited by the length noise of the low finesse cavity that serves as the frequency reference in the DBB. The stability of the cavity is limited by its PZT for active length actuation and the thermal expansion coefficient of its aluminum-spacer.

#### 4.3.3 Laser power stabilization

The power stabilization of the laser system uses the pump current of the BOA as actuator. As an the in-loop sensor, a low noise photodiode was implemented. At this point a single-loop feedback control was sufficient, as the range and bandwidth of the pump current actuation is high enough.

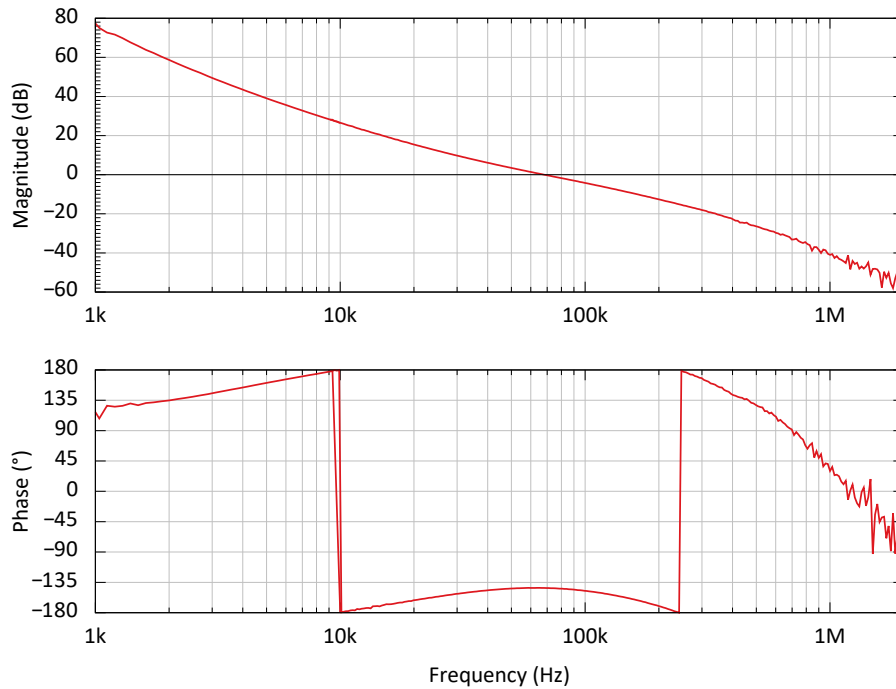


**Figure 4.14:** The open-loop transfer function of the power stabilization is designed to operate with a bandwidth of 70 kHz for good noise performance in the gravitational wave frequency band and for high robustness. Figure from [MW22].

The open-loop transfer function, shown in Figure 4.14, is designed for a low noise performance in the full gravitational wave frequency band. A control bandwidth of 70 kHz with good phase and gain margin for robust, low noise performance noise was chosen. The bandwidth was limited by the used analog controller and the chosen photodiode electronics. The in-loop error point noise of the power stabilization was suppressed for frequencies below 10 kHz by more than one order of magnitude to a value lower than the measurement shot noise.

The power noise measurement photodiode inside the DBB was used as an out-of-loop sensor with 16.3 mW detected power. The noise spectral densities, shown in Figure 4.15, are taken in different operation states of the laser systems. At low frequencies, the power noise measurements with enabled power stabilization were influenced by non-stationary contributions, probably caused by scattered light and air turbulences. These noise sources couple as sensor noise into the in-loop and out-of-loop sensors. In particular, the difference between the measurements with running power stabilization in Figure 4.15 below 100 Hz is caused by the non-stationary noise contributions, which show up by strong differences of the single traces in the averaged measurements. There was no systematic difference observed between the noise at these low frequencies with and without enabled frequency stabilization while operating the power stabilization.

Between 1 kHz and 30 kHz, the uncorrelated sum of the in-loop detector shot noise and the out-of-loop detector shot noise was the limit of the stabilization. At 100 kHz, the servo

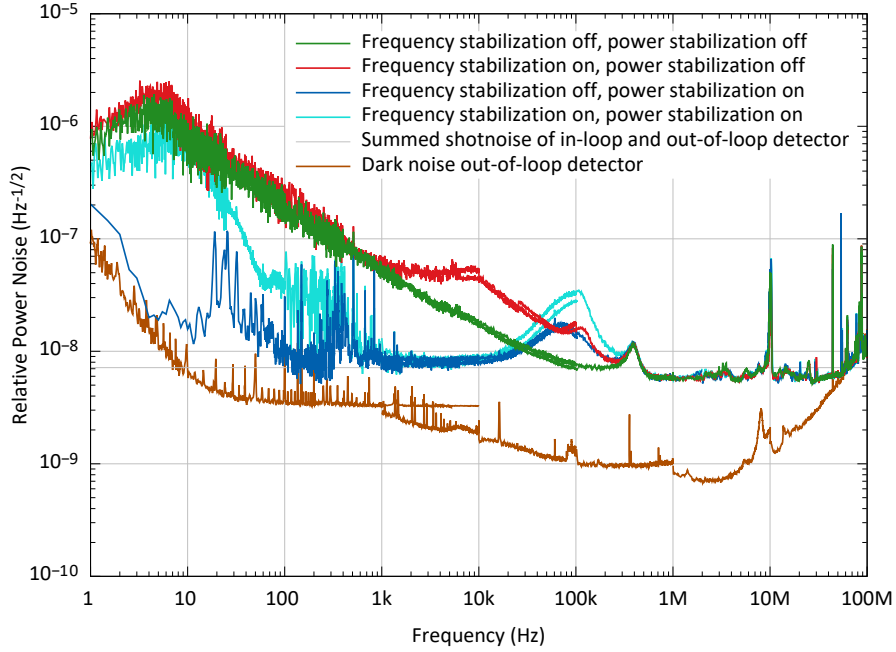


**Figure 4.15:** The RPN as an amplitude spectral density was measured with an out-of-loop detector for several combinations of on/off states of the frequency and power stabilization control loops. A cross-coupling from frequency stabilization to power noise is visible. Figure from [MW22].

bump of the stabilization is present, and at 300 kHz a noise bump of the amplifier's current driver is visible. At higher frequencies, the measurement was limited by the shot noise of the out-of-loop detector, noise peaks from the timing signal of the data acquisition system and by peaks at the phase modulation frequency. The noise floor above 1 kHz was confirmed with measurements using an independent photodiode outside of the DBB as another out-of-loop detector.

With an enabled frequency stabilization, the free-running RPN increases between 1 kHz and 200 kHz, see Figure 4.15. This is due to the residual amplitude modulation (RAM) of the fiber phase modulator. This RAM is caused by an unintended polarization rotation proportional to the applied voltage on the modulator. The next polarizing element in the beam path converts this modulation into an power modulation.

The conversion from phase actuation to laser frequency  $\Delta\nu = \Delta\phi \cdot f$  let to an increased phase actuation  $\Delta\phi$ , which is necessary at lower frequencies  $f$ . This resulted in the higher RAM in the range of the crossover frequency of the two frequency stabilization paths. At these frequencies, higher modulation amplitudes are expected for the laser and the phase actuators, which implies an increased RAM injection into the power stabilization loop.

To lower the RAM, a bias voltage of  $-5.5$  V was applied to the fiber phase modulator. This bias voltage is adjusted to a low polarization rotation operation point of the modulator [Die17]. A fiber polarization beam splitter behind the modulator is used to clean the polarization, which simultaneously converts polarization modulation into RAM.

No measurable polarization fluctuations remain on the beam after this element such that no significant RAM generation is expected at subsequent polarizing components. The RAM of the seed beam was further lowered in the amplifier by 20 dB at low frequencies according to the amplifier transfer function (see Figure 4.8).

When the power stabilization was enabled in addition to the frequency stabilization, the excess power noise between 2 kHz and 20 kHz due to RAM could be suppressed. The servo bump around 100 kHz was, however, increased. With such a high loop gain, the out-of-loop performance of the power stabilization in the gravitational wave frequency range is only limited by the in-loop sensor noise, which can be improved by better shielding and by detecting more laser power.

#### 4.4 Conclusions and outlook

Future ground-based GWDs' designs, which plan for the operation at a wavelength of 1550 nm demand single mode, single frequency laser systems [ET 20] with extremely low noise performance. In this chapter, detailed measurements of the free-running noise and actuator transfer functions of a variety of seed lasers, pre-amplifiers, and power amplifiers as optional subcomponents for such laser systems were presented.

The shown measurements give an independent characterization and an extension to vendor data sheets to support the trade-off between different lasers for future GWDs or other applications with low noise requirements. The characterizations results of the ECDL seed is consistent with previous published measurements of that laser source [Num10; Tsu11], which is a proof of the accuracy of the presented noise measurements.

The frequency noise of the tested laser systems, out of seed lasers and amplifiers, is defined by the seed laser's frequency noise. Similarly, the frequency modulation transfer function from the seed to the amplifier output depends primarily on the seed laser's frequency actuators, up to a delay due to additional propagation time through the amplifiers. The power noise of all analyzed MOPA combinations at frequencies below 10 kHz is dominated by the high power stages, while at higher frequencies, the power noise of one of the seed lasers starts to dominate, see Figure 4.9.

In Section 4.3, the performance of the Orion-BOA combination in a stabilization environment is discussed. High bandwidth and high noise suppression of a frequency stabilization with respect to a high finesse optical reference cavity was demonstrated. Simultaneously, a power stabilization was operated that showed a high loop gain in the detection band of ground-based GWDs. The performance was limited by non-stationary noise below 100 Hz.

Due to the unavailability of an appropriate power actuator for the commercial high power amplifiers, the light power in the stabilization experiment was limited to the output power of the pre-amplifiers to 115 mW. To use the high power stages in future PSL systems, either appropriate power modulation inputs need to be added to the high power amplifiers, which was demonstrated in [Thi19] for solid state amplifiers (see Chapter 3) or an external modulator must be implemented as described in Chapter 5.

Based on the conclusions from above, a laser system with a power amplifier, an optical mode cleaning cavity and out-of-loop detectors for frequency and power noise was set up and is presented in the next chapter. The power amplifier will increase the output power to a range relevant for the proposed ET-LF interferometers [ET 20].





# CHAPTER 5

---

## Stabilized Laser System at 1550 nm Wavelength for Future Gravitational Wave Detectors

---

Silicon mirrors are proposed for some third-generation gravitational wave detectors (GWDs) [ET 20; Rei19a], as discussed in the previous chapters. The use of silicon mirrors requires a change to a longer wavelength like 1.5  $\mu\text{m}$  or to about 2  $\mu\text{m}$ , as silicon is not transparent at the currently used wavelength of 1064 nm. Therefore, reliable single-mode, single-frequency lasers at these wavelengths are required and need to be stabilized to the above-mentioned low noise levels by means of sophisticated methods.

The required output power of the laser system depends on the interferometer configuration and on the desired sensitivity. In case of the European Einstein Telescope (ET) GWD project a laser power of about 3 W is needed to achieve the design sensitivity of its low-frequency interferometers [ET 20].

To reach the needed noise performance of the laser, active feedback stabilizations for the laser power and frequency are necessary. These stabilizations are typically cascaded into a pre-stabilization of the laser system with sensors close to the laser and the final stabilization with sensors in the main vacuum system of the GWD [Kwe12]. In addition to active feedback control GWDs typically use passive noise reduction techniques via optical cavities, so-called mode cleaners, as discussed in Section 2.3.

This chapter reports on the design and operation of a pre-stabilized laser system (PSL) at 1550 nm wavelength. Based on the results presented in Chapter 4 a master oscillator power amplifier (MOPA) arrangement out of the Orion seed laser, the BOA pre-amplifier, and a Boostik power amplifier was identified as the optimal laser source. Together with a pre-mode-cleaner (PMC), this forms the base of a laser system for highly reliable operation and high-speed control capabilities to operate the necessary frequency and power stabilization control loops.

The noise suppression of the stabilization control loops via in-loop sensors were characterized and independent measurements for laser frequency and power noise with out-of-loop sensors were performed. In Section 5.1 the experimental setup is introduced and design decisions, like to operate a MHz bandwidth seed laser frequency pre-stabilization, are presented. The characterization of the laser system with independent out-of-loop measurements is discussed in Section 5.2. The presented results are published in Physical Review D [MKW22] and are accompanied in this chapter by the description of the PMC design in Subsection 5.1.1, a detailed discussion of nonlinear noise coupling at the PMC in Subsection 5.1.2 and a brief review of the cross-spectral density noise measurement technique for sub-shot-noise characterization in Subsection 5.1.6.

## 5.1 Experimental setup

After the detailed characterizations in Chapter 4, the MOPA combination out of the Orion laser, the BOA pre-amplifier and the 2 W Boostik amplifiers was chosen because of the best performance parameters for a GWD PSL. The selection criteria were low free-running frequency and power noise in the Fourier frequency range from 1 Hz to 10 MHz as well as suitable power and frequency actuators for high performance feedback stabilizations.

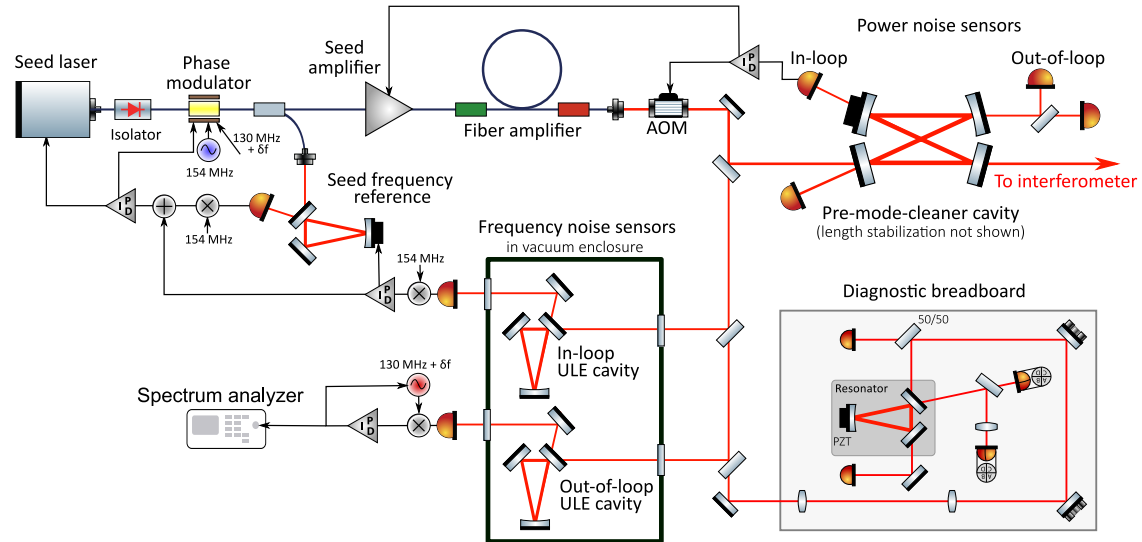


**Figure 5.1:** The schematic setup of the pre-stabilized laser system shows the Orion seed laser with the BOA seed amplifier, the 2 W Boostik fiber amplifier (upper left), and the pre-mode-cleaner (PMC) that transmits the main beam for the GWD interferometer (upper right). One low-power beam for power stabilization and two low-power beams for out-of-loop power noise sensing are transmitted as well. The seed frequency reference and in-vacuum ultra-low expansion glass ceramic (ULE) cavities used as the main frequency references for in-loop and out-of-loop sensing are shown at the lower left. A diagnostic breadboard (DBB) for automated free-running laser noise measurements is depicted at the lower right of the sketch. Figure from [MKW22].

The combination of the Orion laser and the BOA pre-amplifier was tested in a stabilization experiment in Section 4.3. The 2 W erbium-based fiber amplifier, called Boostik amplifier, is seeded with 40 mW and integrated into the PSL. The 2 W and the 10 W versions of this amplifiers with similar free-running noise performance were tested in Chapter 4. For practical reasons the 2 W version was used for the full PSL demonstration described below.<sup>1</sup>

This all-fiber MOPA laser system is integrated into a free-space PSL setup, including out-of-loop sensors for characterization of the stabilizations, as shown in Figure 5.1.

<sup>1</sup> The 2 W version was chosen, because it is available with a standard FC-APC polarization maintaining fiber output that can be extended with patch fibers, connected to a vacuum feed-through or connected to further amplification stages. The higher power versions of these amplifiers are only provided with a fixed attached collimator to the output fiber, due to limited power handling capabilities of the fiber connectors.

A fraction of the laser light is analyzed with an in-house build automated laser analysis tool, called diagnostic breadboard. The free-running power, frequency and pointing noise of the laser can be analyzed as well as the laser beam's spatial mode composition [KW08].

### 5.1.1 Pre-mode-cleaner design

The main laser beam is coupled to a pre-mode-cleaner (PMC), which is a traveling wave optical cavity in a bowtie shape. This cavity is placed in the output beam of the MOPA, shown in Figure 5.1 on the right part. A flat mirror with specified 0.6% power transmittivity is the in-coupling mirror to this rigid-spacer cavity and a mirror with equal properties is used for out-coupling of the main beam, as depicted in Figure 5.2. The bowtie cavity is close to the impedance matched state as only a small fraction of the circulating light is transmitted through the curved mirrors or scattered at the super polished mirrors. The fraction of the light leaving the  $r = -3$  m curved mirrors with 75 ppm specified transmission is used for power stabilization and out-of-loop power noise sensing purposes.

According to PYKAT-simulations [Bro20], 97.2% of the incident light can be transmitted via the out-coupling mirror and 1.2% each through the curved mirrors. Due to the nonperfect impedance matching 0.4% is reflected from the input mirror, even with a perfect matched Gaussian beam. Because of different resonance conditions for the higher order modes (HOMs) of the injected laser beam to the cavity, the transmitted beam is spatially filtered and the HOMs are reflected by the cavity. In the here presented experiment about 7% of the incident light is reflected on resonance because of the reflection of the phase modulation sidebands and 4.5% HOMs, due to a nonperfect shaped injected beam and nonperfect mode-matching to the cavity mode.

The free spectral range (FSR) of the cavity is  $207 \text{ MHz}^1$  and the finesse of 475 is calculated

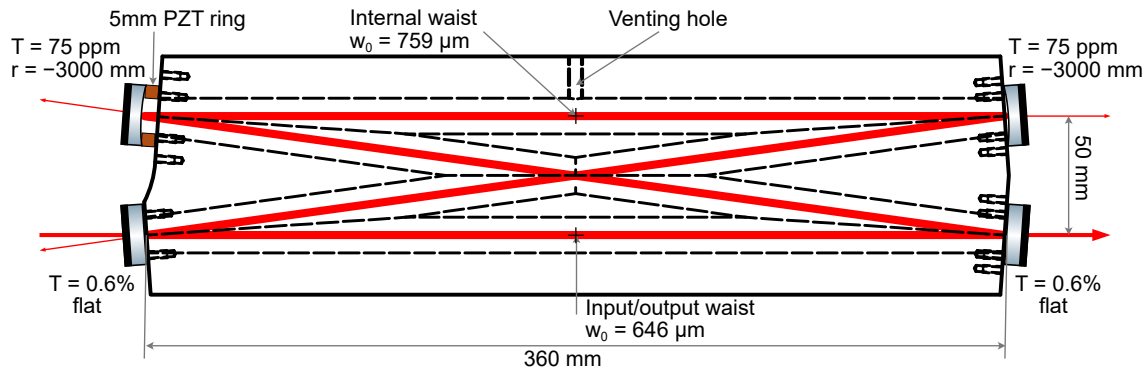


**Figure 5.2:** The top view drawing of the rigid PMC aluminum spacer with sketched mirrors and the piezo-electric length control element (PZT) ring actuator. The mirrors are clamped to the spacer, the clamping structure is not shown. The Gaussian eigenmode of the bowtie resonator has two beam waists with different waist radii, the waist positions are marked with small crosses.

<sup>1</sup> Calculated from the round-trip length of 1.447 m with Equation 2.4.

from the pole frequency of  $(218 \pm 7)$  kHz, measured via an amplitude modulation transfer function [Rak02]. The measured pole frequency is higher than expected from the simulation results, which predicted a pole frequency of 201 kHz. This difference can be canceled in the simulations by insertion of a lower coupling mirrors' power reflectivity of 99.35%.<sup>1</sup>

Due to the even number of cavity mirrors and no significant birefringence in the dielectric coatings, the modes of both linear polarizations are co-resonant in the PMC. The cavity's eigenmode astigmatism can be quantified by 0.2% beam waist radius mismatch between the horizontal and the vertical axis, caused by hitting the spherical curved mirrors at  $4^\circ$  angle of incidence. The position of the HOMs in the FSR can be described by mode spacing, the resonance frequency difference between the fundamental and a first order mode [Sie86; Bon16]. The horizontal first order mode show an intensity modulation in plane with the laser beam propagation in the cavity compared to the fundamental Gaussian mode. The vertical modes show the intensity modulation along the perpendicular axis to the beam propagation plane. The astigmatism of the cavity modes results in a different horizontal and vertical mode spacing simulated to be 47.8 MHz respectively 47.7 MHz for the HOMs distributed over the free spectral range.<sup>2</sup> The measured mode spacing is  $(48.9 \pm 0.2)$  MHz for vertical modes and  $(47.3 \pm 0.2)$  MHz for horizontal. The higher difference in the mode spacing is probably caused by manufacturing tolerances of the mirror curvatures or the mirror clamping, which could deform the mirrors and change their curvature [Hei22].

The length of the PMC is stabilized to the laser frequency with the PDH technique [Dre83; Bla01], using as actuator a 5 mm thick piezo-electric length control element (PZT) ring, placed between the cavity spacer and one of the curved cavity mirrors. The necessary phase modulation sidebands for the PDH error signal generation are imprinted at 154 MHz. This frequency was chosen for all used cavities in the setup to be high enough for an error signal generation with a bandwidth of up to 10 MHz and to not be resonant with any HOMs in the cavities. In the cavity stabilization loop, an analog controller is used in the feedback control, to achieve a control bandwidth of about 2 kHz.

### 5.1.2 Nonlinear noise coupling

It was found that the power noise of the laser beam transmitted through the stabilized PMC is increased compared to the noise of the injected beam (see Figure 5.4). Measurements with added frequency modulations to the laser source implied that a nonlinear coupling from laser frequency noise to power noise in transmission of the PMC occurred. This hypothesis is supported by simulations and explained with a qualitative model in this section to infer the necessary steps for reducing this power noise.

The length of the PMC is actively controlled to meet the resonance condition for the incoming laser light. This feedback control compensates for deviations between the resonance frequency and the laser frequency  $\delta\nu(t)$  up to the control loop's unity gain frequency of 2 kHz. At higher Fourier frequencies, these deviations result in a power drop of

<sup>1</sup> Which is still within the manufacturer tolerances of  $(0.6 \pm 0.1)$  % for the power transmission.

<sup>2</sup> The geometry of the PMC was adjusted for a high mode separation of the fundamental Gaussian eigenmode to the HOMs with order lower than ten.

the circulating power inside the cavity  $P_{intra} = P_{0,intra} + \delta P_{intra}(t)$ , because the resonance condition is not maintained. For small deviations from resonance, the quadratic coupling term is dominant. Hence, a resonance frequency mismatch  $\delta\nu(t)$  results in a relative circulating power change of

$$\frac{\delta P_{intra}(t)}{P_{0,intra}} \approx -\frac{1}{2f_p^2} \delta\nu(t)^2. \quad (5.1)$$

For the approximation of the coupling factor, the definition that at a frequency deviation of  $\delta\nu(t) = \text{FWHM}/2 = f_p$  the circulating power is halved, was used (see Subsection 2.3.1). The coupling factor scales with the inverse square of the cavity pole frequency  $f_p$ . Hence, a cavity with a lower pole frequency show an increased the coupling factor. The power in transmission  $P_{trans}$  of the cavity is linearly connected to the intra-cavity power  $P_{intra}$  via the output mirror transmittivity. Thus, the relative power change in transmission of the cavity is equal to the relative power change of the circulating field given in Equation 5.1. At Fourier frequencies above the cavity pole frequency  $f_p$ , the power noise is filtered by the cavity transfer function, see Figure 2.4.

To further investigate the effect of this nonlinearity, a time domain simulations with the Simulink software package of Matlab was performed: Spectrally shaped random noise is generated and then injected to a squarer. Finally, the output is compared to the input noise spectral densities.

To mimic the frequency noise at high frequencies, white noise data is filtered with a low pass filter and up-converted by mixing with a 1 MHz modulation to frequencies around 1 MHz or the generated white noise is used directly. From this data the input noise spectral density is calculated, see blue curves in Figure 5.3. The data is as well processed by an squarer, to simulate the effect of the nonlinear coupling in a cavity to the transmission power. Finally, noise spectral density of that noise is calculates as well and shown in red curves in Figure 5.3. The signal flow diagram of the simulation can be found in the Appendix in Figure A.1.

Different spectral shapes of the input noise were tested and the most significant coupling and agreement to experimental results were found for broad, high-frequency noise peaks or white noise. The white frequency noise of the Orion laser at frequencies above 10 kHz, in combination with a servo bump of a frequency stabilization could show such noise spectral densities, see e.g. Figure 4.13. The resulting relative power noise is in the order of magnitude of the observed power noise increase of the light transmitted by the PMC, shown in Figure 5.4 (red curve).

By comparing the measurement in Figure 5.4 (red curve) with the simulation in Figure 5.3, the origin of the increased power noise seemed to be an at least 100 kHz broad noise peak or even white noise to generate flat power noise up to 100 kHz. Additionally, it was found that a root mean square (RMS) frequency derivation of a few kHz is required to generate relative power noise levels around  $1 \times 10^{-5} \text{ Hz}^{-1/2}$ . Changes of the input noise peak's center frequency in the MHz range do not affected the shape of the power noise below 100 kHz.

For the description in frequency domain, a modeling with coupling transfer functions is not possible because of the nonlinear coupling. Alternatively, a measure for the coupling

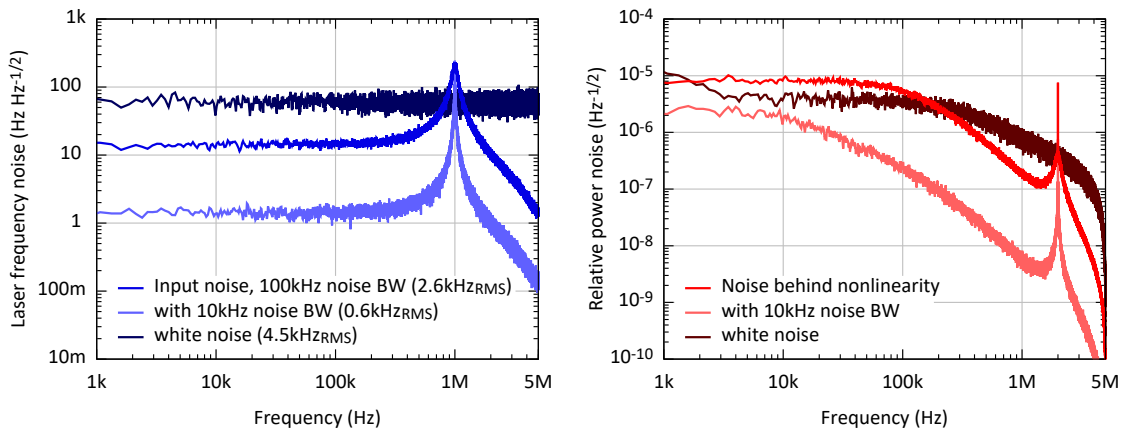


**Figure 5.3:** Within a Simulink simulation, time domain data with a shown corresponding noise spectral densities were generated (blue curves). The time data is then squared, multiplied by the coupling factor, filtered by the cavity transfer function, and the resulting amplitude spectral densities are calculated (red curves). The quadratic nonlinearity result in a down- and up-conversion of the noise peak to frequencies below half the peak bandwidth and to 2 MHz. The resulting power noise level show a dependence on the root mean square (RMS) value of the time data. **Left:** A frequency noise level similar to the measurement of the Orion laser was assumed. The simulations for a noise peak bandwidth (BW) of 100 kHz and 10 kHz are shown, as well as white input noise with a similar RMS values. **Right:** The simulations for a noise peak BW of 100 kHz and 10 kHz shows that the noise increase at low frequencies reach up to the frequency of the noise peak BW. The strong noise decrease above 4 MHz could be a simulation artifact.

strength is the standard deviation or RMS value of the frequency noise above the unity-gain frequency (UGF) of the cavity length stabilization, because this describe an average mismatch from the resonance condition. An increased standard deviation of the frequency noise result in an increase in coupling strength to power noise. Additional simulation<sup>1</sup> confirmed this connection to the standard deviation of the frequency noise.<sup>2</sup>

This nonlinear coupling can be also interpreted as an intermodulation between noise at different Fourier frequencies. For the noise peak at 1 MHz, a classical mixing with a 1 MHz sinusoidal signal would result in a peak at 2 MHz and low frequency components with Fourier frequencies as high as half the BW of the noise peak. For intermodulation, the most relevant frequencies are in the BW of the noise peak, resulting in a mixing similar to a sinusoidal signals but with a random phase [Hob09].<sup>3</sup> For this kind of noise coupling the input noise is often called out-of-band noise, when the intermodulation transforms this noise into the band of interest [Sei10, Section 4.6].

1 Not all of them are shown in Figure 5.3.

2 The standard deviation value can be calculated as the frequency integral over the squared amplitude spectral density. The resulting standard deviation is the square root of the result. Hence, for an overall noise level increase, the standard deviation increase with the same factor.

3 The white noise can be interpreted as a maximal widened noise peak.

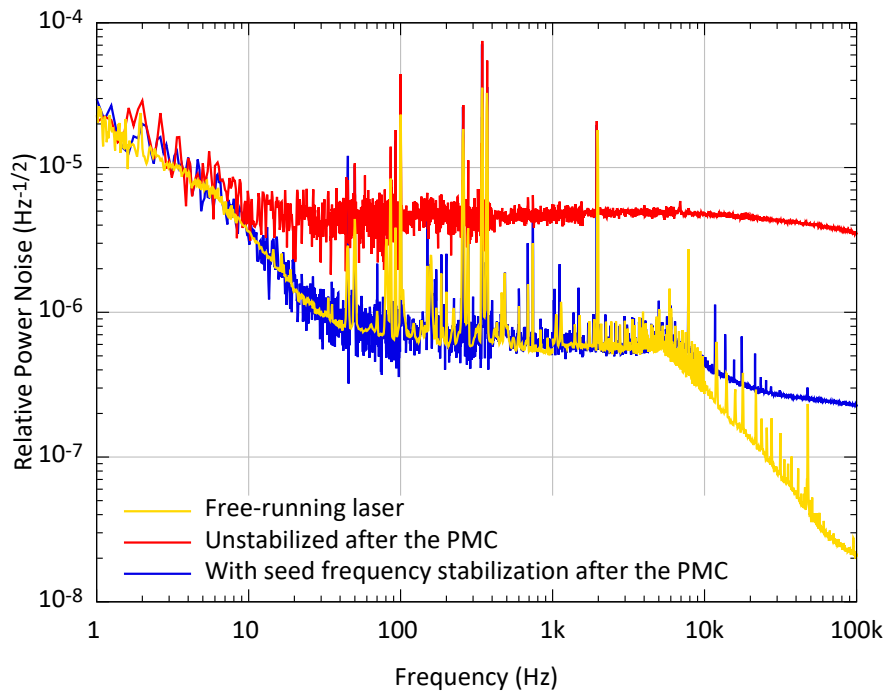


**Figure 5.4:** The power noise of the free-running laser (yellow curve) is lower than the power noise in transmission of the PMC (red curve). This is due to nonlinear frequency-noise to power-noise coupling in the PMC that can be lowered by a fast frequency stabilization of the seed laser (blue curve). (All measurements were taken with disabled power stabilization.) Modified figure from [MKW22].

This reasoning, tests and the simulation lead to the conclusion that the RMS mismatch between cavity resonance frequency and laser frequency defines the nonlinear coupling strength to the excess power noise. The frequency noise of the used seed laser is white above 10 kHz (see Figure 4.2 or 5.9) resulting in a dominant contribution to the standard deviation from the higher Fourier frequencies, assuming that the PMC’s length control compensates for the mismatches at low Fourier frequencies.

### 5.1.3 Seed frequency stabilization

To reduce the excess power noise, described in last subsection, a particularly fast seed laser frequency stabilization is implemented into the setup. This stabilization is later nested in the final frequency stabilization and is therefore referred to as inner loop. A small fraction of the seed laser light is picked off with a fiber coupler after a fiber Faraday isolator and a waveguide fiber phase modulator. The picked-off light is sent via fiber to a breadboard with a triangular, length tunable rigid-spacer cavity. For the stabilization of the laser frequency the PDH technique is used and the feedback signals act on the laser’s pump current and are added to the phase modulator signals to stabilize the frequency below and above 10 kHz respectively. A UGF of 2.1 MHz for this feedback control loop was achieved, see Figure 5.5.



It was not necessary to isolate the seed frequency reference from environmental disturbances as the main frequency stabilization of the PSL in GWDs is performed with so-called outer loops that stabilize the laser with respect to well isolated frequency references. Such references are provided as integral parts of the GWD's optical layout ,e.g. by input mode cleaners, the power recycling cavity or arm cavities. In this experiment isolated ultra-low expansion glass ceramic (ULE) cavities were used to represent such frequency references (see next subsection). The main purpose of the seed frequency stabilization is to suppress the fast frequency fluctuations of the laser that drives the power noise increase in transmission of the PMC. Therefore, the stabilization loop is designed with the very high UGF but also with a gain margin of 6 dB and a phase margin of  $63^\circ$  to ensure robust operation with only small excess noise around the UGF. The achieved noise reduction shown in Figure 5.4 will be further discussed in Subsection 5.2.1.

#### 5.1.4 Frequency stabilization to an isolated reference cavity

For the demonstration of a laser frequency stabilization two almost identical stable triangular cavities with rigid ULE spacers are used. All mirrors of the in-loop cavity and the planar mirrors of the out-of-loop cavity are optically contacted to the spacer. The curved mirror of the out-of-loop cavity is glued.<sup>1</sup> The cavities are placed on fluorine rubber pads inside a vacuum tank with a pressure of  $2 \times 10^{-2}$  mbar for acoustic and seismic shielding. A power of 18.6 mW is sent to the in-loop reference cavity and a power of 6.5 mW is used for the out-of-loop frequency noise measurements, see Figure 5.1.

The free spectral range of the ULE cavities is 702 MHz and the measured pole frequencies are 115 kHz for the in-loop cavity and 132 kHz for the out-of-loop cavity. The laser frequency is stabilized with a UGF of 180 kHz to a fundamental mode resonance of the in-loop ULE cavity. The error signal is generated with the PDH technique and the feedback is split into two paths. The low frequency tuning (below a few Hz) is performed by acting on the length of the seed frequency reference and for higher frequencies, the feedback is added to the error point of the seed frequency stabilization loop. The bode plot of the open-loop transfer functions are shown in Figure 5.5. In addition, the noise suppression magnitudes of the seed stabilization and of the combined nested feedback control loops are shown.

The reduction of the frequency noise is ultimately limited by the magnitude of the total noise suppression, but the sensor noise and frequency noise, potentially added by the laser power amplifiers, can degrade the performance. The sensor noise of the seed reference cavity, like length fluctuations or electronic readout noise limit the effective noise reduction of the inner loop. The pre-stabilized laser beam passes the amplifiers and finally, the laser frequency is sensed by the in-loop ULE cavity. This outer loop stabilization sensor can limit the frequency stability with its sensor noise. Therefore, an out-of-loop frequency sensor was implement for a full noise characterization of the achieved frequency stability.

---

<sup>1</sup> Because at the time of building this cavity, no optically contactable curved mirror was available.



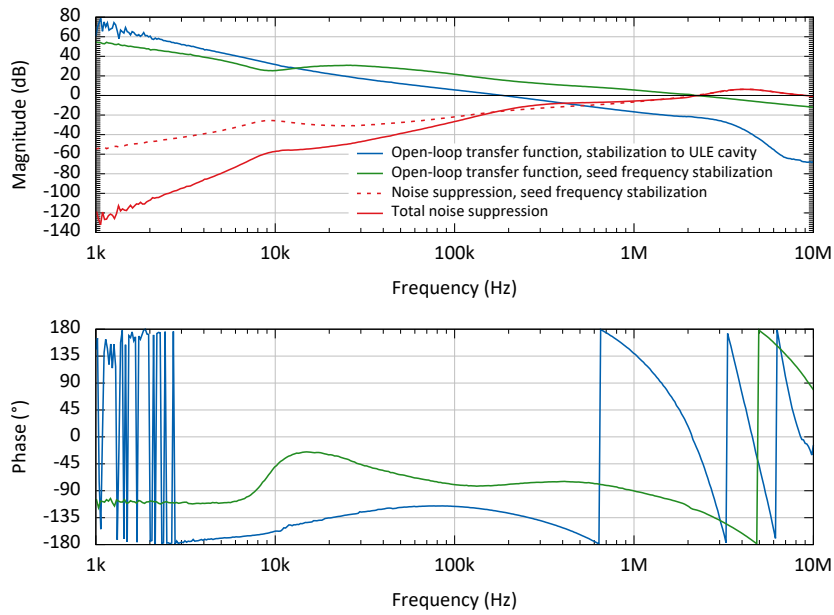


**Figure 5.5:** The bode plot of the open-loop transfer functions measured for the seed frequency stabilization (green) shows a higher UGF than the outer loop (blue), which is the stabilization to the in-loop ULE cavity. The magnitudes of the noise suppression transfer function from the two nested control loops add up to the calculated total noise suppression magnitude (red).

#### Out-of-loop frequency noise measurement

An independent analysis of the frequency noise of the stabilized laser is performed using the out-of-loop ULE cavity. Due to a small length difference of the two rigid ULE cavities, they are not resonant at exactly the same laser frequencies. Measurements show that the resonance frequencies are about 130 MHz apart with a small dependence on the mounting of the cavities and the lab temperature.

Additional phase modulation side bands were imprinted onto the laser at exactly the difference frequency between the two cavity resonance frequencies, by adding the signal to the fiber phase modulator signal. An error signal is generated via demodulation of the photodiode signal in reflection of the out-of-loop cavity with this modulation frequency. This error signal is proportional to the frequency difference between one phase modulation sideband and the out-of-loop cavity's resonance frequency. For a constant modulation frequency the sideband's frequency fluctuations are identical to the frequency fluctuations of the carrier light. Hence the generated error signal carries information of the carrier frequency fluctuations with respect to the out-of-loop's frequency reference.

A feedback control loop with 25 kHz UGF is used to control the phase modulation frequency, such that the phase modulation sideband is kept resonant in the out-of-loop ULE cavity. This ensures that the error signal is always valid and has a constant slope, independent of slow drifts between the in-loop and out-of-loop cavity. The out-of-loop measurement of the frequency noise is performed by capturing the error and control signal of that feedback loop and the measurement results are discussed in Subsection 5.2.1.

### 5.1.5 Power stabilization

The sensor for the power stabilization of the laser system is placed in one of the low-power transmission ports of the PMC. This is beneficial, as the power noise added by the PMC via frequency noise to power noise conversion and beam pointing to power noise conversion can be sensed together with the power noise of the laser source at this port. The power noise from these different origins can simultaneously be suppressed with a single control loop. The light that is transmitted through the other low-power port of the PMC is split equally and detected by two out-of-loop photodiodes. The power in the in-loop and out-of-loop port is detected by InGaAs photodiodes in combination with active transimpedance amplifiers. The two out-of-loop sensors allow for two individual out-of-loop power noise measurement. They are also used for a cross-spectral density measurement, accessing the power noise below the shot noise limit of the out-of-loop detectors [VW22].

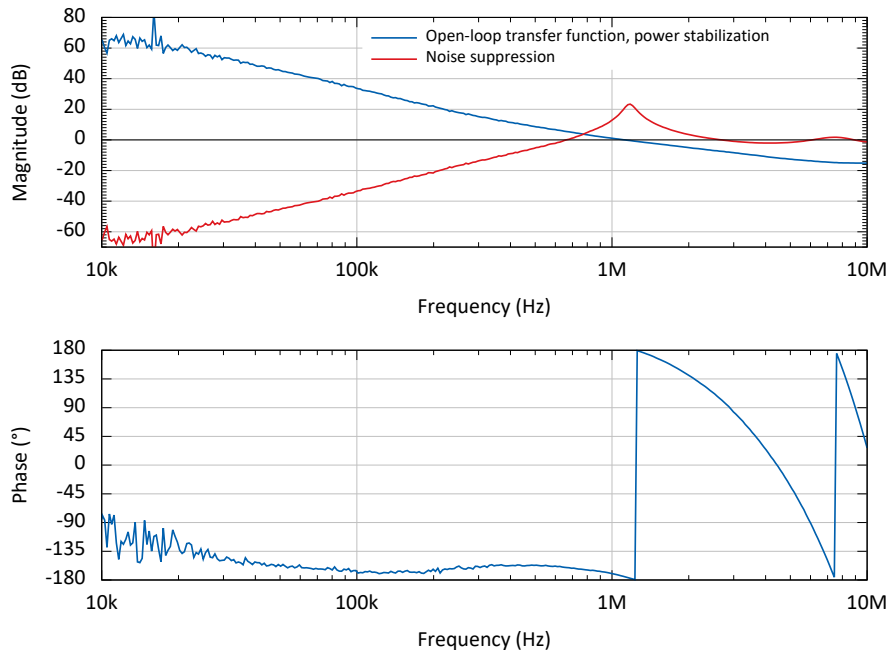


**Figure 5.6:** The measured open-loop transfer function of the laser power stabilization is shown in blue. From this transfer function the magnitude of the noise suppression is calculated and shown in red. The noise suppression steeply improve towards frequencies below the UGF, but at cost of low gain and phase margins resulting in a noise amplification around 1.2 MHz.

Subtracting a reference voltage from the in-loop sensor signal, a laser power error signal is generated and a feedback controller acts on the semiconductor amplifier's pump current for noise suppression at high frequencies. Drifts at low frequencies, below 1 kHz, are compensated with an acousto-optical modulator placed in the in-air propagation path of the 2 W laser beam. In Figure 5.6, the open-loop transfer function of this power stabilization is shown with its UGF of 1.1 MHz.

To improve on the out-of-loop characterization of the power stabilization, a cross-correlation based technique is introduced in the following subsection.

### 5.1.6 Quantum correlation measurement

The cross-spectral density (CSD) measurement between two out-of-loop sensors can help to improve the accuracy in noise characterization. Especially, laser power noise characterization in the scope of GWDs is limited by the shot noise of the sensing beam. The here described method is discussed in full detail in [VW22], where a full quantum mechanic description is presented. Here, a brief introduction on this characterization technique is given.

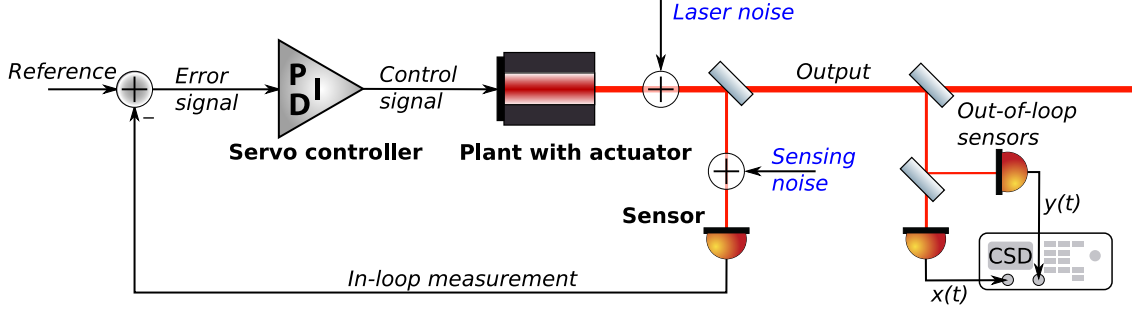


**Figure 5.7:** Schematic setup of a power stabilization with two out-of-loop sensors to perform a cross-spectral density (CSD) besides the conventional out-of-loop measurements.

Figure 5.7 shows the basic sketch of a laser power stabilization with an in-loop sensor and two out-of-loop photodetectors. For a conventional out-of-loop measurement, the spectral density of one of the out-of-loop detector's signals, or the sum of both detectors' signals, is recorded. This measurement is limited by the shot noise of the sensed laser beam, where the limit depends on the sensed power, see Equation 2.10. The shot noise adds a white, frequency independent, noise limitation to the out-of-loop measurement. Considering a relative power noise measurement, the shot noise limited sensitivity scales with  $1/\sqrt{P}$  for the detected laser power  $P$ .

The maximal detectable laser power is limited, by the damage threshold of the photodiodes and the affordable laser power for the out-of-loop sensing. Hence, the achievable shot noise level is limited. As an alternative, the CSD  $S_{xy}^2(f)$  of the two out-of-loop detector signals  $x(t)$  and  $y(t)$  can be used [Ben10]. This CSD is the Fourier transformation of the cross-correlation between the two sensor signals, and according to the convolution theorem, this is the product of the Fourier transformed signals, one of which is complex conjugated [Rey89].

In practice this can be approximated with the complex, windowed fast Fourier transformations (FFTs) of the signals  $FFT_x$  and  $FFT_y$  to [Sta17]:

$$S_{xy}^2(f) \approx \frac{1}{N} \sum_{k=1}^N FFT_{x,k}^*(f) FFT_{y,k}(f), \quad (5.2)$$

as the average of their product, where  $FFT_x^*$  is complex conjugated. Here,  $FFT_{x,k}(f)$  is the FFT of the  $k$ -th measurement interval of the sensor signal  $x(t)$  and similar for  $y(t)$  at Fourier frequency  $f$ . Uncorrelated signal components in the two signal result in a random phase relation between their FFTs. Hence, with an increasing number of averages  $N$  their average

tent to zero. For a high enough number of averages, the remaining complex amplitude describe the correlation between the two signals and is a good approximation for  $S_{xy}^2(f)$ .<sup>1</sup>

The corresponding relative amplitude spectral density of the correlation  $S_{rel. CSD}$  is, in the case of two power detectors [VW22]

$$S_{rel. CSD} = \frac{\sqrt{S_{xy}^2(f)}}{\sqrt{P_x P_y}}, \quad (5.3)$$

where  $P_x$  and  $P_y$  are the mean values of the signals from the two power sensor. High detection powers and a maximization of their product by choosing similar power levels on both detectors is beneficial for a precise power sensing of the individual detectors. This results in a fast convergence and typical better reduction of uncorrelated sensing noise.

The magnitude of the relative CSD  $S_{rel. CSD}$  is the uncorrelated sum of all noise that are correlated for both out-of loop detectors. Thus, the technical laser power noise, introduced in Section 2.3.4, is reproduced by this quantity. Any sensor noise of the in-loop sensor of a power stabilization within its control bandwidth will also be visible, as it is imprinted as laser noise by the control loop (see Section 3.4.1). Additionally (anti-)correlated pointing noise and technical noise measured with both out-of-loop detectors contribute to  $S_{rel. CSD}$ .<sup>2</sup>

All uncorrelated noise do not contribute to the relative CSD  $S_{rel. CSD}$ . Imaging a ideal (classical) laser beam, which can be described in quantum optics as a coherent state, see Section 6.1. By distributing to the two out-of-loop detectors, the field amplitude decreases, but the quantum noise is transformed differently by the beam splitter than the classical field amplitudes: two new coherent states with lowered amplitude are generated, both of which show shot noise upon detection according to their power levels (see Equation 2.10). In the case of a coherent state of the input light field, the shot noise on both detectors is uncorrelated and thus cannot limit the sensitivity of that measurement. The same is true for uncorrelated electronic noise of the detectors, like the noise of their transimpedance amplifiers. Provided, the measurement times are long enough to approximate  $S_{rel. CSD}$  well.

These characteristics make this kind of CSD measurement, called quantum correlation measurement, an ideal tool for out-of-loop characterization of feedback control loops, as several limitations of a single sensor can be surpassed. This technique is only capable to generate spectral data, typically used for noise characterization, because the increase in sensitivity is accomplished by spectral averaging of a product of two signals. Information on the instantaneous laser power cannot be generated with this technique, which would be required to improve the sensor noise in power stabilization loops [VW22].

This technique was already applied for free running laser power noise characterization [VW22], characterization of noise sources in GWDs [LSC17; Bui20b] and for interferometric sensing of liquid surface fluctuations [MA13]. In Subsection 5.2.2, this technique is

1 The convergence with the number of averages can be monitored by the remaining fluctuation of the phase of  $S_{xy}^2(f)$ .

2 A hint that  $S_{rel. CSD}$  is not fully dominated by the technical power noise is given by its phase: If its phase is not close to zero, then this indicates that (partly) anti-correlated noise sources couple.

applied to characterize the power stabilization of the laser system.

In the following section, the measured noise performance of the stabilizations is shown.

## 5.2 Results and discussion

Before characterization of the stabilized noise, the free-running laser noise of the MOPA laser system was monitored with the DBB [KW08]. Every 6 hours, a set of measurements was taken. 47 measurements of the free-running power noise over an exemplary time period of 12 days are shown in Figure 5.8. The data was merged from different whitening stages of one sensor. The merging weighting functions are describes in the appendix A.2. The deviation between the measurements are very small, such that the shown 47 traces mainly lie on top of each other. The frequency independent noise floor between 5 Hz and 10 kHz is caused by the fiber amplifier. A similar noise signature was measured in all tested erbium-based fiber amplifiers and is shaped by the pump-light to output-power transfer function of the amplifier [MW21] or see Chapter 4.

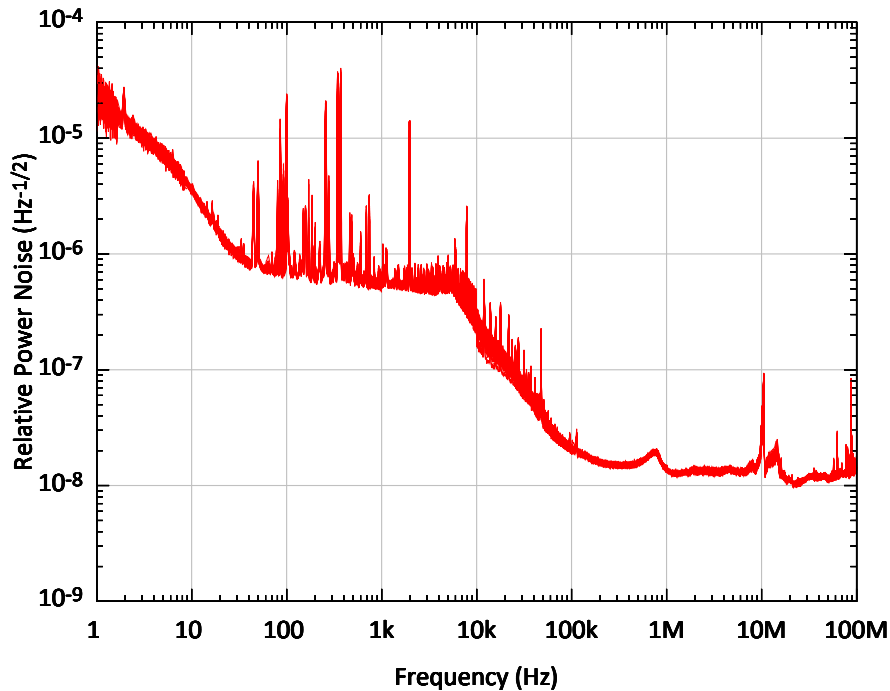


**Figure 5.8:** Free-running relative power noise measurements of the MOPA system (47 independent curves). The measurements are taken over a time period of 12 days with the automated diagnostic breadboard. Modified figure from [MKW22].

The data from the 47 frequency noise measurements is shown in Figure 5.9. This noise shows the typical shape of the noise of an ECDL, namely a  $1/f$ -noise at low frequencies and above 10 kHz an almost frequency independent noise [THB19]. In the full frequency band, the seed laser dominates the measured frequency noise of the MOPA system, see Chapter 4 or [MW21]. These measurements demonstrate the stationarity of the free-running laser noise of the chosen MOPA configuration.

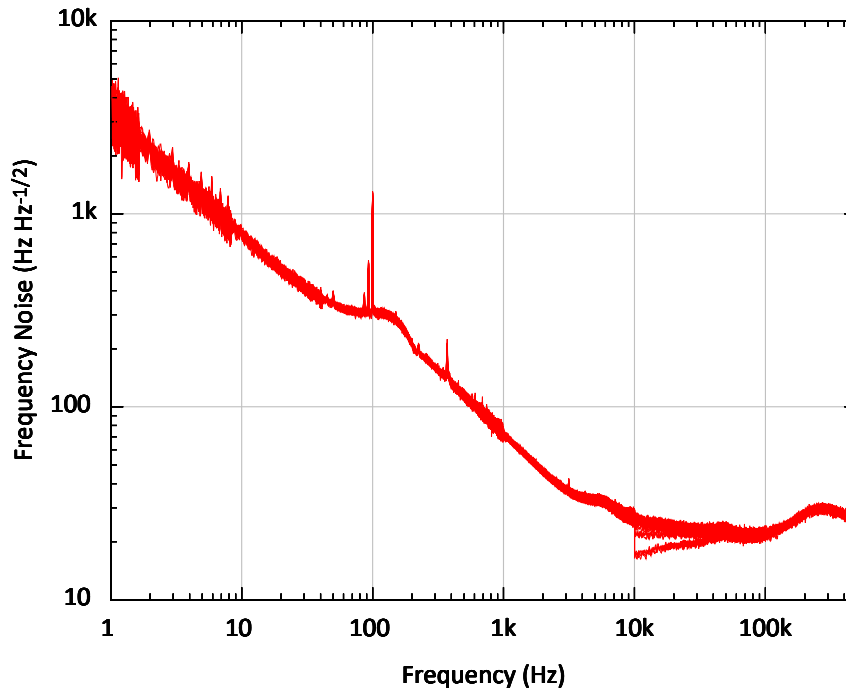


**Figure 5.9:** Free-running frequency noise measurements of the MOPA system (47 independent curves). The measurements are taken over a time period of 12 days. Each curve is compiled from the error and control signal of a length stabilized cavity in the diagnostic breadboard. Above 10 kHz, a different data acquisition system was used, which shows in a few traces measurement artifacts potentially caused by electronic saturation. Modified figure from [MKW22].

### 5.2.1 Frequency stabilizations

To measure the frequency noise of the stabilized laser, three optical cavities, which are not part of the frequency stabilization loops, are available in the setup. The resonator in the DBB, with a 31 mm PZT for length tuning, is designed to measure the frequency noise of the free-running lasers. Because of the length noise of its long PZT, this sensor is not sensitive enough to analyze a frequency stabilized laser. Furthermore, the implemented dither modulation technique limits the highest measurement frequency to a Fourier frequency of 500 kHz. The length stabilization of the PMC uses the PDH technique to generate the error signal. Thereby, frequency noise measurements to higher Fourier frequencies are possible. However, this cavity is similarly to the DBB cavity sensitive to low frequency acoustic noise coupling and via the installed PZT length actuator sensitive to electronic noise. Both effects limit its low frequency performance. For an out-of-loop frequency noise measurement at lower frequencies, the second ULE cavity is used inside the vacuum system.

Figure 5.10 shows the frequency noise of the light that leaves the PMC in the direction of a potential GWD interferometer. Measurements in different states of the inner and outer frequency control loops, as measured with the PMC, are projected to the light transmitted by the PMC. Here, the PMC is taken as a frequency reference to calculate the laser's

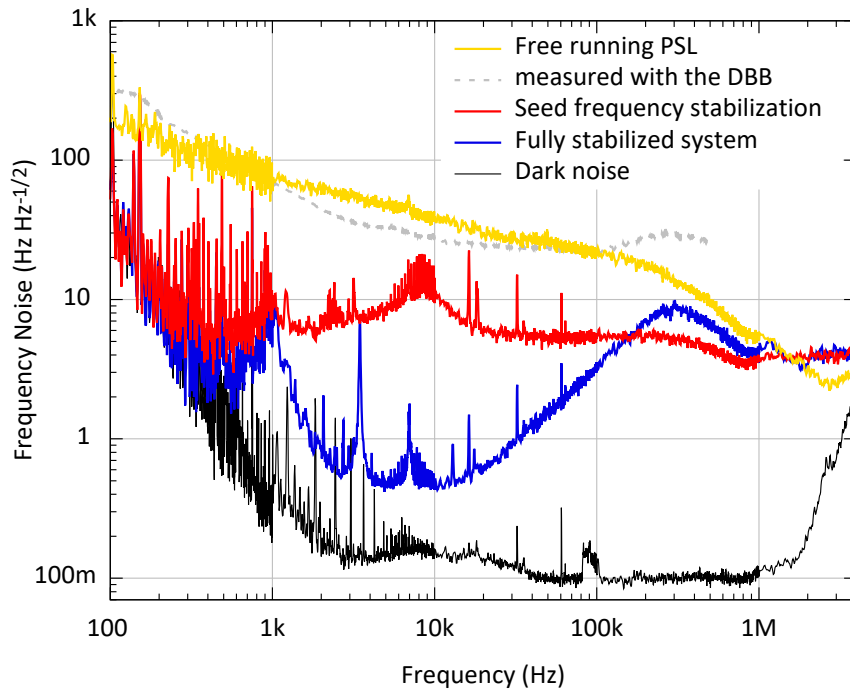


**Figure 5.10:** Frequency noise measurements performed with the PMC. The frequency noise of the free-running laser (yellow curve) is lowered by the seed frequency stabilization (red curve) and is further suppressed by the stabilization to an in-vacuum ULE cavity (blue curve). For comparison, the free-running laser measured with the DBB is shown (dashed curve). Above 200 kHz the PMC passively filter the frequency noise (compare the dashed to the yellow curve). Modified figure from [MKW22].

frequency noise from the error signal of the PMC control loop projected with the noise suppression transfer function of this control loop. The yellow curve shows the free-running noise of the MOPA system and the noise reduction in the red curve results from enabling the inner frequency stabilization loop. The effect of the passive noise filter function of the PMC can be seen: above its pole frequency of 218 kHz the yellow curve is lowered in comparison to the dashed measurement with the DBB in Figure 5.10. As expected, the high gain and phase margins of the inner frequency stabilization avoids any significant increase of the frequency noise above the UGF of 2.1 MHz (Figure 5.10, red curve). The frequency noise reduction below 1 MHz strongly reduces the nonlinearly imprinted power noise in transmission of the PMC (see Figure 5.4).

The outer loop of the frequency stabilization further reduces the frequency noise of the laser system below 100 kHz, shown in Figure 5.10 in the blue curve. But this feedback control loop has lower phase and gain margins, resulting in a moderate increase in frequency noise above its UGF, of 180 kHz, compared to the noise when only the seed stabilization is in operation. At low frequencies, dark noise and PMC length noise contaminate the frequency noise measurements.

At lower frequencies, the out-of-loop frequency noise measurement is performed with a

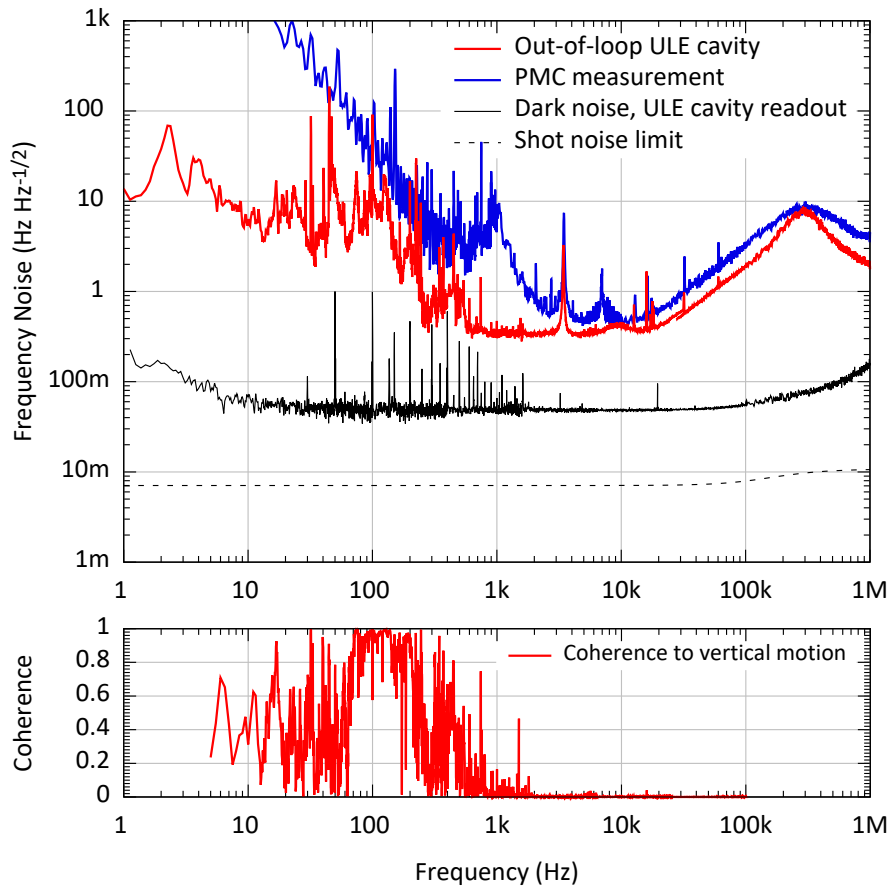


**Figure 5.11:** The out-of-loop frequency noise of the PSL is measured with a second rigid ULE cavity, placed in vacuum. **Top:** from the control and error signals of the sideband-frequency stabilization to the second rigid ULE cavity’s resonance frequency, the frequency noise of the stabilized laser at the PMC output is calculated. The shown dark noise is the dark noise of the error signal, which is the technical noise limit for this measurement. For comparison, the out-of-loop measurement with the PMC from Figure 5.10 is added. Modified figure from [MKW22]. **Bottom:** coherence of the control signal of the out-of-loop ULE cavity to the signal of a vertical geophone, placed on top of the ULE cavities’ vacuum tank. The measured frequency noise show a high coherence to vertical motion below 1 kHz.

second ULE cavity inside the vacuum system. As described above, a phase modulation sideband was stabilized to this ULE cavity with a UGF of 25 kHz and the error and control signal of the utilized feedback control loop revealed the frequency noise of the stabilized laser. Figure 5.11 shows the frequency noise measured with the out-of-loop ULE cavity. It should be noted that the frequency noise is projected to the frequency noise of the light leaving, the PMC for a better comparison with the measurements presented in Figure 5.10. This projection accounts for the pole frequency difference between this ULE cavity and the PMC, and thus the different corner frequencies in their filter transfer function (see Figure 2.4). Coherence measurements between the control signal of the sideband stabilization loop and



a vertical geophone on top of the vacuum tank (L-22D [Kir17]) confirmed that the noise at frequencies below 1 kHz is correlated to vibrations of the vacuum tank, see lower plot in Figure 5.11. Horizontal motions were not measured but potentiality couple similar to the length noise of the ULE cavities. At frequencies above 10 kHz, the achieved noise reduction is limited by the loop gain of the laser frequency stabilization.

With the frequency stabilization of the laser, the nonlinear coupling to power noise is lower at the PMC, described in Subsection 5.1.2, and thereby provides a power noise magnitude that can be stabilized to the shot noise limit of the in-loop detector.

### 5.2.2 Power stabilization

For the active feedback stabilization of the laser power, a photodetector at one of the low-power transmission port of the PMC detects 13 mA photocurrent. This sensor is used in an analog feedback control loop for a high noise suppression below 100 kHz Fourier frequency.

The other, low-power PMC port hosts two similar out-of-loop detectors, optimized for low electronic noise [MK20]. Photocurrents of 7 mA and 8 mA, respectively, are detected. In Figure 5.12, the out-of-loop relative power noise measurement of one of these detectors is shown in blue, which is largely limited by the detection shot noise. This limit can be bypassed with the introduced CSD measurement technique of the signals from the two out-of-loop detectors. This method allows for a power noise detection that is not limited by the shot noise of the out-of-loop detector and, thus, represents the noise on the light relevant to the GWD.

The CSD measurement with two out-of-loop detectors was able to reconstruct the in-loop sensing shot noise: The measurement presented in Figure 5.12, red curve, shows that the power stabilization is limited between 200 Hz and 70 kHz by the shot noise of the in-loop detector, which is at  $5 \times 10^{-9} \text{ Hz}^{-1/2}$ .

Above 70 kHz the power stabilization is loop gain limited and cannot reduce the free-running noise to the shot noise of the in-loop detector, see Figure 5.12. At frequencies around the UGF of 1.1 MHz, the control loop amplifies the measured noise (see the noise suppression in Figure 5.6). This added noise is filtered by the PMC transfer function (see Figure 2.4) and is in a frequency span, where requirements are typically relaxed for ground-based, interferometric GWDs [Wil11]. At frequencies below 200 Hz the control loop performance might be limited by electronic noise, laser beam pointing on the photodiodes and particles passing the laser beam path. The increases towards low frequencies of the in-loop noise can be explained by the electronic dark noise of the in-loop measurement. Even though, the power noise at 1 Hz is roughly one order of magnitude above the shot noise, it is still lower than the power noise achieved in earlier experiments with in-air sensing (e.g. [Kwe12; Thi19]).

A highly reliable, simultaneous operation of the frequency, power and PMC length stabilizations without re-locks for 16.95 h was observed. After that duration the continuous operation was interrupted by human interaction. After the beam pick-offs for all stabilizations and the transmission through the PMC a laser power of 1.6 W was measured, usable for high precision experiments relying on a low noise laser source at 1550 nm wavelength.

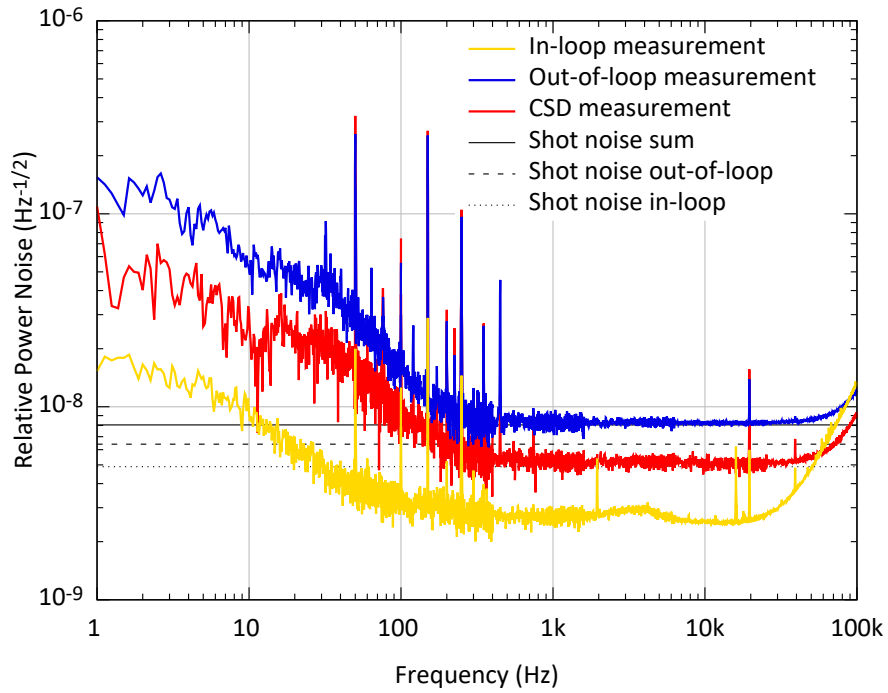


**Figure 5.12:** The out-of-loop relative power noise was measured as an amplitude spectral density with a single photodiode detector (blue curve) and via a cross-spectral density (CSD) measurement between two out-of-loop detectors (red curve). These measurements are compared to the in-loop noise of the power stabilization loop (yellow curve). Above 200 Hz the blue curve is limited by the combined shot noise of the in-loop and out-of-loop detector, whereas the red curve is limited by the shot noise of the in-loop sensor only. Modified figure from [MKW22].

### 5.3 Conclusion and outlook

A stabilized laser system at a wavelength of 1550 nm for future GWDs was presented, built from commercial lasers, low noise sensors, fast actuators, and analog control loops with high UGFs. Based on the aLIGO PMC for 1064 nm wavelength [Pöl12], design decisions for an improved mode cleaner were made, reaching a distinguishability of the vertical and horizontal HOM resonance peaks, a lower pole frequency for improved passive laser noise filtering, a smaller total size, clamped mirrors for renewal and inspection as well as all vacuum compatible material to avoid outgassing, which could contaminate the cavity mirrors.

Due to the observation of nonlinear frequency noise to power noise coupling in the PMC, a nested control loop configuration for the frequency stabilization of the laser was implemented. The inner loop only senses and controls the frequency of the seed laser of a MOPA configuration. This loop provides actuation inputs for an outer loop that will use the GWD interferometer as a frequency reference or its suspended input mode cleaner cavities. In the here presented experiment, an isolated ULE cavity was used to mimic that reference. With this nested frequency stabilization system, significant reduction of the nonlinear coupling was shown and a high UGF for the outer loop was demonstrated to

suppress the free running noise of the laser. This allows for large gains and an associated high noise reduction in GWD interferometer based control loops.

In comparison to the high power laser systems at 1064 nm wavelength, used in currently operating second-generation GWD [Bod20; CCK19], the presented PSL shows increased UGFs of the power and frequency stabilization loops, made possible by the fast, integrated power actuator of the semiconductor amplifier and fiber based phase actuators.

The performance of the power and frequency stabilization was analyzed with out-of-loop sensors. A second in-vacuum ULE cavity in combination with a sideband locking scheme revealed low frequency noise down to  $400 \text{ mHz Hz}^{-1/2}$  and a cross-correlation based out-of-loop power detection scheme confirms a shot-noise limited relative power noise of  $5 \times 10^{-9} \text{ Hz}^{-1/2}$ . Although further work is needed to identify and eliminate sensor noise at low Fourier frequencies, the PSL presented demonstrates a control loop topology and performance suitable for future GWDs. If required, the output power of the PSL can be increased via the above mentioned commercial 10 W fiber amplifier or a large mode area erbium-ytterbium-doped ( $\text{Er}^{3+}:\text{Yb}^{3+}$ ) fiber amplifier with output power levels of 100 W [Var17].

Even though, the here presented results focus on the use in GWDs operating at 1550 nm, the demonstrated PSL can also be used for other high precision metrology experiments and the stabilization concepts can be applied at different wavelength, e.g. for a MOPA laser system with ECDLs and semiconductor pre-amplifier for a GWD operating at  $2 \mu\text{m}$  [Kap20; Rei19a].

In the following chapter, a fraction of the stabilized laser beam is used to generate vacuum squeezed states of light at 1550 nm within the frequency band of ground-based GWDs. The laser stabilizations and their actuators allow for a reduction of laser noise coupling to the squeezing experiment and a characterization of noise coupling paths.



## CHAPTER 6

---

### Squeezed States of Light for Future Gravitational Wave Detectors at a Wavelength of 1550 nm

---

The goal of the gravitational wave detector's (GWD's) stabilized laser system is accomplished, when the technical laser noise levels are low enough not to limit the GWD's sensitivity. When also the other subsystems of a GWD successfully reduce their classical technical noise to that limit, then the detector's sensitivity is limited by quantum noise in most regions of its detection band [Bui20b], see Section 2.1 and Figure 2.2.

Furthermore, reduction of the quantum noise is then desired. The quantum noise in the enhanced Michelson interferometer of the GWD is composed of the detection shot noise and the quantum radiation pressure noise.<sup>1</sup> A quantum noise reduction technique is to inject squeezed vacuum states of light into the output port of the detector, as shown in Figure 2.1. One of these two quantum noise terms can be reduced depending on the phase relation between the squeezed vacuum field and the bright field in the Michelson interferometer [Cav81]. The detection shot noise could as well be improved by increasing the laser power in the interferometer, but at the cost of a higher heat load on the mirrors due to absorption and possible parametric instabilities in the arm cavities [Deg13; EBF10]. The second generation of GWDs, the aLIGO and Advanced Virgo detectors reached a shot-noise reduction of about 3 dB [Tse19; Ace19; McC21]. At GEO600, recently, a quantum shot-noise reduction of 6 dB was demonstrated [Lou21] using squeezed light.

For a quantum noise reduction over the full detection band, the frequency-independent squeezed light can be converted into frequency-dependent states with detuned, over-coupled optical filter cavities [Cav81; Kim01]. This was demonstrated at GWD detection frequencies [Zha20; McC20], and currently intense research activities for integration at the advanced detectors are ongoing.

The use of squeezed light is a key ingredient in the design of all third-generation ground-based GWDs, demanding an effective quantum noise reduction of 10 dB in the gravitational wave detection channel [ET 20; Rei19b]. Some of these future GWDs aim to reduce mirror thermal noise via cryogenic cooling combined with adapted mirror materials like silicon, as discussed in Section 2.1.2. This requires a change in the operating wavelength from 1064 nm to 1550 nm or 2  $\mu\text{m}$  [ET 20; Eva21; Rei19b] and the development of high-efficiency squeezed light sources at these wavelengths.

So far, squeezing levels of 13.1 dB [STS18] and 7.2 dB [Dar21] were demonstrated in the MHz regime at 1550 nm and 2128 nm, respectively. At audio-band frequencies,

---

<sup>1</sup> See equations 2.1 and 2.2 for the case of a simple Michelson interferometer.

11.4 dB [Meh11] and 4 dB [Man18] were achieved at 1550 nm and 1984 nm without the stabilization of the squeezed light phase. With a phase stabilization, 8.2 dB [Sch18a] and 3.9 dB [Yap19] were reported. None of the demonstrated squeezed light sources was able to generate and detect squeezed states of light in the most relevant detection band for third-generation GWDs below a Fourier frequency of 500 Hz. Technical power noise of the used free-running lasers and stray light cause major parts of the low frequency limitations [Thi16; Sch18a; Meh11; Man18]. Thus, a stabilized laser at 1550 nm wavelength in combination with stray light mitigation techniques could be beneficial to generate squeezed light in the full detection band of ground-based GWDs. The stabilized laser system described in Chapter 5 was used as the main laser source of the squeezed light source presented in this chapter.

This chapter begins in Section 6.1 with an introduction of the quantum mechanic description of coherent light, the generation of squeezed vacuum states, and an extended model for the detection with a balanced homodyne detector (BHD), followed by the review of the effects caused by phase noise and optical loss for squeezed vacuum states. Based on a paper published in Physical Review Letters [MWV22], the experimental results are described in the next sections. Here, the two design concepts of the optical parametric amplifier (OPA) cavities, which are used in current operating GWDs at 1064 nm wavelength, are tested at 1550 nm wavelength. Linear, half monolithic OPA cavities are used at GEO600 and Virgo. With this kind of OPA the highest squeezing factors have been demonstrated: 15 dB in the MHz range [Vah16] and 12.0 dB in the audio band [MV18], the latter of which is relevant for all second-generation GWDs, which operate at 1064 nm wavelength. The LIGO GWDs use a bowtie OPA design [Chu11; Wad15]. In a separate experiment this OPA design generated 11.6 dB squeezed light in the audio band [Ste12].

Section 6.3 presents the performance of the linear cavity OPA at MHz frequencies by evaluating models for the optical loss and phase noise of the squeezed fields. Thereby, the quantum efficiency of the detection positive-intrinsic-negative (PIN) photodiodes at 1550 nm wavelength is precisely estimated. In the following section, a bowtie cavity OPA is characterized with similar squeezing measurements. All the characterized contributions to the loss and phase noise budget limit the maximum achievable quantum noise reduction via squeezed states of light in the presented experiment. In a similar way, they would also limit the improvement in a GWD.

The generation and detection of sub-audio-band squeezed vacuum states of light are presented in Section 6.5. These measurements performed with the bowtie OPA cover the frequency range of current and proposed interferometric, ground-based GWDs.

## 6.1 Squeezed states of light

In this section the theoretical backgrounds of the generation and detection of squeezed vacuum states are introduced mostly based on the description in [GK04; Boy08; Ste15], starting with the quantization of electromagnetic field presented in the next subsection.

### 6.1.1 Quantization of the electromagnetic field

For simplicity a plane electromagnetic wave, traveling along the  $z$ -axis with a linear polarization is assumed. Its quantization can be expressed in different operator bases [GK04]:

$$\hat{E}(t) = E_0 [\hat{a}(t) + \hat{a}^\dagger(t)] \sin(kz) \quad \text{or} \quad (6.1)$$

$$\hat{E}(t) = 2E_0 \left[ \hat{X}_1 \cos(2\pi\nu t) + \hat{X}_2 \sin(2\pi\nu t) \right] \sin(kz). \quad (6.2)$$

The field could be described with the time dependent annihilation operator  $\hat{a}(t) = \hat{a}(0) \exp(-2\pi i\nu t)$  and creation operator  $\hat{a}^\dagger(t) = \hat{a}^\dagger(0) \exp(2\pi i\nu t)$  together with the electric field amplitude  $E_0$ , which contains the polarization vector and scaling factors. The electromagnetic wave is modeled as standing wave along the  $z$ -axis, with the wave number  $k = 2\pi/\lambda$  and the temporal frequency  $\nu$ .

Alternatively the quadrature basis can be chosen, connecting via

$$\hat{X}_1 = \frac{1}{2}(\hat{a}(0) + \hat{a}^\dagger(0)) \quad \text{and} \quad \hat{X}_2 = \frac{i}{2}(\hat{a}(0) - \hat{a}^\dagger(0)) \quad (6.3)$$

to the annihilation and creation operators. Here, the quadrature operator  $\hat{X}_1$  is interpreted as the in-phase oscillating amplitude of the electric wave, called the amplitude quadrature and  $\hat{X}_2$  is the orthogonal operator, named the phase quadrature operator. The operator of the magnetic field of this electromagnetic wave have a similar composition, connected via the Maxwell equations to the electric field operator  $\hat{E}(t)$  [GK04].

The fluctuations of the quantity measured by the operators can be described by their variance  $\Delta^2$ , when they are applied to a quantum state  $|\Psi\rangle$ :

$$\langle \Psi | \Delta^2 \hat{X} | \Psi \rangle = \langle \Psi | \hat{X}^2 | \Psi \rangle - \langle \Psi | \hat{X} | \Psi \rangle^2. \quad (6.4)$$

The square root of this variance is the standard deviation. It can be shown that the two quadrature operators satisfy the commutator relation

$$[\hat{X}_1, \hat{X}_2] = \frac{i}{2}, \quad (6.5)$$

resulting in an uncertainty relation for the product of the variances as [GK04]:

$$\Delta^2 \hat{X}_1 \Delta^2 \hat{X}_2 \geq \frac{1}{16}. \quad (6.6)$$

This uncertainty relation translate into the measured quantum noise, like the shot noise measured with a photodetector.

For a minimum uncertainty state, the product of the variances is minimized. A set of quantum states with such minimum uncertainty are the coherent states  $|\alpha\rangle$ , which are the eigenstates of the annihilation operator:

$$\hat{a}|\alpha\rangle = \alpha|\alpha\rangle. \quad (6.7)$$

The real part of  $\alpha$  is proportional to the amplitude of the field in Equation 6.1 and the imaginary part is proportional to the magnetic field amplitude. These kinds of quantum states are a good description of ideal laser beams, with a power proportional to  $|\alpha|^2$ . Thus, the vacuum state  $|0\rangle$  has a coherent amplitude of  $\alpha = 0$ , which also corresponds to the zero photon state [GK04].

The coherent states are minimum uncertainty states, where the variances are equal for both quadratures:

$$\langle\alpha|\Delta^2\hat{X}_1|\alpha\rangle = \frac{1}{4} = \langle\alpha|\Delta^2\hat{X}_2|\alpha\rangle. \quad (6.8)$$

Instead of the equally distributed uncertainties to the two quadratures, Equation 6.6 allows for a variance reduction in one quadrature, if the variance of the other quadrature is increased accordingly. More generally one can define the quadrature operator rotated by the angle  $\phi$  as

$$\hat{X}_\phi = \hat{X}_1 \cos \phi + \hat{X}_2 \sin \phi. \quad (6.9)$$

Then, a state can be called quadrature squeezed, if there is a quadrature for which the variance is lower than the variance of the vacuum state:

$$\Delta^2\hat{X}_{\phi,sqz} < \frac{1}{4}. \quad (6.10)$$

The quadrature with lowest variance is then called the squeezed quadrature, while the orthogonal quadrature is called the antisqueezed quadrature. The antisqueezed quadrature show an increase in variance, so that the uncertainty relation in Equation 6.6 holds for all orthogonal quadratures.

### 6.1.2 Generation of squeezed vacuum states

A method of generating quadrature squeezed states of light is the degenerate parametric down-conversion, a detailed discussion of which can be found in e.g. [Boy08]. This process is based on the nonlinear interaction of light fields in an optical medium, like a crystal with a second-order nonlinear susceptibility  $\chi^{(2)}$ . A bright laser field, with twice the wavelength as the signal field, is used as the pump field for the process.

The interaction between the light fields can be described by the interaction Hamiltonian [GK04]

$$\hat{H}_I = i\hbar(\eta^*\hat{a}\hat{a} - \eta\hat{a}^\dagger\hat{a}^\dagger) \quad \text{with} \quad \eta = \chi^{(2)}\beta. \quad (6.11)$$

Here, the pump field was approximated by its coherent amplitude  $\beta$ . And the time evolution of the operators cancel by choosing the pump frequency to be twice the signal frequency.

The corresponding time evolution operator of the Hamiltonian in Equation 6.11 is

$$\hat{U}_I(t) = \exp(-i\hat{H}_I t/\hbar) = \exp(\eta^*t\hat{a}\hat{a} - \eta t\hat{a}^\dagger\hat{a}^\dagger). \quad (6.12)$$



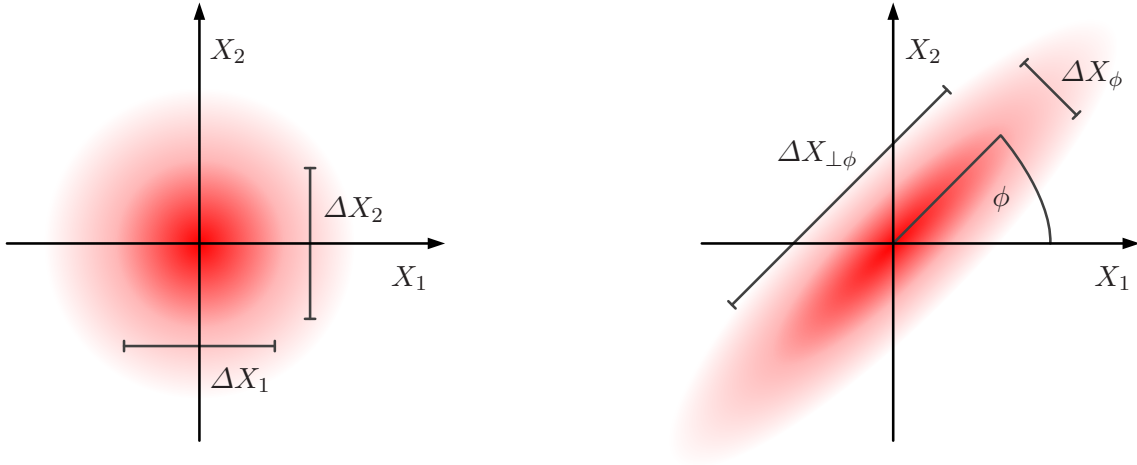


**Figure 6.1:** The schematic probability distributions of states of light in the quadrature basis. **Left:** the vacuum state can be represented as a "ball" with equal standard deviations in both quadratures. **Right:** a quadrature squeezed vacuum state can be characterized by its squeezing angle  $\phi$  and the standard deviations along the quadratures aligned and orthogonal to the squeezing angle.

By setting  $\xi = 2\eta^*t = 2t\chi^{(2)}\beta^*$  this equals to the squeezing operator [GK04]:

$$\hat{S}(\xi) = \exp \left[ \frac{1}{2}(\xi^* \hat{a} \hat{a} - \xi \hat{a}^\dagger \hat{a}^\dagger) \right]. \quad (6.13)$$

Applying the squeezing operator  $\hat{S}(\xi)$  on the vacuum state  $|0\rangle$ , the squeezed vacuum states are defined as

$$|0, \xi\rangle = \hat{S}(\xi)|0\rangle. \quad (6.14)$$

For a squeezed state with a the complex squeezing parameter  $\xi = re^{i\theta}$  with  $0 \leq r < \infty$ , the maximal difference in variances of two quadratures is at  $\phi = \theta/2$  and the orthogonal quadrature at  $\perp \phi = \phi + 90^\circ$ , see Equation 6.9 for the quadrature at angle  $\phi$ . The variances of these two quadratures are [GK04]:

$$\langle 0, \xi | \Delta^2 \hat{X}_\phi | 0, \xi \rangle = \frac{1}{4} e^{-2r}, \quad (6.15)$$

$$\langle 0, \xi | \Delta^2 \hat{X}_{\perp\phi} | 0, \xi \rangle = \frac{1}{4} e^{2r}. \quad (6.16)$$

A schematic view of these quantities is depicted in Figure 6.1 in comparison to the vacuum state.

For the realization in an experiment, the strength of the 'squeezing' is given by the squeeze parameter  $r = 2t\chi^{(2)}|\beta|$ . The angle of the quadrature with minimal variance is defined by the phase of the second harmonic field, represented by the coherent amplitude  $\beta$ . To achieve a high squeezing factor, a medium with a strong second order optical non-

linearity described by  $\chi^{(2)}$ , a high intensity of the second harmonic pump field  $|\beta|^2$ , and a long interaction time  $t$  is needed. These requirements are met in the experiment presented below using periodically poled potassium titanyl phosphate (PPKTP) crystals with high second-order nonlinear susceptibility [AMS13]. These PPKTP crystals are parts of double resonant optical cavities. The resonant power buildup of the second-harmonic pump field and a particularly focusing of the pump beam into the crystal boosts the factor  $\beta$ . The resonance for the fundamental wavelength effectively increases the interaction time  $t$ .

The phase relation between the second-harmonic pump field and the fundamental field has to stay matched during propagation. Otherwise, the parametric amplification angle would change with propagation, lowering the overall squeezing strength. Hence, a spatial phase matching condition has to be fulfilled for an efficient squeezing generation. This requirement can be formulated as a condition for the wave numbers of the involved fields, in the case of the parametric down-conversion or second-harmonic generation as [Boy08]:

$$\Delta k = 2k_\nu - k_{2\nu} = 2\frac{n_\nu 2\pi\nu}{c} - \frac{n_{2\nu} 2\pi 2\nu}{c} . \quad (6.17)$$

For an optimal phase matching, the mismatch  $\Delta k$  should be zero, resulting in the requirement for the refractive indices  $n$  to being equal at both optical frequencies  $\nu$  and  $2\nu$ . There are various techniques to reach this condition [Boy08], of which, in the presented experiments, the method of quasi-phase-matching is applied. For this technique, the sign of the nonlinear coupling coefficient is inverted periodically in the crystal with a periodicity length of  $\Lambda$ . This results in a possible modification of Equation 6.17 to

$$\Delta k \approx 2k_\nu - k_{2\nu} - 2\pi/\Lambda , \quad (6.18)$$

with the cost of a reduction of the nonlinear coupling coefficient by  $2/\pi$  [Boy08]. The fine tuning of this phase matching condition is then done via heating of the PPKTP crystal, which result in a differential change of the terms in Equation 6.18, due to the change of refractive indices and the poling length with temperature.

Finally, the propagation of the Gaussian beams have to be considered. Due to the different wavelength of the fundamental and second-harmonic beams, the Gouy-phases and beam radii of these beams evolve differently along the propagation axis. This results in an optimal focus radius of the Gaussian beams, in dependence on the optical path length in the nonlinear crystal [BK68].

Based on the quantum mechanic description of quadrature squeezed vacuum states in this subsection, the detection of these states of light are discussed in the following subsections.

### 6.1.3 Balanced homodyne detection

The balanced homodyne detection is the most commonly used tool to detect squeezed vacuum states of light. By interfering the squeezed light with a bright coherent field, the variance of an arbitrarily oriented quadrature of the squeezed field can be read out. The coherent amplitude of the bright coherent field, called the local oscillator, defines the amplification factor and its phase defines the orientation of the measured quadrature.

The balanced detection allows for an essential reduction of technical noise coupling to

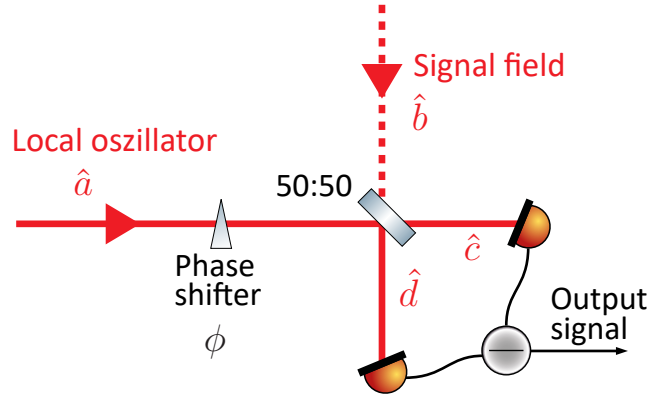


**Figure 6.2:** Schematic setup of a balanced homodyne detector.

the measurement. The signal field and the local oscillator interfere at a 50 % beam splitter. Photodiodes detect the light power at both output ports, see Figure 6.2. A common mode rejection, especially for the technical power noise of the local oscillator field, can be realized by subtracting the two photocurrents of the photodiodes. The direct current subtraction can further improve the signal-to-noise ratio, as only the current difference has to be measured by a transimpedance amplifier [Ste12].

This common mode rejection depends on the balance of the splitting and detection efficiency for the two detected beams, i.e. the precise 50 % splitting at the beam splitter and equal responsivities of the individual photodiodes. A model for this is given in [Ste15] and is here extended to the frequency-depending effect caused by a time delay between the detection at the two photodiodes. The detection at different times can be caused by beam path length differences to the photodiodes or an asymmetry in electric connection wires.

The description of the laser beams can be simplified to the transformation of the annihilation and creation operators, because they linearly depend on the field operators in Equation 6.1. For an ideal 50 % beam splitter and with a phase shift of  $\phi$  of the local oscillator field, the annihilation operators of the output fields can be written as

$$\hat{c} = \frac{1}{\sqrt{2}}(\hat{a}e^{i\phi} + \hat{b}), \quad (6.19)$$

$$\hat{d} = \frac{1}{\sqrt{2}}(-\hat{a}e^{i\phi} + \hat{b}). \quad (6.20)$$

Here, the real beam splitter convention is used, which ensures energy conservation by adding  $180^\circ$  of phase to one of the reflected beams. The power measurements of the output fields with the photodiodes can be represented with the these operators and are

proportional to

$$\hat{c}^\dagger \hat{c} = \frac{1}{2}(\hat{a}^\dagger \hat{a} + \hat{b}^\dagger \hat{b} + \hat{b}^\dagger \hat{a} e^{i\phi} + \hat{a}^\dagger \hat{b} e^{-i\phi}) \text{ and} \quad (6.21)$$

$$\hat{d}^\dagger \hat{d} = \frac{1}{2}(\hat{a}^\dagger \hat{a} + \hat{b}^\dagger \hat{b} - \hat{b}^\dagger \hat{a} e^{i\phi} - \hat{a}^\dagger \hat{b} e^{-i\phi}) . \quad (6.22)$$

The laser power is detected as a photocurrent by the photodiodes. For identical responsivities of the detectors, an exact 50% beam splitting ratio, and no time delay between the measurements, the power difference can then be calculated [Ste15]:

$$\hat{c}^\dagger \hat{c} - \hat{d}^\dagger \hat{d} = \hat{b}^\dagger \hat{a} e^{i\phi} + \hat{a}^\dagger \hat{b} e^{-i\phi} . \quad (6.23)$$

For a further evaluation of Equation 6.23 a linearization of the operators is performed and the input field operators  $\hat{a}$  and  $\hat{b}$  are substituted to

$$\hat{a} = \alpha + \delta \hat{a} \quad \text{and} \quad \hat{b} = \beta + \delta \hat{b} , \quad (6.24)$$

taking  $\alpha$  and  $\beta$  as the coherent amplitude of the fields and  $\delta \hat{a}$  and  $\delta \hat{b}$  as their quantum fluctuation. Furthermore, the input field  $\hat{a}$  is defined as the bright coherent field, serving as the local oscillator, with a real amplitude  $\alpha$ . For the other field  $\hat{b}$ , called the signal field, a coherent amplitude of  $\beta = 0$  is assumed. This is the case, if the signal field is a vacuum state or a squeezed vacuum state. The quadrature operators are defined and linearized accordingly

$$\hat{X}_1^a = \frac{1}{2}(\hat{a} + \hat{a}^\dagger) = \alpha + \frac{1}{2}(\delta \hat{a} + \delta \hat{a}^\dagger) = \alpha + \delta \hat{X}_1^a , \quad (6.25)$$

$$\hat{X}_2^a = \frac{i}{2}(\hat{a} - \hat{a}^\dagger) = \frac{i}{2}(\delta \hat{a} - \delta \hat{a}^\dagger) = \delta \hat{X}_2^a , \quad (6.26)$$

and similar for the field described by  $\hat{b}$ .

By assuming that the quadratic terms of the noise terms  $\delta \hat{a} \delta \hat{b} \rightarrow 0$  are small compared to the terms with coherent amplitudes  $\alpha$ , Equations 6.23 is linearized to

$$\hat{c}^\dagger \hat{c} - \hat{d}^\dagger \hat{d} = \alpha(\delta \hat{b} e^{-i\phi} + \delta \hat{b}^\dagger e^{i\phi}) = 2\alpha \delta \hat{X}_{-\phi}^b . \quad (6.27)$$

Analog to Equation 6.9,

$$\delta \hat{X}_\phi^b = \delta \hat{X}_1^b \cos \phi + \delta \hat{X}_2^b \sin \phi \quad (6.28)$$

is the quadrature operator of the linearized signal field  $\hat{b}$  under an angle  $\phi$ . In this ideal case, the output signal of the BHD is proportional to the amplitude of the signal field measured along the quadrature  $\hat{X}_{-\phi}$ . The angle of the quadrature  $\phi$  is determined by the phase relation between the local oscillator field and the signal field.

By adding a small power loss  $\varepsilon$  for one output field<sup>1</sup> and a time delay between the measurements, the limits to the common mode rejection of the BHD can be modeled. The time delay  $\tau$  between the two measurements leads together with the measurement Fourier frequency  $f$  to a phase shift of  $2\pi\tau f$ . This results in modifications of Equation 6.27, which can then be further evaluated in Fourier space:

$$[\hat{c}^\dagger \hat{c}](t) - (1 - \varepsilon)[\hat{d}^\dagger \hat{d}](t - \tau) \xrightarrow[\text{transformation}]{\text{Fourier}} \mathcal{F}[\hat{c}^\dagger \hat{c}] - (1 - \varepsilon)e^{-2\pi i \tau f} \mathcal{F}[\hat{d}^\dagger \hat{d}]. \quad (6.29)$$

The notation of the Fourier transformation  $\mathcal{F}[\ ]$  of the operators is omitted in the following two equations for simplicity. Using the linearized quadrature operators it follows after Fourier transformation:

$$\begin{aligned} & \hat{c}^\dagger \hat{c} - (1 - \varepsilon)e^{-2\pi i \tau f} \hat{d}^\dagger \hat{d} \\ &= \left(1 - e^{-2\pi i \tau f} + \varepsilon e^{-2\pi i \tau f}\right) \left(\alpha^2 \delta(f)/2 + \alpha \delta \hat{X}_1^a\right) + \left(1 + e^{-2\pi i \tau f} - \varepsilon e^{-2\pi i \tau f}\right) \alpha \delta \hat{X}_{-\phi}^b, \end{aligned} \quad (6.30)$$

with the Dirac delta function  $\delta(f)$ . For measurements at frequencies  $f \ll 1/\tau$  and  $\tau f \varepsilon \rightarrow 0$  this can be approximated to

$$\begin{aligned} \hat{c}^\dagger \hat{c} - (1 - \varepsilon)(1 - 2\pi i \tau f) \hat{d}^\dagger \hat{d} &\approx (\varepsilon - 2\pi i \tau f) \left(\alpha^2 \delta(f)/2 + \alpha \delta \hat{X}_1^a\right) + (2 - \varepsilon - 2\pi i \tau f) \alpha \delta \hat{X}_{-\phi}^b \\ &\approx \underbrace{\varepsilon \alpha^2 \delta(f)/2}_{\textcircled{1}} + \underbrace{\varepsilon \alpha \delta \hat{X}_1^a}_{\textcircled{2}} - \underbrace{2\pi i \tau f \alpha \delta \hat{X}_1^a}_{\textcircled{3}} + \underbrace{(2 - \varepsilon - 2\pi i \tau f) \alpha \delta \hat{X}_{-\phi}^b}_{\textcircled{4}}. \end{aligned} \quad (6.31)$$

The single terms of Equation 6.31 can be related to different effects caused by imbalances in the balanced homodyne detection:

- ① This term describe a constant offset of the homodyne detector signal. This offset directly show the actual power imbalance  $\varepsilon$  at the balanced homodyne detection.
- ② The power noise of the local oscillator can be seen as the fluctuations times the coherent amplitude  $\alpha \delta \hat{X}_1^a$ . The technical power noise couples proportional to the power imbalance  $\varepsilon$  to the measurement and thereby could limit the sensitivity to the signal field's amplitude.
- ③ A delay between the photodiodes signals causes a coupling for the local-oscillator power noise, which rises with the measurement frequency  $f$ . This effect is relevant, when the power noise of the local oscillator is not reduced at high measurement frequencies  $f$ . The coupling strength is proportional to the delay, typically introduced by a difference in the beam path length of the two homodyne detector arms.<sup>2</sup>

1 Similar results can be derived with the assumption of a small deviation in the splitting ratio into the two BHD arms.

2 This effect was observed when operating the laser system without a seed frequency stabilization and thereby white power noise up to 200 kHz was present Figure 5.4.

- ④ This term shows the actual effect to the signal field quadrature measurement. As long as  $\varepsilon \ll 1^1$  and  $2\pi\tau f \ll 1$  the measurement distortion due to the delay and imbalance is very low.

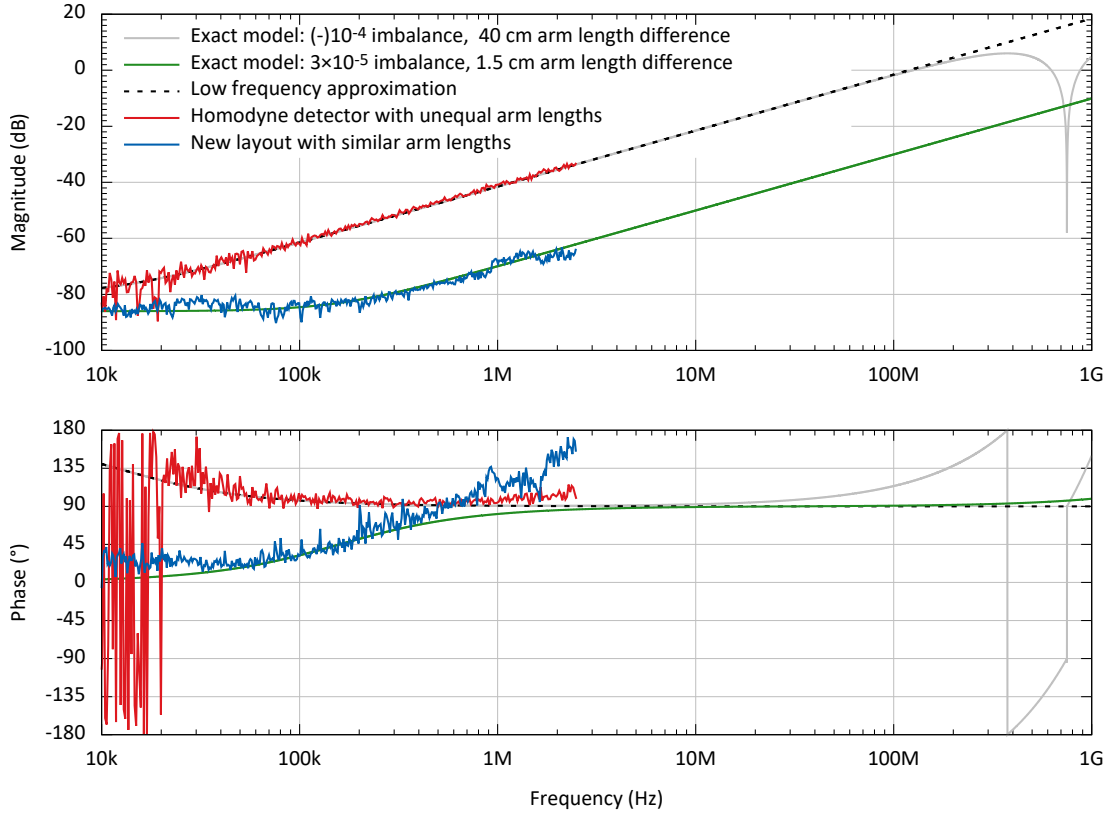


**Figure 6.3:** The transfer functions from a power modulation imprinted to the local oscillator beam to the output signal of the BHD are shown. The signals are normalized for relative power modulation and relative output signal of the BHD. The imbalance  $\varepsilon$  of the BHD beam splitter defines the flat region, while the arm length difference defines the coupling strength at high frequencies. Phase deviations above 1 MHz are caused by the different transfer function of the power modulation monitor photodiode and the output of the BHD electronics. For the arm length difference of 40 cm, the exact model predicts a phase warping at 750 MHz.

The imbalance in light power detection and propagation time of the signal in both arms of the BHD define the coupling strength for power fluctuation of the local oscillator field. This can be modeled by Equation 6.31 and can be measured and simulated as shown in Figure 6.3.

1 For simplicity a loss was assumed in one of the BHD arms rather than a non perfect beam splitting ratio that lead to similar results. Typically the loss difference between the two BHD arms are less than 0.1%, which has a very low impact to the total squeezing loss, described in next subsection.

#### 6.1.4 Optical loss and phase noise

Two most important limiting factors for the achievable noise reduction with squeezed light are the optical loss for the squeezed light field and the phase noise. These factors can be modeled by a superposition of the squeezed state with a vacuum state and the superposition with the orthogonal quadrature of the squeezed state.

Based on Equation 6.15 and Equation 6.16, the variances of the squeezed quadrature  $\Delta^2 \hat{X}_-$  and the antisqueezed quadrature  $\Delta^2 \hat{X}_+$ , normalized to the variance of the vacuum state are defined as

$$\Delta^2 \hat{X}_- = \frac{\langle 0, \xi | \Delta^2 \hat{X}_\phi | 0, \xi \rangle}{\langle 0 | \Delta^2 \hat{X}_\phi | 0 \rangle}, \quad (6.32)$$

$$\Delta^2 \hat{X}_+ = \frac{\langle 0, \xi | \Delta^2 \hat{X}_{\perp\phi} | 0, \xi \rangle}{\langle 0 | \Delta^2 \hat{X}_{\perp\phi} | 0 \rangle}. \quad (6.33)$$

To model the influence of optical loss for a squeezed vacuum state, one can image a loss-less beam splitter mirror placed in the beam path. Its power reflection is similar to the optical loss, which is by

$$\eta = 1 - \text{optical loss} \quad (6.34)$$

related to the optical efficiency  $\eta$  of the squeezed light generation and detection. Hence, the transmitted field is the superposition of the squeezed field and a vacuum field being reflected at the beam splitter. With this model the normalized variances of a squeezed state with optical loss are [PCK92; Vah16]

$$\Delta^2 \hat{X}_- = 1 - \eta_{tot} \frac{4\sqrt{P/P_{thr}}}{\left(1 + \sqrt{P/P_{thr}}\right)^2 + (f/f_p)^2}, \quad (6.35)$$

$$\Delta^2 \hat{X}_+ = 1 + \eta_{tot} \frac{4\sqrt{P/P_{thr}}}{\left(1 - \sqrt{P/P_{thr}}\right)^2 + (f/f_p)^2}, \quad (6.36)$$

where  $P$  is the actual second-harmonic pump power,  $f_p$  is the pole frequency of the OPA cavity at the fundamental wavelength,  $\eta_{tot}$  is the total efficiency and  $f$  is the measurement frequency. The threshold power  $P_{thr}$  describes the power level, at which the round-trip losses in the OPA are equal to the parametric gain and thereby a bright laser oscillation starts for higher amplifications factors. In the later experiments and for this equation, the operation range is chosen to be below the threshold power  $P < P_{thr}$ . The optical efficiencies  $\eta_i$  of the single components in the propagation path of the squeezed states of light lead the total efficiency

$$\eta_{tot} = \prod_i \eta_i. \quad (6.37)$$

Typical loss factors are the OPA's escape efficiency, absorption and reflection at anti-

reflective (AR) coatings during propagation, and the quantum efficiency of the photodiodes of the BHD [Vah16]. The escape efficiency for an OPA cavity is given by  $\eta_{esc} = T_2/(T_2 + \text{cavity round-trip loss})$ , where  $T_2$  is the power transmissivity of the out-coupling mirror for the squeezed field. These loss factors are further discussed with the results of the squeezed light measurements in sections 6.3 and 6.4.

The phase noise between the squeezed and local oscillator fields let a fraction of the other quadrature couple to the measurement. The standard deviation of the phase noise defines this coupling strength, which can be described as a phase offset  $\theta_{pn}$  from the measured quadrature. This phase offset results in the redefinition of the expected variances [ATF06; Vah16]:

$$V_- \approx \Delta^2 \hat{X}_- \cos^2(\theta_{pn}) + \Delta^2 \hat{X}_+ \sin^2(\theta_{pn}) , \quad (6.38)$$

$$V_+ \approx \Delta^2 \hat{X}_+ \cos^2(\theta_{pn}) + \Delta^2 \hat{X}_- \sin^2(\theta_{pn}) . \quad (6.39)$$

Note that the phase noise amplitude  $\theta_{pn}$  has to be calculated as the RMS value over the time required to take a measurement point.

In conclusion, optical loss, non-perfect efficiencies, and phase noise at the generation, propagation, and detection limit the achievable noise reduction in the squeezed quadrature. Thus, special attention was paid to these critical factors in the design and realization of the experiment described in the next section.

## 6.2 Experimental setup

A simplified sketch of the experimental setup is shown in Figure 6.4. The main laser is stabilized in power and frequency. This stabilized laser system was described in detail Chapter 5. Approximately 310 mW of the laser system's output power are split off after the PMC and serve as the main laser input field (Main laser) for the squeezing setup. Via an electro-optical modulator (EOM), which is driven at a frequency of 115 MHz, a phase modulation is imprinted on the light field. This enables the length stabilization of four optical cavities to establish the resonance condition for their input laser fields via the Pound–Drever–Hall (PDH) sensing scheme [Dre83]. The feedback signals of the individual control loops are sent to the cavities' PZTs. For better clarity, the cavity control loops are not shown in Figure 6.4.

A fraction of the main laser beam is injected into the second harmonic generator (SHG) where the pump beam for the OPAs downstream is generated. Another part of the main laser beam is used as a local oscillator (LO) for the BHD, after it passes a triangular mode cleaner cavity (MC) providing a spatially filtered beam with insignificant low astigmatism [Ueh97]. For balanced homodyne detection, the local oscillator is spatially overlapped with the signal field coming from an OPA. This light field can contain the squeezed states (SQZ). The signal field's amplitude is read out along the quadrature defined by the phase of the local oscillator phase, see Subsection 6.1.3.

About 0.5 % of the incident light is reflected from the tilted BHD photodiodes. These PIN InGaAs photodiodes have an anti-reflection coated sensor of 2 mm diameter, the commonly used size in GWDs [Las22], and two curved mirrors serve as retro-reflectors to recycle the reflected light for a higher effective photodiode quantum efficiency. Additionally, quarter



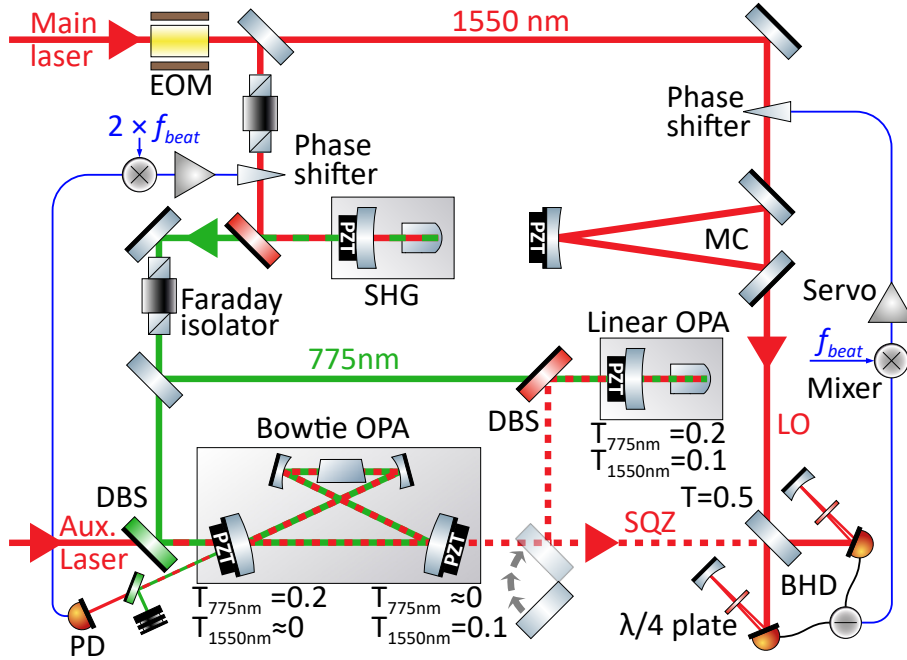


**Figure 6.4:** The simplified schematic of the squeezing setup shows in the upper part the second harmonic generator (SHG) and the mode cleaner cavity (MC) for spatial filtering of the local oscillator (LO). The two optical parametric amplifier (OPA) cavities for squeezed light generation and the balanced homodyne detector (BHD) are depicted in the lower part. Figure from [MWV22].

wave plates are placed in front of the retro-reflectors, thereby rotating the recycled light into the orthogonal polarization. In this way, the interference of residual backreflections from the homodyne detector toward the OPA cavities in the polarization of the squeezed light are suppressed. Thereby, less (phase) noise is added [Sch18b].

The experimental setup contains two different OPAs, which are constructed in a linear and bowtie configuration, respectively. As shown in Figure 6.4 a movable mirror in the signal input port of the BHD can be used to select which of the OPA output fields is sent towards the BHD. Common to both OPAs is that they are designed to be double resonant for light at a wavelength of 1550 nm and of 775 nm. The 775 nm pump field is used to stabilize the cavities on resonance, whereas the vacuum squeezed states of light are produced at 1550 nm. A segmented heating scheme of the nonlinear crystal ensures good quasi-phase-matching of the corresponding fields for an efficient squeezed light generation and simultaneous resonance of both fields [Sch18a; MV20].

### 6.3 Quantum efficiency of the used 1550nm photodiodes

In a first step, to determine the absolute photodiode quantum efficiency and to characterize all relevant parameters of the setup, the linear OPA is employed. The hemilithic linear OPA cavity contains a PPKTP crystal with the dimensions  $1.0 \times 2.0 \times 11.5$  mm. The highly reflective (HR), curved crystal face serves as the cavity end mirror, while the plane

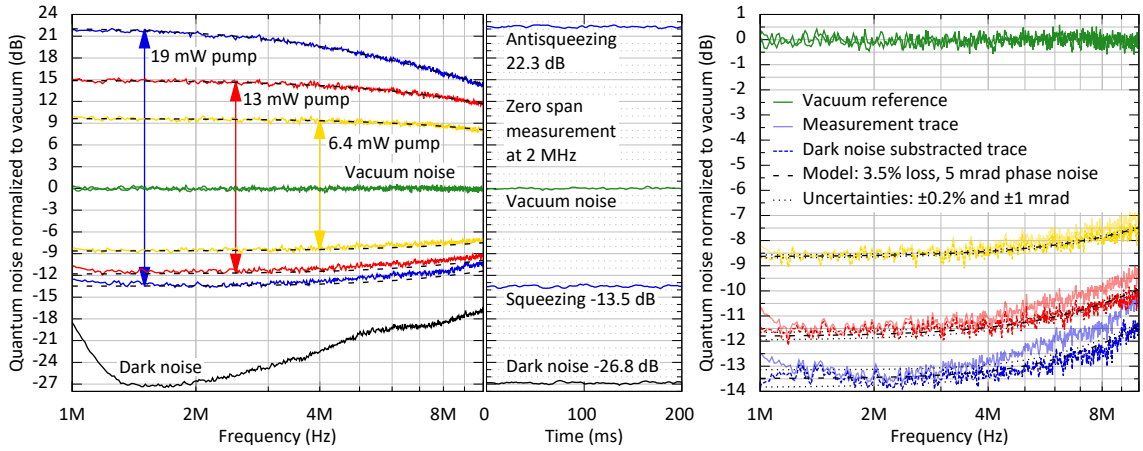


**Figure 6.5:** Homodyne measurements with the signal input from the linear OPA. **Left:** noise spectra of the (anti)squeezing using three different OPA pump powers normalized to the vacuum noise reference for 20 mW local oscillator power at Fourier frequencies between 1 MHz and 10 MHz. The measurements were modeled to estimate the optical loss and phase noise for the squeezed states. The best fits (see black dashed curves) were obtained with an optical loss of  $(3.5 \pm 0.2)\%$  and a phase noise of  $(5 \pm 1)$  mrad. All spectra are captured with a resolution bandwidth (RBW) of 300 kHz, a video bandwidth (VBW) of 100 Hz (left and right). **Center:** a zero span measurement at 2 MHz over 200 ms time confirms the detection of  $(13.5 \pm 0.1)$  dB squeezing (RBW 100 kHz, VBW 30 Hz). **Right:** enlargement of the measured quantum noise reduction of the left-hand graph. The uncertainties of the model fits are illustrated with dotted black lines. Modified figure from [MWV22].

face has an anti-reflective (AR) coating. A partly transmissive mirror is used for the pump light in-coupling and the squeezed light out-coupling. The generated squeezed states are separated from the pump field via a dichroic beam splitter (DBS) and sent toward the BHD.

For three different OPA pump powers the corresponding quantum noise variances are measured at the output of the BHD and presented in reference to the vacuum noise in Figure 6.5. With a pump power of 19 mW, a maximum quantum noise reduction of up to  $(13.5 \pm 0.1)$  dB is measured, which is the highest demonstrated vacuum noise reduction at this wavelength to date. As pointed out at the beginning of this chapter, the highest so far reported noise reduction at 1550 nm was 13.1 dB [STS18].

Taking the measurements with the lower pump powers into account, a consistent model which describes the optical loss and phase noise for the corresponding (anti)squeezing is derived, based on equations 6.35 to 6.39. For all the measurements shown in Figure 6.5, this model implies a total detection efficiency of  $(96.5 \pm 0.2)\%$  and  $(5 \pm 1)$  mrad phase noise.

The overall detection efficiency can be divided into the known individual contributions, as summarized in Tabular 6.1. First, the homodyne contrast was measured to  $(99.50 \pm 0.05)\%$ , which corresponds to an optical loss of  $(1.0 \pm 0.1)\%$  [Hei22]. Second, the transmission loss through three lenses and the AR-coated beam splitter was determined to  $(0.05 \pm 0.02)\%$  in an independent measurement. Third, the OPA's escape

efficiency was calculated to be  $(99.0 \pm 0.4) \%$  based on the measurements of the FSR ( $3443.0 \pm 0.2$ ) MHz, the cavity FWHM ( $59.2 \pm 0.2$ ) MHz and the transmission of the coupling mirror ( $10.15 \pm 0.02$ ) % at a wavelength of 1550 nm.<sup>1</sup> Furthermore, in an independent measurement the highly reflective (HR) coating of the PPKTP crystal was characterized by determining the reduction of the reflected power at 1550 nm of the light, which is coupled into the OPA via the back side of the crystal, when the OPA is on resonance. The measured reduction of  $(1.25 \pm 0.13) \%$  implies a residual transmission of the HR coating of  $(340 \pm 40)$  ppm (parts per million). To explain the escape efficiency,  $(280 \pm 180)$  ppm single path loss through the PPKTP crystal remains, which includes the absorption in the crystal, scattering and reflection of the AR coating of the crystal.

**Table 6.1:** Loss budget of the linear OPA

	1 – loss
Contrast of $(99.50 \pm 0.05) \%$	$(99.0 \pm 0.1) \%$
Escape efficiency	$(99.0 \pm 0.4) \%$
Transmission through 7.5 AR coated surfaces <sup>a</sup>	$(99.95 \pm 0.02) \%$
Quantum efficiency of the photodiodes	$(98.5 \pm 0.7) \%b$
Total efficiency expected from squeezing fits	$(96.5 \pm 0.2) \%$

<sup>a</sup> OPA coupling mirror, three lenses and the AR surface of the beam splitter in one the BHD's arms.

<sup>b</sup> To fit the total loss.

From all these measurements one can conclude that, in order to be in agreement with the model parameters as derived from the measurements shown in Figure 6.5, the absolute quantum efficiency of the homodyne detector photodiodes has to be  $(98.5 \pm 0.7) \%$  including the enhanced sensitivity of 0.5 % gained with the retro-reflectors.

## 6.4 Bowtie squeezer

Based on the precise characterization of the detection efficiency and given the above loss estimation for the PPKTP crystal material, the bowtie OPA is studied in more detail. This OPA design aimed for minimal astigmatism of the squeezed field mode in order to obtain a high contrast with any non-astigmatic Gaussian beam as it is used e.g. for the BHD local oscillator beam or in GWDs. To this end, two concave mirrors ( $r = -100$  mm) focus the beam into the double-sided  $0.5^\circ$  wedged and AR coated 11.5 mm long PPKTP crystal. The focus radius inside the crystal is  $47 \mu\text{m}$ , which requires a higher pump power compared to the linear cavity, where the waist size is  $40 \mu\text{m}$  in radius. The two coupling mirrors are convex,  $r = 1000$  mm, to further reduce astigmatism, which is introduced by the bowtie geometry and spherical curved mirrors, and to provide an OPA output field with a low beam divergence. All cavity mirrors are clamped on a rigid aluminum spacer with one PZT per coupling mirror for cavity length actuation, as shown in Figure 6.4. Inside the cavity, the laser beam is reflected under an angle of incidence of  $5^\circ$  from the mirrors.

<sup>1</sup> The FSR and FWHM were measured with a bright laser beam at 1550 nm wavelength with strong phase modulation sidebands imprinted for calibration. The power transmission of the coupling mirror was measured with a power stabilized laser.

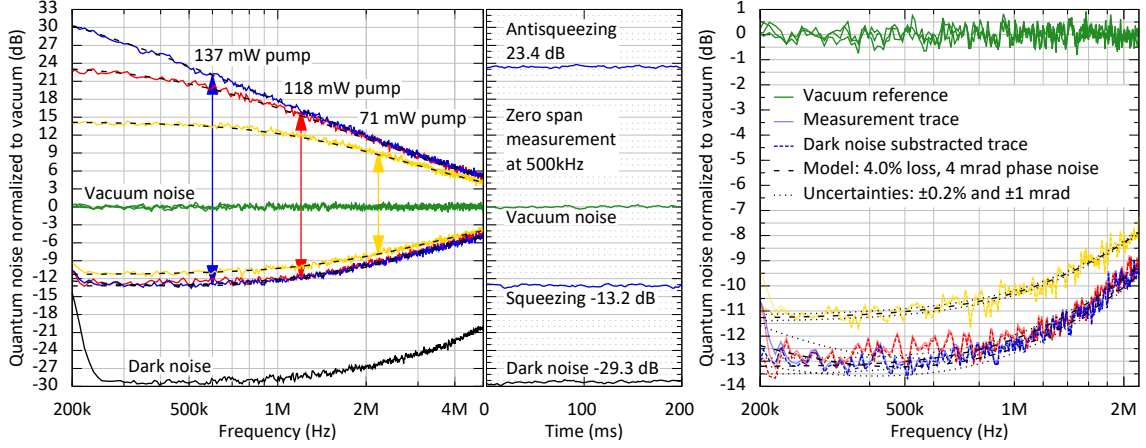


**Figure 6.6:** Homodyne measurements with the signal input from the bowtie OPA. **Left:** noise spectra of the (anti)squeezing using three different OPA pump powers normalized to the vacuum noise reference for 20 mW local oscillator power at Fourier frequencies between 200 kHz and 5 MHz. Given the high electronic dark noise clearance a noise subtraction has only minor impact on the model (black dashed), which was found to fit best with  $(4.0 \pm 0.2)$  % optical loss and  $(4 \pm 1)$  mrad phase noise. All spectra are captured with a RBW 100 kHz and VBW 100 Hz (left and right). **Center:** zero span measurement at 500 kHz over 200 ms time confirms the detection of  $(13.2 \pm 0.1)$  dB squeezing (RBW 50 kHz, VBW 30 Hz). **Right:** enlargement of the measured quantum noise reduction of the left-hand graph. The uncertainties of the model fit are illustrated with the dotted black lines. Modified figure from [MWV22].

The loss budget of the bowtie OPA is summarized in Tabular 6.2: the BHD contrast measurement of  $(99.85 \pm 0.05)$  % experimentally confirms the aimed low level of astigmatism and results in a squeezing detection loss of only  $(0.3 \pm 0.1)$  %, which is introduced by the non-perfect mode overlap between the local oscillator (LO) and signal field. Similar to the linear OPA, the bowtie OPA’s escape efficiency was determined to be  $(98.7 \pm 0.6)$  %, calculated from individual measurements of the FSR  $(464.74 \pm 0.04)$  MHz, the FWHM  $(8.14 \pm 0.04)$  MHz, and the 1550 nm coupler transmission of  $(10.303 \pm 0.012)$  %.

**Table 6.2:** Loss budget of the bowtie OPA

	1 – loss
Contrast of $(99.85 \pm 0.05)$ %	$(99.7 \pm 0.1)$ %
Escape efficiency	$(98.7 \pm 0.6)$ %
Transmission through 3.5 AR coated surfaces <sup>a</sup>	$(99.98 \pm 0.02)$ %
Quantum efficiency of the photodiodes	$(98.5 \pm 0.7)$ % <sup>b</sup>
Total efficiency expected from squeezing fits	$(96.0 \pm 0.2)$ % <sup>c</sup>

<sup>a</sup> OPA coupling mirror, one lens and the AR surface in one arm of the BHD.

<sup>b</sup> Value from the linear OPA loss budget.

<sup>c</sup> This value is within the expected loss  $(96.9 \pm 1.4)$  %.

Compared to the linear OPA, the bowtie OPA shows a slightly lower escape efficiency. This can be explained by the higher transmission of the 775 nm coupling mirror at 1550 nm wavelength of  $(3340 \pm 120)$  ppm. With the above estimation of the BHD-photodiode quantum efficiency, the total optical loss budget for the bowtie squeezing path adds up to  $(3.1 \pm 1.4)$  %, which is in agreement with the expected optical loss taken from the fits of the measurements as presented in Figure 6.6 of  $(4.0 \pm 0.2)$  %.

The highest squeezing level measured with the bowtie OPA is  $(13.2 \pm 0.1)$  dB at a harmonic pump power of 137 mW and is thus comparable in squeezing strength to the results achieved with the linear OPA.

One important difference between the two OPA topologies presented here is the coupling of backscattered light from the BHD: Backreflections of the local oscillator at the BHD photodiodes or retro-reflectors can travel in the direction of the OPA cavity. The phase of the backreflected field is modulated by vibrations of the reflection surface and changes of the optical pathlength. In the case of the linear OPA, this field can directly interfere with the squeezed eigenmode in the cavity and, thereby, degrade the noise reduction [Sch18b]. The bowtie configuration is less sensitive to backscattered light because of the two distinct traveling wave directions inside the cavity. This intrinsic suppression of backscattered light coupling is comparable in strength to a conventional Faraday Isolator [Chu11], but without introducing additional optical loss. This is an advantage for the squeezing generation at audio-band frequencies and below, where a high sensitivity of squeezing generation to backscattered light has been verified [Chu11; Ste12; Sch18b].

## 6.5 Squeezed states at low frequencies

In contrast to the relatively short measurement times required at MHz frequencies, where no active phase control scheme was necessary to capture the presented measurements, the phase of the (anti)squeezed state has to be stabilized to the readout quadrature of the BHD to demonstrate the performance below 10 kHz. Following the coherent control scheme [Vah06], a frequency shifted auxiliary control field was injected into the bowtie OPA. A beat signal between the auxiliary laser field and the main laser field is used for an offset phase lock loop (PLL) that stabilize the laser frequency difference to 7.15 MHz (not shown in Figure 6.4). This optical beat frequency readout  $f_{beat}$  also serves as the electronic local oscillator input source for the error signal generation required for phase stabilization, which circumvents a very high bandwidth PLL.<sup>1</sup>

In this configuration squeezing measurements were performed from 10 kHz down to below 1 Hz and the noise spectra are shown in Figure 6.7. Each trace is computed from a 120 s long time series, sampled with 22 kS/s. The averaging factor varies between 38 for frequencies below 1.7 Hz and 377 k for the frequencies between 1.7 kHz and 10 kHz. The measurement time was limited to about 120 s due to noise transients, occurring approximately every few 100 s. It is suspected, that single dust particles, passing the beam in one arm of the BHD, might be the origin of these events [Ste12]. Time traces with at least one of these events led to noise spectra with a noise shoulder below a few 10 Hz and were sorted out.

---

<sup>1</sup> The beat frequency is doubled with an electronic mixer for the pump phase error signal generation.

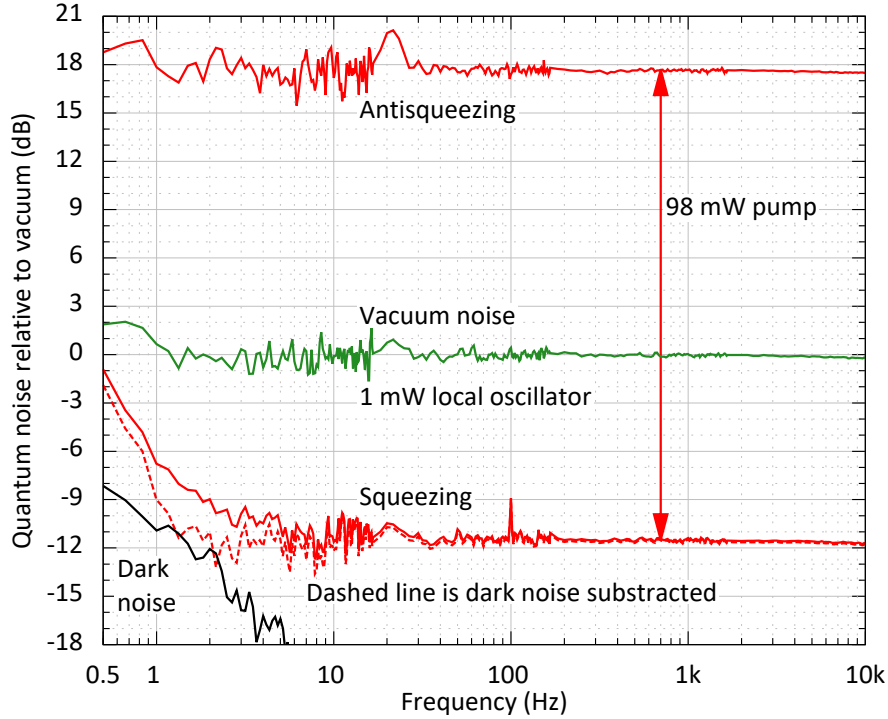


**Figure 6.7:** Quantum noise measurements from 10 kHz down to 0.5 Hz obtained with the bowtie OPA. The results correspond to a harmonic OPA pump power of 98 mW and are plotted relative to the vacuum noise reference. The dashed curve illustrates the squeezing level after the electronic dark noise was subtracted. A quantum noise reduction of up to 11.5 dB could be measured with only 17.5 dB of antisqueezing. All traces are computed from continuous time series, with 120 s length and at least 38 averages. Modified figure from [MWV22].

A quantum noise reduction of up to 11.5 dB is detected at audio-band frequencies with as little as 17.5 dB antisqueezing. Below a few Hz, the residual electronic dark noise contribution limits the direct squeezing measurement, but the dark noise subtraction reveals the full potential of the squeezed light source, leading to a squeezing level of 9 dB at 1 Hz frequency.

At these low measurement frequencies several increased noise couplings were observed in the squeezing setup. For example the laser power noise shows up at the BHD stage below 2 Hz, probably caused by air flow and microscopic particles passing the beams. To reduce the power noise coupling, the local oscillator power was optimized and the balancing of the BHD was carefully adjusted. Above 2 Hz the measurement is mostly limited by the technical noise of the coherent control field beating with the local oscillator field. This noise source added frequency independent noise at  $-18$  dB relative to the vacuum noise and led to about 0.5 dB squeezing degradation.



## 6.6 Conclusion and outlook

In conclusion, this is the first demonstration of strongly squeezed vacuum states of light at a wavelength of 1550 nm at detection frequencies spanning the complete range of current [Aas15; Ace15; Aku20; Doo16] and third-generation ground-based GWDs [ET 20; Abb17e]. Squeezing at frequencies from 10 kHz down to 0.5 Hz was measured with a quantum noise reduction of up to 11.5 dB, which highlights the potential of the proposed quantum noise reduction schemes for future GWDs with silicon test masses, e.g. the low frequency interferometers of the Einstein Telescope GWD [ET 20].

Without the special technical difficulties for squeezing measurements that arise from the long measurement time in the audio band, 13 dB quantum noise reduction at MHz frequencies was demonstrated, for both the linear and the bowtie OPA configuration. However, the bowtie design might be beneficial for the application in GWDs as it shows an intrinsic immunity to backscattering [Chu11; Ste12], but requires further optimization of the cavity mirror coatings to reach an escape efficiency as high as the one achieved with the linear OPA. In addition, the careful design of the bowtie cavity geometry demonstrated a very low astigmatism, competitive to linear designs. The gained knowledge on the 2 mm photodiode quantum efficiency, the optical loss of current PPKTP crystal material and the investigation of limitations for the audio-band and sub-audio-band squeezing, pave the way for the design of squeezed light sources and photodetectors for future GWDs operating at 1550 nm wavelength.

An improved beam path for the squeezed light, by further shielding or surrounding with a vacuum chamber, can help to reduce the jitter events. These events are probably caused by particles passing the beam path and, thereby, limit the measurement time with stationary noise to about 120 s in the presented experiment. In addition, the observed noise limitation due to the coherent control field can be solved by a filter cavity in this beam path or the use of a frequency shifted part of the stabilized main laser beam for coherent control. Finally, the power noise coupling below 2 Hz to the measurement can be reduced by adding power stabilization loop for the local oscillator power, with a sensor close to the BHD.





# CHAPTER 7

---

## Summary and Outlook

---

In this thesis, classical, stabilized laser sources and non-classical, squeezed light sources suitable for interferometric ground-based gravitational wave detectors (GWDs) were designed, built, and investigated. The motivation of this thesis was to improve the current GWD's laser systems at 1064 nm wavelength and to demonstrate concepts for laser systems and squeezed light sources for future detectors, especially those with a proposed laser wavelength of 1550 nm.

Two single-pass, low noise, high power solid-state laser amplifiers with good spatial beam quality at a wavelength of 1064 nm were examined in Chapter 3. In the corresponding publication [Thi19], the characterization of these amplifiers was presented for the first time in literature. The results helped to redesign the laser systems of most current GWDs and to improve their noise performance, reliability, and available laser power by integrating these amplifiers [CCK19; Bod20]. The implementation of a high-power pump light actuator further enhanced the amplifiers' capabilities for laser power stabilization. Their low complexity and high robustness make such amplifiers good candidates for various applications.

Third-generation ground-based GWDs, like the Einstein Telescope [ET 20] or Cosmic Explorer [Eva21], are proposed to host interferometers with cryogenic cooled silicon mirrors for thermal noise reduction. The high absorption of silicon at 1064 nm require a change of the laser wavelength. To this end, comparative tests and characterizations of laser sources and amplifiers at 1550 nm with the focus on the potential usage in stabilized laser systems for future GWDs were discussed in Chapter 4 [MW22].

Based on the findings from Chapter 4, an optimal master oscillator power amplifier configuration for the prototype of a stabilized laser system at 1550 nm regarding the demands of ground-based GWDs was presented in Chapter 5 [MKW22]. Revealed non-linear couplings of frequency noise at the mode cleaner cavity limited the power noise performance of the laser system.<sup>1</sup> The introduced novel seed-laser stabilization could eliminate this limitation. Furthermore, significantly increased stabilization bandwidths with high noise suppression, compared to previous laser stabilizations in the context of GWDs, were realized via integrated fiber actuators. Independent out-of-loop measurements verified the low noise performance of the stabilized laser system. With an independent reference, a frequency noise reduction down to  $400 \text{ mHz Hz}^{-1/2}$  was demonstrated and with a cross-correlation based out-of-loop detection a shot-noise limited relative power noise of  $5 \times 10^{-9} \text{ Hz}^{-1/2}$  at frequencies down to 200 Hz was confirmed. Finally, further steps to

---

<sup>1</sup> There are no reports on this effect in laser systems operated in current GWDs.

integrate such a laser system into the stabilizations of a future GWD's interferometer were highlighted in Chapter 5.

The developed stabilized laser system was employed in Chapter 6 to drive two squeezed light sources at 1550 nm wavelength [MWV22]. Quadrature squeezed vacuum states of light with a 13.5 dB non-classical noise reduction were demonstrated at MHz frequencies. This is the highest value shown at a laser wavelength compatible with silicon mirrors so far. This achievement allowed a precise characterization of the photodiode quantum efficiency at 1550 nm for a sensor size relevant for future GWDs [Gro16]. Detailed analysis of frequency-dependent noise coupling to the balanced homodyne detector revealed the advantage of the stabilized laser system for the squeezed light detection in the audio band. A non-classical noise reduction of 11.5 dB was demonstrated in the audio and sub-audio bands using enhanced backscatter coupling reduction techniques. These were the first measurements of squeezed light at 1550 nm wavelength covering the full detection band of current and proposed ground-based GWDs.

The results at 1550 nm wavelength should help in the interferometer design of future GWDs to trade off acceptable laser noise coupling strengths with an achievable laser noise performance. More accurate definitions of requirements for laser systems and other subsystems of proposed GWD could be derived from this.

Based on the insights gained with the presented prototype, a similar stabilized laser system is under construction to be the main laser source for one of two 10 m-scale silicon interferometers within the ETpathfinder in Maastricht [ETp20; Uti22], a test facility for the Einstein Telescope (ET). For this, the interfacing to a control and data acquisition system, further developed optical layouts, and better-engineered circuits shall be integrated to the laser system.

Further investigations have to be performed to improve the sensor noise performance at frequencies below 100 Hz, as well as the low-frequency noise and transients in the squeezing measurements. For this purpose, in-vacuum sensors, improved stray light control, and advanced electronics are in preparation to be integrated and tested.

High-power fiber amplifiers are proposed to deliver increased laser powers demanded by some updated current and future GWDs operating at 1064 nm [Eva21; Wel20; Wel21; Hoc22] and 1550 nm [LIG21; Var17] wavelengths. At this point, the demonstrated use of in-fiber actuators and pump light actuation can give hints for developing fast, low noise, and reliable laser stabilizations for such high-power laser systems.

Besides the application in GWDs, the presented results can be adopted for the laser stabilizations with cryogenic silicon cavities for optical clocks or time comparisons via fiber links [Mat17; Sch22]. The squeezed light sources can be used for sub-shot-noise sensing [Vah18] or quantum cryptography [Geh15] since the wavelength of 1550 nm is compatible with low-loss telecommunications fibers.

---

## Acknowledgments

---

At the end of this thesis, I would like to thank many people for their help and support.

The opportunity to do great science in an environment that is designed to support you is a high privilege. I would like to thank Karsten Danzmann for establishing such a setting at the Albert Einstein Institute in Hannover.

Since my Bachelor thesis, Benno Willke supported me as the group leader of the Laser Group, which later expanded to the Laser and Squeezed Light Group. To have the freedom to realize my own ideas and to be sure of support in doing so is a great advantage under the supervision of Benno Willke. Thank you for all your support, work to make this possible, and great discussions!

For turning the fanciest ideas into real things, I would like to express my warmest thanks to the electronics workshop, mechanics workshop, and IT teams. None of the presented science was possible without you.

Not working alone in the lab is not only more fun, but it also brings the advantages of learning a lot of new things, having someone to discuss with right away, and not having to solve every problem on your own. Patrick, Nina, Nicole, Jan-Simon, Marina, and Henning, it is and was a great pleasure to work in the labs of the AEI with you!

Thank you to all members and former members of the Laser and Squeezed Light Group for all the joyful time we spent together for up to eight years, debating at group meetings or just in a random office, having a barbecue in the park, and sharing offices.

Especially for proofreading parts of this thesis and so many helpful comments, I want to thank Marina, Henning, Nicole, Nina, and Jasper.

Major parts of this thesis have been published first in journals. I would like to thank all co-authors for their help and collaboration on the respective projects.

For the good and longstanding cooperation with the Laser Development Group at the Laser Zentrum Hannover, I would like to thank, in particular, Peter Weßels and Phillip.

I also thank the neoLASE team for their patience and help to test my ideas.

Being part of the collaboration of the LIGO is a great honor. Sharing scientific knowledge in this large community, having a mutual interest and a common purpose of detecting gravitational waves is exceptional!

Particularly, I thank my family and especially Eva for all your support!

Thank you!



---

## Bibliography

---

- [Aas15] Aasi, J. et al. (LIGO Scientific Collaboration): ‘Advanced LIGO’. *Classical and Quantum Gravity* (Mar. 2015), vol. 32(7): p. 074001. DOI: 10.1088/0264-9381/32/7/074001.
- [Aba11] Abadie, J. et al. (LIGO Scientific Collaboration): ‘A gravitational wave observatory operating beyond the quantum shot-noise limit’. *Nature Physics* (Sept. 2011), vol. 7(12): pp. 962–965. DOI: 10.1038/nphys2083.
- [Abb16] Abbott, B. P. et al. (LIGO Scientific Collaboration and Virgo Collaboration): ‘Observation of Gravitational Waves from a Binary Black Hole Merger’. *Phys. Rev. Lett.* (6 Feb. 2016), vol. 116: p. 061102. DOI: 10.1103/PhysRevLett.116.061102. URL: <https://link.aps.org/doi/10.1103/PhysRevLett.116.061102>.
- [Abb17a] Abbott, B. P. et al. (Collaborations: LIGO Scientific, Virgo, Fermi GBM, INTEGRAL, IceCube, AstroSat Cadmium Zinc Telluride Imager Team, IPN, Insight-Hxmt, ANTARES, Swift, AGILE Team, 1M2H Team, Dark Energy Camera GW-EM, DES, DLT40, GRAWITA, Fermi-LAT, ATCA, ASKAP, Las Cumbres Observatory Group, OzGrav, DWF (Deeper Wider Faster Program), AST3, CAASTRO, VINROUGE, MASTER, J-GEM, GROWTH, JAGWAR, CaltechNRAO, TTU-NRAO, NuSTAR, Pan-STARRS, MAXI Team, TZAC Consortium, KU, Nordic Optical Telescope, ePESSTO, GROND, Texas Tech University, SALT Group, TOROS, BOOTES, MWA, CALET, IKI-GW Follow-up, H.E.S.S., LOFAR, LWA, HAWC, Pierre Auger, ALMA, Euro VLBI Team, Pi of Sky, Chandra Team at McGill University, DFN, ATLAS Telescopes, High Time Resolution Universe Survey, RIMAS, RATIR, SKA South Africa/MeerKAT): ‘Multi-messenger Observations of a Binary Neutron Star Merger’. *Astrophys. J. Lett.* (2017), vol. 848(2): p. L12. DOI: 10.3847/2041-8213/aa91c9. arXiv: 1710.05833 [astro-ph.HE].
- [Abb17b] Abbott, B. P. et al. (LIGO Scientific Collaboration and Virgo Collaboration): ‘Search for Post-merger Gravitational Waves from the Remnant of the Binary Neutron Star Merger GW170817’. *The Astrophysical Journal* (Dec. 2017), vol. 851(1): p. L16. DOI: 10.3847/2041-8213/aa9a35.
- [Abb17c] Abbott, B. P. et al. (LIGO Scientific Collaboration, Virgo Collaboration, 1M2H Collaboration, Dark Energy Camera GW-EM Collaboration, and DES Collaboration): ‘A gravitational-wave standard siren measurement of the Hubble constant’. *Nature* (Oct. 2017), vol. 551(7678): pp. 85–88. DOI: 10.1038/nature24471.

- [Abb17d] Abbott, B. P. et al. (LIGO Scientific Collaboration, Virgo Collaboration, Fermi-GBM Collaboration, and INTEGRAL Collaboration): ‘Gravitational Waves and Gamma-rays from a Binary Neutron Star Merger: GW170817 and GRB 170817A’. *Astrophys. J. Lett.* (2017), vol. 848(2): p. L13. DOI: 10.3847/2041-8213/aa920c. arXiv: 1710.05834 [astro-ph.HE].
- [Abb17e] Abbott, B. P. et al. (LIGO Scientific Collaboration): ‘Exploring the sensitivity of next generation gravitational wave detectors’. *Classical and Quantum Gravity* (Jan. 2017), vol. 34(4): p. 044001. DOI: 10.1088/1361-6382/aa51f4.
- [Abb18] Abbott, B. P. et al. (LIGO Scientific Collaboration and Virgo Collaboration): ‘GW170817: Measurements of Neutron Star Radii and Equation of State’. *Physical Review Letters* (Oct. 2018), vol. 121(16): p. 161101. DOI: 10.1103/physrevlett.121.161101.
- [Abb19] Abbott, B. P. et al. (LIGO Scientific Collaboration and Virgo Collaboration): ‘GWTC-1: A Gravitational-Wave Transient Catalog of Compact Binary Mergers Observed by LIGO and Virgo during the First and Second Observing Runs’. *Phys. Rev. X* (3 Sept. 2019), vol. 9: p. 031040. DOI: 10.1103/PhysRevX.9.031040. URL: <https://link.aps.org/doi/10.1103/PhysRevX.9.031040>.
- [Abb20a] Abbott, B. P. et al. (LIGO Scientific Collaboration, Virgo Collaboration, and KAGRA Collaboration): ‘Prospects for observing and localizing gravitational-wave transients with Advanced LIGO, Advanced Virgo and KAGRA’. *Living Reviews in Relativity* (Sept. 2020), vol. 23(1). DOI: 10.1007/s41114-020-00026-9.
- [Abb20b] Abbott, R. et al. (LIGO Scientific Collaboration and Virgo Collaboration): *GWTC-2: Compact Binary Coalescences Observed by LIGO and Virgo During the First Half of the Third Observing Run*. 2020. arXiv: 2010.14527 [gr-qc].
- [Abb21a] Abbott, R. et al. (LIGO Scientific Collaboration and Virgo Collaboration): ‘GWTC-2.1: Deep Extended Catalog of Compact Binary Coalescences Observed by LIGO and Virgo During the First Half of the Third Observing Run’. (Aug. 2021), vol. arXiv: 2108.01045 [gr-qc].
- [Abb21b] Abbott, R. et al. (LIGO Scientific Collaboration and Virgo Collaboration): ‘Population Properties of Compact Objects from the Second LIGO–Virgo Gravitational-Wave Transient Catalog’. *The Astrophysical Journal Letters* (May 2021), vol. 913(1): p. L7. DOI: 10.3847/2041-8213/abe949.
- [Abb21c] Abbott, R. et al. (LIGO Scientific Collaboration and Virgo Collaboration): ‘Tests of general relativity with binary black holes from the second LIGO–Virgo gravitational-wave transient catalog’. *Physical Review D* (June 2021), vol. 103(12): p. 122002. DOI: 10.1103/physrevd.103.122002.
- [Abb21d] Abbott, R. et al. (LIGO Scientific Collaboration, Virgo Collaboration, and KAGRA Collaboration): *Constraints on the cosmic expansion history from GWTC-3*. 2021. DOI: 10.48550/ARXIV.2111.03604.

- 
- [Abb21e] Abbott, R. et al. (LIGO Scientific Collaboration, Virgo Collaboration, and KAGRA Collaboration): *GWTC-3: Compact Binary Coalescences Observed by LIGO and Virgo During the Second Part of the Third Observing Run*. 2021. arXiv: 2111.03606 [gr-qc].
- [Abb21f] Abbott, R. et al. (LIGO Scientific Collaboration, Virgo Collaboration, and KAGRA Collaboration): *Tests of General Relativity with GWTC-3*. 2021. DOI: 10.48550/ARXIV.2112.06861.
- [Abb21g] Abbott, R. et al. (LIGO Scientific Collaboration, Virgo Collaboration, and KAGRA Collaboration): *The population of merging compact binaries inferred using gravitational waves through GWTC-3*. 2021. DOI: 10.48550/ARXIV.2111.03634.
- [Abb22a] Abbott, R. et al. (LIGO Scientific Collaboration, Virgo Collaboration, and KAGRA Collaboration): ‘First joint observation by the underground gravitational-wave detector, KAGRA, with GEO600’. (Mar. 2022), vol. arXiv: 2203.01270 [gr-qc].
- [Abb22b] Abbott, R. et al. (LIGO Scientific Collaboration, Virgo Collaboration, and KAGRA Collaboration): ‘Search for continuous gravitational wave emission from the Milky Way center in O3 LIGO-Virgo data’. *Physical Review D* (Aug. 2022), vol. 106(4): p. 042003. DOI: 10.1103/physrevd.106.042003.
- [AC00] Abramovici, A. and J. Chapsky: *Feedback Control Systems: A Fast-Track Guide for Scientists and Engineers*. Springer US, 2000. ISBN: 9780792379355. URL: <https://books.google.de/books?id=nsUXUh-DFuEC>.
- [Ace15] Acernese, F. et al.: ‘Advanced Virgo: a second-generation interferometric gravitational wave detector’. *Classical and Quantum Gravity* (Dec. 2015), vol. 32(2): p. 024001. DOI: 10.1088/0264-9381/32/2/024001.
- [Ace19] Acernese, F. et al. (Virgo Collaboration): ‘Increasing the Astrophysical Reach of the Advanced Virgo Detector via the Application of Squeezed Vacuum States of Light’. *Phys. Rev. Lett.* (23 Dec. 2019), vol. 123: p. 231108. DOI: 10.1103/PhysRevLett.123.231108. URL: <https://link.aps.org/doi/10.1103/PhysRevLett.123.231108>.
- [Adh20] Adhikari, R. X. et al.: ‘A cryogenic silicon interferometer for gravitational-wave detection’. *Classical and Quantum Gravity* (July 2020), vol. 37(16): p. 165003. DOI: 10.1088/1361-6382/ab9143.
- [AK01] Abbott, R. S. and P. J. King: ‘Diode-pumped Nd:YAG laser intensity noise suppression using a current shunt’. *Review of Scientific Instruments* (2001), vol. 72(2): p. 1346. DOI: 10.1063/1.1334627.
- [Aku19] Akutsu, T. et al. (KAGRA Collaboration): ‘First cryogenic test operation of underground km-scale gravitational-wave observatory KAGRA’. *Classical and Quantum Gravity* (July 2019), vol. 36(16): p. 165008. DOI: 10.1088/1361-6382/ab28a9. URL: <https://doi.org/10.1088/1361-6382/ab28a9>.



- [Aku20] Akutsu, T. et al. (KAGRA Collaboration): ‘Overview of KAGRA: Detector design and construction history’. *Progress of Theoretical and Experimental Physics* (Aug. 2020), vol. 2021(5). DOI: 10.1093/ptep/ptaa125.
- [All20] Allocca, A. et al.: ‘Interferometer Sensing and Control for the Advanced Virgo Experiment in the O3 Scientific Run’. *Galaxies* (Dec. 2020), vol. 8(4): p. 85. DOI: 10.3390/galaxies8040085.
- [AMS13] Ast, S., M. Mehmet, and R. Schnabel: ‘High-bandwidth squeezed light at 1550 nm from a compact monolithic PPKTP cavity’. *Optics Express* (May 2013), vol. 21(11): p. 13572. DOI: 10.1364/oe.21.013572.
- [And84] Anderson, D. Z.: ‘Alignment of resonant optical cavities’. *Appl. Opt.* (Sept. 1984), vol. 23(17): pp. 2944–2949. DOI: 10.1364/AO.23.002944. URL: <http://ao.osa.org/abstract.cfm?URI=ao-23-17-2944>.
- [ATF06] Aoki, T., G. Takahashi, and A. Furusawa: ‘Squeezing at 946nm with periodically poled KTiOPO<sub>4</sub>’. *Optics Express* (2006), vol. 14(15): p. 6930. DOI: 10.1364/oe.14.006930.
- [Avi06] Avino, S. et al.: ‘Low-noise adaptive optics for gravitational wave interferometers’. *Classical and Quantum Gravity* (Sept. 2006), vol. 23(20): pp. 5919–5925. DOI: 10.1088/0264-9381/23/20/013.
- [Bai21] Bailes, M. et al.: ‘Gravitational-wave physics and astronomy in the 2020s and 2030s’. *Nature Reviews Physics* (Apr. 2021), vol. 3(5): pp. 344–366. DOI: 10.1038/s42254-021-00303-8.
- [Bak19] Baker, J. et al.: *The Laser Interferometer Space Antenna: Unveiling the Millihertz Gravitational Wave Sky*. 2019. DOI: 10.48550/ARXIV.1907.06482.
- [Bar06] Bartolo, R. E. et al.: ‘Achieving narrow linewidth low-phase noise external cavity semiconductor lasers through the reduction of 1/f noise’. *Novel In-Plane Semiconductor Lasers V*. Ed. by Mermelstein, Carmen and David P. Bour. Vol. 6133. International Society for Optics and Photonics. SPIE, 2006: p. 61330I. DOI: 10.1117/12.646901. URL: <https://doi.org/10.1117/12.646901>.
- [Bar18] Barsottia, L. et al.: *Updated Advanced LIGO sensitivity design curve*. <https://dcc.ligo.org/LIGO-T1800044/public>. Jan. 2018.
- [Ben10] Bendat, J. S.: *Random Data - Analysis and Measurement Procedures*. John Wiley & Sons Inc, Mar. 2010. 640 pp. ISBN: 0470248777. URL: [https://www.ebook.de/de/product/10358567/js\\_bendat\\_random\\_data\\_analysis\\_and\\_measurement\\_procedures\\_4e.html](https://www.ebook.de/de/product/10358567/js_bendat_random_data_analysis_and_measurement_procedures_4e.html).
- [BK62] Boyd, G. D. and H. Kogelnik: ‘Generalized Confocal Resonator Theory’. *Bell System Technical Journal* (July 1962), vol. 41(4): pp. 1347–1369. DOI: 10.1002/j.1538-7305.1962.tb03281.x.
- [BK68] Boyd, G. D. and D. A. Kleinman: ‘Parametric Interaction of Focused Gaussian Light Beams’. *Journal of Applied Physics* (July 1968), vol. 39(8): pp. 3597–3639. DOI: 10.1063/1.1656831.



- 
- [Bla01] Black, E. D.: ‘An introduction to Pound–Drever–Hall laser frequency stabilization’. *American Journal of Physics* (Jan. 2001), vol. 69(1): pp. 79–87. DOI: 10.1119/1.1286663.
- [BLF20] Bailly, G., O. Llopis, and A. Fernandez: ‘High Spectral Purity Optical Source Stabilized on a Fiber Ring Resonator’. *IEEE Photonics Technology Letters* (Mar. 2020), vol. 32(5): pp. 255–258. DOI: 10.1109/1pt.2020.2970269.
- [BMW20] Bode, N., F. Meylahn, and B. Willke: ‘Sequential high power laser amplifiers for gravitational wave detection’. *Opt. Express* (Sept. 2020), vol. 28(20): pp. 29469–29478. DOI: 10.1364/OE.401826.
- [BO12] Bogan, C. and P. Oppermann: *aLIGO PSL EPICS user manual*. Tech. rep. LIGO-T0900634-v2. Albert-Einstein-Institut Hannover, 2012. URL: <https://dcc.ligo.org/LIGO-T0900634/public>.
- [Bod20] Bode, N. et al.: ‘Advanced LIGO Laser Systems for O3 and Future Observation Runs’. *Galaxies* (2020), vol. 8(4). ISSN: 2075-4434. DOI: 10.3390/galaxies8040084. URL: <https://www.mdpi.com/2075-4434/8/4/84>.
- [Bod22] Bode, N. In preparation. PhD thesis. Leibniz Universität Hannover, 2022.
- [Bon16] Bond, C. et al.: ‘Interferometer techniques for gravitational-wave detection’. *Living Reviews in Relativity* (Dec. 2016), vol. 19(1). DOI: 10.1007/s41114-016-0002-8.
- [Boy08] Boyd, R. W.: *Nonlinear Optics*. Elsevier Science & Techn., May 2008. 640 pp. URL: [https://www.ebook.de/de/product/15309400/robert\\_w\\_boyd\\_nonlinear\\_optics.html](https://www.ebook.de/de/product/15309400/robert_w_boyd_nonlinear_optics.html).
- [Bro20] Brown, D. D. et al.: ‘Pykat: Python package for modelling precision optical interferometers’. *SoftwareX* (July 2020), vol. 12: p. 100613. DOI: 10.1016/j.softx.2020.100613.
- [Bui20a] Buikema, A. et al.: ‘Sensitivity and Performance of the Advanced LIGO Detectors in the Third Observing Run’. (2020), vol. DOI: 10.48550/ARXIV.2008.01301.
- [Bui20b] Buikema, A. et al.: ‘Sensitivity and performance of the Advanced LIGO detectors in the third observing run’. *Phys. Rev. D* (6 Sept. 2020), vol. 102: p. 062003. DOI: 10.1103/PhysRevD.102.062003. URL: <https://link.aps.org/doi/10.1103/PhysRevD.102.062003>.
- [Cav81] Caves, C. M.: ‘Quantum-mechanical noise in an interferometer’. *Physical Review D* (Apr. 1981), vol. 23(8): pp. 1693–1708. DOI: 10.1103/physrevd.23.1693.
- [CCK19] Cleva, F., J.-P. Coulon, and F. Kéfélian: ‘Characterization, Integration and Operation of a 100-W Solid State Amplifier in the Advanced-VIRGO Pre-Stabilized Laser System’. *CLEO Europe 2019*. Munich, Germany, June 2019. URL: <https://hal.archives-ouvertes.fr/hal-02080528>.

- [CEK03] Cranch, G. A., M. A. Englund, and C. K. Kirkendall: ‘Intensity noise characteristics of erbium-doped distributed-feedback fiber lasers’. *IEEE Journal of Quantum Electronics* (2003), vol. 39(12): pp. 1579–1587.
- [Chu11] Chua, S. S. Y. et al.: ‘Backscatter tolerant squeezed light source for advanced gravitational-wave detectors’. *Opt. Lett.* (Dec. 2011), vol. 36(23): pp. 4680–4682. DOI: 10.1364/OL.36.004680.
- [Cla16] Clark, J. A. et al.: ‘Observing gravitational waves from the post-merger phase of binary neutron star coalescence’. *Classical and Quantum Gravity* (Mar. 2016), vol. 33(8): p. 085003. DOI: 10.1088/0264-9381/33/8/085003.
- [Cle21] Cleva, F. et al.: ‘Laser power stabilization for Advanced VIRGO’. *2021 Conference on Lasers and Electro-Optics Europe & European Quantum Electronics Conference (CLEO/Europe-EQEC)*. IEEE, June 2021. DOI: 10.1109/cleo/europe-eqec52157.2021.9542330.
- [CM22] Cahillane, C. and G. Mansell: ‘Review of the Advanced LIGO gravitational wave observatories leading to observing run four’. *Galaxies* 2022, 10(1), 36; (Feb. 2022), vol. DOI: 10.3390/galaxies10010036. arXiv: 2202.00847 [gr-qc].
- [CMS21] Cahillane, C., G. L. Mansell, and D. Sigg: ‘Laser frequency noise in next generation gravitational-wave detectors’. *Opt. Express* (Dec. 2021), vol. 29(25): pp. 42144–42161. DOI: 10.1364/OE.439253. URL: <http://opg.optica.org/oe/abstract.cfm?URI=oe-29-25-42144>.
- [Cra19] Craig, K. et al.: ‘Mirror Coating Solution for the Cryogenic Einstein Telescope’. *Physical Review Letters* (June 2019), vol. 122(23): p. 231102. DOI: 10.1103/physrevlett.122.231102.
- [Dar21] Darsow-Fromm, C. et al.: ‘Squeezed light at 2128 nm for future gravitational-wave observatories’. *Opt. Lett.* (Dec. 2021), vol. 46(23): pp. 5850–5853. DOI: 10.1364/OL.433878. URL: <http://opg.optica.org/ol/abstract.cfm?URI=ol-46-23-5850>.
- [Day22] Day, M. L. et al.: ‘Limits on atomic qubit control from laser noise’. *npj Quantum Information* (June 2022), vol. 8(1). DOI: 10.1038/s41534-022-00586-4.
- [Deg13] Degallaix, J. et al.: ‘Bulk optical absorption of high resistivity silicon at 1550 nm’. *Optics Letters* (June 2013), vol. 38(12): p. 2047. DOI: 10.1364/ol.38.002047.
- [Del22] Delta Elektronika GmbH. [https://www.delta-elektronika.nl/upload/DATA\\_SHEET\\_SM800.pdf](https://www.delta-elektronika.nl/upload/DATA_SHEET_SM800.pdf). 2022.
- [Die17] Diehl, J. F. et al.: ‘Control of residual amplitude modulation in Lithium Niobate phase modulators’. *Optics Express* (Dec. 2017), vol. 25(26): p. 32985. DOI: 10.1364/oe.25.032985.

- 
- [Dig01] Digonnet, M. J. F.: *Rare-Earth-Doped Fiber Lasers and Amplifiers, Revised and Expanded*. Optical Science and Engineering. pp. 68f., 543ff. Taylor & Francis, 2001. ISBN: 9780824741648. URL: <https://books.google.de/books?id=cogRJ6Lr-1gC>.
- [Dol13] Dolgovskiyand, V. et al.: ‘Ultra-stable microwave generation with a diode-pumped solid-state laser in the 1.5- $\mu\text{m}$  range’. *Applied Physics B* (Dec. 2013), vol. 116(3): pp. 593–601. DOI: 10.1007/s00340-013-5740-7.
- [Doo16] Dooley, K. L. et al.: ‘GEO 600 and the GEO-HF upgrade program: successes and challenges’. *Classical and Quantum Gravity* (Mar. 2016), vol. 33(7): p. 075009. DOI: 10.1088/0264-9381/33/7/075009. URL: <https://doi.org/10.1088/0264-9381/33/7/075009>.
- [Dre83] Drever, R. W. P. et al.: ‘Laser phase and frequency stabilization using an optical resonator’. *Applied Physics B* (1983), vol. 31(2): pp. 97–105.
- [Ebe93] Ebeling, K.: *Integrated Optoelectronics : Waveguide Optics, Photonics, Semiconductors*. p. 469. Berlin, Heidelberg: Springer Berlin Heidelberg, 1993. ISBN: 9783642781667.
- [EBF10] Evans, M., L. Barsotti, and P. Fritschel: ‘A general approach to optomechanical parametric instabilities’. *Physics Letters A* (Jan. 2010), vol. 374(4): pp. 665–671. DOI: 10.1016/j.physleta.2009.11.023.
- [Eri08] Erickson, C. J. et al.: ‘An ultrahigh stability, low-noise laser current driver with digital control’. *Review of Scientific Instruments* (July 2008), vol. 79(7): p. 073107. DOI: 10.1063/1.2953597.
- [ET 18] ET design team: *ET-D sensitivity curve txt file*. <https://apps.et-gw.eu/tds/?content=3&r=14065>. Feb. 2018.
- [ET 20] ET steering committee: *Design report Update 2020 for the Einstein Telescope*. Tech. rep. Einstein gravitational wave Telescope, 2020. URL: <https://apps.et-gw.eu/tds/ql/?c=15418>.
- [ETp20] ETpathfinder Team: *ETpathfinder Design Report*. Tech. rep. ET-0011A-20. Nikhef, Maastricht University, University of Antwerp, Ghent University, Katholieke Universiteit Leuven, Université Catholique de Louvain, Hasselt University, Vrije Universiteit Brussel, Fraunhofer Institute for Laser Technology, RWTH Aachen, University of Twente, Eindhoven University of Technology, Liege Université, VITO, TNO, 2020.
- [Eva20] Evans, M. et al.: *Unofficial sensitivity curves (ASD) for aLIGO, Kagra, Virgo, Voyager, Cosmic Explorer, and Einstein Telescope*. <https://dcc.ligo.org/LIGO-T1500293/public>. Apr. 2020.
- [Eva21] Evans, M. et al.: *A Horizon Study for Cosmic Explorer: Science, Observatories, and Community*. 2021. DOI: 10.48550/ARXIV.2109.09882. URL: <https://arxiv.org/abs/2109.09882>.

- [FEF14] Fritschel, P., M. Evans, and V. Frolov: ‘Balanced homodyne readout for quantum limited gravitational wave detectors’. *Optics Express* (Feb. 2014), vol. 22(4): p. 4224. DOI: 10.1364/oe.22.004224.
- [Fla20] Flaminio, R.: ‘Status and plans of the Virgo gravitational wave detector’. *Ground-based and Airborne Telescopes VIII*. Ed. by Marshall, Heather K., Jason Spyromilio, and Tomonori Usuda. SPIE, Dec. 2020. DOI: 10.1117/12.2565418.
- [Fra] Franzen, A.: *ComponentLibrary*.  
<http://www.gwoptics.org/ComponentLibrary/>.
- [Fre07] Frede, M. et al.: ‘Fundamental mode, single-frequency laser amplifier for gravitational wave detectors’. *Optics Express* (Jan. 2007), vol. 15(2): p. 459. DOI: 10.1364/oe.15.000459.
- [GE18] Gras, S. and M. Evans: ‘Direct measurement of coating thermal noise in optical resonators’. *Phys. Rev. D* (12 Dec. 2018), vol. 98: p. 122001. DOI: 10.1103/PhysRevD.98.122001. URL: <https://link.aps.org/doi/10.1103/PhysRevD.98.122001>.
- [Geh15] Gehring, T. et al.: ‘Implementation of continuous-variable quantum key distribution with composable and one-sided-device-independent security against coherent attacks’. *Nature Communications* (Oct. 2015), vol. 6(1). DOI: 10.1038/ncomms9795.
- [GK04] Gerry, C. and P. Knight: *Introductory Quantum Optics*. Cambridge University Press, Oct. 2004. DOI: 10.1017/cbo9780511791239.
- [Gro16] Grote, H. et al.: ‘High power and ultra-low-noise photodetector for squeezed-light enhanced gravitational wave detectors’. *Optics Express* (Aug. 2016), vol. 24(18): p. 20107. DOI: 10.1364/oe.24.020107.
- [Har02] Harry, G. M. et al.: ‘Thermal noise in interferometric gravitational wave detectors due to dielectric optical coatings’. *Classical and Quantum Gravity* (Feb. 2002), vol. 19(5): pp. 897–917. ISSN: 1361-6382. DOI: 10.1088/0264-9381/19/5/305. URL: <http://dx.doi.org/10.1088/0264-9381/19/5/305>.
- [HC80] Hansch, T. W. and B. Couillaud: ‘Laser frequency stabilization by polarization spectroscopy of a reflecting reference cavity’. *Optics Communications* (Dec. 1980), vol. 35(3): pp. 441–444. DOI: 10.1016/0030-4018(80)90069-3.
- [Hei22] Heinze, J.: ‘Generation and Application of Squeezed States of Light in Higher-Order Spatial Laser Modes’. PhD thesis. Gottfried Wilhelm Leibniz Universität Hannover, 2022.
- [Hil08] Hild, S. et al.: ‘Using the etalon effect for in situ balancing of the Advanced Virgo arm cavities’. *Classical and Quantum Gravity* (Dec. 2008), vol. 26(2): p. 025005. DOI: 10.1088/0264-9381/26/2/025005.
- [Hob09] Hobbs, P. C. D.: *Building Electro-Optical Systems*. John Wiley & Sons, Inc., July 2009. DOI: 10.1002/9780470466339.

- 
- [Hoc21] Hochheim, S. et al.: ‘Low noise spliceless single-frequency chirally-coupled-core all-fiber amplifier’. *Fiber Lasers XVIII: Technology and Systems*. Ed. by Zervas, Michalis N. and Cesar Jauregui-Misas. SPIE, Mar. 2021. DOI: 10.1117/12.2577441.
- [Hoc22] Hochheim, S. et al.: ‘Single-Frequency 336 W Spliceless All-Fiber Amplifier Based on a Chirally-Coupled-Core Fiber for the Next Generation of Gravitational Wave Detectors’. *Journal of Lightwave Technology* (Apr. 2022), vol. 40(7): pp. 2136–2143. DOI: 10.1109/jlt.2021.3133814.
- [KAG19] KAGRA collaboration: ‘KAGRA: 2.5 generation interferometric gravitational wave detector’. *Nature Astronomy* (Jan. 2019), vol. 3(1): pp. 35–40. DOI: 10.1038/s41550-018-0658-y.
- [KAG22] KAGRA Collaboration: ‘Performance of the KAGRA detector during the first joint observation with GEO 600 (O3GK)’. (Mar. 2022), vol. arXiv: 2203.07011 [astro-ph.IM].
- [Kap20] Kapasi, D. P. et al.: ‘Tunable narrow-linewidth laser at 2  $\mu\text{m}$  wavelength for gravitational wave detector research’. *Opt. Express* (Feb. 2020), vol. 28(3): pp. 3280–3288. DOI: 10.1364/OE.383685.
- [KB85] Kane, T. J. and R. L. Byer: ‘Monolithic, unidirectional single-mode Nd:YAG ring laser’. *Opt. Lett.* (Feb. 1985), vol. 10(2): pp. 65–67. DOI: 10.1364/OL.10.000065. URL: <http://opg.optica.org/ol/abstract.cfm?URI=ol-10-2-65>.
- [Kim01] Kimble, H. J. et al.: ‘Conversion of conventional gravitational-wave interferometers into quantum nondemolition interferometers by modifying their input and/or output optics’. *Phys. Rev. D* (2 Dec. 2001), vol. 65: p. 022002. DOI: 10.1103/PhysRevD.65.022002. URL: <https://link.aps.org/doi/10.1103/PhysRevD.65.022002>.
- [Kir17] Kirchhoff, R. et al.: ‘Huddle test measurement of a near Johnson noise limited geophone’. *Review of Scientific Instruments* (Nov. 2017), vol. 88(11): p. 115008. DOI: 10.1063/1.5000592. URL: <https://doi.org/10.1063/1.5000592>.
- [Kun22] Kuns, K. et al.: *Cosmic Explorer Strain Sensitivity*. <https://dcc.cosmicexplorer.org/cgi-bin/DocDB/ShowDocument?docid=T2000017>. Feb. 2022.
- [KW08] Kwee, P. and B. Willke: ‘Automatic laser beam characterization of monolithic Nd:YAG nonplanar ring lasers’. *Applied Optics* (Nov. 2008), vol. 47(32): p. 6022. DOI: 10.1364/ao.47.006022.
- [KW19] Kaufer, S. and B. Willke: ‘Optical AC coupling power stabilization at frequencies close to the gravitational wave detection band’. *Optics Letters* (Apr. 2019), vol. 44(8): p. 1916. DOI: 10.1364/ol.44.001916.
- [KWD09] Kwee, P., B. Willke, and K. Danzmann: ‘Shot-noise-limited laser power stabilization with a high-power photodiode array’. *Optics Letters* (Sept. 2009), vol. 34(19): p. 2912. DOI: 10.1364/ol.34.002912.

- [Kwe09] Kwee, P.: ‘Laser Characterization and Stabilization for Precision Interferometry’. PhD thesis. Gottfried Wilhelm Leibniz Universität Hannover, 2009.
- [Kwe12] Kwee, P. et al.: ‘Stabilized high-power laser system for the gravitational wave detector advanced LIGO’. *Optics Express* (Apr. 2012), vol. 20(10): p. 10617. DOI: 10.1364/oe.20.010617.
- [Las] Laser Zentrum Hannover e.V. <https://www.lzh.de>.
- [Las22] Laser Components GmbH. <https://www.lasercomponents.com/de-en/product/high-quantum-efficiency-photodiodes/> (accessed on 31 May 2022). 2022.
- [LCG09] LCGT Special Working Group: *Study report on LCGT interferometer observation band*. Sept. 2009. URL: [http://gwwiki.icrr.u-tokyo.ac.jp/JGWiki/LCGT/subgroup/ifo/BW?action=AttachFile&do=get&target=lcgt\\_bw09.pdf](http://gwwiki.icrr.u-tokyo.ac.jp/JGWiki/LCGT/subgroup/ifo/BW?action=AttachFile&do=get&target=lcgt_bw09.pdf).
- [LIG19] LIGO Scientific Collaboration: *Instrument Science White Paper 2019*. Tech. rep. LIGO, 2019.
- [LIG21] LIGO Scientific Collaboration: *Instrument Science White Paper 2021*. Tech. rep. LIGO, 2021. URL: <https://dcc.ligo.org/LIGO-T2100298/public>.
- [Lou21] Lough, J. et al.: ‘First Demonstration of 6 dB Quantum Noise Reduction in a Kilometer Scale Gravitational Wave Observatory’. *Phys. Rev. Lett.* (4 Jan. 2021), vol. 126: p. 041102. DOI: 10.1103/PhysRevLett.126.041102. URL: <https://link.aps.org/doi/10.1103/PhysRevLett.126.041102>.
- [LSC17] LSC Instrument Authors: ‘Quantum correlation measurements in interferometric gravitational-wave detectors’. *Phys. Rev. A* (4 Apr. 2017), vol. 95: p. 043831. DOI: 10.1103/PhysRevA.95.043831. URL: <https://link.aps.org/doi/10.1103/PhysRevA.95.043831>.
- [LW05] Lutz, H. and W. Wendt: *Taschenbuch der Regelungstechnik*. Deutsch, 2005. ISBN: 3817117493.
- [MA13] Mitsui, T. and K. Aoki: ‘Measurements of liquid surface fluctuations at sub-shot-noise levels with Michelson interferometry’. *Physical Review E* (Apr. 2013), vol. 87(4): p. 042403. DOI: 10.1103/physreve.87.042403.
- [Mag20] Maggiore, M. et al.: ‘Science case for the Einstein telescope’. *Journal of Cosmology and Astroparticle Physics* (Mar. 2020), vol. 2020(03): pp. 050–050. DOI: 10.1088/1475-7516/2020/03/050.
- [Man18] Mansell, G. L. et al.: ‘Observation of Squeezed Light in the 2  $\mu\text{m}$  Region’. *Phys. Rev. Lett.* (20 May 2018), vol. 120: p. 203603. DOI: 10.1103/PhysRevLett.120.203603. URL: <https://link.aps.org/doi/10.1103/PhysRevLett.120.203603>.
- [Mat17] Matei, D. G. et al.: ‘1.5  $\mu\text{m}$  Lasers with Sub-10 mHz Linewidth’. *Physical Review Letters* (June 2017), vol. 118(26). DOI: 10.1103/physrevlett.118.263202.



- 
- [McC20] McCuller, L. et al.: ‘Frequency-Dependent Squeezing for Advanced LIGO’. *Phys. Rev. Lett.* (17 Apr. 2020), vol. 124: p. 171102. DOI: 10.1103/PhysRevLett.124.171102. URL: <https://link.aps.org/doi/10.1103/PhysRevLett.124.171102>.
- [McC21] McCuller, L. et al.: ‘LIGO’s quantum response to squeezed states’. *Phys. Rev. D* (6 Sept. 2021), vol. 104: p. 062006. DOI: 10.1103/PhysRevD.104.062006. URL: <https://link.aps.org/doi/10.1103/PhysRevD.104.062006>.
- [Meh11] Mehmet, M. et al.: ‘Squeezed light at 1550nm with a quantum noise reduction of 12.3dB’. *Opt. Express* (Dec. 2011), vol. 19(25): pp. 25763–25772. DOI: 10.1364/OE.19.025763.
- [MK20] Meylahn, F. and P. Kwee. <https://dcc.ligo.org/LIGO-D2000510/public>. 2020.
- [MKW22] Meylahn, F., N. Knust, and B. Willke: ‘Stabilized laser system at 1550 nm wavelength for future gravitational-wave detectors’. *Phys. Rev. D* (12 June 2022), vol. 105: p. 122004. DOI: 10.1103/PhysRevD.105.122004. URL: <https://link.aps.org/doi/10.1103/PhysRevD.105.122004>.
- [Mor94] Morrison, E. et al.: ‘Automatic alignment of optical interferometers’. *Appl. Opt.* (Aug. 1994), vol. 33(22): pp. 5041–5049. DOI: 10.1364/AO.33.005041. URL: <http://ao.osa.org/abstract.cfm?URI=ao-33-22-5041>.
- [Mue05] Mueller, G.: ‘Beam jitter coupling in advanced LIGO’. *Optics Express* (2005), vol. 13(18): p. 7118. DOI: 10.1364/opex.13.007118.
- [Mue16] Mueller, C. L. et al.: ‘The advanced LIGO input optics’. *Review of Scientific Instruments* (Jan. 2016), vol. 87(1): p. 014502. DOI: 10.1063/1.4936974.
- [MV18] Mehmet, M. and H. Vahlbruch: ‘High-efficiency squeezed light generation for gravitational wave detectors’. *Classical and Quantum Gravity* (Dec. 2018), vol. 36(1): p. 015014. DOI: 10.1088/1361-6382/aaf448. URL: <https://doi.org/10.1088/1361-6382/aaf448>.
- [MV20] Mehmet, M. and H. Vahlbruch: ‘The Squeezed Light Source for the Advanced Virgo Detector in the Observation Run O3’. *Galaxies* (2020), vol. 8(4). ISSN: 2075-4434. DOI: 10.3390/galaxies8040079. URL: <https://www.mdpi.com/2075-4434/8/4/79>.
- [MW21] Meylahn, F. and B. Willke: *Stabilized laser systems at 1550nm wavelength for future gravitational wave detectors*. 2021. arXiv: 2112.03792 [physics.optics].
- [MW22] Meylahn, F. and B. Willke: ‘Characterization of Laser Systems at 1550 nm Wavelength for Future Gravitational Wave Detectors’. *Instruments* (2022), vol. 6(1). ISSN: 2410-390X. DOI: 10.3390/instruments6010015. URL: <https://www.mdpi.com/2410-390X/6/1/15>.

- [MWV22] Meylahn, F., B. Willke, and H. Vahlbruch: ‘Squeezed States of Light for Future Gravitational Wave Detectors at a Wavelength of 1550 nm’. *Phys. Rev. Lett.* (12 Sept. 2022), vol. 129: p. 121103. DOI: 10.1103/PhysRevLett.129.121103. URL: <https://link.aps.org/doi/10.1103/PhysRevLett.129.121103>.
- [Ner21] Nery, M. T. et al.: ‘Laser power stabilization via radiation pressure’. *Optics Letters* (Apr. 2021), vol. 46(8): p. 1946. DOI: 10.1364/ol.422614.
- [Ner22] Nery, M. T.: *Laser Power Stabilization via Radiation Pressure*. Springer International Publishing, 2022. DOI: 10.1007/978-3-030-95868-8.
- [Ng21] Ng, K. K. Y. et al.: ‘Probing Multiple Populations of Compact Binaries with Third-generation Gravitational-wave Detectors’. *The Astrophysical Journal Letters* (May 2021), vol. 913(1): p. L5. DOI: 10.3847/2041-8213/abf8be.
- [NKT] NKT Photonics A/S. <https://www.nktphotonics.com/lasers-fibers/2016/06/07/new-koheras-basik-adjustik-fiber-lasers/>.
- [NKT21] NKT Photonics A/S. <https://www.nktphotonics.com>. 2021.
- [NM02] Novak, S. and A. Moesle: ‘Analytic Model for Gain Modulation in EDFAs’. *J. Lightwave Technol.* (June 2002), vol. 20(6): p. 975. URL: <http://opg.optica.org/jlt/abstract.cfm?URI=jlt-20-6-975>.
- [NP ] NP Photonics Inc. <http://www.npphotonics.com>.
- [Num10] Numata, K. et al.: ‘Performance of planar-waveguide external cavity laser for precision measurements’. *Optics Express* (Oct. 2010), vol. 18(22): p. 22781. DOI: 10.1364/oe.18.022781.
- [Opt21] OptaSense Inc. <https://rio-lasers.com>. 2021.
- [PCK92] Polzik, E. S., J. Carri, and H. J. Kimble: ‘Atomic spectroscopy with squeezed light for sensitivity beyond the vacuum-state limit’. *Applied Physics B Photophysics and Laser Chemistry* (Sept. 1992), vol. 55(3): pp. 279–290. DOI: 10.1007/bf00325016.
- [Pöl12] Pöld, J.: *aLIGO bow-tie Pre-Modecleaner document*. Tech. rep. Albert-Einstein-Institut Hannover, 2012. URL: [dcc.ligo.org/LIGO-T0900616/public](http://dcc.ligo.org/LIGO-T0900616/public).
- [Pos] Pospiech, M.: *LaTeX Thesis Template*. <http://www.matthiaspospiech.de/latex/templates/thesis/>.
- [Rak02] Rakhmanov, M. et al.: ‘Dynamic resonance of light in Fabry-Perot cavities’. *Physics Letters A* (2002), vol. 305(5): pp. 239–244. ISSN: 0375-9601. DOI: [https://doi.org/10.1016/S0375-9601\(02\)01469-X](https://doi.org/10.1016/S0375-9601(02)01469-X). URL: <https://www.sciencedirect.com/science/article/pii/S037596010201469X>.
- [Ral99] Ralph, T. C. et al. *Optical and Quantum Electronics* (1999), vol. 31(5/7): pp. 583–598. DOI: 10.1023/a:1006943801659.
- [Rei19a] Reitze, D. et al.: *Cosmic Explorer: The U.S. Contribution to Gravitational-Wave Astronomy beyond LIGO*. 2019. arXiv: 1907.04833 [astro-ph.IM].



- 
- [Rei19b] Reitze, D. et al.: ‘Cosmic Explorer: The U.S. Contribution to Gravitational-Wave Astronomy beyond LIGO’. *Bulletin of the AAS* (Sept. 2019), vol. 51(7). <https://baas.aas.org/pub/2020n7i035>. URL: <https://baas.aas.org/pub/2020n7i035>.
- [Rey89] Reynolds, G. O. et al.: *The New Physical Optics Notebook*. SPIE, Jan. 1989. DOI: 10.1117/3.2303.
- [Sau16] Saulson, P. R.: *Fundamentals of Interferometric Gravitational Wave Detectors*. WORLD SCIENTIFIC, June 2016. DOI: 10.1142/10116.
- [Sch18a] Schönbeck, A.: ‘Compact squeezed-light source at 1550nm’. PhD thesis. Universität Hamburg, 2018.
- [Sch18b] Schreiber, E.: ‘Gravitational-wave detection beyond the quantum shot-noise limit’. 43 pp. PhD thesis. Gottfried Wilhelm Leibniz Universität Hannover, 2018.
- [Sch22] Schioppo, M. et al.: ‘Comparing ultrastable lasers at  $7 \times 10^{-17}$  fractional frequency instability through a 2220 km optical fibre network’. *Nature Communications* (Jan. 2022), vol. 13(1). DOI: 10.1038/s41467-021-27884-3.
- [Sei10] Seifert, F.: ‘Power Stabilization of High Power Lasers for Second Generation Gravitational Wave Detectors’. PhD thesis. Leibniz Universität Hannover, 2010.
- [SGM99] Shaddock, D. A., M. B. Gray, and D. E. McClelland: ‘Frequency locking a laser to an optical cavity by use of spatial mode interference’. *Optics Letters* (Nov. 1999), vol. 24(21): p. 1499. DOI: 10.1364/ol.24.001499.
- [Sie86] Siegman, A. E.: *Lasers*. University science books, 1986.
- [Som06] Somiya, K. et al.: ‘Frequency noise and intensity noise of next-generation gravitational-wave detectors with RF/DC readout schemes’. *Phys. Rev. D* (12 June 2006), vol. 73: p. 122005. DOI: 10.1103/PhysRevD.73.122005. URL: <https://link.aps.org/doi/10.1103/PhysRevD.73.122005>.
- [Som07] Somiya, K. et al.: ‘Erratum: Frequency noise and intensity noise of next-generation gravitational-wave detectors with RF/DC readout schemes’. *Physical Review D* (Feb. 2007), vol. 75(4): p. 049905. DOI: 10.1103/physrevd.75.049905.
- [Spe16] Sperling, J.: ‘Characterizing maximally singular phase-space distributions’. *Physical Review A* (July 2016), vol. 94(1): p. 013814. DOI: 10.1103/physreva.94.013814.
- [Sri19] Srivastava, V. et al.: ‘Detection prospects of core-collapse supernovae with supernova-optimized third-generation gravitational-wave detectors’. *Physical Review D* (Aug. 2019), vol. 100(4): p. 043026. DOI: 10.1103/physrevd.100.043026.

- [Sta17] Stanford Research Systems: *Operating Manual and Programming Reference, Model SR785 Dynamic Signal Analyzer*. Stanford Research Systems, Inc. 2017. URL: <https://www.thinksrs.com/downloads/pdfs/manuals/SR785m.pdf>.
- [Ste12] Stefszky, M. S. et al.: ‘Balanced homodyne detection of optical quantum states at audio-band frequencies and below’. *Classical and Quantum Gravity* (June 2012), vol. 29(14): p. 145015. DOI: 10.1088/0264-9381/29/14/145015. URL: <https://doi.org/10.1088/0264-9381/29/14/145015>.
- [Ste15] Steinlechner, S. et al.: ‘Local-oscillator noise coupling in balanced homodyne readout for advanced gravitational wave detectors’. *Physical Review D* (Oct. 2015), vol. 92(7): p. 072009. DOI: 10.1103/physrevd.92.072009.
- [Ste18] Steinlechner, J.: ‘Development of mirror coatings for gravitational-wave detectors’. *Philosophical Transactions of the Royal Society A: Mathematical, Physical and Engineering Sciences* (Apr. 2018), vol. 376(2120): p. 20170282. DOI: 10.1098/rsta.2017.0282.
- [Sto08] Stolpner, L. et al.: ‘Low noise planar external cavity laser for interferometric fiber optic sensors’. *SPIE Proceedings*. Ed. by Sampson, David D. SPIE, Apr. 2008. DOI: 10.1117/12.786226.
- [STS18] Schönbeck, A., F. Thies, and R. Schnabel: ‘13dB squeezed vacuum states at 1550nm from 12mW external pump power at 775nm’. *Opt. Lett.* (Jan. 2018), vol. 43(1): pp. 110–113. DOI: 10.1364/OL.43.000110.
- [TAT08] Takahashi, K., M. Ando, and K. Tsubono: ‘Stabilization of laser intensity and frequency using optical fiber’. *Journal of Physics: Conference Series* (July 2008), vol. 122: p. 012016. DOI: 10.1088/1742-6596/122/1/012016.
- [TED11] Troxel, D. L., C. J. Erickson, and D. S. Durfee: ‘Note: Updates to an ultra-low noise laser current driver’. *Review of Scientific Instruments* (Sept. 2011), vol. 82(9): p. 096101. DOI: 10.1063/1.3630950.
- [THB19] Tran, M. A., D. Huang, and J. E. Bowers: ‘Tutorial on narrow linewidth tunable semiconductor lasers using Si/III-V heterogeneous integration’. *APL Photonics* (Nov. 2019), vol. 4(11): p. 111101. DOI: 10.1063/1.5124254. URL: <https://doi.org/10.1063/1.5124254>.
- [Thi16] Thies, F.: ‘Erzeugung von gequetschtem Licht in einem kompakten Aufbau’. MA thesis. Leibniz Universität Hannover, 2016.
- [Thi19] Thies, F. et al.: ‘Nd:YVO4 high-power master oscillator power amplifier laser system for second-generation gravitational wave detectors’. *Opt. Lett.* (Feb. 2019), vol. 44(3): pp. 719–722. DOI: 10.1364/OL.44.000719.
- [Tho21] Thorlabs Inc. <https://www.thorlabs.com>. 2021.
- [Tse19] Tse, M. et al.: ‘Quantum-Enhanced Advanced LIGO Detectors in the Era of Gravitational-Wave Astronomy’. *Phys. Rev. Lett.* (23 Dec. 2019), vol. 123: p. 231107. DOI: 10.1103/PhysRevLett.123.231107. URL: <https://link.aps.org/doi/10.1103/PhysRevLett.123.231107>.

- 
- [Tsu11] Tsuchida, H.: ‘Characterization of White and Flicker Frequency Modulation Noise in Narrow-Linewidth Laser Diodes’. *IEEE Photonics Technology Letters* (June 2011), vol. 23(11): pp. 727–729. DOI: 10.1109/1pt.2011.2132127.
- [Tün12] Tünnermann, H. et al.: ‘Gain dynamics and refractive index changes in fiber amplifiers: a frequency domain approach’. *Opt. Express* (June 2012), vol. 20(12): pp. 13539–13550. DOI: 10.1364/OE.20.013539.
- [TWF05] Tröbs, M., P. Weßels, and C. Fallnich: ‘Power- and frequency-noise characteristics of an Yb-doped fiber amplifier and actuators for stabilization’. *Optics Express* (2005), vol. 13(6): p. 2224. DOI: 10.1364/opeX.13.002224.
- [Ueh97] Uehara, N. et al.: ‘Modeling of efficient mode-matching and thermal-lensing effect on a laser-beam coupling into a mode-cleaner cavity’. *Modeling and Simulation of Higher-Power Laser Systems IV*. Ed. by Farrukh, Usamah O. and Santanu Basu. Vol. 2989. International Society for Optics and Photonics. SPIE, 1997: pp. 57–68. DOI: 10.1117/12.273681. URL: <https://doi.org/10.1117/12.273681>.
- [Uti22] Utina, A. C. et al.: ‘ETpathfinder: a cryogenic testbed for interferometric gravitational-wave detectors’. *Classical and Quantum Gravity* (Sept. 2022), vol. DOI: 10.1088/1361-6382/ac8fdb.
- [Vah06] Vahlbruch, H. et al.: ‘Coherent Control of Vacuum Squeezing in the Gravitational-Wave Detection Band’. *Phys. Rev. Lett.* (1 July 2006), vol. 97: p. 011101. DOI: 10.1103/PhysRevLett.97.011101. URL: <https://link.aps.org/doi/10.1103/PhysRevLett.97.011101>.
- [Vah16] Vahlbruch, H. et al.: ‘Detection of 15 dB Squeezed States of Light and their Application for the Absolute Calibration of Photoelectric Quantum Efficiency’. *Phys. Rev. Lett.* (11 Sept. 2016), vol. 117: p. 110801. DOI: 10.1103/PhysRevLett.117.110801. URL: <https://link.aps.org/doi/10.1103/PhysRevLett.117.110801>.
- [Vah18] Vahlbruch, H. et al.: ‘Laser Power Stabilization beyond the Shot Noise Limit Using Squeezed Light’. *Physical Review Letters* (Oct. 2018), vol. 121(17): p. 173601. DOI: 10.1103/physrevlett.121.173601.
- [Var17] Varona, O. De et al.: ‘Single-frequency fiber amplifier at 1.5  $\mu\text{m}$  with 100 W in the linearly-polarized TEM00 mode for next-generation gravitational wave detectors’. *Opt. Express* (Oct. 2017), vol. 25(21): pp. 24880–24892. DOI: 10.1364/OE.25.024880.
- [VW22] Venneberg, J. R. and B. Willke: ‘Quantum correlation measurement of laser power noise below shot noise’. *Opt. Continuum* (May 2022), vol. 1(5): pp. 1077–1084. DOI: 10.1364/OPTCON.450479. URL: <http://opg.optica.org/optcon/abstract.cfm?URI=optcon-1-5-1077>.
- [Wad15] Wade, A. R. et al.: ‘A squeezed light source operated under high vacuum’. *Scientific Reports* (Dec. 2015), vol. 5(1). DOI: 10.1038/srep18052. URL: <https://doi.org/10.1038/srep18052>.

- [Wel20] Wellmann, F. et al.: ‘Performance study of a high-power single-frequency fiber amplifier architecture for gravitational wave detectors’. *Applied Optics* (Sept. 2020), vol. 59(26): p. 7945. DOI: 10.1364/ao.401048.
- [Wel21] Wellmann, F. et al.: ‘Low noise 400 W coherently combined single frequency laser beam for next generation gravitational wave detectors’. *Optics Express* (Mar. 2021), vol. 29(7): p. 10140. DOI: 10.1364/oe.420350.
- [Wil08] Willke, B. et al.: ‘Stabilized lasers for advanced gravitational wave detectors’. *Classical and Quantum Gravity* (2008), vol. 25(11): p. 114040. URL: <http://stacks.iop.org/0264-9381/25/i=11/a=114040>.
- [Wil11] Willke, B. et al.: *Pre-Stabilized Laser Design Requirements*. July 2011. URL: <https://dcc.ligo.org/LIGO-T050036/public>.
- [Win11] Winkelmann, L. et al.: ‘Injection-locked single-frequency laser with an output power of 220 W’. *Applied Physics B* (Feb. 2011), vol. 102(3): pp. 529–538. DOI: 10.1007/s00340-011-4411-9.
- [Yap19] Yap, M. J. et al.: ‘Squeezed vacuum phase control at 2  $\mu\text{m}$ ’. *Opt. Lett.* (Nov. 2019), vol. 44(21): pp. 5386–5389. DOI: 10.1364/OL.44.005386. URL: <http://opg.optica.org/ol/abstract.cfm?URI=ol-44-21-5386>.
- [YGE15] Yam, W., S. Gras, and M. Evans: ‘Multimaterial coatings with reduced thermal noise’. *Physical Review D* (Feb. 2015), vol. 91(4): p. 042002. DOI: 10.1103/physrevd.91.042002.
- [Zha20] Zhao, Y. et al.: ‘Frequency-Dependent Squeezed Vacuum Source for Broadband Quantum Noise Reduction in Advanced Gravitational-Wave Detectors’. *Phys. Rev. Lett.* (17 Apr. 2020), vol. 124: p. 171101. DOI: 10.1103/PhysRevLett.124.171101. URL: <https://link.aps.org/doi/10.1103/PhysRevLett.124.171101>.

---

## List of Figures

---

1.1	Illustration of the effect by a gravitational wave to the distances between free-falling masses. . . . .	2
1.2	Amplitude spectral density of the strain sensitivity of a aLIGO in comparison to proposed third-generation ground-based GWDs. . . . .	3
2.1	Simplified optical layout of a typical ground-based gravitational wave detector	6
2.2	Noise budget of aLIGO Hanford during observation run O3. . . . .	9
2.3	Optical cavity schematic . . . . .	13
2.4	The transfer function of an optical cavity. . . . .	17
3.1	Schematic setup of the neoVAN amplifier experiment. . . . .	24
3.2	The output power of the neoVAN-4S-HP in dependence of the seed power. .	26
3.3	RPN of the neoVAN amplifiers. . . . .	27
3.4	RPN of the neoVAN-4S-HP amplifier for Fourier frequencies up to 100 MHz.	27
3.5	Frequency noise measurements of the neoVAN amplifiers performed with the DBB. . . . .	28
3.6	Pointing noise measurement of the neoVAN amplifiers. . . . .	28
3.7	Long-term measurement of the output power of the neoVAN amplifier. . . .	30
3.8	The transfer functions from the input of the current modulator to relative output signals. . . . .	31
3.9	Signal flow diagram of a feedback control loop. . . . .	32
3.10	A bode plot of the open-loop transfer function of the power stabilization. .	35
3.11	Out-of-loop power noise measurement of the stabilized amplifier output power.	36
4.1	Simplified stabilization setup of the low power laser system at 1550 nm wavelength together with the DBB. . . . .	41
4.2	The free-running frequency noise of the different seed lasers and MOPA combinations at 1550 nm wavelength. . . . .	44
4.3	The free-running RPN of the 1550 nm seed lasers. . . . .	44
4.4	The frequency actuation transfer functions of the fiber laser and of the Orion laser. . . . .	46
4.5	The cross-couplings from frequency actuation to the output power of the Orion laser and fiber laser. . . . .	46
4.6	The free-running RPN at the output of the pre-amplifiers. . . . .	47
4.7	Pump current to output power transfer function for the pre-amplifiers. . . .	47
4.8	Transfer functions of the seed power modulation to the output power of the pre-amplifiers. . . . .	49

4.9	The free-running RPN of the power amplifiers. . . . .	49
4.10	The transfer functions from seed power modulations to power modulations of the power amplifiers. . . . .	50
4.11	Multiple-path feedback control loop. . . . .	52
4.12	The open-loop transfer function of the frequency stabilization measured in the low-power stabilization test experiment. . . . .	53
4.13	Control signal noise and the error signal noise of the frequency stabilization. . . . .	56
4.14	Open-loop transfer function of the power stabilization. . . . .	57
4.15	RPN for several combinations of on/off states of the frequency and power stabilization control loops. . . . .	58
5.1	The schematic setup of the pre-stabilized laser system with out-of-loop sensors and DBB. . . . .	62
5.2	Drawing of the PMC for 1550 nm wavelength. . . . .	63
5.3	Simulated amplitude spectral densities after nonlinear noise coupling. . . . .	66
5.4	Free-running laser power noise in transmission of the PMC. . . . .	67
5.5	Bode plot of the open-loop transfer functions measured for the seed frequency stabilization and the stabilization for the in-loop ULE cavity. . . . .	69
5.6	Bode plots of the laser power stabilization transfer functions. . . . .	70
5.7	Schematic setup of a power stabilization with out-of-loop CSD sensing. . . . .	71
5.8	Free-running relative power noise measurements of the MOPA system over a time period of 12 days. . . . .	73
5.9	Free-running frequency noise measurements of the MOPA system over a time period of 12 days. . . . .	74
5.10	Frequency noise measurements performed with the PMC. . . . .	75
5.11	Out-of-loop frequency noise of the PSL measured with a second rigid ULE cavity. . . . .	76
5.12	Out-of-loop relative power noise measured as an amplitude spectral density and as a CSD. . . . .	78
6.1	Illustration of a vacuum and a quadrature squeezed state. . . . .	85
6.2	Schematic setup of a balanced homodyne detector. . . . .	87
6.3	Simulations and measurements of the power modulation to homodyne detection transfer function. . . . .	90
6.4	Simplified schematic of the squeezing setup. . . . .	93
6.5	Homodyne measurements with the signal input from the linear OPA. . . . .	94
6.6	Homodyne measurements with the signal input from the bowtie OPA. . . . .	96
6.7	Quantum noise measurements from 10 kHz down to 0.5 Hz obtained with the bowtie OPA. . . . .	98
A.1	Simulink model of nonlinear noise coupling. . . . .	125
A.2	Current modulator schematics. . . . .	126

# A Appendix

For generating the setup drawings in this thesis, the ComponentLibrary was used [Fra]. FINESSE and PYKAT [Bro20] were used to simulate the cavity beam parameters, and the L<sup>A</sup>T<sub>E</sub>X template from reference [Pos] was used for the layout of this thesis.

The measurement data presented in this thesis is archived in a Git and is available on request at <https://gitlab.aei.uni-hannover.de/lasergroup/fathie/>

## A.1 Note on the terms classical and non-classical light

Throughout this thesis, the quantum mechanical properties of the light field are considered to explain, e.g., the shot noise, quantum radiation pressure noise, or squeezed states of light. Nevertheless, the light generated by a laser or a MOPA laser system is named ‘classical’, while the quadrature squeezed vacuum states of light are named ‘non-classical’. This naming is motivated by the different behavior of these quantum states.

The coherent states  $|\alpha\rangle$  (see Equation 6.7), which describe a quantum noise limited laser field, are categorized as classical, because most of their transformations by optics, like by a beam splitter, are equivalent to the results for a non-quantum mechanical description. In the case of a coherent input field (and the vacuum state on the other input), the output fields behind a beam splitter are just two independent coherent states with reduced coherent amplitudes.

Apart from this example, a spitted squeezed field results in two entangled fields, which means that there is no quantum mechanic description of one output field without taking the other field into account. Measurements of one output field can show correlations of the quantum noise with measurements of the other output field [GK04].

For a more general and mathematical definition, the quasi-probability distribution  $P(\alpha)$  in phase-space, called Glauber–Sudarshan function, is introduced to describe the density operator of a quantum state

$$\hat{\rho} = \int P(\alpha) |\alpha\rangle\langle\alpha| d^2\alpha \tag{A.1}$$

in the base of the coherent states  $|\alpha\rangle$  [GK04].

Gerry and Knight [GK04] specify based on this definition: “States for which  $P(\alpha)$  is positive everywhere or no more singular than a delta function, are classical whereas those for which  $P(\alpha)$  is negative or more singular than a delta function are nonclassical.”

For classical states,  $P(\alpha)$  can be interpreted as a probability density. For example, a coherent state with amplitude  $\beta$  is described by  $P(\alpha) = \delta^2(\alpha - \beta)$  [GK04].  $P(\alpha)$  for a quadrature squeezed state shows regions of negative values and, thus, can not be interpreted as a probability density [Spe16; GK04].



## A.2 Merging data from different signal whitening stages

The laser noise spectral densities presented in chapters 3, 4, and 5 were measured over different frequency bins and stitched together for a high data point density in the logarithmic plots. In addition, different signal whitening circuits were used to reach, depending on the measurement parameters and the frequency bin, the best clearance from dark noise. In the post-processing, the data is normalized with transfer functions of the whitening circuits.

Nevertheless, small deviations of the characterized and actual transfer functions of the whitening circuits and different dark noise clearance margins result in small steps at the transitions, which can be seen figures of Chapter 4.

In Chapter 5, an additional post-processing step has been applied to the data: The data traces  $d_i(f)$  of the spectral densities are multiplied by real weighting functions  $0 < w_i(f) < 1$  to guarantee a smooth transition. They were chosen so that

$$\sum_i w_i(f) = 1 , \quad (\text{A.2})$$

for all measurement frequencies  $f$ . The final data trace  $d(f)$  is calculated as

$$d(f) = \sum_i d_i(f)w_i(f) . \quad (\text{A.3})$$

For the presented measurements in Chapter 5, the higher weighting function  $w_1(f)$  was chosen as the product of two first-order high-pass filter:

$$w_1(f) = \frac{f^2}{f_c^2 + f^2} , \quad (\text{A.4})$$

$f_c$  is the corner frequency for the transition between the two weighting functions. The lower weighting function is then constructed by  $w_2(f) = 1 - w_1(f)$ .

The corner frequency  $f_c$  is adjusted for the transient at the point where the dark noise clearance and calibration certainty is similar for both whitening electronics.

For the measured laser power noise, the corner frequencies are 3 kHz to hand off from the measurement with the aLIGO like data acquisition system to a Moku:Lab and at 10 MHz to change between the AC stage in the photodiode electronics to the RF stage. In the case of the laser frequency noise, the corner frequency is at 3 kHz to hand off from the measurement with the aLIGO like data acquisition system to the Moku:Lab.

The data traces are linearly interpolated between neighbor data points for data points on a joint frequency base. The scrips are available on request at

<https://gitlab.aei.uni-hannover.de/lasergroup/fathie/-/blob/master/Laser1550/DBBcharacterization/plots/Interpolated>.



### A.3 Nonlinear noise coupling simulation

With the program Simulink, a part of Matlab2016b, a noise source and a nonlinear noise coupling mechanism were simulated using its DSP library. Here random time data is generated and processed, as depicted in Figure A.1.

The simulation file is available on request at

<https://gitlab.aei.uni-hannover.de/lasergroup/fathie/-/blob/master/Simulations/SimulinkNonlinearNoise/NonlinearNoiseCoupling3.slx>.

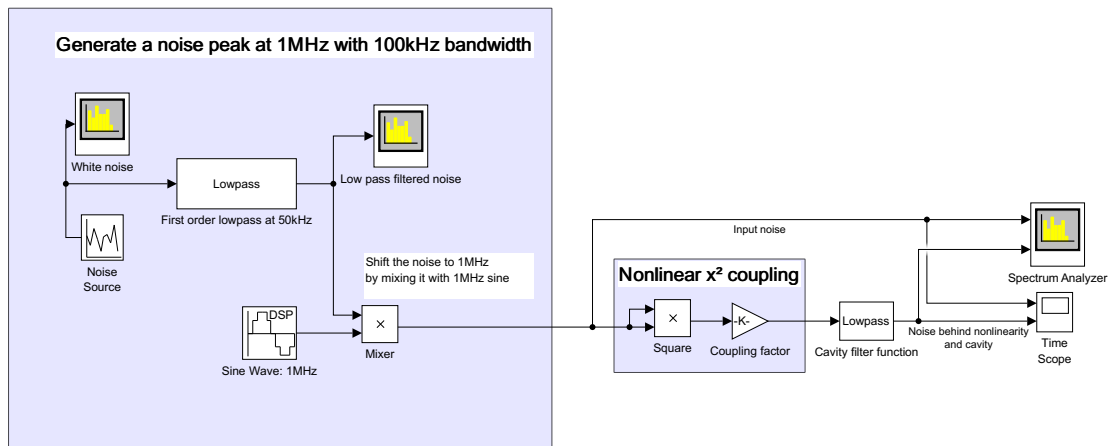


**Figure A.1:** To generate a noise peak around 1 MHz, low-pass filtered white noise is mixed with a sinusoidal signal at 1 MHz. The pole frequency of the low-pass filter corresponds to half of the noise bandwidth of the peak. The generated noise is measured and sent to a multiplier used to square the signal. The spectral density of the squared time signal is measured again.



## Publications

### First author publications

1. Meylahn, F., N. Knust, and B. Willke: ‘Stabilized laser system at 1550 nm wavelength for future gravitational-wave detectors’. *Phys. Rev. D* (12 June 2022), vol. 105: p. 122004. DOI: 10.1103/PhysRevD.105.122004. URL: <https://link.aps.org/doi/10.1103/PhysRevD.105.122004>.
2. Meylahn, F. and B. Willke: ‘Characterization of Laser Systems at 1550 nm Wavelength for Future Gravitational Wave Detectors’. *Instruments* (2022), vol. 6(1). ISSN: 2410-390X. DOI: 10.3390/instruments6010015. URL: <https://www.mdpi.com/2410-390X/6/1/15>.
3. Meylahn, F., B. Willke, and H. Vahlbruch: ‘Squeezed States of Light for Future Gravitational Wave Detectors at a Wavelength of 1550 nm’. *Phys. Rev. Lett.* (12 Sept. 2022), vol. 129: p. 121103. DOI: 10.1103/PhysRevLett.129.121103. URL: <https://link.aps.org/doi/10.1103/PhysRevLett.129.121103>.
4. Thies, F. et al.: ‘Nd:YVO4 high-power master oscillator power amplifier laser system for second-generation gravitational wave detectors’. *Opt. Lett.* (Feb. 2019), vol. 44(3): pp. 719–722. DOI: 10.1364/OL.44.000719.

### Other publications

1. Bode, N., F. Meylahn, and B. Willke: ‘Sequential high power laser amplifiers for gravitational wave detection’. *Opt. Express* (Sept. 2020), vol. 28(20): pp. 29469–29478. DOI: 10.1364/OE.401826.
2. Wellmann, F. et al.: ‘Performance study of a high-power single-frequency fiber amplifier architecture for gravitational wave detectors’. *Applied Optics* (Sept. 2020), vol. 59(26): p. 7945. DOI: 10.1364/ao.401048.
3. Wellmann, F. et al.: ‘High power, single-frequency, monolithic fiber amplifier for the next generation of gravitational wave detectors’. *Optics Express* (Sept. 2019), vol. 27(20): p. 28523. DOI: 10.1364/oe.27.028523.
4. Schönbeck, A., F. Thies, and R. Schnabel: ‘13dB squeezed vacuum states at 1550nm from 12mW external pump power at 775nm’. *Opt. Lett.* (Jan. 2018), vol. 43(1): pp. 110–113. DOI: 10.1364/OL.43.000110.

## Collaboration publications

1. Abbott, R. et al.: ‘Constraints on dark photon dark matter using data from LIGO’s and Virgo’s third observing run’. *Phys. Rev. D* (2022), vol. 105(6): p. 063030. DOI: 10.1103/PhysRevD.105.063030. arXiv: 2105.13085 [astro-ph.CO].
2. Abbott, R. et al.: *First joint observation by the underground gravitational-wave detector, KAGRA, with GEO600*. Mar. 2022. DOI: 10.48550/arXiv.2203.01270. arXiv: 2203.01270 [gr-qc].
3. Abbott, R. et al.: *Model-based cross-correlation search for gravitational waves from the low-mass X-ray binary Scorpius X-1 in LIGO O3 data*. Sept. 2022. DOI: 10.48550/arXiv.2209.02863. arXiv: 2209.02863 [astro-ph.HE].
4. Abbott, R. et al.: ‘Narrowband Searches for Continuous and Long-duration Transient Gravitational Waves from Known Pulsars in the LIGO-Virgo Third Observing Run’. *The Astrophysical Journal* (June 2022), vol. 932(2): p. 133. DOI: 10.3847/1538-4357/ac6ad0.
5. Abbott, R. et al.: ‘Search for continuous gravitational wave emission from the Milky Way center in O3 LIGO-Virgo data’. *Physical Review D* (Aug. 2022), vol. 106(4): p. 042003. DOI: 10.1103/physrevd.106.042003.
6. Abbott, R. et al.: *Search for Gravitational Waves Associated with Fast Radio Bursts Detected by CHIME/FRB During the LIGO–Virgo Observing Run O3a*. Mar. 2022. DOI: 10.48550/arXiv.2203.12038. arXiv: 2203.12038 [astro-ph.HE].
7. Abbott, R. et al.: ‘Search for Gravitational Waves Associated with Gamma-Ray Bursts Detected by Fermi and Swift during the LIGO–Virgo Run O3b’. *Astrophys. J.* (2022), vol. 928(2): p. 186. DOI: 10.3847/1538-4357/ac532b. arXiv: 2111.03608 [astro-ph.HE].
8. Abbott, R. et al.: *Search for gravitational waves from Scorpius X-1 with a hidden Markov model in O3 LIGO data*. Jan. 2022. DOI: 10.48550/arXiv.2201.10104. arXiv: 2201.10104 [gr-qc].
9. Abbott, R. et al.: ‘Search for intermediate mass black hole binaries in the third observing run of Advanced LIGO and Advanced Virgo’. *Astron. Astrophys.* (2022), vol. 659: A84. DOI: 10.1051/0004-6361/202141452. arXiv: 2105.15120 [astro-ph.HE].
10. Abbott, R. et al.: ‘Search for Substellar-Mass Binaries in the First Half of Advanced LIGO’s and Advanced Virgo’s Third Observing Run’. *Phys. Rev. Lett.* (6 Aug. 2022), vol. 129: p. 061104. DOI: 10.1103/PhysRevLett.129.061104. URL: <https://link.aps.org/doi/10.1103/PhysRevLett.129.061104>.
11. Abbott, R. et al.: ‘Search of the early O3 LIGO data for continuous gravitational waves from the Cassiopeia A and Vela Jr. supernova remnants’. *Phys. Rev. D* (2022), vol. 105(8): p. 082005. DOI: 10.1103/PhysRevD.105.082005. arXiv: 2111.15116 [gr-qc].

12. Abbott, R. et al.: ‘Searches for Gravitational Waves from Known Pulsars at Two Harmonics in the Second and Third LIGO–Virgo Observing Runs’. *Astrophys. J.* (May 2022), vol. 935(1). DOI: 10.3847/1538-4357/ac6acf.
13. Utina, A. et al.: *ETpathfinder: a cryogenic testbed for interferometric gravitational-wave detectors*. 2022. DOI: 10.48550/ARXIV.2206.04905. URL: <https://arxiv.org/abs/2206.04905>.
14. Abbott, B. P. et al.: ‘A Gravitational-wave Measurement of the Hubble Constant Following the Second Observing Run of Advanced LIGO and Virgo’. *Astrophys. J.* (2021), vol. 909(2): p. 218. DOI: 10.3847/1538-4357/abdc7. arXiv: 1908.06060 [astro-ph.CO].
15. Abbott, R. et al.: ‘All-sky search for continuous gravitational waves from isolated neutron stars in the early O3 LIGO data’. *Phys. Rev. D* (8 Oct. 2021), vol. 104: p. 082004. DOI: 10.1103/PhysRevD.104.082004. URL: <https://link.aps.org/doi/10.1103/PhysRevD.104.082004>.
16. Abbott, R. et al.: ‘All-sky search for gravitational wave emission from scalar boson clouds around spinning black holes in LIGO O3 data’. (Nov. 2021), vol. DOI: 10.1103/PhysRevD.105.102001. arXiv: 2111.15507 [astro-ph.HE].
17. Abbott, R. et al.: ‘All-sky search in early O3 LIGO data for continuous gravitational-wave signals from unknown neutron stars in binary systems’. *Phys. Rev. D* (2021), vol. 103: p. 064017. DOI: 10.1103/PhysRevD.103.064017. arXiv: 2012.12128 [gr-qc].
18. Abbott, R. et al.: ‘Constraints from LIGO O3 Data on Gravitational-wave Emission Due to R-modes in the Glitching Pulsar PSR J0537–6910’. *Astrophys. J.* (2021), vol. 922(1): p. 71. DOI: 10.3847/1538-4357/ac0d52. arXiv: 2104.14417 [astro-ph.HE].
19. Abbott, R. et al.: ‘Constraints on cosmic strings using data from the third Advanced LIGO–Virgo observing run’. *Phys. Rev. Lett.* (2021), vol. 126: p. 241102. DOI: 10.1103/PhysRevLett.126.241102. arXiv: 2101.12248 [gr-qc].
20. Abbott, R. et al.: *Constraints on the cosmic expansion history from GWTC-3*. Nov. 2021. DOI: 10.48550/ARXIV.2111.03604. arXiv: 2111.03604 [astro-ph.CO].
21. Abbott, R. et al.: ‘Diving below the spin-down limit: Constraints on gravitational waves from the energetic young pulsar PSR J0537-6910’. *Astrophys. J.* (2021), vol. 913: p. L27. DOI: 10.3847/2041-8213/abffcd. arXiv: 2012.12926 [astro-ph.HE].
22. Abbott, R. et al.: ‘GWTC-2: Compact Binary Coalescences Observed by LIGO and Virgo During the First Half of the Third Observing Run’. *Phys. Rev. X* (2021), vol. 11: p. 021053. DOI: 10.1103/PhysRevX.11.021053. arXiv: 2010.14527 [gr-qc].
23. Abbott, R. et al.: *GWTC-2.1: Deep Extended Catalog of Compact Binary Coalescences Observed by LIGO and Virgo During the First Half of the Third Observing Run*. Aug. 2021. DOI: 10.48550/arXiv.2108.01045. arXiv: 2108.01045 [gr-qc].

24. Abbott, R. et al.: *GWTC-3: Compact Binary Coalescences Observed by LIGO and Virgo During the Second Part of the Third Observing Run*. Nov. 2021. DOI: 10.48550/arXiv.2111.03606. arXiv: 2111.03606 [gr-qc].
25. Abbott, R. et al.: ‘Observation of gravitational waves from two neutron star-black hole coalescences’. *Astrophys. J. Lett.* (2021), vol. 915: p. L5. DOI: 10.3847/2041-8213/ac082e. arXiv: 2106.15163 [astro-ph.HE].
26. Abbott, R. et al.: ‘Open data from the first and second observing runs of Advanced LIGO and Advanced Virgo’. *SoftwareX* (2021), vol. 13: p. 100658. DOI: 10.1016/j.softx.2021.100658. arXiv: 1912.11716 [gr-qc].
27. Abbott, R. et al.: ‘Population Properties of Compact Objects from the Second LIGO-Virgo Gravitational-Wave Transient Catalog’. *Astrophys. J. Lett.* (2021), vol. 913(1): p. L7. DOI: 10.3847/2041-8213/abe949. arXiv: 2010.14533 [astro-ph.HE].
28. Abbott, R. et al.: ‘Search for continuous gravitational waves from 20 accreting millisecond X-ray pulsars in O3 LIGO data’. *Phys. Rev. D* (2021), vol. 105(2): p. 022002. DOI: 10.1103/PhysRevD.105.022002. arXiv: 2109.09255 [astro-ph.HE].
29. Abbott, R. et al.: ‘Search for Gravitational Waves Associated with Gamma-Ray Bursts Detected by Fermi and Swift During the LIGO-Virgo Run O3a’. *Astrophys. J.* (2021), vol. 915(2): p. 86. DOI: 10.3847/1538-4357/abee15. arXiv: 2010.14550 [astro-ph.HE].
30. Abbott, R. et al.: ‘Search for Lensing Signatures in the Gravitational-Wave Observations from the First Half of LIGO–Virgo’s Third Observing Run’. *Astrophys. J.* (2021), vol. 923(1): p. 14. DOI: 10.3847/1538-4357/ac23db. arXiv: 2105.06384 [gr-qc].
31. Abbott, R. et al.: ‘Searches for Continuous Gravitational Waves from Young Supernova Remnants in the Early Third Observing Run of Advanced LIGO and Virgo’. *Astrophys. J.* (2021), vol. 921(1): p. 80. DOI: 10.3847/1538-4357/ac17ea. arXiv: 2105.11641 [astro-ph.HE].
32. Abbott, R. et al.: ‘Tests of general relativity with binary black holes from the second LIGO-Virgo gravitational-wave transient catalog’. *Phys. Rev. D* (2021), vol. 103(12): p. 122002. DOI: 10.1103/PhysRevD.103.122002. arXiv: 2010.14529 [gr-qc].
33. Abbott, R. et al.: *Tests of General Relativity with GWTC-3*. Dec. 2021. DOI: 10.48550/arXiv.2112.06861. arXiv: 2112.06861 [gr-qc].
34. Abbott, R. et al.: *The population of merging compact binaries inferred using gravitational waves through GWTC-3*. Nov. 2021. DOI: 10.48550/arXiv.2111.03634. arXiv: 2111.03634 [astro-ph.HE].
35. McCuller, L. et al.: ‘LIGO’s quantum response to squeezed states’. *Phys. Rev. D* (6 Sept. 2021), vol. 104: p. 062006. DOI: 10.1103/PhysRevD.104.062006. URL: <https://link.aps.org/doi/10.1103/PhysRevD.104.062006>.

36. Abbott, B. P. et al.: ‘A guide to LIGO–Virgo detector noise and extraction of transient gravitational-wave signals’. *Class. Quant. Grav.* (2020), vol. 37(5): p. 055002. DOI: 10.1088/1361-6382/ab685e. arXiv: 1908.11170 [gr-qc].
37. Abbott, B. P. et al.: ‘GW190425: Observation of a Compact Binary Coalescence with Total Mass  $\sim 3.4M_{\odot}$ ’. *Astrophys. J. Lett.* (2020), vol. 892: p. L3. DOI: 10.3847/2041-8213/ab75f5. arXiv: 2001.01761 [astro-ph.HE].
38. Abbott, B. P. et al.: ‘Model comparison from LIGO–Virgo data on GW170817’s binary components and consequences for the merger remnant’. *Class. Quant. Grav.* (2020), vol. 37(4): p. 045006. DOI: 10.1088/1361-6382/ab5f7c. arXiv: 1908.01012 [gr-qc].
39. Abbott, B. P. et al.: ‘Optically targeted search for gravitational waves emitted by core-collapse supernovae during the first and second observing runs of advanced LIGO and advanced Virgo’. *Phys. Rev. D* (2020), vol. 101(8): p. 084002. DOI: 10.1103/PhysRevD.101.084002. arXiv: 1908.03584 [astro-ph.HE].
40. Abbott, R. et al.: ‘Gravitational-wave constraints on the equatorial ellipticity of millisecond pulsars’. *Astrophys. J. Lett.* (2020), vol. 902: p. L21. DOI: 10.3847/2041-8213/abb655. arXiv: 2007.14251 [astro-ph.HE].
41. Abbott, R. et al.: ‘GW190412: Observation of a Binary-Black-Hole Coalescence with Asymmetric Masses’. *Phys. Rev. D* (2020), vol. 102(4): p. 043015. DOI: 10.1103/PhysRevD.102.043015. arXiv: 2004.08342 [astro-ph.HE].
42. Abbott, R. et al.: ‘GW190521: A Binary Black Hole Merger with a Total Mass of  $150 M_{\odot}$ ’. *Phys. Rev. Lett.* (2020), vol. 125: p. 101102. DOI: 10.1103/PhysRevLett.125.101102. arXiv: 2009.01075 [gr-qc].
43. Abbott, R. et al.: ‘GW190814: Gravitational Waves from the Coalescence of a 23 Solar Mass Black Hole with a 2.6 Solar Mass Compact Object’. *Astrophys. J.* (2020), vol. 896(2): p. L44. DOI: 10.3847/2041-8213/ab960f. arXiv: 2006.12611 [astro-ph.HE].
44. Abbott, R. et al.: ‘Properties and astrophysical implications of the 150 Msun binary black hole merger GW190521’. *Astrophys. J. Lett.* (2020), vol. 900: p. L13. DOI: 10.3847/2041-8213/aba493. arXiv: 2009.01190 [astro-ph.HE].
45. Buikema, A. et al.: ‘Sensitivity and performance of the Advanced LIGO detectors in the third observing run’. *Phys. Rev. D* (6 Sept. 2020), vol. 102: p. 062003. DOI: 10.1103/PhysRevD.102.062003. URL: <https://link.aps.org/doi/10.1103/PhysRevD.102.062003>.
46. Hamburg, R. et al.: ‘A Joint Fermi-GBM and LIGO/Virgo Analysis of Compact Binary Mergers From the First and Second Gravitational-wave Observing Runs’. *Astrophys. J.* (2020), vol. 893: p. 100. DOI: 10.3847/1538-4357/ab7d3e. arXiv: 2001.00923 [astro-ph.HE].



47. Abbott, B. P. et al.: ‘All-sky search for continuous gravitational waves from isolated neutron stars using Advanced LIGO O2 data’. *Phys. Rev. D* (2019), vol. 100(2): p. 024004. DOI: 10.1103/PhysRevD.100.024004. arXiv: 1903.01901 [astro-ph.HE].
48. Abbott, B. P. et al.: ‘All-sky search for long-duration gravitational-wave transients in the second Advanced LIGO observing run’. *Phys. Rev. D* (2019), vol. 99(10): p. 104033. DOI: 10.1103/PhysRevD.99.104033. arXiv: 1903.12015 [gr-qc].
49. Abbott, B. P. et al.: ‘All-Sky Search for Short Gravitational-Wave Bursts in the Second Advanced LIGO and Advanced Virgo Run’. *Phys. Rev. D* (2019), vol. 100(2): p. 024017. DOI: 10.1103/PhysRevD.100.024017. arXiv: 1905.03457 [gr-qc].
50. Abbott, B. P. et al.: ‘Binary Black Hole Population Properties Inferred from the First and Second Observing Runs of Advanced LIGO and Advanced Virgo’. *Astrophys. J. Lett.* (2019), vol. 882(2): p. L24. DOI: 10.3847/2041-8213/ab3800. arXiv: 1811.12940 [astro-ph.HE].
51. Abbott, B. P. et al.: ‘Constraining the  $p$ -Mode- $g$ -Mode Tidal Instability with GW170817’. *Phys. Rev. Lett.* (2019), vol. 122(6): p. 061104. DOI: 10.1103/PhysRevLett.122.061104. arXiv: 1808.08676 [astro-ph.HE].
52. Abbott, B. P. et al.: ‘Directional limits on persistent gravitational waves using data from Advanced LIGO’s first two observing runs’. *Phys. Rev. D* (2019), vol. 100(6): p. 062001. DOI: 10.1103/PhysRevD.100.062001. arXiv: 1903.08844 [gr-qc].
53. Abbott, B. P. et al.: ‘GWTC-1: A Gravitational-Wave Transient Catalog of Compact Binary Mergers Observed by LIGO and Virgo during the First and Second Observing Runs’. *Phys. Rev. X* (2019), vol. 9(3): p. 031040. DOI: 10.1103/PhysRevX.9.031040. arXiv: 1811.12907 [astro-ph.HE].
54. Abbott, B. P. et al.: ‘Low-latency Gravitational-wave Alerts for Multimessenger Astronomy during the Second Advanced LIGO and Virgo Observing Run’. *Astrophys. J.* (2019), vol. 875(2): p. 161. DOI: 10.3847/1538-4357/ab0e8f. arXiv: 1901.03310 [astro-ph.HE].
55. Abbott, B. P. et al.: ‘Narrow-band search for gravitational waves from known pulsars using the second LIGO observing run’. *Phys. Rev. D* (2019), vol. 99(12): p. 122002. DOI: 10.1103/PhysRevD.99.122002. arXiv: 1902.08442 [gr-qc].
56. Abbott, B. P. et al.: ‘Properties of the binary neutron star merger GW170817’. *Phys. Rev. X* (2019), vol. 9(1): p. 011001. DOI: 10.1103/PhysRevX.9.011001. arXiv: 1805.11579 [gr-qc].
57. Abbott, B. P. et al.: ‘Search for Eccentric Binary Black Hole Mergers with Advanced LIGO and Advanced Virgo during their First and Second Observing Runs’. *Astrophys. J.* (2019), vol. 883(2): p. 149. DOI: 10.3847/1538-4357/ab3c2d. arXiv: 1907.09384 [astro-ph.HE].
58. Abbott, B. P. et al.: ‘Search for gravitational waves from a long-lived remnant of the binary neutron star merger GW170817’. *Astrophys. J.* (2019), vol. 875(2): p. 160. DOI: 10.3847/1538-4357/ab0f3d. arXiv: 1810.02581 [gr-qc].



59. Abbott, B. P. et al.: ‘Search for gravitational waves from Scorpius X-1 in the second Advanced LIGO observing run with an improved hidden Markov model’. *Phys. Rev. D* (2019), vol. 100(12): p. 122002. DOI: 10.1103/PhysRevD.100.122002. arXiv: 1906.12040 [gr-qc].
60. Abbott, B. P. et al.: ‘Search for gravitational-wave signals associated with gamma-ray bursts during the second observing run of Advanced LIGO and Advanced Virgo’. *Astrophys. J.* (2019), vol. 886: p. 75. DOI: 10.3847/1538-4357/ab4b48. arXiv: 1907.01443 [astro-ph.HE].
61. Abbott, B. P. et al.: ‘Search for intermediate mass black hole binaries in the first and second observing runs of the Advanced LIGO and Virgo network’. *Phys. Rev. D* (2019), vol. 100(6): p. 064064. DOI: 10.1103/PhysRevD.100.064064. arXiv: 1906.08000 [gr-qc].
62. Abbott, B. P. et al.: ‘Search for Substellar Mass Ultracompact Binaries in Advanced LIGO’s Second Observing Run’. *Phys. Rev. Lett.* (2019), vol. 123(16): p. 161102. DOI: 10.1103/PhysRevLett.123.161102. arXiv: 1904.08976 [astro-ph.CO].
63. Abbott, B. P. et al.: ‘Search for the isotropic stochastic background using data from Advanced LIGO’s second observing run’. *Phys. Rev. D* (2019), vol. 100(6): p. 061101. DOI: 10.1103/PhysRevD.100.061101. arXiv: 1903.02886 [gr-qc].
64. Abbott, B. P. et al.: ‘Search for Transient Gravitational-wave Signals Associated with Magnetar Bursts during Advanced LIGO’s Second Observing Run’. *Astrophys. J.* (2019), vol. 874(2): p. 163. DOI: 10.3847/1538-4357/ab0e15. arXiv: 1902.01557 [astro-ph.HE].
65. Abbott, B. P. et al.: ‘Searches for Continuous Gravitational Waves from 15 Supernova Remnants and Fomalhaut b with Advanced LIGO’. *Astrophys. J.* (2019), vol. 875(2): p. 122. DOI: 10.3847/1538-4357/ab113b. arXiv: 1812.11656 [astro-ph.HE].
66. Abbott, B. P. et al.: ‘Searches for Gravitational Waves from Known Pulsars at Two Harmonics in 2015-2017 LIGO Data’. *Astrophys. J.* (2019), vol. 879(1): p. 10. DOI: 10.3847/1538-4357/ab20cb. arXiv: 1902.08507 [astro-ph.HE].
67. Abbott, B. P. et al.: ‘Tests of General Relativity with GW170817’. *Phys. Rev. Lett.* (2019), vol. 123(1): p. 011102. DOI: 10.1103/PhysRevLett.123.011102. arXiv: 1811.00364 [gr-qc].
68. Abbott, B. P. et al.: ‘Tests of General Relativity with the Binary Black Hole Signals from the LIGO-Virgo Catalog GWTC-1’. *Phys. Rev. D* (2019), vol. 100(10): p. 104036. DOI: 10.1103/PhysRevD.100.104036. arXiv: 1903.04467 [gr-qc].
69. Albert, A. et al.: ‘Search for Multimessenger Sources of Gravitational Waves and High-energy Neutrinos with Advanced LIGO during Its First Observing Run, ANTARES, and IceCube’. *Astrophys. J.* (2019), vol. 870(2): p. 134. DOI: 10.3847/1538-4357/aaf21d. arXiv: 1810.10693 [astro-ph.HE].

70. Burns, E. et al.: ‘A Fermi Gamma-ray Burst Monitor Search for Electromagnetic Signals Coincident with Gravitational-Wave Candidates in Advanced LIGO’s First Observing Run’. *Astrophys. J.* (2019), vol. 871(1): p. 90. DOI: 10.3847/1538-4357/aaf726. arXiv: 1810.02764 [astro-ph.HE].
71. Soares-Santos, M. et al.: ‘First Measurement of the Hubble Constant from a Dark Standard Siren using the Dark Energy Survey Galaxies and the LIGO/Virgo Binary–Black-hole Merger GW170814’. *Astrophys. J. Lett.* (2019), vol. 876(1): p. L7. DOI: 10.3847/2041-8213/ab14f1. arXiv: 1901.01540 [astro-ph.CO].
72. Tse, M. et al.: ‘Quantum-Enhanced Advanced LIGO Detectors in the Era of Gravitational-Wave Astronomy’. *Phys. Rev. Lett.* (23 Dec. 2019), vol. 123: p. 231107. DOI: 10.1103/PhysRevLett.123.231107. URL: <https://link.aps.org/doi/10.1103/PhysRevLett.123.231107>.
73. Abbott, B. P. et al.: ‘Full Band All-sky Search for Periodic Gravitational Waves in the O1 LIGO Data’. *Phys. Rev. D* (2018), vol. 97(10): p. 102003. DOI: 10.1103/PhysRevD.97.102003. arXiv: 1802.05241 [gr-qc].
74. Abbott, B. P. et al.: ‘GW170817: Implications for the Stochastic Gravitational-Wave Background from Compact Binary Coalescences’. *Phys. Rev. Lett.* (2018), vol. 120(9): p. 091101. DOI: 10.1103/PhysRevLett.120.091101. arXiv: 1710.05837 [gr-qc].
75. Abbott, B. P. et al.: ‘GW170817: Measurements of neutron star radii and equation of state’. *Phys. Rev. Lett.* (2018), vol. 121(16): p. 161101. DOI: 10.1103/PhysRevLett.121.161101. arXiv: 1805.11581 [gr-qc].
76. Abbott, B. P. et al.: ‘Prospects for Observing and Localizing Gravitational-Wave Transients with Advanced LIGO, Advanced Virgo and KAGRA’. *Living Rev. Rel.* (2018), vol. 21(1): p. 3. DOI: 10.1007/s41114-018-0012-9. arXiv: 1304.0670 [gr-qc].
77. Abbott, B. P. et al.: ‘Search for Subsolar-Mass Ultracompact Binaries in Advanced LIGO’s First Observing Run’. *Phys. Rev. Lett.* (2018), vol. 121(23): p. 231103. DOI: 10.1103/PhysRevLett.121.231103. arXiv: 1808.04771 [astro-ph.CO].
78. Abbott, B. P. et al.: ‘Search for Tensor, Vector, and Scalar Polarizations in the Stochastic Gravitational-Wave Background’. *Phys. Rev. Lett.* (2018), vol. 120(20): p. 201102. DOI: 10.1103/PhysRevLett.120.201102. arXiv: 1802.10194 [gr-qc].
79. Abbott, B. P. et al.: ‘A gravitational-wave standard siren measurement of the Hubble constant’. *Nature* (2017), vol. 551(7678): pp. 85–88. DOI: 10.1038/nature24471. arXiv: 1710.05835 [astro-ph.CO].
80. Abbott, B. P. et al.: ‘Estimating the Contribution of Dynamical Ejecta in the Kilonova Associated with GW170817’. *Astrophys. J. Lett.* (2017), vol. 850(2): p. L39. DOI: 10.3847/2041-8213/aa9478. arXiv: 1710.05836 [astro-ph.HE].

81. Abbott, B. P. et al.: ‘First narrow-band search for continuous gravitational waves from known pulsars in advanced detector data’. *Phys. Rev. D* (2017), vol. 96(12). [Erratum: *Phys.Rev.D* 97, 129903 (2018)]: p. 122006. DOI: 10.1103/PhysRevD.96.122006. arXiv: 1710.02327 [gr-qc].
82. Abbott, B. P. et al.: ‘Gravitational Waves and Gamma-rays from a Binary Neutron Star Merger: GW170817 and GRB 170817A’. *Astrophys. J. Lett.* (2017), vol. 848(2): p. L13. DOI: 10.3847/2041-8213/aa920c. arXiv: 1710.05834 [astro-ph.HE].
83. Abbott, B. P. et al.: ‘GW170608: Observation of a 19-solar-mass Binary Black Hole Coalescence’. *Astrophys. J.* (2017), vol. 851(2): p. L35. DOI: 10.3847/2041-8213/aa9f0c. arXiv: 1711.05578 [astro-ph.HE].
84. Abbott, B. P. et al.: ‘GW170814: A Three-Detector Observation of Gravitational Waves from a Binary Black Hole Coalescence’. *Phys. Rev. Lett.* (2017), vol. 119(14): p. 141101. DOI: 10.1103/PhysRevLett.119.141101. arXiv: 1709.09660 [gr-qc].
85. Abbott, B. P. et al.: ‘GW170817: Observation of Gravitational Waves from a Binary Neutron Star Inspiral’. *Phys. Rev. Lett.* (2017), vol. 119(16): p. 161101. DOI: 10.1103/PhysRevLett.119.161101. arXiv: 1710.05832 [gr-qc].
86. Abbott, B. P. et al.: ‘Multi-messenger Observations of a Binary Neutron Star Merger’. *Astrophys. J. Lett.* (2017), vol. 848(2): p. L12. DOI: 10.3847/2041-8213/aa91c9. arXiv: 1710.05833 [astro-ph.HE].
87. Abbott, B. P. et al.: ‘On the Progenitor of Binary Neutron Star Merger GW170817’. *Astrophys. J. Lett.* (2017), vol. 850(2): p. L40. DOI: 10.3847/2041-8213/aa93fc. arXiv: 1710.05838 [astro-ph.HE].
88. Abbott, B. P. et al.: ‘Search for Post-merger Gravitational Waves from the Remnant of the Binary Neutron Star Merger GW170817’. *Astrophys. J. Lett.* (2017), vol. 851(1): p. L16. DOI: 10.3847/2041-8213/aa9a35. arXiv: 1710.09320 [astro-ph.HE].
89. Albert, A. et al.: ‘Search for High-energy Neutrinos from Binary Neutron Star Merger GW170817 with ANTARES, IceCube, and the Pierre Auger Observatory’. *Astrophys. J. Lett.* (2017), vol. 850(2): p. L35. DOI: 10.3847/2041-8213/aa9aed. arXiv: 1710.05839 [astro-ph.HE].



# Curriculum Vitae

## Personal Information

---

Fabian Pascal Meylahn,  
birth name Thies

Born on March 25th, 1992 in Filderstadt, Germany

## University Studies

---

since 10/2016	Doctoral studies in Physics Max Planck Institute for Gravitational Physics and Institute for Gravitational Physics, Leibniz Universität Hannover, Germany
10/2014 - 09/2016	Master of Science in Physics Leibniz Universität Hannover, Germany
04/2012 - 09/2014	Bachelor of Science in Physics Leibniz Universität Hannover, Germany
10/2011 - 03/2012	Bachelor of Science in Physics Universität Hamburg, Germany

## Education

---

06/2011	Abitur Rudolf-Steiner-Schule Hamburg-Bergedorf, Germany
---------	--

Hannover, 26. September 2022

